Measurements of ICRF Power Deposition and Thermal Transport with an ECE Grating Polychromator on the Alcator C-Mod Tokamak

by

Peter Joseph Larkin O'Shea

B.E., University of Saskatchewan (1988)

Submitted to the Department of Physics
in partial fulfillment of the requirements for the degree of

Doctor of Philosophy in Physics

at the

MASSACHUSETTS INSTITUTE OF TECHNOLOGY

March 1997

Author .....
Department of Physics
March 30, 1997

Certified by .....
Professor Miklos Porkolab
Director of the Plasma Science & Fusion Center
Thesis Supervisor

Certified by .....
Dr. Amanda Hubbard
Alcator C-Mod Research Scientist
Thesis Supervisor

Accepted by .....
Dr. George Koster
Chairman, Departmental Committee on Graduate Students

Measurements of ICRF Power Deposition and Thermal Transport with an ECE Grating Polychromator on the Alcator C-Mod Tokamak

by

Peter Joseph Larkin O'Shea

Submitted to the Department of Physics
on March 30, 1997, in partial fulfillment of the
requirements for the degree of
Doctor of Philosophy in Physics

Abstract

ICRF provides Alcator C-Mod with up to 3.5 MW of power at 80 MHz using two double-strap antennas. By varying the magnetic field and the mix of ion species, a variety of heating regimes have been studied. To investigate electron heating regimes, mixtures of He^3 and H were used in plasmas at 6.5T. Efficient ($< 80\%$) direct electron heating has been observed in this scenario and is attributed to mode conversion to the ion Bernstein wave (IBW). Measurements of the mode conversion power deposition using a nine channel grating polychromator (GPC) indicate that the IBW damping can be very strong, with central power densities $> 25MW/m^3$ and FWHM widths of $\approx 0.2a$. The presence of $> 8\%$ deuterium "impurity" in these plasmas is shown to significantly broaden the power deposition profiles. The GPC has also been used to study the heating mechanisms in the two standard C-Mod heating scenarios: $D(H)$ and $D(He^3)$ minority heating at 5.3T and 7.9T respectively. Mode conversion can provide a significant fraction of the heating in $D(He^3)$ plasmas, with 60% efficiency and profiles which are peaked well off axis ($r/a \approx 0.6$) at the highest He^3 concentrations ($n_{He^3}/n_e \approx 0.2$). Data from $D(H)$ experiments illustrate techniques to measure minority ion tails using electron temperature dynamics. In addition, evidence is presented for $D(H)$ mode conversion heating at high hydrogen concentration.

Thesis Supervisor: Professor Miklos Porkolab
Title: Director of the Plasma Science & Fusion Center

Thesis Supervisor: Dr. Amanda Hubbard
Title: Alcator C-Mod Research Scientist

Acknowledgements

This thesis was not written in a vacuum [1], and I would like to thank here those people that helped make this experience a positive one (I apologize to anyone that I forget). I am generally grateful for all the help that I have received over the years from the scientists, engineers, technicians and staff that make up the excellent Alcator C-Mod team. Particular thanks are due to Bill Beck, Charlie Cauley, Ed Fitzgerald, and Frank Silva for their extra efforts to help me get things done at key times. I am glad to have been involved with the ECE system and am indebted to Tom Hsu and the group at the University of Maryland whose wonderful design skills have allowed a strong diagnostic set to be integrated. Many thanks to Charlie Lasnier for his help in carefully breaking down the GPC at Lawrence Livermore and his tips in resurrecting it at MIT. Thanks to Frank Shefton for his help keeping things cool ($\approx 4K$!). I am also very fortunate to have worked closely with the RF group, the successes of which are partially documented in this thesis. I am especially grateful for many fruitful discussions with Paul Bonoli and Yuichi Takase regarding the heating experiments and useful feedback on my analysis.

For help with everything from torquing flanges to detailed scrutiny of my thesis, I am very much indebted to my co-supervisor, Dr. Amanda Hubbard. Her kind words and occasional swift kick kept me moving through the tough patches. My thesis supervisor, Prof. Miklos Porkolab, has been an inspiration. His insights into plasma waves and tremendous memory and experience with heating experiments have provided important guidance for this thesis. His leadership of the RF group and tireless work as lab director have helped Alcator C-Mod continue to provide excellent research and maintain support through harsh budgetary cuts.

Fellow students at the fusion center have made the tough years bearable and the good years so much more enjoyable during my period at MIT. To Darren Garnier, Yongkyoon In, Dan Lo, Tom Luke, Rob Nachtrieb, Jim Reardon, Jeff Schachter, Gerry Tinios, thank you! Thanks to Bobby, Adam, JT, and Ben for helping to make

[1] Ask anyone that heard me scream.

running a special part of my time here. Thanks to Edi and Peter and Patty for topping a large and interesting cast of room-mates. Thanks to Tom Quinn, Bruce, and my fellow Caustic Rebels for helping me find hockey and finally become a whole Canadian. Thanks to Rosebud. Thanks to the H.C. gang of Tom, Bill, Steve, Dave, Joanne, Jen, Sheila, and Marie, whose enduring friendship I value greatly. Unlimited thanks are due to my adopted family, Mike, Susan, and Natalie-Rose. It wouldn't have happened without you guys. I am very proud and thankful for my family, and am happy to be number three in the wonderful jumble of characters that are the O'Shea kids. Most of all, thanks to my incredible parents whose courage, generosity, and support are the foundation of all that is good in my life.

For our children.

Contents

List of Figures

List of Tables

Chapter 1

Introduction

As with any thesis, the topics considered here will be specific and focussed. The work represented in this thesis however is a part of a large network of related efforts within the fusion community. In this section, the motivation for this thesis will be given in the context of the goal of this larger research effort which is a safe and longterm source of energy.

1.1 Energy and Fusion

Energy alternatives to fossil fuels have been actively sought since the energy crisis in the 1970's when the transient nature of the world's reserves was first widely appreciated. Although the crisis is over for now, the problems of exhaustibility and environmental impact still remain. Among the renewable resource options, only nuclear energy schemes have the potency required to replace fossil fuels and provide the bulk of the growing global energy demands into the foreseeable future. Both fusion and fission tap the immense energy bound in nuclei which is roughly a million times more concentrated than the chemical energy of conventional sources. The hazards of plant operation and the waste products of fission plants are similarly concentrated and this has influenced the wide belief in North America that fission is an unacceptable energy solution. Fusion energy has the same advantages as fission, without its dangers of plant meltdown, weapons proliferation, or long term waste problems. The

fusion energy potential represented by the deuterium in the world's oceans could support the current world consumption for billions of years. It is the goal of the fusion research community to develop reactors which economically exploit the advantages of fusion as an energy source.

Fusion is the energy source for the stars. The gravitational force of huge quantities of hydrogen creates high temperature and density in the stellar core. Thermal energies are so great that the electrons are stripped from the atomic nuclei creating a completely ionized material called a plasma. As the temperature increases, the distance of closest approach during collisions between the positively charged ions decreases. When the ions pass within the short range of influence of the nuclear force, they may fuse by undergoing one of the following nuclear reactions:

$$\begin{aligned} D + D &\longrightarrow T(1.01\text{MeV}) + p(3.02\text{MeV}) \\ D + D &\longrightarrow He^3(0.82\text{MeV}) + n(2.45\text{MeV}) \\ D + T &\longrightarrow He^4(3.5\text{MeV}) + n(14.1\text{MeV}) \\ D + He^3 &\longrightarrow He^4(3.6\text{MeV}) + p(14.7\text{MeV}) \end{aligned} \tag{1.1}$$

The energy released by these reactions is the energy source for the star. This energy makes its way to the surface where it is radiated away as light. Gravity compresses the core and increases the density. The energy released from the fusion reactions increases the temperature. The fusion reaction rates typically increase with both density and temperature, as does the outward pressure exerted by the plasma. The star thus reaches an equilibrium where the central pressure caused by the fusion process balances the crush of gravity. The light we see is the result of the inner fusion "fire" in which hydrogen is being "burned" to form helium "ash". Fusion reactor concepts here on earth seek to reproduce this stellar process on a much smaller scale and thus without the aid of gravity as a source of confinement. It is relatively easy to create fusion reactions in the laboratory, and the reaction processes described in Eq. 1.1 are well understood. Considering fusion as a potential source of power imposes very serious constraints on the reactor scheme employed. Many varied schemes have

been considered, but in the most promising, fusion occurs due to high energy collisions in a hot hydrogen plasma, as in the sun. In a laboratory or reactor, external heat must be applied to achieve the conditions necessary for the fusion process to begin. If part of the energy released from the fusion remains in the plasma and is sufficient to maintain the temperature, then the process can be sustained without further external heating. It is a goal of the fusion energy research community to achieve this "ignited" plasma condition in a reactor.

1.2 Magnetic Fusion

Fusion grade plasmas can reach temperatures in excess of 100 million degrees centigrade and can not be contained by any solid material. However the charged particles which make up a plasma are constrained to move largely along lines of magnetic field as sketched in Fig. 1-1. For this reason, containment schemes consisting of closed magnetic field line geometries have been pursued aggressively.

1.2.1 Tokamaks

The most promising magnetic fusion reactor concept is the *tokamak* [1], a toroidally [2] shaped field geometry, in which a large current is driven around the torus which both heats the plasma and establishes a helical twist to the magnetic field lines thus greatly enhancing particle and energy confinement. A thorough review of the major physics and engineering features of tokamaks is given by Wesson [1]. Chen [2] provides a more detailed overview of plasma physics. The basic geometry is shown in Fig. 1-2. Charged particles may circle the device freely, but must diffuse relatively slowly across the field lines to escape. Fusion reactors will use a 50-50 mixture of deuterium and tritium, and thus (see Eq. 1.1) the fusion products are positively charged He^4 (alpha particles) and neutrons. Neutrons are unaffected by the magnetic field and carry their energy out of the reactor where it can be absorbed and become available for

[1] Tokamak is a contraction from the Russian TOroidalnaya KAmera MAgnitaya Katushka, which roughly means toroidal chamber with magnetic coil.

[2] toroidal$\approx$ "doughnut shaped"

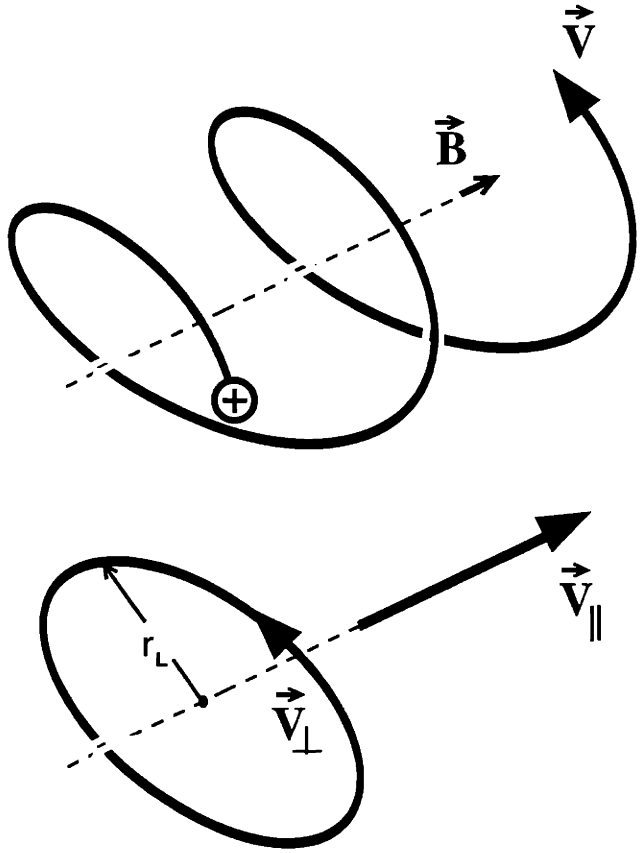

Figure 1-1: Sketch showing the motion of a charged particle in a uniform magnetic field. Motion perpendicular to the magnetic field is subject to a force $\propto q\ \mathbf{V} \times \mathbf{B}$ and results in circular orbits with the characteristic *cyclotron* frequency $\Omega \equiv qB/m$, with a size specified by the *Larmor* radius $r_L \equiv V_\perp/\Omega$. Motion parallel to the magnetic field is unaffected. The combined result as shown at the top is a spiral motion around the magnetic field.

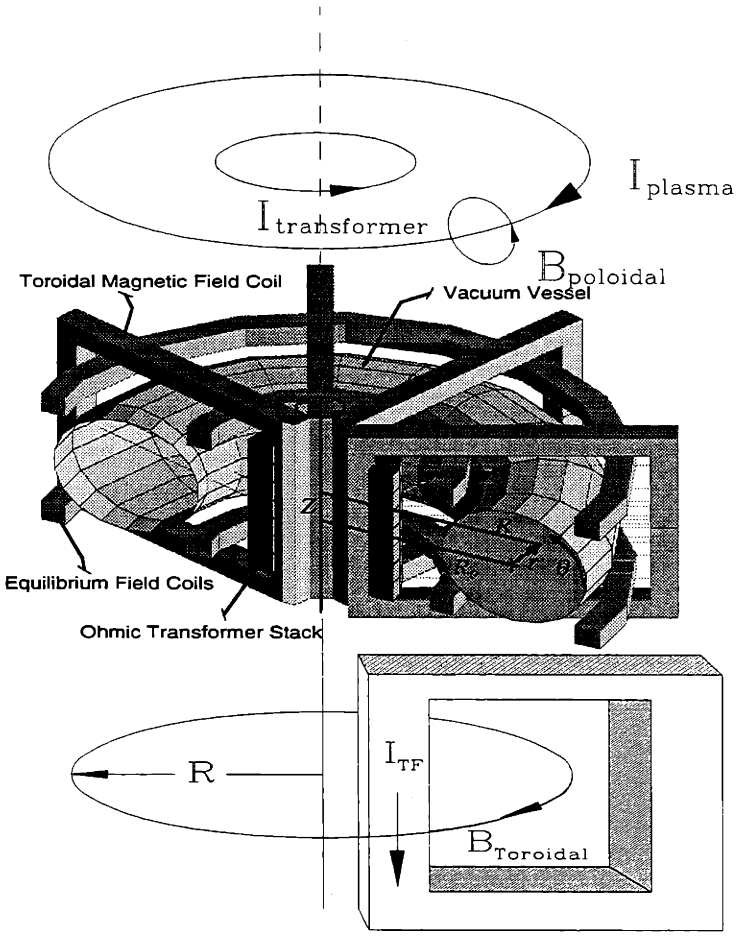

Figure 1-2: Cross section and schematics showing the distinguishing features of the tokamak. The toroidal field coils produce the dominant component of the containment field. The large plasma current driven by the transformer stack provides an essential poloidal component to the magnetic field in addition to ohmic heating for the discharge.

power production. The alpha particles are confined by the magnetic field and their portion of the fusion energy can heat the plasma through collisions. Through this mechanism the plasma can ignite and become a self sustaining fusion energy source. A simple condition, called Lawson's criterion [3], for achieving an ignited plasma can be derived from an energy balance analysis of a magnetically confined plasma. As a minimal requirement, the alpha fusion power source must balance the power losses due to radiation. As a result, there is a minimum requirement for the *fusion product* expressed below:

$$n_0 \tau_E \gtrsim 10^{20} [sec/m^3] \tag{1.2}$$

where: n_0 is the plasma density.

τ_E is the energy confinement time.

1.2.2 Auxiliary heating and energy confinement

Lawson's criterion implicitly assumes operation near the optimal temperature of $\sim$ 20 - 30keV. Tokamak plasmas are ohmically heated by their externally driven current. However the resistivity of a plasma decreases as the temperature increases ($\eta \propto T_e^{-3/2}$) and so for a given plasma current, the ohmic power input decreases as the temperature is raised. For this reason, so-called *auxiliary* heating sources are typically needed to approach optimal temperatures. Unfortunately, a universal observation on tokamaks has been that the energy confinement tends to degrade as external power is applied. This is described by the so-called Goldston [4] L-mode ("L" stands for "Low" energy confinement mode; see below.) scaling law: $\tau_E \propto (P_{ohmic} + P_{aux})^{-1/2}$. This trade off between increasing the plasma temperature with additional heating and reducing the energy confinement is of central importance to the design of future fusion reactors. An empirical scaling law representing the best fit to the international database of tokamak results has been established to quantify this result. It provides a prediction, based on basic plasma and engineering parameters, for the energy confinement time, $\tau_E \equiv W/P_{tot}$, where W is the total energy stored in the tokamak, and

P_{tot} is the total input power [5]:

$$\tau_{E\ ITER-89}(sec) = .048 \times I_p^{0.85} R_0^{1.2} a^{0.3} \kappa^{0.5} \langle n_e \rangle^{0.1} B_T^{0.2} A^{0.5} P_{tot}^{-0.5} \tag{1.3}$$

where I_p is the plasma current (MA), R_0 and a are the major and minor radii (m) of the tokamak, respectively, κ is the vertical elongation of the discharge, $\langle n_e \rangle$ is the average plasma density ($10^{20} m^{-3}$), B_T is the toroidal magnetic field (Tesla), and A is the atomic mass number of the plasma ions. As is implied by the need for empirical scaling laws, tokamak transport is currently not well explained theoretically. A major development in this decade has been the emergence of a distinct new mode of improved energy confinement called "H-mode" (H standing for "High" confinement). The "H" indicates that the energy confinement is significantly higher than that predicted by Eq. 1.3. Transitions to H-mode can be very sudden ($<$ 1 msec) and although conditions in the plasma edge appear to control the onset, the improved energy and particle confinement result in large increases in the central plasma pressure and the global stored energy ($\tau_H \lesssim 2.5\tau_L$ for Alcator C-Mod to date). A result emerging from international studies indicates the existance of a threshold for H-mode onset in the power density at the plasma edge (r = a). The use of auxilary power to exceed this threshold appears to be as effective as ohmic power, indicating that the relationship between auxilary power and energy confinement is very complicated.

The goal of this introduction to magnetic fusion is to indicate the key roles played and interrelations of auxiliary heating and energy confinement in tokamaks. Both subjects are topics of this thesis. Primary emphasis is placed on heating experiments with high power radio frequency waves. In Chapt. 10, the dynamics of thermal transport are examined using the externally launched wave power as a time dependent heat source.

1.2.3 Diagnostics of fusion plasmas

Many physics issues regarding the magnetic confinement of fusion plasmas remain unresolved and require intensive experimental study in order to indicate the dom-

inant effects involved. The harsh environment of fusion plasmas requires remote non-intrusive diagnostic techniques. The work in this thesis will rely most heavily on measurements of the plasma temperature and the principles and techniques involved are discussed in Chapts. 4 and 5.

1.2.4 Plasma waves

The study of fusion plasmas involves the consideration of the dynamics of a many-body system with long range particle interactions and large free energy. That these systems exhibit a rich spectrum of collective behavior comes as no surprise. Though complex, the theory of plasma waves has successfully described many phenomena of great importance to the advancement of fusion technology. Two distinct regimes of plasma waves play key roles in this thesis. The primary source of auxiliary power on Alcator C-Mod is ICRF wave heating (see Chapt. 1.3.2). The primary diagnostic tool for this thesis is an electron cyclotron wave emission (ECE) temperature diagnostic (see Chapt. 5.4). The unifying theory behind these two distinct wave applications will be described in Chapt. 2.

1.3 Alcator C-Mod

1.3.1 Alcator C-Mod parameters

Alcator C-Mod is the third in a series of tokamaks built and operated at the MIT Plasma Fusion Center [6]. The most distinguishing feature of these tokamaks is a particularly high toroidal magnetic field[3]. This feature allows very high plasma densities to be achieved, and values for the fusion product to rival that at other much larger (and more expensive) tokamaks throughout the world. For this reason, Alcator C-Mod is often described as a *compact high performance* tokamak. The plasma parameters are given in table 1.1. Figure 1-3 shows the Alcator C-Mod tokamak in cross section.

[3]Alcator is an contraction from the Italian ALto CAmpo TORus meaning high field torus.

Parameter	*Standard Symbol*	*Achieved (Max.) Value*	*units*
Major Radius	R_0	0.67	m
Minor Radius	a	0.21	m
Magnetic Field	B_T	7.9 (9)	T
Plasma Current	I_p	1.2 (3)	MA
Electron Density	n_e	$\leqslant 1.1 \times 10^{21}$	m^{-3}
Electron Temperature	T_e	$\leqslant 6$	keV
Ion Temperature	T_i	$\leqslant 4.5$	keV
Auxiliary Heating	P_{ICRF}	3.5 (8)*	MW
Elongation	κ	0.95 - 1.85	
Current Flattop Time		~ 1	s

* planned.

Table 1.1: Alcator C-Mod plasma parameters.

1.3.2 ICRF Heating

Auxiliary heating on Alcator C-Mod is provided by ion cyclotron range of frequency (ICRF) heating. Currently, two 80 MHz transmitters deliver up to 3.5 megawatts of power to two double-strap antennas. These antennas are designed to launch fast magnetosonic waves from the midplane of the low field side of the tokamak. More detailed discussion of the theory and strategies of ICRF heating is given in Chapt. 3.

1.3.3 Temperature Diagnostics

Accurate temperature measurements are crucial to understanding plasma behavior and tokamak performance. It is the ion temperature which ultimately determines the fusion rate. The electron temperature is generally different from that of the ions and is often more crucial to many plasma physics phenomena. On Alcator C-Mod there are two major independent measurements of both the ion and electron temperature.

- **Ion temperature:** The fusion rate is a sensitive known function of the density and *ion* temperature in a plasma. With assumptions about the profile shape, the ion temperature can be inferred from count rates on calibrated neutron detectors [7] outside the tokamak. It should be noted that the neutron rate from $H - He^3$ plasmas is too low to provide ion temperature information.

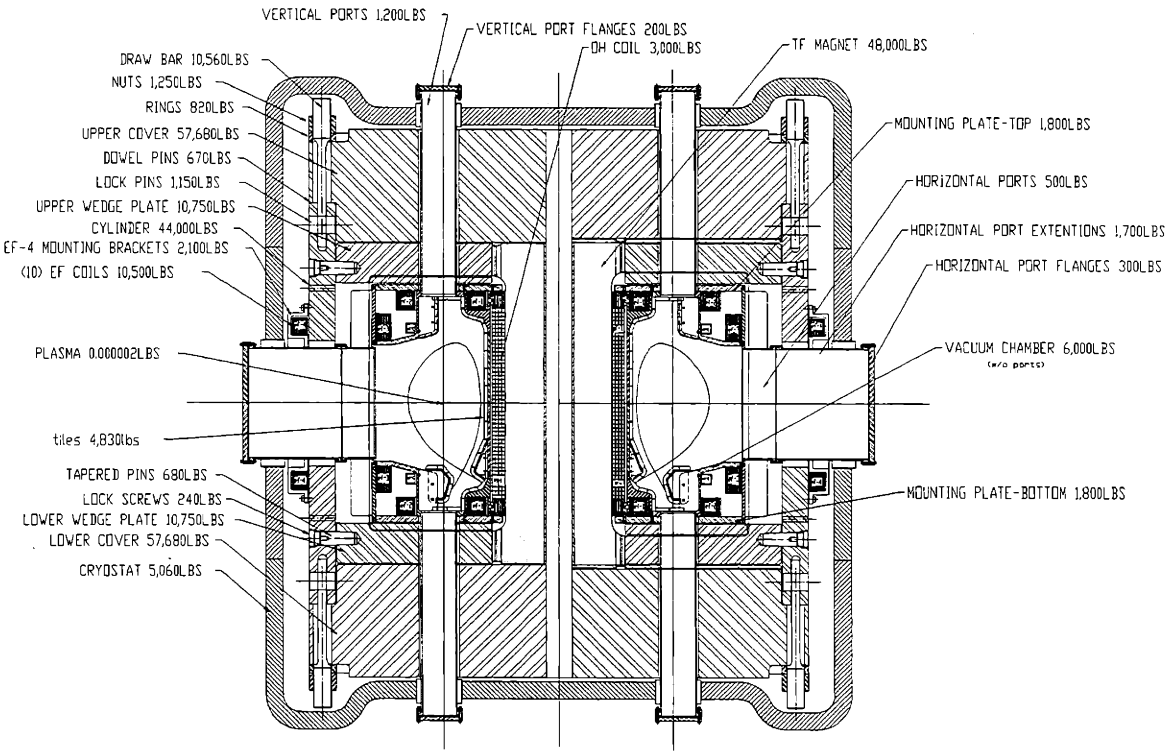

Figure 1-3: Alcator C-Mod cross-section.

Highly ionized states of high-Z impurity atoms exist near the plasma core and spectroscopic measurements of x-ray line emission [8] are used to measure the ion temperature profiles. Five scannable chords allow profile information to be obtained.

- **Electron temperature:** Coherent Thomson scattering [9] is a potentially powerful technique which uses high power laser pulses to scatter from plasma electrons. The system can provide fairly robust measurements of the electron temperature and with absolute calibration on neutral gas can also provide density measurements. The extreme technical challenges involved with this diagnostic significantly limit its availability.

  As will be described in Chapt. 4, electron cyclotron emission ECE from the plasma can be used to measure temperature profiles. The Alcator C-Mod ECE system allows in situ calibration and routine simultaneous operation of two complementary diagnostic instruments, a scanning Michelson interferometer,

and a grating polychromator, as shown in Fig. 1-4 [10]. The system is described in detail in Chapt. 5.

1.3.4 Cyclotron motion

Figure 1-1 showed the basic motion of charged particles in a magnetic field. This *cyclotron* behavior is a central theme of this thesis. As seen above, *ion* cyclotron resonances are exploited to provide a source of auxiliary heating and *electron* cyclotron emission is used as a temperature diagnostic. The cyclotron frequency for a particle of charge, q, in a magnetic field, B, is given by (MKS units):

$$\omega_c = \frac{qB}{m\gamma} \equiv \frac{\Omega}{\gamma} \tag{1.4}$$

where γm is the relativistic mass. Relativistic effects can be important for electrons (see Chapt. 5) but may be ignored for ions in the plasmas considered here. Relativistic effects aside, the key features of this expression are that the cyclotron frequency is determined by the fundamental ratio of charge to mass, q/m, and proportional to the magnetic field intensity. Knowing these proportionalities and the handy expression for the value of the fundamental electron cyclotron frequency:

$$f_{ECE} \approx 28 \text{ GHz/Tesla}, \tag{1.5}$$

allows the easy calculation of Ω for any particle.

1.3.5 Other Diagnostics

Carrying out even simple physics experiments in the harsh environment of tokamak plasmas requires the successful operation of many sophisticated engineering and diagnostic systems. For the sake of clarity and brevity, only those elements which are most crucial to the conclusions of this thesis will be discussed here. Methods for determining the ion ratios in the plasma provide essential support for the D-He3 and H-He3 heating experiments of Chapts. 7 and 8 respectively. For considerations of

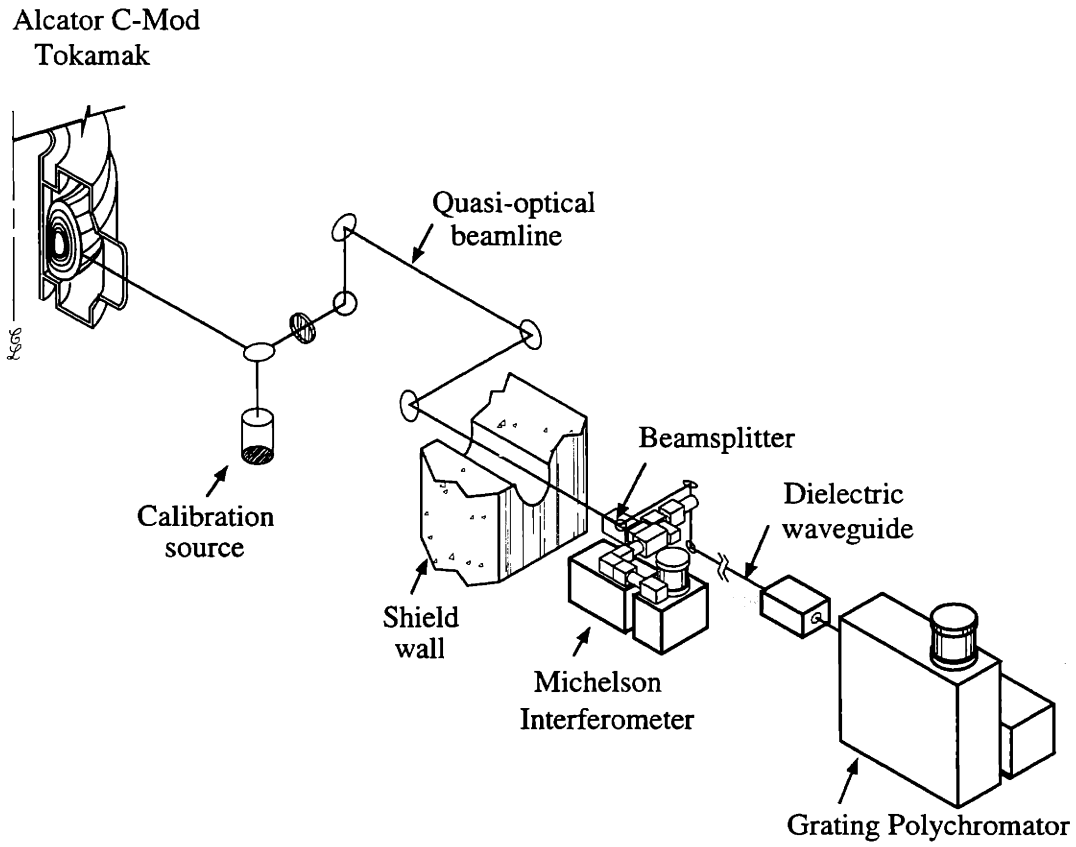

Figure 1-4: Isometric view of the Alcator C-Mod ECE diagnostics. The two complementary diagnostics both utilize the front-end quasioptical beamline [11]. Once in the adjoining lab, wire grids are used to perform mode selection and to split the signal between the the two instruments.

flow, they are discussed in appendix A. Briefly, the calibration of the He^3 gas puffing relies heavily on the two-color interferometer, the Z-meter, and the delivery and measurment systems for neutral gas. The neutral particle analyzer is the main instrument used to obtain the density ratio of deuterium and hydrogen, of key importance in Chapts. 8 and 9.

1.4 Outline of thesis

A brief summary of each chapter is given here.

- **Chapter 2:** Summarizes the formalism of plasma waves, emphasis on the principles and assumptions required to understand and describe the key wave phenomena involved in this thesis.

- **Chapter 3:** Gives the details of the crucial ICRF wave physics for the thesis. In particular, the dynamics of the competition between minority ion heating and mode conversion electron heating are described and given physical interpretation. The expected differences between the $D(He^3)$ and $D(H)$ scenarios are discussed.

- **Chapter 4:** The theory of electron cyclotron emission (ECE) is reviewed with emphasizing the issues of relevance for applications to tokamak diagnostics.

- **Chapter 5:** The ECE diagnostic system on Alcator C-Mod is described. In particular the grating polychromator (GPC) instrument on Alcator C-Mod is described and its performance is analysed. Certain operational techniques and improvements to the instrument are described.

- **Chapter 6:** A description of various analysis techniques for radio frequency heating experiments is given. Highly time resolved temperature measurements from the GPC provide the principal information. Particular emphasis is given to mode conversion heating experiments in which power is coupled directly from a mode converted ion Bernstein wave to the electrons.

- **Chapter 7:** Analysis of the $D - He^3$ heating experiments is described. Significant IBW mode conversion is observed over nearly the entire range of minority concentrations used to date. This somewhat suprising result is compared with the predictions of simulation codes. An attempt to reconcile this result with distinctly different results on the PLT tokamak is made.

- **Chapter 8:** Results from $H - He^3$ mode conversion experiments are described. Though peaked power depostion profiles with record power densities were seen in early experiments, attempts to use this localized electron heat source to conduct transport studies were confounded by a spatial broadening effect. Analysis given in this chapter attributes this result to the presence of increased levels of deuterium compared to earlier experiments.

- **Chapter 9:** In contrast to the $D - He^3$ experiments, highly efficient minority ion absorption is observed in $D(H)$ experiments. A novel technique for estimating minority ion energies is described.

  Electron heating was observed in a high hydrogen concentration D-H plasma. The data for this shot are analysed to determine the likely heating mechanism. The most likely explanation is IBW mode conversion, which has not been previously observed for D-H tokamak plasmas.

- **Chapter 10:** Measurements of transient electron temperature phenomena can be used to study thermal transport (a central issue for the development of more efficient magnetic confinement). Power modulation experiments in $H - He^3$ were conducted with the intent of conducting transport studies. Though a thorough study was not possible (see Chapt. 8), analysis of early data was carried out. This chapter is intended to briefly describe the techniques and issues involved, to allow a starting point for future work.

Appendices:

- **Appendix A:** This appendix describes how the ion fractions were determined for the various ICRF experiments. The calibration of the He^3 puffing system resulted in a measurement of the plasma screening of helium.

- **Appendix B:** This appendix makes specific comments on the use of filter gratings for low-pass filters.

Chapter 2

Waves in magnetized plasmas

2.1 Introduction

A subject which unifies this thesis is the propagation of electromagnetic waves in plasmas. On Alcator C-Mod, high power waves in the ion cyclotron range of frequencies (ICRF) are launched into the plasma to heat it to temperatures beyond what can be achieved through ohmic heating alone. The main thrust of this thesis is to study the different mechanisms through which power is transfered to the plasma. The primary diagnostic tool for these studies is an electron temperature diagnostic (see Chapts. 4 and 5) which measures the plasma's thermal electron cyclotron emission (ECE). The former uses megawatts of externally applied power at 80 MHz to actively heat the plasma. In the latter, microwatts of plasma emission at frequencies near 300 GHz are passively detected to infer the plasma temperature. Though the two systems are extremely different in many ways, plasma waves play an essential role in both. In this chapter, we will lay out a general formalism which describes both the ICRF wave physics that we wish to study, and the ECE physics which is essential to the electron temperature diagnostic. Because these results are applied to tokamak plasmas, special attention is paid to the case of wave propagation *perpendicular* to the magnetic field ($\theta \approx \pi/2$).

2.2 The wave equation

A short derivation of magnetized plasma wave theory is given below. Oscillating wave quantities are assumed to vary as $exp(i\ \mathbf{k}\cdot\mathbf{r} - i\ \omega t)$, with real ω and complex $\mathbf{k}$. The amplitudes of the oscillations are assumed to be small and only linear terms are kept in the wave equations. A coordinate system is chosen so that the assumed uniform external magnetic field is $\mathbf{B} = B_0\hat{\mathbf{z}}$, and the wavevector lies in the $x-z$ plane so that $\mathbf{k} = k\ \cos\theta\ \hat{\mathbf{z}} + k\ \sin\theta\ \hat{\mathbf{x}}$. Standard manipulations of Maxwell's equations give the starting point for our derivation of the wave equation:

$$\nabla \times (\nabla \times \mathbf{E}) = -\frac{1}{c^2}\left[\frac{\partial^2 \mathbf{E}}{\partial t^2} + 4\pi\frac{\partial \mathbf{J}}{\partial t}\right] \tag{2.1}$$

If the plasma current is viewed as the displacement current response of a dielectric medium, the dielectric tensor, $\overleftrightarrow{K}$, can be defined such that:

$$\overleftrightarrow{K}\cdot\mathbf{E} \equiv \mathbf{E} + (4\pi i/\omega)\mathbf{J} \tag{2.2}$$

With some vector manipulation and the further definition of the index of refraction, $\mathbf{N} = c\mathbf{k}/\omega$, the wave equation then becomes:

$$\mathbf{N}(\mathbf{N}\cdot\mathbf{E}) - N^2\mathbf{E} + \overleftrightarrow{K}\cdot\mathbf{E} = 0 \tag{2.3}$$

In order to evaluate $\overleftrightarrow{K}$, the current must be expressed in terms of the electric field. In general, the plasma current is obtained from the distribution averaged motion of each particle species:

$$\mathbf{J} = \sum_j n_j q_j \int_{-\infty}^{\infty} f(\mathbf{v_j})\mathbf{v_j}\mathbf{d^3v} \tag{2.4}$$

where: j labels the sum over the plasma species

and: q_j is the "signed" charge, $ie\ \pm Z_j e$ for $^{\text{ions}}_{\text{electrons}}$ respectively.

Because the interaction between each particle and the wave field is mediated by the Lorentz force which depends on the particle velocity, solving for the self consistent wave current is in general extremely difficult. In §2.4 the linear wave equation is given for the case of plasma species with Maxwellian velocity distributions. Below, the so called "cold-plasma" approximation is made which allows a much simpler solution.

2.3 Cold plasma approximation

The cold-plasma assumption is that for a given solution to the dispersion relationship the phase velocity of the wave is much greater than the thermal velocity of the electrons (and thus the ions too). As the condition must hold for both the parallel and perpendicular components of the phase velocity it is most conveniently expressed by the two inequalities:

$$\begin{aligned} \frac{\omega}{k_{\parallel} v_{th_e}} &\gg 1 \\ k_{\perp} \rho_i &\ll 1 \end{aligned} \tag{2.5}$$

where ρ_i is the ion gyro radius. This approximation is often very accurate, and greatly simplifies the expressions, but the assumption used will fail at resonances, *ie* where $k \rightarrow \infty$. We proceed then, knowing that near resonances, kinetic effects must be introduced to produce the proper behavior.

With the assumption of zero streaming velocity for each particle, the wave perturbed velocities are obtained from the self consistent solution of the equations of motion governed by the Lorentz force law:

$$-i\omega m_j \mathbf{v_j} = Z_j q_j (\mathbf{E} + \frac{1}{c} \mathbf{v_j} \times \mathbf{B_0}) \tag{2.6}$$

Vector algebra and Maxwell's equations allow the velocity to be expressed as functions

of the electric field as desired. The solutions are given below:

$$\begin{aligned} v_x &= \frac{q_j}{m_j\omega}\frac{iE_x - (\Omega_j/\omega)E_y}{1-\Omega_j^2/\omega^2} \\ v_y &= \frac{q_j}{m_j\omega}\frac{iE_y - (\Omega_j/\omega)E_x}{1-\Omega_j^2/\omega^2} \\ v_z &= \frac{iq_jE_z}{m_j\omega} \end{aligned} \tag{2.7}$$

Inspection of Eq. 2.7 makes clear the tensor nature of $\overleftrightarrow{K}$. With the introduction of the so called *Stix parameters* [12] given below,

$$\begin{aligned} \text{where: } P &\equiv 1-\sum_j \frac{\omega_{pj}^2}{\omega^2} \\ R &\equiv 1-\sum_j \frac{\omega_{pj}^2}{\omega^2}\left(\frac{\omega}{\omega+\Omega_j}\right) \\ L &\equiv 1-\sum_j \frac{\omega_{pj}^2}{\omega^2}\left(\frac{\omega}{\omega-\Omega_j}\right) \\ S &\equiv \frac{R+L}{2} = 1-\sum_j \frac{\omega_{pj}^2}{\omega^2-\Omega_j^2} \\ D &\equiv \frac{R-L}{2} \end{aligned} \tag{2.8}$$

the wave equation (Eq. 2.3) may finally be expressed explicitly in matrix form:

$$\begin{bmatrix} S-N^2\cos^2\theta & -iD & N^2\sin\theta\cos\theta \\ iD & S-N^2 & 0 \\ N^2\sin\theta\cos\theta & 0 & P-N^2\sin^2\theta \end{bmatrix} \begin{bmatrix} E_x \\ E_y \\ E_z \end{bmatrix} = 0. \tag{2.9}$$

2.3.1 Dispersion relationship

Non-trivial solutions, *ie* $\mathbf{E} \neq 0$, are given by setting the determinant of the matrix to zero. This yields the dispersion relationship for cold-plasma waves which may be

expressed as:

$$\begin{aligned} AN^4 - BN^2 + C &= 0 \\ \text{where: } A &= S\sin^2\theta + P\cos^2\theta \\ B &= RL\sin^2\theta + PS\left(1+\cos^2\theta\right) \\ C &= PRL \end{aligned} \tag{2.10}$$

Equation 2.10 can be rewritten in another form as shown below:

$$\tan^2\theta = \frac{-P(N^2-R)(N^2-L)}{S(N^2-RL/S)(N^2-P)} \tag{2.11}$$

Cut-offs

A wave is said to reach cutoff when $N \rightarrow 0$. Cutoff layers separate regions of propagation and evanescence for a given wave. If the evanescent region is thin enough, incident waves can tunnel through. Thick evanescent layers result in reflection. Mapping cutoff layers in a plasma is thus of great importance when considering whether one region of the plasma is accessible from another for a particular wave [1]. Equation 2.10 implies that the cutoff condition, $\mathbf{N} = c\mathbf{k}/\omega \rightarrow 0$, requires $P = 0$, $R = 0$, or $L = 0$.

Resonances

Equation 2.11 illustrates the nature of cold plasma resonances, defined by $N \rightarrow \infty$. There are two basic types of resonances:

$\theta = \mathbf{0}$: Occurs where $S \rightarrow \infty$. This occurs for either $R \rightarrow \infty$ ($\omega = \omega_{ce}$), or $L \rightarrow \infty$ ($\omega = \omega_{ci}$), and obviously corresponds to cyclotron resonance.

$\theta = \pi/\mathbf{2}$: Occurs where $S \rightarrow 0$, called the "hybrid" resonance.

[1] Unfortunately the answer is often the response dreaded by all querying travellers, "You can't get there from here"

Polarization

In the coordinate system we have set up, the x-y plane is perpendicular to the magnetic field. When considering the interaction of plasma waves with the cyclotron motion of particles it is important to determine the sense of rotation of the wave electric field in this plane. In this case, instead of using the E_x, E_y basis to describe the wave polarization, a more useful and equivalent basis is used:

$$\begin{aligned} E^+ &= E_x + iE_y \qquad \text{Right-hand circular component} \\ E^- &= E_x - iE_y \qquad \text{Left-hand circular component} \end{aligned} \tag{2.12}$$

E^+ is the component of the electric field which rotates in the same sense as ion gyro motion and so is the important component when heating with ICRF. Equation 2.9 can be used to determine the cold plasma wave polarization as a simple row-column multiplication yields:

$$iE_x/E_y = (N^2 - S)/D \tag{2.13}$$

2.3.2 Ion cyclotron waves

The dispersion relationship for cold plasma waves was given in Eq. 2.10. In the ion cyclotron range of frequencies (ICRF), with $\omega \ll \omega_{ce}$, one finds that $|P| \gg |S|$, thus for waves with any appreciable parallel wave component ($|\theta - \pi/2| > \sqrt{m_e/m_i}$) the coefficients in equation 2.10 become:

$$\begin{aligned} A &\approx P\cos^2\theta \\ B &\approx PS\left(1+\cos^2\theta\right) \\ C &= PRL \end{aligned} \tag{2.14}$$

For low frequency ($\omega \ll \omega_{ce}$), the approximate forms for the Stix parameters for a single ion species plasma are:

$$\begin{array}{llll} \overset{R}{L} & \approx 1 + \frac{\gamma\,\omega_{ci}}{\omega_{ci} \pm \omega} & S & \approx 1 + \dfrac{\gamma\,\omega_{ci}^2}{\omega_{ci}^2 - \omega^2} \\ P & = 1 - \alpha \approx -\alpha & D & \approx \dfrac{\gamma\,\omega\,\omega_{ci}}{\omega^2 - \omega_{ci}^2} \end{array} \tag{2.15}$$

Where:

$$\begin{aligned} \alpha &\equiv \omega_{pe}^2/\omega^2 \\ \gamma &\equiv c^2/V_A^2 = \omega_{pi}^2/\omega_{ci}^2 \end{aligned}$$

Using the above expressions and making the further assumption that $\gamma \gg 1$ the dispersion relationship relevant for the ion cyclotron waves used in fusion experiments is given by:

$$N^4 \cos^2\theta - \frac{\gamma\omega_{ci}^2\,(1+\cos^2\theta)}{\omega_{ci}^2 - \omega^2} N^2 + \frac{\gamma^2\omega_{ci}^2}{\omega_{ci}^2 - \omega^2} = 0 \tag{2.16}$$

The above equation is a quadratic in N^2, with two basic solutions. The nature of the two modes for near perpendicular propagation is captured by first taking $\omega \approx \omega_{ci}$ and balancing terms (2) and (3) to get:

$$N_1^2 \approx \frac{\gamma}{1+\cos^2\theta} \tag{2.17}$$

and, for large N^2 and $\omega \neq \omega_{ci}$, we balance terms (1) and (2) to obtain an expression for the second solution:

$$N_2^2 \cos^2\theta \approx \gamma(1+\cos^2\theta)\frac{\omega_{ci}^2}{\omega_{ci}^2 - \omega^2} \tag{2.18}$$

The first solution is the dispersion equation for the so called "fast" wave. At lower frequencies this same root is called the compressional Alfvén wave. The second root is called the electromagnetic ion cyclotron wave and is the high frequency limit of the

shear Alfvén wave. In these discussions it will be refered to simply as the "slow" wave. In Chapt. 3 we will return to these two modes when describing how ion cyclotron waves can be used to heat fusion plasmas.

2.3.3 Electron cyclotron waves

We now examine the high frequency limit ($\omega \approx \omega_{ce} \gg \omega_{ci}, \omega_{pi}$) of the cold plasma dispersion relationship. The high frequency behavior of the various terms is best extracted with the assumption $m_e/m_i \rightarrow 0$. With some vigorous algebraic manipulation of the solutions to Eq. 2.10, the Appleton-Hartree form of the dispersion relationship is obtained:

$$N^2 = 1 - \frac{2\alpha\omega^2(1-\alpha)}{2\omega^2(1-\alpha) - \omega_{ce}^2 \sin^2\theta \pm \omega_{ce}\Delta} \tag{2.19}$$

$$\text{where: } \Delta = \sqrt{\omega_{ce}^2 \sin^4\theta + 4\omega^2(1-\alpha)^2\cos^2\theta} \tag{2.20}$$

For $\theta = \pi/2$, we can simplify each of the two solutions above to give the more familiar expressions:

$$N_{X-MODE}^2 = \frac{(1-\alpha)^2\omega^2 - \omega_{ce}^2}{(1-\alpha)\omega^2 - \omega_{ce}^2} \tag{2.21}$$

and

$$N_{O-MODE}^2 = 1 - \alpha \tag{2.22}$$

The ordinary mode, or "O-mode", is so called because its dispersion relation is the same as that for simple unmagnetized plasma oscillations. This is because the O-mode electric field is is oriented along the magnetic field in magnetized plasmas and the wave current is free to flow along the field lines. For the extraordinary mode, or "X-mode", $\mathbf{E_1}$ is polarized perpendicular to the magnetic field and its dynamics are much different. In Chapt. 4, we will see that the accessibility to the plasma core

is very different for the two modes and this influences which mode can be used for electron temperature measurements.

2.4 Hot plasma waves

2.4.1 Electromagnetic waves

The cold plasma approximation (roughly: $\omega/k \gg v_{th_j}$) allows a wide variety of wave phenomena to be studied accurately and with relative simplicity. There are obvious cases where this approximation breaks down, most notably at plasma resonances where the cold plasma dispersion relations indicate that $k \rightarrow \infty$. When the thermal velocities of a species of particles cannot be ignored, the calculation of the wave perturbed plasma current in Eq. 2.4 becomes quite difficult. As the Lorentz force is velocity dependant, one must properly account for the full equilibrium velocity distribution, f_0, of the plasma when computing the net particle response to the wave fields. This is done by calculating the first order perturbation to the velocity *distribution function*, f_1, in the linearized Vlasov-Maxwell equation:

$$\left(\frac{\partial}{\partial t} + \mathbf{v}\cdot\nabla_{\vec{x}} + \frac{q}{m}\frac{\mathbf{v}\times\mathbf{B_0}}{c}\cdot\nabla_{\vec{v}}\right) f_1 = \frac{-q}{m}\left(\mathbf{E_1} + \frac{\mathbf{v}\times\mathbf{B_1}}{c}\right)\cdot\nabla_{\vec{v}} f_0 \qquad (2.23)$$

Although the treatment of the particle orbits is now more involved than in the cold plasma case, one can still write down a general expression for the linearized perturbation to the distribution function of a given particle species:

$$f_1 = \frac{2q}{m}\sum_{l,n}\left[\frac{J_l(k_\perp v_\perp/\Omega)A\ 2l\Omega/k_\perp - i2v_\perp J_l'(k_\perp v_\perp/\Omega)B + 2v_\parallel J_l(k_\perp v_\perp/\Omega)C}{i(\omega - l\Omega - k_\parallel v_\parallel)}\right] \qquad (2.24)$$

In the above, $J_n()$ is the n^th order Bessel function, and:

$$\begin{aligned} A &= E_x \frac{\partial f_0}{\partial v_\perp^2} + \frac{v_\parallel}{\omega}(k_\parallel E_x + k_\perp E_z)(\frac{\partial f_0}{\partial v_\parallel^2} - \frac{\partial f_0}{\partial v_\perp^2}) \\ B &= E_y \frac{\partial f_0}{\partial v_\perp^2} + \frac{v_\parallel}{\omega} k_\parallel E_y (\frac{\partial f_0}{\partial v_\parallel^2} - \frac{\partial f_0}{\partial v_\perp^2}) \\ C &= E_z \frac{\partial f_0}{\partial v_\parallel^2} \end{aligned}$$

This result is complicated but very valuable. It allows one to examine how the net plasma response to wave fields depends on the details of the equilibrium velocity distribution of a particular species. We consider here the *simplest* case of a Maxwellian velocity distribution with $f_0(v) \propto e^{-mv^2/2kT}$. Having chosen a form for f_0, Eq. 2.24 is then used to generate the wave perturbation to the velocity distribution function for a *particular* plasma species. This result may then be used in Eq. 2.4 to calculate the net perturbed plasma current associated with a wave. Though this current has been considerably more difficult to calculate than for a cold plasma, we may now generate the hot-plasma version of the dispersion tensor by the same process outlined previously. The expressions for each of the elements which result are given here for reference: With the following definitions:

$$Z(\zeta) \equiv \frac{1}{\sqrt{\pi}} \int_{-\infty}^{\infty} \frac{e^{-s^2}}{s-\zeta} ds \qquad Im(\zeta) > 0 \tag{2.25}$$

$$\zeta_n \equiv (\omega + n\omega_c)/k_\parallel \; v_{th}$$

$$b \equiv k_\perp^2 \; v_{th}/2\omega_c \tag{2.26}$$

the hot-plasma dielectric tensor elements may be expressed as:

$$K_{xx} = 1 + \sum_j \frac{\omega_p^2}{\omega^2} \frac{e^{-b}}{b} \zeta_0 \sum_{-\infty}^{\infty} n^2 I_n(b) Z(\zeta_n) \tag{2.27}$$

$$K_{yy} = \sum_j \frac{\omega_p^2}{\omega^2} \frac{e^{-b}}{b} \zeta_0 \sum_{-\infty}^{\infty} \{n^2 I_n(b) + 2b^2[I_n(b) - I_n'(b)]\} Z(\zeta_n)$$

$$K_{xy} = -K_{yx} = i \sum_j \pm \frac{\omega_p^2}{\omega^2} e^{-b} \zeta_0 \sum_{-\infty}^{\infty} n[I_n(b) - I_n'(b)] Z(\zeta_n)$$

$$K_{xz} = K_{zx} = \sum_j \frac{\omega_p^2}{\omega^2} \frac{e^{-b}}{\sqrt{2b}} \zeta_0 \sum_{-\infty}^{\infty} n I_n(b) Z'(\zeta_n)$$

$$K_{yz} = -K_{zy} - i \sum_j \pm \frac{\omega_p^2}{\omega^2} \left(\frac{b}{2}\right)^{1/2} e^{-b} \zeta_0 \sum_{-\infty}^{\infty} [I_n(b) - I_n'(b)] Z'(\zeta_n)$$

$$K_{zz} = 1 - \sum_j \frac{\omega_p^2}{\omega^2} e^{-b} \zeta_0 \sum_{-\infty}^{\infty} I_n(b) Z'(\zeta_n)$$

In the above, $I_n()$ is the modified Bessel function of the first kind which results from integrating over velocity space. Included below are the definitions of some of the plasma parameters used in these expressions:

$$\begin{aligned} \omega_{p_j}^2 &= n_{0_j} Z_j^2 e^2 / \epsilon_0 m_j \\ \zeta_{nj} &= (\omega + n\ \omega_{cj}) / k_{\|}\ v_{th_j} \\ \omega_{cj} &= |Z_j e B_0 / m_j| \\ v_{th_j}^2 &= 2k\ T_j / m_j \\ b_j &= \frac{1}{2}\ k_\perp^2 r_{Lj} = k_\perp^2\ T_j / m_j \omega_{cj}^2 \end{aligned} \tag{2.28}$$

This treatment reproduces all of the modes predicted by cold-plasma theory, but also predicts many new classes of waves. These hot-plasma modes are generally of shorter wavelength than the cold plasma modes and have wave dynamics which are more longitudinal than transverse in nature. We will see in Chapt. 3 that the cold-plasma resonances really represent localized regions where the the hot and cold modes interact with each other strongly and in general lead to wave damping. The details of these wave interactions are of great importance for plasma heating applications which involve plasma waves.

2.4.2 Hot electrostatic waves

With the inclusion of finite plasma temperature, the plasma dispersion relationship can be solved for purely electrostatic waves, that is waves for which $\mathbf{E} \parallel \mathbf{k}$. The ion Bernstein wave (IBW) is a hot plasma wave which is of importance to this thesis.

Although the IBW in general exhibits electromagnetic properties which are of key importance when considering mode conversion (see Chapt. 3), the electrostatic approximation provides a useful starting point for determining the IBW wave properties. The electrostatic IBW dispersion relationship is given by [12]:

$$\epsilon(\mathbf{k},\omega) = 1 + \sum_j \frac{2\omega_{pj}^2}{k^2 v_{tj}^2}\left[1 + \frac{\omega}{k_\parallel v_{tj}} \sum_{n=-\infty}^{\infty} I_n(b_j) e^{-b_j} Z(\zeta_{nj})\right] = 0 \qquad (2.29)$$

A detailed investigation of the IBW in tokamaks is given in [13].

Chapter 3

ICRF heating of fusion plasmas

3.1 Introduction

When deciding how to heat fusion plasmas with electromagnetic waves, some advantages of heating *ions* are immediately clear. As seen in Chapt. 1, fusion is dependent on achieving high thermal energies of the plasma *ions* and so being able to heat them directly is obviously advantageous. The high ion mass relative to electrons means that the ion cyclotron range of frequencies (ICRF) represents the lowest of all the resonant plasma frequencies. For high power RF transmitter technology, lower frequencies mean simpler, less expensive devices. For these and other reasons, ICRF heating is being actively investigated on most major tokamak devices worldwide. ICRF provides the only source of auxiliary heating on Alcator C-Mod. This chapter delves into the most important ICRF physics issues affecting our experiments.

3.2 ICRF heating experiments on C-Mod

As a wave propagates into an inhomogeneous plasma, its wavevector, $\mathbf{k}$ (and thus $\mathbf{N}$) can vary. A generalization of Snell's law, however, dictates that the components of $\mathbf{k}$ remain constant along the direction in which the plasma is uniform . In a tokamak, the toroidal symmetry of the plasma establishes n_ϕ, the toroidal mode number of the wave fields, as the conserved quantity. An important expression relating the mode

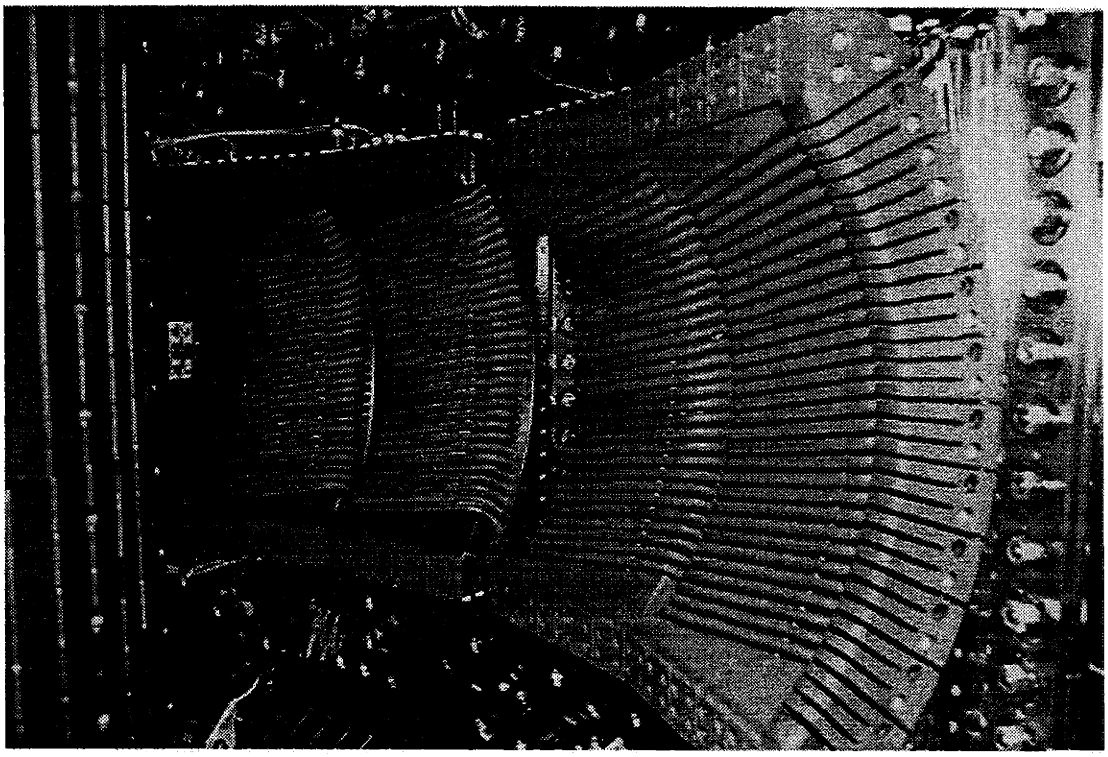

Figure 3-1: Picture of the two two-strap antennas mounted on the outboard vacuum vessel wall of Alcator C-Mod. Each current strap is protected from direct plasma contact by a Faraday screen. The current strap at the extreme left is just visible through the rungs of the Faraday screen. The inner wall is lined with square molybdenum tiles for protection from plasma disruptions.

number to the parallel component of the wave vector is given below [14]:

$$k_{\|} \equiv \mathbf{k} \cdot \mathbf{B} = \frac{1}{R}\left[n_{\phi} - m/q\right] = \frac{n_{\phi}}{R} - \frac{m\ B_{\theta}}{r\ B_{z}} \tag{3.1}$$

On Alcator C-Mod, the ICRF antennas have two toroidally separated current straps (see Fig. 3-1) which are driven out of phase (so called $0 : \pi$ phasing). The geometry of the antennas establishes a power spectrum which spans a range of poloidal mode numbers. The power spectrum of the *vacuum* fields at the plasma edge is shown in Fig. 3-2. As n_{ϕ} is conserved, each component of the antenna spectrum can be treated independently. The propagation and damping behaviors in the plasma can be very sensitive to the parallel wave number so it should be noted that the power

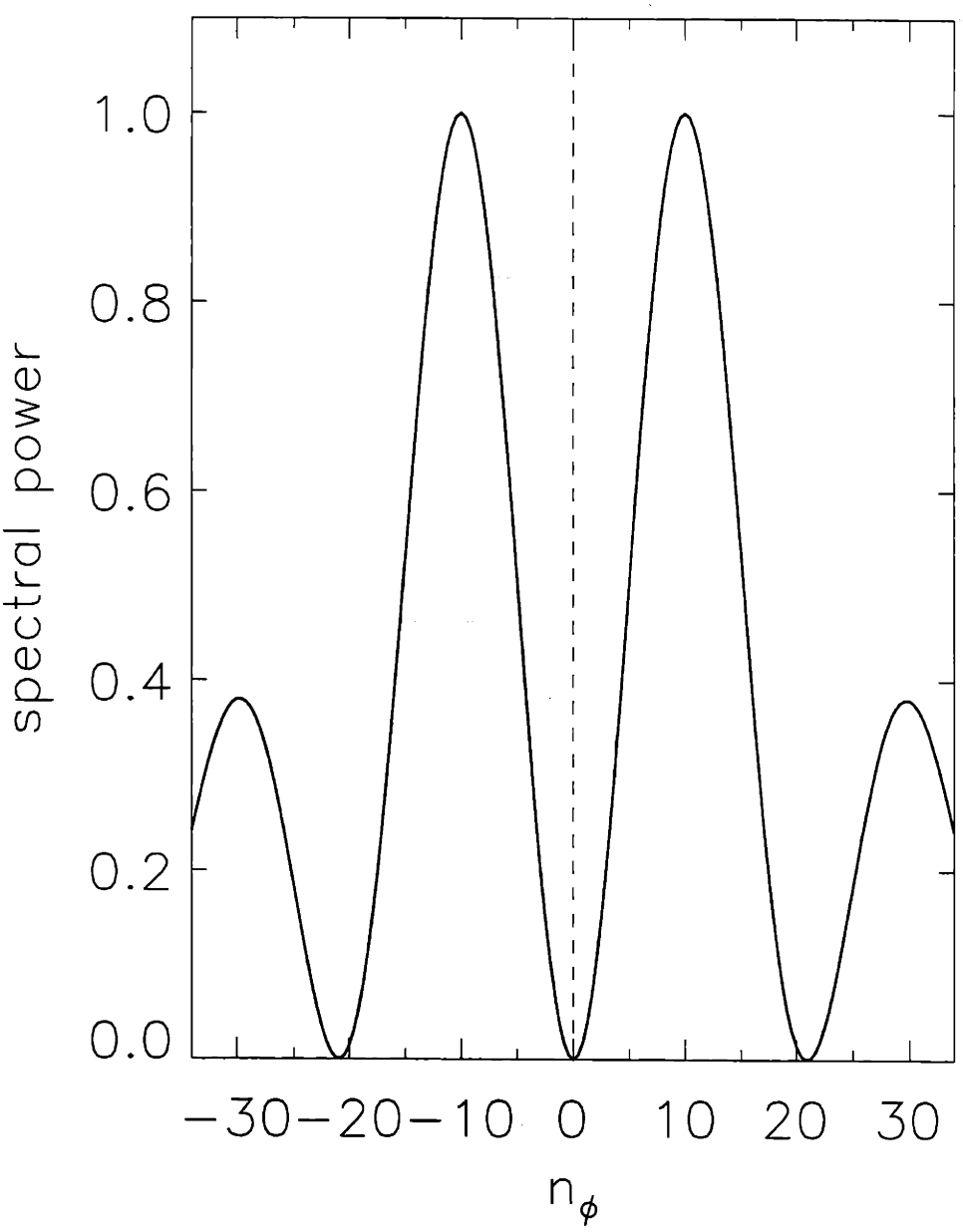

Figure 3-2: Toroidal mode number vacuum power spectrum established by the two-strap antennas on Alcator C-Mod ($0{:}\pi$ phasing). n_ϕ is a conserved quantity which allows each component of the spectrum to be handled independently.

spectrum *inside the plasma* can be significantly different than the *vacuum* spectrum. For example, in §3.3.2 we will see that the fast wave must tunnel through an evanescent region in the plasma edge before it can propagate freely. Higher values of $k_{\|}$ are more evanescent and thus the plasma effectively "filters out" the high $k_{\|}$ components launched by the antennas. This and other phenomena must be taken into account to calculate the resultant spectrum in the plasma. The precise spectrum in experiments is not known and is part of the reason why ICRF heating is still an area of basic research in tokamaks. The peak in the *vacuum* power spectrum occurs at $n_\phi = \pi\ (R_0 + a)/d\ \approx 10$ where d is the separation between the two current straps of the antennas, and for simplicity in future treatments the parallel wave number for the fast wave will be taken to be:

$$k_{\|} \approx \frac{10}{R} \tag{3.2}$$

A rough *upper* bound on the poloidal mode numbers describing the waves in the tokamak is $m_{\max} \approx k_\perp r$. For the fast wave, Eq. 2.17 yields the approximate dispersion relationship for perpendicular propagation

$$\begin{aligned} \frac{\omega}{k_\perp} &\approx \frac{\Omega_i}{\omega_{pi}} c, \\ \text{or } N_\perp^2 &\approx \frac{\omega_{pi}^2}{\Omega_i^2}. \end{aligned} \tag{3.3}$$

Evaluating this for typical D(H) parameters, $\omega = 2\pi \times 80$ MHz $\approx 2\omega_{cD}$, and $n_e \approx 2 \times 10^{20}$ gives $k_\perp \lesssim 90 m^{-1}$. Thus the approximation of Eq. 3.2 is reasonable for the fast wave near the center ($m_{\max}/q \lesssim n_\phi/2$ inside the inversion radius). In §3.5 we will see that mode conversion of the fast wave can take place to a shorter wavelength branch of the hot plasma dispersion relationship, the ion Bernstein wave (IBW). The poloidal mode numbers needed to represent the IBW can be much higher, and can dominate the toroidal mode number in Eq. 3.1, resulting in a much larger value for $|k_{\|}|$. This $k_{\|}$ "upshift" can be of importance to the IBW damping.

3.3 Ion cyclotron waves in a tokamak

In the discussion of the previous section we saw that at a given point in the plasma and for a specified n_ϕ component of the antenna power spectrum, $k_\parallel$ (and thus N_z) is known. Using the low frequency approximation for the dispersion relation coefficients (see Eq. 2.14) and doing some algebra, we can rewrite the dispersion relation such that the *perpendicular* wave number, N_x, is the dependant variable. The result is a very useful expression for the dispersion relationship:

$$N_x^2 = \frac{(N_z^2 - R)(N_z^2 - L)}{S - N_z^2} \tag{3.4}$$

This form of the dispersion relationship explicitly shows the presence of three singularities, two cutoffs and one resonance. The implications of these singularities are very important for understanding ICRF heating experiments. The details for each heating scenario can vary and will be discussed in more detail for each case, but some general properties are described here. It will be seen that the plasma has some surprises in store for the experimentalist.

3.3.1 Wave polarization

The power available to heat ions near the fundamental ion cyclotron resonance may be expressed as [15]:

$$P = \frac{\omega_{pi}^2 |E_1^+|^2}{k_\parallel v_{ti} 16\pi^{1/2}} exp\left[-\left(\frac{\omega - \omega_{ci}}{k_\parallel v_{ti}}\right)^2\right] \tag{3.5}$$

where $E_1^+ \equiv E_x + iE_y$ is the left hand circularly polarized component of the wave electric field, *ie* having the same rotational sense as ions about the magnetic field. The results of §2.3 can be used to determine E_1^+ at the cyclotron resonance: (normalized

to E_y):

$$\left|\frac{E^+}{E_y}\right|_{\omega=\omega_{ci}} = \begin{cases} 0 & \text{Fast wave} \\ 2 & \text{Slow wave} \end{cases} \tag{3.6}$$

This clearly indicates that the slow wave is best suited for ion heating at the fundamental resonance.

3.3.2 Accessibility

Access to the inner wall of a tokamak for high power antennas is extremely limited. Typical systems launch power from the outboard midplane, which corresponds to the low-field side of the plasma. If the cyclotron resonance for the transmitter frequency is located at the plasma center, $\omega = \omega_{ci}(R_0)$, then between the antenna and the plasma center, $\omega > \omega_{ci}$ is necessarily true. Inspecting the dispersion relationship of Eq. 2.18 indicates that the slow wave is cut off under these conditions. The fast wave has *much* better accessibility. As $L < 0,\ S < 0,$ and $R > 0$ when $\omega > \omega_{ci}$, Eq. 3.4 shows that the only cutoff is for $N_z^2 \geq R \approx 1/3\ \omega_{pi}^2/\omega_{ci}^2$. For typical C-Mod parameters ($N_z \approx 10, B \approx 5T$, deuterium plasma), the requirement for fast wave propagation is $n_e \gtrsim 1.5 \times 10^{19}\ m^{-3}$ which is satisfied everywhere except in the extreme edge of the discharge.

3.4 Minority heating

As both accessibility *and* proper polarization are necessary conditions for heating, the previous discussion seems to show that neither ion cyclotron mode can heat ions, as each fails on one count. To surmount these problems, it was noted that hot-plasma theory shows that a single ion plasma can be heated at its second harmonic due to finite Larmor radius effects. Although this is a relatively weak interaction, heating experiments of this type have been successful. In attempting this 2^{nd} harmonic ion heating in deuterium plasmas on the ATC [16], and T-4 [17] tokamaks, anomalously

high absorption efficiencies and the presence of highly energetic hydrogen ions were observed. This was quickly attributed to "parasitic" absorption by trace levels of hydrogen which remained in the discharge vessel. Since the discovery of this so-called "minority heating", it has become one of the standard heating mechanisms in tokamaks. The strong heating results from an enhancement of the E^+ component of the fast wave electric field at the fundamental cyclotron frequency of a minority ion. For small enough minority concentrations, the polarization of the fast wave is dominated by the majority ion species, provided it has a different value of q/m. The left-hand circular component of the fast wave for frequencies near ω_{ci} is given below:

$$\left|\frac{E^+}{E_y}\right|^2 = \frac{(\omega/\omega_{ci}-1)^2(\omega/\omega_{ci}-cos^2\theta)^2}{|\omega/\omega_{ci}(1+cos^2\theta)|^2} \approx (\omega/\omega_{ci}-1)^2 \qquad \text{for: } \theta \approx \pi/2 \tag{3.7}$$

Table 3.1 gives this normalized polarization for values of the heating frequency relevant to common minority heating scenarios. Table 3.1 reiterates the point that the

ω/ω_{cD}	$\left\|\frac{E^+}{E_y}\right\|^2$	*Heating Scenario*
1	0	Majority fundamental
2	1	$D(H)$ minority
4/3	1/9	$D(He^3)$ minority

Table 3.1: Polarization of fast wave for various frequencies near ω_{cD}

fast wave cannot heat the majority ion species (generally deuterium in Alcator C-Mod experiments) at its fundamental cyclotron frequency. Comparing the second and third rows of table 3.1 a second important result is apparent. The ion heating polarization component is much smaller for $D(He^3)$ than for $D(H)$ minority heating, leading to lower single pass power absorption in the former case. Fast wave power that is not absorbed at the cyclotron harmonic continues to propagate towards the high field side of the plasma. It then encounters a second resonance which is a result of the presence of two ion species. The physics of the wave interaction with the so called ion-ion hybrid resonance is quite complicated and will be outlined in §3.5. In general, this resonance layer leads to partial reflection, transmission, and absorption

due to other wave processes. Power that is transmitted continues to the high field edge plasma where it encounters the $N_{\|}^2 = R$ cutoff and is reflected back again. Strong RF wave electric fields in the edge plasma due to multiple reflections can lead to impurity generation or additional mode conversion processes. The point made here is that the relatively weak minority ion heating of the $D(He^3)$ scenario can give rise to much more complicated wave physics.

3.4.1 Minority ion tail

Consider a typical minority heating scenario with a centrally located ion cyclotron resonance layer. Minority ions encounter the resonance region repeatedly as they orbit the machine. The exact location of the resonance for each particle is determined by the expression $\Omega(r) = \omega - k_{\|} v_{\|}$. Each pass through the resonance gives each minority ion a kick in perpendicular velocity space. These kicks create a diffusion in energy space such that the average energy of each particle increases steadily with time. For the ensemble of minority ions, this corresponds to steady heating. Stix [12] has treated this problem in great detail using quasi-linear theory to solve the Fokker-Planck equation for the energy distribution function of ions for minority heating. In the special case of *steady state* heating, one can analytically solve for the magnetic-surface and pitch-angle averaged distribution function. Stix specifies the velocity

distribution for the case of small Larmor radii by:

$$\ln f(v) = -\frac{E}{T_e(1+\xi)}\left[1+\frac{R_f(T_e-T_f+\xi T_e)}{T_f(1+R_f+\xi)}K(E/E_f)\right] \tag{3.8}$$

$$\begin{aligned}
\text{where: } E &\equiv mv^2/2, \qquad R_f = n_f Z_f^2 l_f/n_e l_e \\
l_f &\equiv (m_f/2T_e)^{1/2}, \qquad \epsilon \equiv \frac{2}{3\sqrt{\pi}} \\
\xi &\equiv \frac{m<P_\perp>}{8\pi^{1/2}n_e n Z^2 e^4 \ln\Lambda}\left(\frac{2T_e}{m_e}\right)^{1/2} \\
E_f(\xi) &\equiv \frac{mT_f}{m_f}\left[\frac{1+R_f+\xi}{2\epsilon(1+\xi)}\right]^{2/3} \\
&\text{and:} \\
K(x) &\equiv \frac{1}{x}\int_0^x \frac{du}{1+u^{3/2}} \\
&= \frac{2}{x}\left[\frac{1}{6}\ln\frac{1-\sqrt{x}+x}{1+2\sqrt{x}+x}+\frac{1}{\sqrt{3}}\left(\frac{\pi}{6}+\tan^{-1}\frac{2\sqrt{x}-1}{\sqrt{3}}\right)\right]
\end{aligned}$$

In the above, Z, m, n, and v represent the charge number, mass, density, and velocity of the minority ions, and the "f" subscript denotes the same quantities for the field (bulk plasma) ions. It should be emphasized that the above is a *velocity* distribution function [1]. For the analysis of the minority tail energy, it will be most useful to work with the *energy* distribution function. Since the number of particles within corresponding increments of velocity and energy are by definition equal, *ie* $dN = g(E)dE = f(v)4\pi v^2 dv$, then we have:

$$g(E) \propto \sqrt{E}\, f(v) \tag{3.9}$$

Examples of the calculated energy distribution function are shown in Fig. 3-3 for typical C-Mod parameters. The energy distribution at low power densities has a well defined maximum at an energy on the order of the plasma thermal energy. At very

[1] By averaging over pitch angles, the resulting distribution function is isotropized for simplicity and thus might more appropriately be called a distribution of *speeds*. Work on the PLT tokamak [18] has both confirmed general behaviors predicted from the Stix distribution and measured anisotropies in the minority ion distribution function which can be important in some applications

high heating powers the distribution is drawn out far beyond the plasma temperature, well suited by the term "tail". Though Eq. 3.8 already embodies simplifying assumptions and approximations, some of the basic behaviors of the minority tail energy are still obscured by the formalism. Two useful expressions are given here which will allow easier insight into results from minority heating experiments. The drag on a high energy minority ion begins to be dominated by electron collisions above a certain critical energy given by [19]

$$E_{minor}|_{crit} = 16\ T_e\ M_{minor} \left(\frac{n_{maj}\ Z_{maj}^2}{n_e\ M_{maj}} \right)^{2/3}, \tag{3.10}$$

where n is the plasma density and Z, and M are the atomic and mass numbers for minority and majority ions, subscripted by "minor" and "maj" respectively. When electrons dominate the drag on electrons, the basic scaling of the tail energy is given by [20]

$$E_{tail} \propto \frac{M_{minor}}{Z_{minor}^2} \frac{< p > T_e^{3/2}}{n_e\, n_{minor}} \tag{3.11}$$

The above formalism can be used to describe the steady state of the minority ion population for a given set of plasma and heating conditions. To fully characterize the ICRF as a bulk plasma heating source and to establish a basis for measuring the minority ion tail, we must now examine the interaction between the minority ions and the plasma proper.

Collisional drag on energetic minority ions

In the standard C-Mod heating scenario, the fast wave launched from the plasma edge heats minority ions to high energies. Bulk plasma heating occurs indirectly as the minority ions lose energy through collisions with both majority ions and electrons. The response of the electron temperature to a change in RF power is thus mediated by the minority ion population. A brief description is given below of the so called

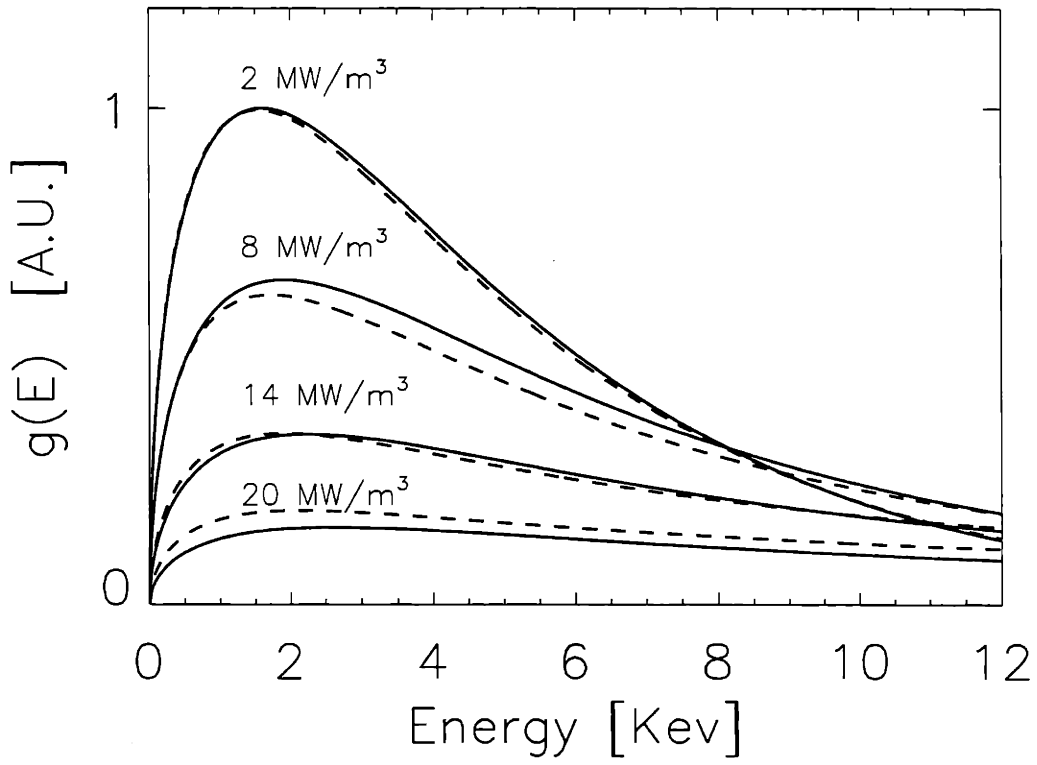

Figure 3-3: Energy distribution functions as calculated using Eqs. 3.8 and 3.9 for various ICRF power densities. The plasma parameters for the calculations are $T_e = 3$ keV, $n_e = 1.8 \times 10^{20} m^{-3}$, $Z_{eff} = 1.5$, minority ion fraction = 4%. The solid lines are calculations for He^3 ions in Deuterium majority plasma for the power densities indicated. For comparison, the distribution functions for Hydrogen minority ions and the same conditions are shown in dashed lines but calculated for 1/4 the power densities indicated.

"slowing down" process of high energy ions in a plasma.

There are many different energy and momentum exchange processes in plasmas. Although the time scales of the various processes can vary widely, many of them are often loosely described as "slowing down" times. A slowing down time, τ_S, for a test particle is most correctly (and thankfully most commonly) defined by the expression:

$$\frac{dV_i}{dt} = -\frac{V_i}{\tau_S} \tag{3.12}$$

It should be emphasized that the above relationship describes the rate of change of the *velocity* (or momentum) of the test particle "i" due to collisions with the background plasma.

Collisions in plasmas are mediated by the Coulomb force whose cross-section varies as ${V_{rel}}^{-3}$, where V_{rel} is the relative velocity between two colliding charged particles. The overall slowing down time is determined from the combined influence of collisions with bulk electrons and ions, with the effective collision *frequencies* adding so that:

$$\frac{1}{\tau_S} = \frac{1}{\tau_{Se}} + \frac{1}{\tau_{Si}} \tag{3.13}$$

For typical heating experiments on Alcator C-Mod the minority ions have energies $E_{minority} \sim 20 - 100 \times T_e$. Thus the relative velocity for collisions between minority and bulk ions is determined by the minority ion energy. However, for $E_{minority} \ll T_e \times (m_{minority}/m_e)$, a *very* good approximation on C-Mod, the thermal velocity of the electrons determines the relative velocity for collisions between minority ions and electrons. Under these conditions the electron and ion slowing down times for test ions of charge and mass, Z_t and m_t, in a field (bulk) plasma with ion charge and

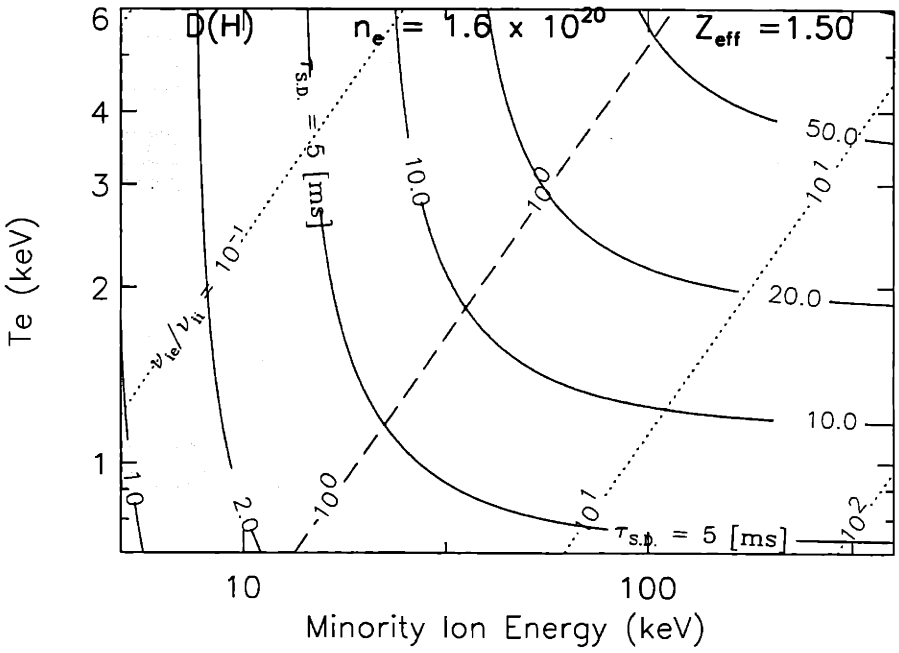

Figure 3-4: Contours of minority ion (momentum) slowing down time. Contours ν_{ie}/ν_{ii}, the partition between energy loss to bulk electrons and bulk ions respectively, are also shown.

mass, Z_f and m_f, are given by:

$$\tau_{Se} = \frac{3\,(2\pi)^{3/2}\epsilon_0^2\, m_t\, m_e\, v_{te}^3}{n_e\, Z_t^2\, e^4\, \ln\Lambda} \approx 11.7\,[ms] \times M_t \frac{T_e^{3/2}}{Z_t^2 n_{20}} \tag{3.14}$$

$$\tau_{Si} = \frac{4\pi\epsilon_0^2\, m_t\, m_f\, v_t^3}{n_f\, Z_f^2\, Z_t^2\, \ln\Lambda} \frac{m_t}{m_t + m_f} \approx 0.206\,[ms] \times \frac{M_f\, E_{min}^{3/2}}{\sqrt{M_t}\, Z_t^2\, Z_f^2\, n_{f_{20}}} \frac{M_t}{M_t + M_f} \tag{3.15}$$

Here Λ is the coulomb logarithm (≈ 16 for C-Mod plasmas) and depends only weakly on plasma parameters. T_e and E_{min} are in units of keV, and the densities subscripted "20" are in units of $10^{20} m^{-3}$. Contours of the slowing down time as functions of minority ion energy and electron temperature are shown in Fig. 3-4. For discussions of ICRF heating, we will be more interested in the rate of exchange of minority ion

energy with the bulk plasma. As the *momentum* slowing down times are the most commonly used time-scales, it is useful to express *energy* exchange times in terms of them. The average power loss of a minority ion due to collisions with either electrons or other ions is equal to the drag force acting on that minority ion times the ion velocity. The energy transfer in the case of electrons is nearly 100% efficient because of the mass imbalance. Thus to a good approximation:

$$P_e = F_{drag_e} v_t = m_t \frac{v_t^2}{\tau_{Se}} = \frac{E_{test}}{\tau_{Se}/2} \equiv \frac{E_{test}}{\tau_{Ee}} \tag{3.16}$$

In the case of collisions with ions, the scattering of the test ion (mass m_t) with each collision is significant and this reduces the energy transfer to the field ions (mass m_f) from that calculated from the frictional loss [1]:

$$P_i = F_{drag_i} v_t \frac{m_t}{m_t + m_f} = \frac{E_{test}}{\tau_{Se}\left(\frac{m_t+m_f}{2m_t}\right)} \equiv \frac{E_{test}}{\tau_{Ei}} \tag{3.17}$$

So (momentum) slowing down times may be converted for use in energy transfer problems with the expressions:

$$\begin{aligned} \tau_{Ee} &= \tau_{Se}/2. \\ \tau_{Ei} &= \tau_{Si}\frac{m_f + m_t}{2m_t} \end{aligned} \tag{3.18}$$

Measurements of the minority ion "tail" energy are of use in monitoring the behavior of minority ion heating experiments. On Alcator C-Mod, direct measurements are not typically possible. At very low densities, the neutral particle analyzer can be used to measure the tail. However, at the higher densities of the standard ICRF target plasmas, central minority ions which become neutralized through charge exchange are typically restripped before reaching the edge of the plasma, thus cutting off this diagnostic channel to the plasma core. To the end of measuring minority ion tails, a useful result to be taken from Eqs. 3.14 and 3.18 is that the energy slowing down time is independent of energy (ie $\tau_{Ee} \neq \tau_{Ee}(E)$). An interesting consequence

of this result is that measurements of electron temperature dynamics can be a useful probe of the minority ion tail energy. This perhaps surprising result is seen by considering the expression for the total power being transferred to electrons by the entire distribution of minority ions:

$$p_e|_{minority} = n_m \int_0^\infty g(E)\frac{E}{\tau_{ee}}dE = \frac{n_{min}}{\tau_{ee}}\int_0^\infty g(E)EdE \equiv n_m\frac{E_{tail}}{\tau_{ee}} \qquad (3.19)$$

The minority tail energy, E_{tail}, has been implicitly defined above as the average energy of the minority ion distribution. This simple result states that at any instant in time, the power loss of the minority ions on the electron species is proportional to the tail energy. Of course the minority ions at any instant are also losing energy to the bulk ions. However, even when slowing down on ions dominates, which is true at low tail energies, the result of Eq. 3.19 remains unchanged. The electron power loss channel of the minority ions is a particularly good indicator of the total tail energy. Even if bulk ion temperature diagnostics were available with similar accuracy and time resolution as the electron temperature diagnostics, they would not provide as simple a measurement of the tail energies. This is because the slowing down time on bulk ions is a function of minority ion energy (see equation 3.15) and no simplifications analogous to those of Eq. 3.19 can be made. In Chapt. 6 the particulars of the techniques to extract minority tail information from the grating polychromator measurements of electron temperature will be given. In the next section the dynamics of the decay of the overall minority ion energy will be studied in order to provide the theoretical basis for a minority tail diagnostic.

3.4.2 Dynamics of the minority tail slowing down

Although in discussion of Eq. 3.14 we noted that by measuring only the power lost by the minority ions to electrons we could measure their total energy, that is not to say that the ions are not important. Obviously, in order to solve for the time evolution of the tail energy, interactions with ions must be considered and in fact can dominate the *time derivative* of $E_{tail}(t)$. In the analysis that follows, consider the situation

where at t=0 the ICRF power is abruptly turned off and the energy distribution of minority ions decays freely down to a thermal distribution in equilibrium with the background plasma at temperature, T. It will be assumed that each minority ion slows down independently and each according to its instantaneous energy. Consider a test ion of the minority species with an initial energy $E_0 \gg T$. From Eqs. 3.14, 3.15, and 3.18 we find that the differential equation which governs the decay of this test ion is given by:

$$\begin{aligned} \frac{dE}{dt} &= -\frac{E}{\tau_{Ee}} - \frac{E}{\tau_{Ei}} \\ &= -\frac{E}{\tau_1} - \frac{E_0^{3/2}}{\tau_2(E_0)} E^{-1/2} \end{aligned} \tag{3.20}$$

with $E(0) \equiv E_0$ and $\tau_1, and\ \tau_2(E_0)$ are independent of time.

The solution to this equation is given by:

$$\begin{aligned} E(t, E_0)) &= E_0 \left[e^{-\frac{3}{2}t/\tau_1} + \left(\frac{\tau_1}{\tau_2(E_0)} \right) \left(e^{-\frac{3}{2}t/\tau_1} - 1 \right) \right]^{2/3} \\ &\approx E_0\ e^{-t/\tau_1} \text{ for: } \tau_1 \ll \tau_2(E_0) \\ &\approx E_0\ (1 - \frac{3}{2}\frac{t}{\tau_2(E_0)})^{2/3} \text{ for: } \tau_1 \gg \tau_2(E_0) \end{aligned} \tag{3.21}$$

This equation is useful as it illustrates the nature of the competition between slowing down on electrons and ions. The ratio $\tau_1/\tau_2(E_0)$ is the relative strength of the *initial* ion slowing down to electron slowing down. From Eqs. 3.14, 3.15 we have: $\tau_1/\tau_2(E_0) = 3/4\sqrt{\pi}(m_t^{3/2}/(m_f\sqrt{m_e}))Z_{eff}(T_e/E_0)^{3/2}$. At large values of t, Eq. 3.21 indicates that the minority energy drops abruptly to zero. In reality, the minority ions thermalize with the bulk plasma and the slowing down on ions slows as the energy approaches the plasma temperature. To be rigorous, a fully general expression for the ion slowing down should be used, but to a good approximation, the low energy dynamics of the slowing down are captured by using the modified differential

equation:

$$\begin{aligned} \frac{dE}{dt} &= -\frac{(E-T)}{\tau_{Ee}} - \frac{(E-T)}{\tau_{Ei}} \\ &= -\frac{E}{\tau_1} + \frac{T}{\tau_1} - \frac{E_0^{3/2}}{\tau_2(E_0)} E^{-1/2} + T\,\frac{E_0^{3/2}}{\tau_2(E_0)} E^{-3/2} \end{aligned} \tag{3.22}$$

This equation does not lend itself easily to an analytic solution, but is easily solved numerically. Such numerical solutions are used later in the calculation of the distribution averaged decay of the minority population energy. A comparison of the solutions to Eqs. 3.20 and 3.22 is shown in Fig. 3-5.

We are now in a position to calculate the dynamic response of the minority ion population taken as a whole to suddenly turning off the ICRF power from steady state conditions. The time evolution of the average energy (E_{tail}) is defined as:

$$E_{tail}(t) = \int_0^\infty g(E_0) E(t, E_0) dE_0 \tag{3.23}$$

For $E(t, E_0)$, the time evolution of the energy of a test ion with initial energy E_0, we can use either Eq. 3.21 or the solution to Eq. 3.22. We also have an expression for the statistical distribution of starting energies from Eqs. 3.8 and 3.9. So for a given set of bulk plasma parameters, minority concentration, and steady state ICRF minority heating power density, we can compute the expected tail energy and its turn-off transient. Figure 3-6 shows example results of such calculations. In Chapt. 9 we will use the results of this type of calculation to determine the minority ion tail energy from simple measurements of the electron temperature.

3.5 Mode Conversion

3.5.1 Introduction and motivation

Early ICRF experiments focused on *ion* heating and demonstrated the effectiveness of ICRF as an auxiliary heat source in tokamaks. Under conditions described below,

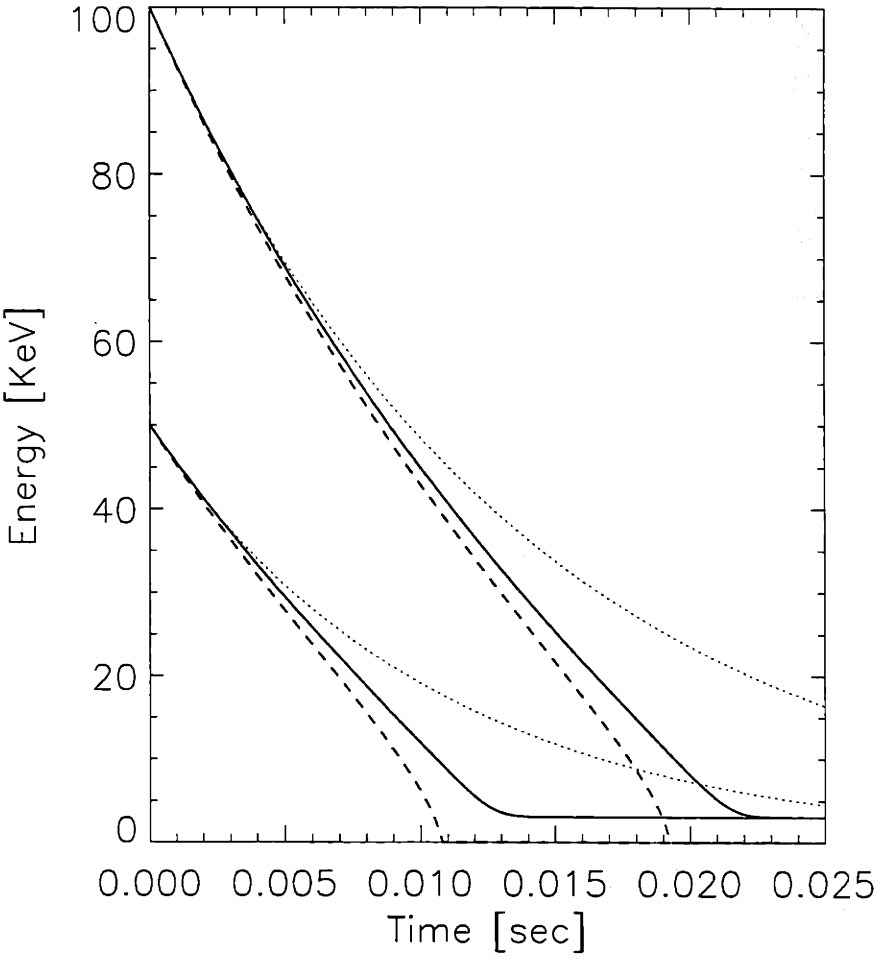

Figure 3-5: Time histories of the free decay of test hydrogen ion energies after ICRF turnoff. The plasma parameters for this calculation were $T_e = 3keV$, $n_e = 1.8 \times 10^{20} m^{-3}$, $Z_{eff} = 1.5$ The solid lines represent numerical solutions to Eq. 3.22, the dashed lines represent the analytic solution given by Eq. 3.21. A purely exponential decay at the *initial* energy slowing down rate is shown in dots for comparison.

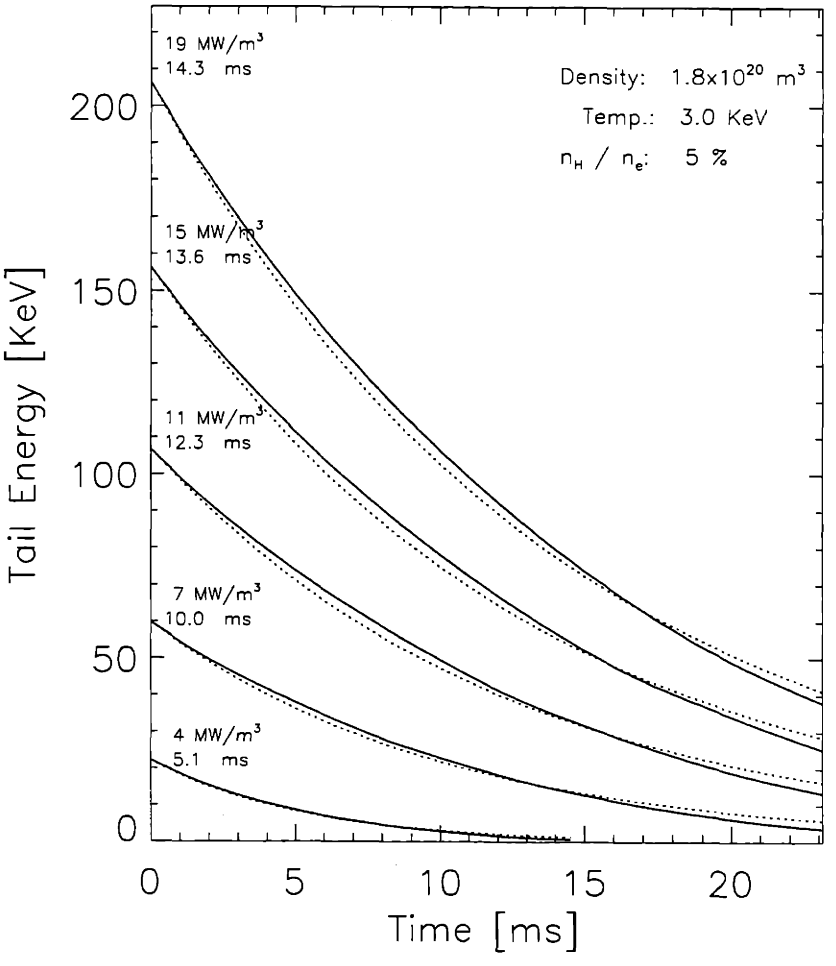

Figure 3-6: Figure showing the decay of the hydrogen minority tail energy after the source power is suddenly turned off. Each curve represents the weighted average of the energy decays of an ensemble of test ions whose energy distribution is the Stix distribution (see Eq. 3.8) for the steady state power density indicated. Also indicated is best fit exponential decay time (dotted line).

significant ICRF power can be coupled *directly* to *electrons*. The ability to couple power to the plasma electrons allows the plasma current to be affected, either by changing the electron temperature and thus the plasma resistivity or by driving current directly with ICRF waves. Controlling the details of the plasma current profile is of great interest because it can result in improvements in tokamak stability and confinement. Although *electron* cyclotron resonance heating (ECRH) in principle can do this very effectively, the current state of ECRH power technology cannot match the high power levels or pulse durations of ICRF systems, particularly at the high frequencies needed for future reactors. For this reason, there has been growing interest in exploring direct electron heating regimes in ICRF experiments.

The fast magnetosonic wave can damp *directly* on electrons through electron Landau damping (ELD) and transit time magnetic pumping (TTMP). These damping mechanisms are strongest for $\omega/k_{\|} \approx \sqrt{T_e/m_e}$ and for finite $\beta_e \equiv 2\mu_0 n_e T_e/B^2$. While fast wave direct electron heating and current drive have been performed successfully on other tokamaks [21, 22], the current conditions on Alcator C-Mod ($\omega/k_{\|}v_{th} \approx 2$, and $\beta_e < 1\%$) result in weak single pass absorption. A more efficient and more versatile way of heating electrons in ICRF experiments is via mode conversion to the ion Bernstein wave.

In a two ion species plasma, there is an ion-ion hybrid resonance layer between the two ion cyclotron resonance layers. When the fast magnetosonic wave encounters this layer, power can be converted into another wave mode, the ion Bernstein wave (IBW). The Landau damping of the IBW can be very strong due to an upshift in the $k_{\|}$ spectrum due to its relatively short wavelength (see §3.2). As will be seen in the following section, mode conversion heating has an additional advantage over direct electron heating by the fast wave in that it can occur *off-axis*, the precise location being controllable by the magnetic field and ion mixture. Mode convsersion heating on tokamaks is currently an area of great interest in the international fusion community. Efficient electron heating has been obtained using mode conversion on Alcator C-Mod in $H - He^3$ and $D - He^3$ plasmas [23]. The analysis of these experiments constitute the bulk of this thesis and add to the recent results on TFTR [24], Tore Supra [25], and

ASDEX [26]. In Chapt. 9 analysis is presented of electron heating which is most likely due to IBW mode conversion in a D-H plasma. This heating regime will be revisited in the near future. If confirmed, these results represent the first demonstration of such a scenario for tokamaks.

3.5.2 Ion-ion hybrid resonance:

In a two ion species plasma, an additional $N_{\|}^2 = S$ resonance occurs between the cyclotron resonances of the two ion species [27]. For $N_{\|}^2 \ll \omega_{pi}^2/\omega_{ci}^2$ the *ion-ion hybrid* resonance frequency can be found by balancing the $\omega_{p_j}^2/\omega^2 - \Omega_j^2$ terms of the two ions against each other and is given by:

$$\omega_{ii}^2 = \Omega_{c_1}\Omega_{c_2} Z_1 Z_2 \left(\frac{M_1 X_1 + M_2 X_2}{M_2 Z_1^2 X_1 + M_1 Z_2^2 X_2} \right) \tag{3.24}$$

where M, Z and X refer to the atomic mass unit, atomic number, and density fraction ($X_i \equiv n_i / \sum_{ionsj} n_j$) respectively for the ion species. On Alcator C-Mod, $(\omega_{ci} N_{\|})^2/\omega_{pi}^2 \lesssim 0.05$, and the error made in the resonance location by neglecting $N_{\|}$ in Eq. 3.24 is $< 0.5cm$.

3.5.3 Dispersion relationship near ion-ion hybrid resonance

At the ion-ion hybrid resonance, cold plasma theory breaks down and kinetic effects must be included. With thermal effects included, the presence of additional plasma modes becomes apparent and it has been shown in general [28, 29, 30] that the resonance of cold plasma modes gives rise to "mode conversion" to these hot modes which tend to damp quickly. If in the general solutions to Eq. 2.3 the relevant expressions are expanded to lowest order in $b = k_{\perp}^2 \rho^2/2$, the dispersion relation of Eq. 3.4 is

modified to become [31]:

$$\begin{aligned} aN_x^4 - bN_x^2 + c &= 0 \qquad (3.25) \\ \text{where: } a &= S/K_{zz} - K_{xx}^1, \qquad b = N_z^2 - S, \\ c &= (N_z^2 - R)(N_z^2 - L) \\ K_{zz} &= -(\omega_{pe}/k_\parallel v_e)^2 Z'(\omega/k_\parallel v_e), \\ K_{xx}^1 &= \sum_j (\omega_{pj}^2 v_j^2/2\omega_{cj}^2)\left[(\omega^2 - \omega_{cj}^2)^{-1} + (\omega^2 - 4\omega_{cj}^2)^{-1}\right] \end{aligned}$$

Here Z' is the derivative of the Fried Conte dispersion function [32]. Analysis of this "hot" plasma dispersion relationship reveals the presence of another root of the electromagnetic dispersion relationship, the so called ion Bernstein wave (IBW).

Equation 2.29 gave the electrostatic approximation to the IBW dispersion relation. IBW solutions exist between each cyclotron harmonic of the majority ion species above the fundamental. For $\omega_{pi}/\Omega_i >> 1$, the solution to the lowest frequency branch for a single species plasma may be expressed as

$$N_\perp^2 = \frac{1}{T_i}\left[\frac{m_i c^2}{3}\frac{4\Omega_i^2 - \omega^2}{\omega^2}\right] + N_\parallel^2\, G(\omega, B) \qquad (3.26)$$

where G is a function of frequency ω and magnetic field, B, and to a good approximation can be ignored [33]. By comparing this expression with Eq. 3.3, it is apparent that, except for very near $\omega = 2\Omega_i$, $(k_\perp)_{\text{IBW}} >> (k_\perp)_{\text{Fast Wave}}$ for a single ion species plasma. The dispersion curves for the fast wave and IBW for the case of a *pure deuterium* plasma at 8 Tesla are sketched in Fig. 3-7. As shown, the two modes remain distinct and well separated in this case.

In the previous section we saw that the introduction of a minority ion species gives rise to the ion-ion hybrid resonance for the fast wave. In the cold plasma picture this leads to a divergence of $k_\perp \to \infty$. Proper hot-plasma treatment instead shows that *electromagnetic* behavior of the IBW allows it to interact with the fast wave. It can

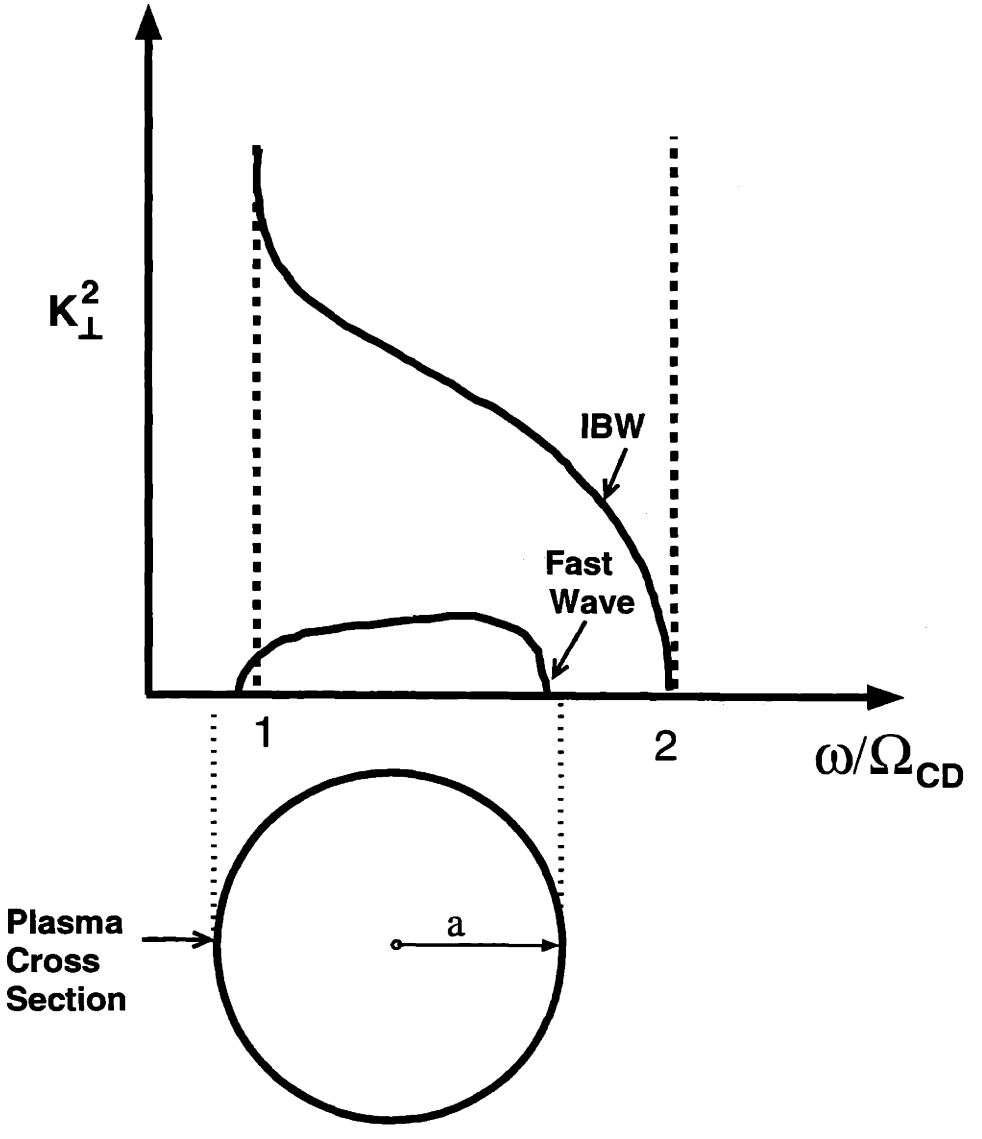

Figure 3-7: Schematic diagram of the dispersion relations for the fast wave and ion Bernstein wave in a *pure* deuterium plasma. The geometry shown roughly represents that of the standard Alcator C-Mod $D(He^3)$ heating scenario, B = 8 Tesla, $\omega = 2\pi \times 80$ MHz. The curves sketched here represent the solutions which can be obtained from simple cold plasma theory for the fast wave (Eq. 3.3), and from a simple electrostatic treatment of the IBW (Eq. 3.26).

be shown [34, 35, 36] that for

$$\frac{n_{min}}{n_{maj}} \gtrsim 2\frac{k_{\|}v_{\|min}}{\omega}\left[\frac{Z_{maj}^2 M_{min}}{Z_{min}^2 M_{maj}}\right]\left(\frac{1}{1-\left(\frac{Z_{maj}M_{min}}{Z_{min}M_{maj}}\right)^2}+\frac{k_{\|}^2c^2}{\omega_{p_{maj}}^2}\right), \tag{3.27}$$

there is a confluence between the fast and ion Bernstein wave solutions, and *mode conversion* occurs. When this is the case, the modifications to the dispersion relations near the ion-ion hybrid resonance are substantial [37] and are sketched in Fig. 3-8.

3.5.4 Mode conversion efficiency:

It can be shown that for high field launch in a tokamak, the fast wave encounters the mode conversion layer before the left-hand cutoff ($n_{\|}^2 = L$) and is converted with 100% efficiency to the IBW. In the case of a low field launch (as in Alcator C-Mod) the fast wave encounters the left-hand cutoff first. The fast wave is evanescent in the region between the cutoff and the mode conversion layer. In order to determine the amount of power coupled to the IBW, the coefficients of Eq. 3.25 can be expanded in a Taylor series about the mode conversion radius, R_S. The dispersion relation is then converted to a differential equation [38] through an inverse Fourier transformation. The asymptotic behavior of the integral solutions determines the tunneling and absorption coefficients for the fast wave [31]. The fraction of the incident fast wave power that tunnels through the mode conversion layer and propagates away as a fast wave on the other side is designated by "T", the transmission coefficient. Similarly, "R" designates the reflected fast wave power fraction and "M" gives the mode conversion efficiency. Although the general case is difficult to treat, in the case of low-field incidence on an isolated mode conversion layer (far enough removed from any ion cyclotron resonance that ion damping can be ignored), and for $k_{\|} = 0$, the coefficients are given by [30]:

$$T = e^{-2\eta} \qquad R = (1-T)^2 \qquad M = T(1-T) \tag{3.28}$$

$$\text{where, } \eta \approx \frac{\pi\omega_{p_1}R_0}{4c}\frac{\alpha\,(\mu-1)^2}{\mu(\mu+\alpha)}\left(\frac{f(1+\mu)}{2(1+\alpha)}\right)^{1/2}, \tag{3.29}$$

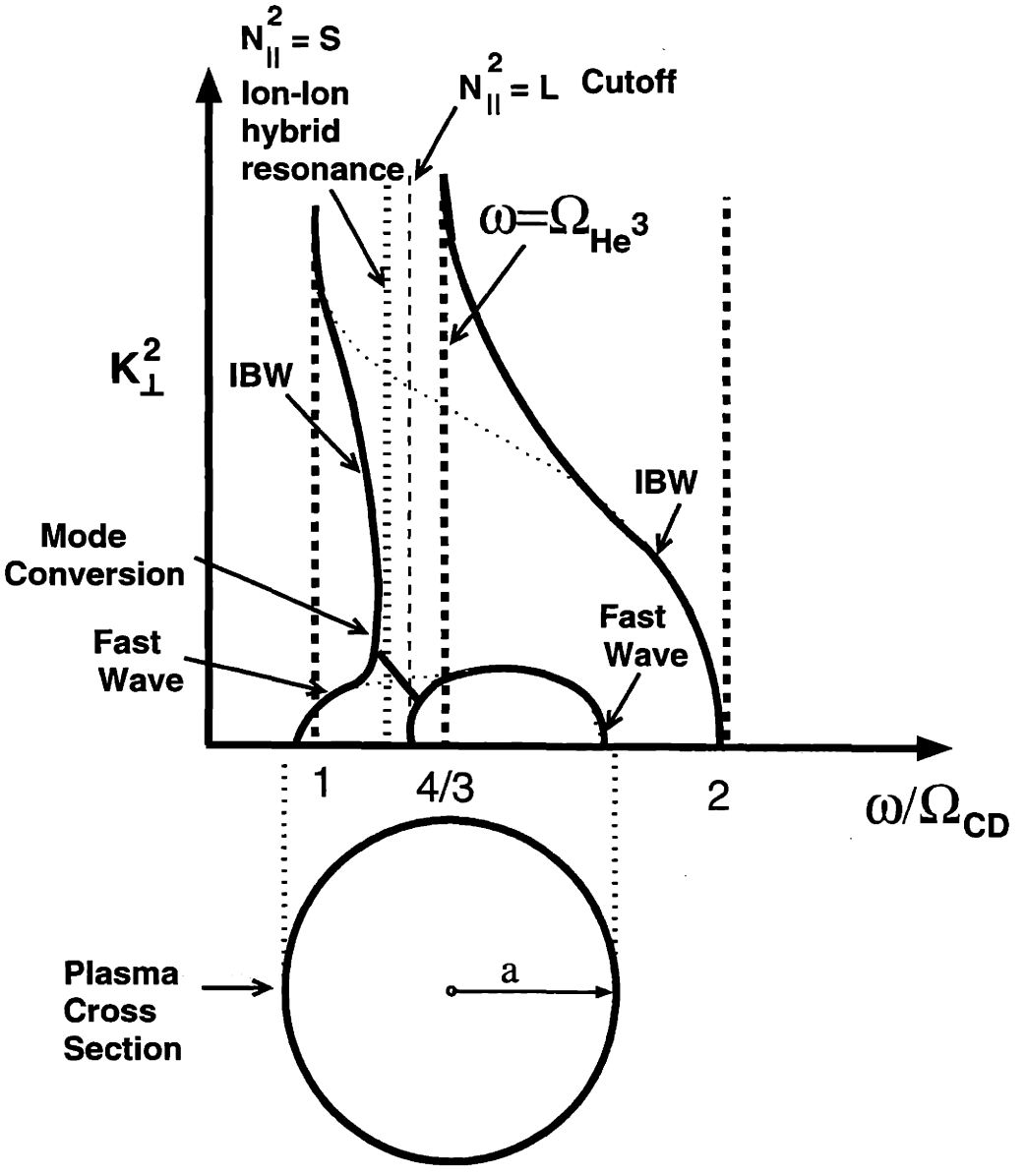

Figure 3-8: Schematic diagram of the dispersion relations for the fast wave and ion Bernstein wave in a $D(He^3)$ plasma for $n_{He^3}/n_e \approx 0.2$, B = 8 Tesla, $\omega = 2\pi \times 80$ MHz. The modifications to the dispersion relationships near the ion-ion hybrid resonance are substantial (*cf* Fig. 3-7). In this case, power in fast waves launched from the low field side can undergo mode conversion to ion Bernstein waves near the ion-ion hybrid resonance.

where $f = (1 + \mu\alpha)/(\mu + \alpha)$ for a two ion plasma with $\alpha = Z_2 n_2 / Z_1 n_1$, and $\mu = Z_1 m_2 / Z_2 m_1$. Note that in the above, $R+T+M = 1$. Also note that since $0 < T < 1$, the above equation predicts a maximum mode conversion efficiency of 25%, that is $M_{Max} = 0.25$ for $\eta_{optimal} \approx 0.35$. This is a simple single-pass treatment, however, and when reflections from cutoff layers are included, standing wave patterns can enhance the fields near the mode conversion layer which can result in significantly higher mode conversion efficiencies near $\eta = \eta_{optimal}$ [39, 25].

3.6 Parametric dependence of minority heating

Wave physics considered here indicates mechanisms through which the absorption channels compete with each other. A hot plasma correction to the fast wave polarization is given and its interpretation underscores the nature of this competition.

As we have seen, the minority ion populations in these heating experiments can be raised to high energies and their velocity distribution can become distinctly non thermal. Hot plasma theory is needed to calculate the expected effects of this subpopulation on the fast wave. When thermal effects of the minority tail are considered, it is found that Eq. 3.7 must be modified. The result for $\theta = \pi/2$ [15] may be expressed as

$$\left|\frac{E^+}{E_y}\right|^2 = \frac{(\omega/\omega_{ci} - 1)^2}{(1+\sigma^2)}, \tag{3.30}$$

$$\text{where } \sigma^2 = \frac{\pi}{4}\left(\frac{n_{min}}{n_{maj}}\frac{M_{maj}}{M_{min}}\frac{Z_{min}^2}{Z_{maj}^2}\right)^2 \left(1 - \frac{\Omega_{maj}^2}{\omega^2}\right)^2 \left(\frac{\omega}{k_\parallel v_{min}}\right)^2.$$

Here, E^+ is the component of the fast wave electric field which heats ions. This result is interesting because it indicates that kinetic effects for the minority ions are *required* in order to obtain the E^+ predicted by simple cold plasma analysis. At sufficiently low minority ion energies ($E_{min} \propto v_{min}^2$), σ^2 becomes large and the ion heating is lost. Physical insight into this effect is obtained by recognizing that for small minority ion

concentrations

$$\sigma \approx \sqrt{\pi/2}\,\frac{\delta_{MC}}{\Delta_{dop}}, \tag{3.31}$$

where,

$$\Delta_{dop} \equiv R\,\frac{k_{\|}\,v_{min}}{\sqrt{2}\omega} \tag{3.32}$$

is the doppler width of the minority ion resonance and $\delta_{MC} = R_{\Omega_{min}} - R_{\omega_{ii}}$ (*cf* Eq. 3.24) is the separation between the ion-ion hybrid resonance layer and the minority ion cyclotron layer to first order.

3.7 Minority ion heating vs. Mode conversion

Equation 3.30 indicates that minority heating power is strongest when the doppler width of the minority cyclotron resonance is large and easily encompasses the ion-ion hybrid resonance ($\sigma^2 << 1$). The threshold between the minority heating and the mode conversion regimes is given by $\sigma = 1$. Near this threshold, these two heating mechanisms compete with each other in a very delicate balance. Key parameters which govern the competition are the energy and density of the minority ions. As an example, Eq. 3.11 indicates that the tail energy and the minority density are inversely related (the deposited power is distributed among a greater number of ions). Increasing the minority density by 10% decreases v_{min}^2 by 10% as the deposited power is distributed among a greater number of ions. From Eq. 3.30 both of these changes increase σ^2 (the greater minority density moves the ion-ion hybrid layer further from the cyclotron resonance and the decreased minority energy decreases the doppler width). The resulting 30% increase in σ^2 reduces $|E^+|^2$ by $\approx$ 15% for $\sigma \approx 1$. The reduction in minority ion heating (*cf* Eq. 3.5) further reduces v_{min} and the ion heating channel will begin to collapse. Meanwhile Eq. 3.27 indicates that these changes favor mode conversion and the reduced ion absorption is replaced by stronger electron heating.

Alcator C-Mod currently has two standard modes of operation corresponding to two different minority heating scenarios:

D(H): Minority hydrogen in deuterium at 5.3 Tesla.

D($\mathbf{He^3}$): Minority helium-3 in deuterium at 7.9 Tesla.

Minority *ion* heating is the intended absorption mechanism in both cases. We have seen however that mode conversion into the IBW gives strong *electron* heating, and can compete with minority absorption. It is important to determine which of these two distinctly different heating mechanisms will dominate in a given experiment.

It was seen in §3.4 that based on the basic *cold-plasma* fast wave polarization, the single-pass ion absorption in $D(He^3)$ is nearly an order of magnitude weaker than in the $D(H)$ case. The relatively weak ion absorption in the $D(He^3)$ case suggests that competition with mode conversion will be strongest in this scenario. Measurements in Chapt. 7 will in fact show that mode conversion has been the dominant heating mechanism in the $D(He^3)$ experiments to date.

Chapter 4

Electron Cyclotron Emission (ECE) in Tokamaks

Early treatment of electron cyclotron emission (ECE) concerned parasitic power loss from thermonuclear plasmas [40]. The first examination of ECE as a potential temperature diagnostic was by Engelman [41]. ECE emission is now routinely used on all major tokamaks to measure electron temperature and diagnose non-thermal electrons. In this chapter, an overview of the principles involved in ECE temperature measurements in tokamak plasmas will be given. This discussion parallels that given by Hutchinson [42].

4.1 Radiation from gyro motion of charged particles

We have seen the basic expression governing cyclotron motion in Eq. 1.4. The centripetal acceleration of the orbital motion of charges gives rise to radiation at the cyclotron frequency. The Schott-Trubnikov [43] equation gives the power density

radiated by a test charge as seen in the lab frame:

$$\frac{d^2P}{d\omega d\Omega_s} = \frac{e^2\omega^2}{8\pi^2\epsilon_0 c}\sum_{m=1}^{\infty}\left[\left(\frac{cos\theta-\beta_{\|}}{sin\theta}\right)^2 J_m^2(\xi)+\beta_{\perp}^2 J'^2_m(\xi)\right]\frac{\delta\left(\left[1-\beta_{\|}cos\theta\right]\omega-m\omega_c\right)}{1-\beta_{\|}cos\theta}$$
$$\text{where: } \xi=\frac{\omega}{\omega_c}\beta_{\perp}sin\theta \tag{4.1}$$

It is important to note that even for the case of a charged particle in purely harmonic circular motion about a magnetic field line, the radiation has components at higher harmonics of the basic cyclotron frequency, $\omega_m = m\omega_c/(1-\beta_{\|}cos\theta)$. This is an effect due to the finite transit time for light across a Larmor radius.

4.2 Thermal ECE plasma emissivity

As a simplifying starting assumption, we will consider a *diffuse* plasma (characterizable by an refractive index close to unity). In this case, the total plasma emission is approximated by adding up the radiation contributions from each plasma particle. For a given velocity distribution, $f(\beta_{\perp},\beta_{\|})$, this plasma emissivity calculation can be expressed in integral form:

$$j(\omega,\theta) = c^3\int\frac{d^2P}{d\omega d\Omega_s}(1-\beta_{\|}cos\theta)f(\beta_{\perp},\beta_{\|})2\pi\beta_{\perp}d\beta_{\perp}\beta_{\|} \tag{4.2}$$

The factor of $(1-\beta_{\|}cos\theta)$ accounts for the difference between the power loss in the particle frame and the lab frame. It is often easiest to deal with the frequency integrated emissivity, j_m, and the associated shape function, ϕ, defined implicitly below:

$$j_m(\omega) = j_m\phi(\omega-\omega_m), \quad \int\phi(\omega)d\omega = 1 \tag{4.3}$$

For a *nonrelativistic* ($\beta \ll 1$) Maxwellian plasma, the frequency integrated emissivity can be calculated directly and is given by:

$$j_m = \frac{e^2\omega_m^2 n_e}{8\pi^2\epsilon_0 c}\frac{m^{2m-1}}{(m-1)!}(sin\theta)^{2(m-1)}(cos^2\theta+1)\left(\frac{T}{2m_e c^2}\right)^m \tag{4.4}$$

4.3 Radiation transport

In addition to radiating, gyrating charged particles can *absorb* energy from electromagnetic waves of the appropriate frequency. The propagation of energy in a plasma thus involves a continuous emission and reabsorption. It is crucial to the application of ECE as a temperature diagnostic that this behavior is well understood. The local balance between emission and absorption is expressed in Eq. 4.5.

$$\frac{dI}{ds} = j(\omega) - \alpha(\omega)I \tag{4.5}$$

In Eq. 4.5, the intensity of radiation, I $[W/m^2 \cdot st \cdot s^{-1}]$, is the power radiated per unit area per steradian per unit angular frequency. The absorption coefficient, $\alpha\,[m^{-1}]$, is the fractional absorbed power per unit path length, ds. Integrating the above equation along a trajectory through a region of plasma (as sketched in Fig. 4-1) allows one to express the final intensity by Eq. 4.6.

$$I(s_2) = I(s_1)e^{-\tau_{21}} + \int_{s_1}^{s_2} j(w)e^{\tau-\tau_2}ds \tag{4.6}$$

Where τ is the "optical depth" given by:

$$\tau(s) \equiv \int^s \alpha(\omega)ds, \qquad \tau_{21} \equiv \tau_2 - \tau_1 \tag{4.7}$$

As a useful example, assume that j/α is constant across the plasma slab of Fig. 4-1. In this case, with $d\tau = \alpha(\omega)ds$, Eq. 4.6 becomes:

$$I(s_2) = I(s_1)e^{-\tau_{21}} + (j/\alpha)\left[1 - e^{-\tau_{21}}\right] \tag{4.8}$$

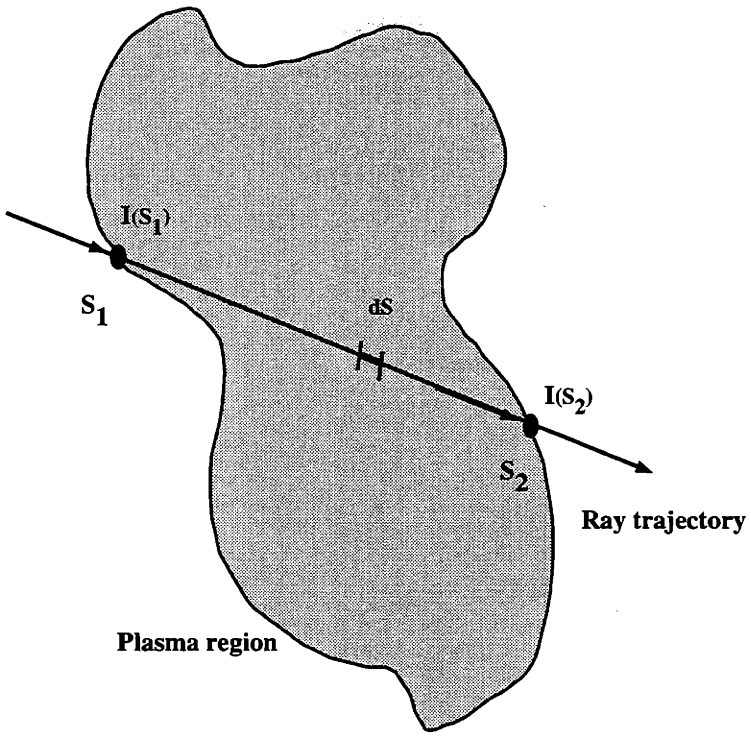

Figure 4-1: Sketch illustrating geometry for calculation of radiative transfer expressed in Eq. 4.6.

Consider a plasma slab for which $\tau_{21} \gg 1$, *ie* a slab which is "optically thick" (this is general, as the slab can be chosen to be arbitrarily thick. See §4.5 for a more detailed discussion of optical depth). In this case the incident radiation is completely absorbed and the emerging radiation intensity is:

$$I_{\tau \gg 1} = j/\alpha \tag{4.9}$$

We can further consider the case where the slab is in thermal equilibrium with a blackbody enclosure at temperature, T. Applying detailed balance to the equilibrium gives:

$$I_{equil}(\omega) = B(\omega) \tag{4.10}$$

where $B(\omega)$ is the characteristic blackbody radiation intensity given by Planck's formula:

$$\begin{aligned} B(\omega) &= \frac{\hbar\omega^3}{8\pi^3c^2}\frac{1}{e^{\hbar\omega/T}-1} \\ &= \frac{\omega^2 T}{8\pi^3c^2} \qquad \text{for } \hbar\omega \ll T \end{aligned} \tag{4.11}$$

The last expression is the infrared limit or the Rayleigh-Jeans approximation for $B(\omega)$ and is very accurate for ECE emission in fusion plasmas. So, combining Eqs. 4.9 and 4.10, we obtain

$$j/\alpha = B(\omega) = \frac{\omega^2 T}{8\pi^3c^2} \tag{4.12}$$

which is Kirchhoff's law. This result is far more general than is implied by the conditions of our thought experiment. The important thing to note is that the expression on the right-hand side is a function *only* of the temperature (and fundamental constants), despite the fact that both numerator and denominator on the left-hand side generally depend on the local plasma parameters. Their equation tells us that the *ratio* of the emissivity to the absorption coefficient can not depend on parameters other than temperature. This conclusion is true even in non equilibrium thermal plasmas. The assumptions of optical thickness and equilibrium were useful in obtaining Eq. 4.12, but the result is general.

4.4 ECE Applications in tokamaks

In §1.2.1 we saw that the dominant component of the magnetic field (toroidal) varies as $|B| \propto R^{-1}$. Thus when viewing a given harmonic of cyclotron emission along the midplane of the tokamak, there is simple mapping from frequency to major radius ($\omega \rightarrow B \rightarrow R$), and the cyclotron resonance occurs at a localized position along the major radius. The cyclotron frequency is not only a function of position in the tokamak, however. The precise value for each electron is also a function of its velocity.

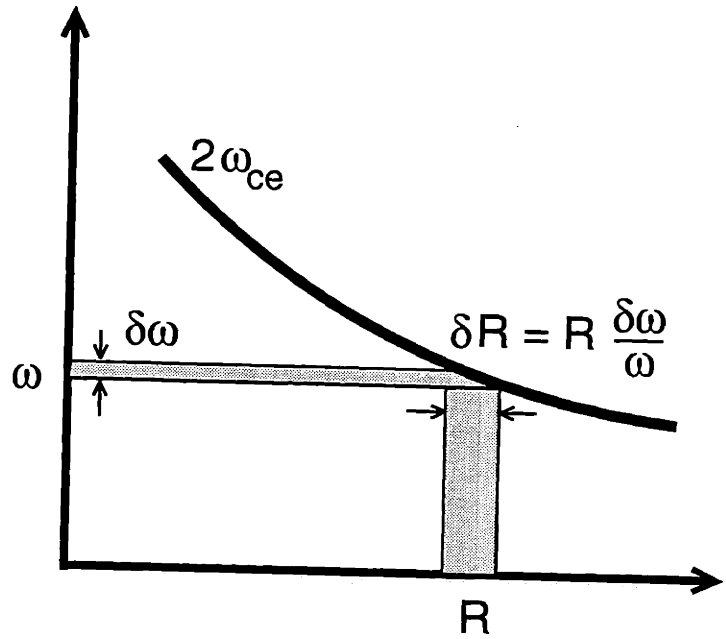

Figure 4-2: Cartoon of the map from frequency to spatial resolution.

As observed from an angle θ to the magnetic field, the velocity dependance is given by:

$$\begin{aligned} \omega_m &= \frac{m\Omega(1-\beta^2)^{1/2}}{(1-\beta_{\|}\cos\theta)} \\ \text{Where } \beta &= \sqrt{1-v^2/c^2} \end{aligned} \tag{4.13}$$

The net effect for a thermal distribution of electrons is to broaden the spatial region over which particles experience cyclotron resonance at a given frequency. This relationship between frequency and spatial broadening is sketched in Fig. 4-2, and a more detailed discussion is found in §5.4.5. In tokamak plasmas, density and temperature typically vary slowly over the width of the emission region for a given frequency. In this sense the emission layers are "narrow" and the expression for the overall optical depth for this resonance layer for the m^{th} cyclotron harmonic, τ_m, may be simplified

as follows:

$$\begin{aligned}\tau_m &\equiv \int \alpha_m(\omega)ds = \int \alpha_m(\omega)\left|\frac{d(m\Omega)}{ds}\right|^{-1} d(m\Omega) \\ &= \frac{R}{\Omega}\int \alpha(\omega)d\Omega = \frac{R}{\Omega}\alpha_m \int \phi(\omega - m\Omega)d\Omega \\ &= \frac{R\alpha_m}{m\Omega}\end{aligned} \tag{4.14}$$

For the simplified case of a diffuse, non-relativistic plasma the integrated emission may be expressed as

$$\alpha_m|_{diffuse} \equiv \frac{\pi}{2c}\omega_{pe}^2 \frac{m^{2m-1}}{(m-1)!}(sin\theta)^{2(m-1)}(cos^2\theta + 1)\left(\frac{T}{2m_e c^2}\right)^{m-1}. \tag{4.15}$$

Together the last two equations provide a rough estimate for the optical depth of a given electron cyclotron resonance in a tokamak. The results of considering finite density and polarization effects are discussed further in §4.5. Finally, from Eq. 4.8, the intensity of the ECE emission when viewed remotely from the plasma edge will be:

$$I(\omega_0) = \frac{{\omega_0}^2 T(s)}{8\pi^3 c^2}(1 - e^{-\tau_m}) \tag{4.16}$$

Equation 4.16 details the relationship between ECE emission intensity and temperature, $(I \rightarrow T)$. It should be noted that this equation ignores the effect of multiple reflections through the resonance region. Together these relationships establish the basis for ECE as a temperature diagnostic $(I(\omega) \rightarrow T(R))$. ECE temperature diagnostics are generally very well suited for tokamaks, but it is important to appreciate the limits of applicability that exist.

4.5 Cutoffs & Optical depth

For use as a reliable tokamak temperature diagnostic, one wishes to use an ECE mode which is accessible from the low field plasma edge (ie free of intervening cutoff layers)

and for which the plasma is optically thick (and thus radiates at black-body levels). Of the first few harmonics of the X and O modes, 2^{nd} harmonic X-mode radiation best meets these criteria. In this section, we briefly discuss how fundamental plasma phenomena affected this choice but detailed considerations will be limited to the case actually used for the C-Mod measurements discussed in later chapters.

4.5.1 Cutoffs

We require that the emitted radiation be free to propagate to the collection optics, which are necessarily located outside the plasma. This is not always the case in tokamaks. The dispersion relation for the wave mode being examined must be free of reflective cutoffs and absorptive resonances along the entire path from the emission region to the entrance aperture of the optics. The monotonic decrease of the magnetic field with major radius ensures that secondary resonances will not be encountered, but at sufficiently high density cutoff layers can make the ECE from the core inaccessible at the outboard edge.

As seen in Chapt. 2, The O-mode is cut off for $\omega < \omega_p$. For fundamental emission and standard 5.3 Tesla operation on Alcator C-Mod this limits the central density to $n_e \lesssim 2.7 \times 10^{20} m^{-3}$. This is too low to cover C-Mod's operating range in which densities in excess of $10^{21} m^{-3}$ have already been observed. Higher O-mode harmonics are optically thin even at the highest densities and thus O-mode is not used for temperature measurements.

The X-mode cutoff condition important for tokamaks is that emission cuts off for $\omega_H < \omega < \omega_R$, where:

$$\begin{aligned} \omega_R &= \frac{1}{2}\Omega[1 + (1 + 4\omega_p^2/\Omega^2)^{1/2}] \\ \omega_H &= \sqrt{\Omega^2 + \omega_p^2} \end{aligned} \tag{4.17}$$

For low field side views of the tokamak this means that the fundamental emission is cutoff for any finite frequency. For 2^{nd} harmonic X-mode, $\omega_R > \omega_H$, and the cutoff

condition of consequence in our experiments is,

$$\omega \leq \omega_R. \tag{4.18}$$

Substituting $\omega = 2\Omega$ and and the definition of ω_R into Eq. 4.18 we obtain the simple expression for cutoff to be:

$$\omega_p^2 \equiv n_e e^2/m_e\epsilon_0 \geq 2\Omega^2 \tag{4.19}$$

Using the definitions for the cyclotron and plasma frequencies, a more convenient expression gives the cutoff condition in terms of a cutoff density density expressed in units of $10^{20}\ m^{-3}$ in terms of the magnetic field in Tesla as:

$$n_{20} > n_{c.o.} \approx 0.2 \times B_T^2. \tag{4.20}$$

After pellet injection or during high quality H-modes, the density can rise to levels sufficient to temporarily cutoff the ECE signal. During this time the diagnostic can provide no temperature information, but just as a given frequency is being cutoff, Eq. 4.20 provides a snapshot of the density at that channel location which can be a useful cross check of other density diagnostics. This in principle can be used to cross calibrate the Thomson scattering diagnostic for which alignment problems can cause the instrument to become uncalibrated. In practice, the technique was used only occasionally on a shot to shot basis because the alignment changed too frequently (even within a given shot).

4.5.2 Optical depth

Equation 4.16 indicates that when $\tau \gg 1$ the radiated intensity from a given cyclotron resonance is the blackbody level which is a known function of the temperature only. It is thus important for ECE temperature diagnostics to use emission for which the plasma is optically thick. Later in §4.6 and §5.4 we will see that optical thickness is also important when considering nonthermal electrons and radial resolution respec-

tively.

An estimate for the optical depth for application in the ECE measurements on C-Mod is obtained by evaluating Eqs. 4.14 and 4.15 for $\theta \approx \pi/2$ and $m = 2$. This yields the expression:

$$\begin{aligned} \tau_2|_{diffuse} &= \frac{R\alpha_2}{2\Omega} \\ &\approx \frac{\pi\ R}{\Omega\ c}\ \frac{\omega_{pe}^2\ T_e}{m_e c^2} \end{aligned} \tag{4.21}$$

As indicated by the subscript, this expression results from the diffuse plasma assumption. We know from Chapt. 2 that there can be significant dispersive effects for electron cyclotron waves in dense plasmas. More detailed analysis is best done by discussing the X and O modes separately. When the effects of finite density are small, the new results may be conveniently expressed as corrections to the results of the previous section. In general this is not possible for the fundamental cyclotron resonance of tokamaks, however for $m \geq 2$, Eq. 4.15 may be re-expressed as:

$$\alpha_m^{X/O} = \alpha_m|_{diffuse}\ \eta_m^{X/O} \tag{4.22}$$

A useful expression for use with X-mode is given below. Corrections should be applied for the $m = 2$ case [44] but when they are applicable, the optical depth is generally large and the precise value of τ is not important except very near the cutoff density [42].

$$\eta_m^X = \left[\frac{(1-X)^2m^2-1}{(1-X)m^2-1}\right]^{m-3/2}\left[1+\frac{mX}{(1-X)m^2-1}\right]^2 \tag{4.23}$$

$$\text{Where: } X \equiv \frac{\omega_{pe}^2}{m^2\Omega^2} \tag{4.24}$$

Figure 4-3 gives τ_2 vs density and temperature. For typical core conditions on C-Mod, it can be seen that $\tau > 10$.

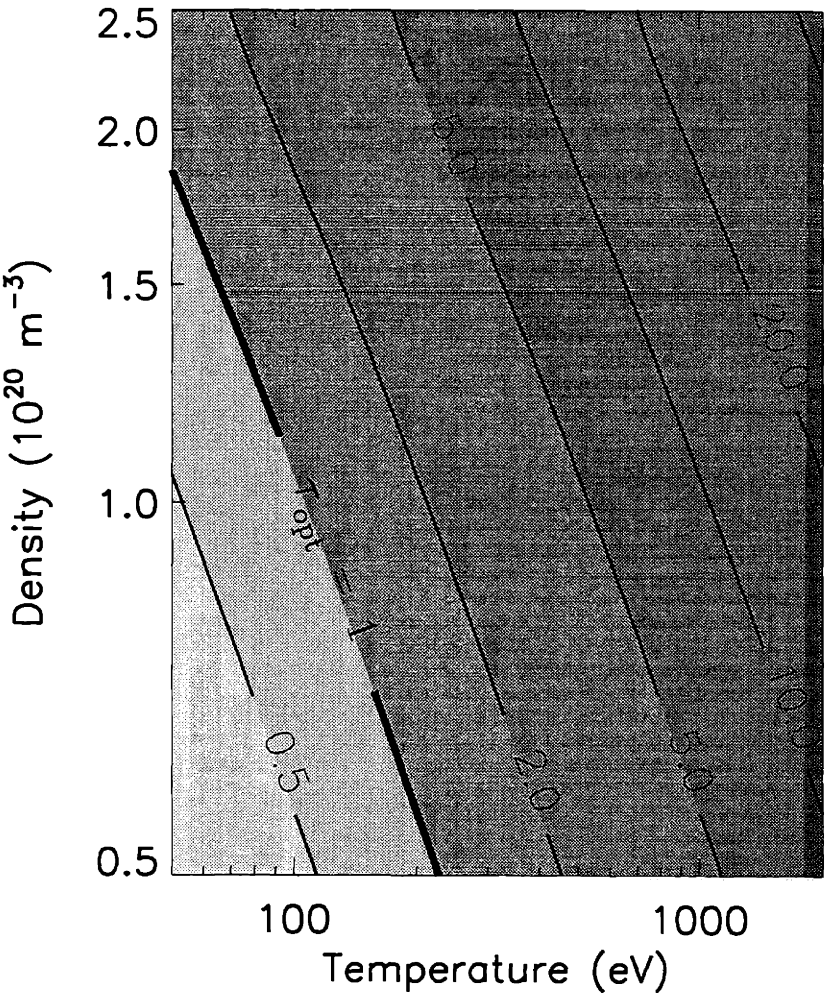

Figure 4-3: Contours of optical depth for 2^{nd} harmonic X-mode ECE and plasma conditions found in the plasma edge on Alcator C-Mod. The nominal threshold for using ECE for temperature measurements is $\tau_{optical} \gtrsim 1$. For smaller optical depths, the plasma is said to be optically "grey" and the standard analysis for the optically "black" case *underestimates* the temperature. This calculation assumes $B_0 = 5.3T$ and R = 89 cm.

Harmonic	$R_{min}cm$	$R_{max}cm$
1	44.5	none
2	59.3	90.0
3	66.8	67.5

Table 4.1: Table indicating the extent of the overlap-free region for the first three cyclotron harmonics.

4.6 Harmonic overlap & non-thermal emission

In this section we investigate the limits to the utility of ECE diagnostics on tokamaks which are imposed by specific properties of the tokamak itself.

4.6.1 Harmonic overlap

For ECE to provide useful information, the radiation received by a detector in a certain frequency band must come from a single localized region in the plasma. Consider an ECE diagnostic viewing along the midplane of a tokamak (as on Alcator). Radiation at a given harmonic from a point on the high field side of the tokamak can correspond to that at a higher harmonic from another point on the low field side of the tokamak. Upon reaching the collection optics, the radiation from these physically distinct locations is indistinguishable and thus of little use to the diagnostician. This situation of harmonic overlap must be avoided. This consideration imposes a limit to the range of radii which can be unambiguously probed. The range decreases as the cyclotron harmonic being used increases and also as the tokamak aspect ratio (R_0/a) decreases. This is quantified in Eq. 4.25.

$$R_{min} = (R_0 + a)\frac{n}{n+1} \leq R \leq (R_0 - a)\frac{n}{n-1} = R_{max} \tag{4.25}$$

For Alcator C-Mod ($R_0 = 67\text{cm}, a = 22cm$) the overlap free ranges are shown for the first three harmonics in table 4.1. Considering optical depth, cutoff considerations, and harmonic overlap, it should be apparent why 2^{nd} harmonic X-mode has been used on Alcator C-Mod.

4.6.2 Non-thermal emission

In § 4.2 it is assumed that the velocity distribution function for the electrons is Maxwellian. When this is not true, the interpretation of the signals as temperatures can be misleading. In tokamaks, operating at very low densities can give rise to such a situation. Ohmic heating relies on Coulomb collisions of the current carrying electron population. Because the collision cross-section decreases sharply with increasing velocity ($\propto V^{-3}$), it is possible to create a "runaway" sub-population of electrons which have extremely high energies and carry most of the plasma current. This an undesirable operational state for many reasons. One is that very high energy electrons are poorly confined and in bombarding the vessel produce xrays and and component damage. When the runaway population is small, the effect on the use of the ECE as a temperature diagnostic can be minimal. This is because the nonthermal population is relativistic and thus the cyclotron radiation is down-shifted in frequency. When viewing the emission from the low-field side of the machine this means that the radiation from the relativistic component has to pass through through a region where the bulk electrons emit at the same frequency. For optically thick plasmas, it is re-absorbed efficiently and the re-emitted radiation is representative of the thermal bulk.

When the deviation from a Maxwellian distribution is strong, the emission can be strongly influenced or even dominated by the non-thermal electron component. Although the interpretation of ECE in such circumstances can be of use in studying the non-thermal electrons [45] such studies are beyond the scope of this thesis. It is noted here that the significant distortion of the ECE frequency spectrum from the typical behavior seen in Fig. 5-1 can be used as an indication that non-thermal electrons are present. This is used in typical operation as a warning that the target density is being set too low.

Chapter 5

ECE Diagnostics on Alcator C-Mod

5.1 Introduction

The theory of ECE emission on tokamaks is of little practical use unless experiments to measure the emission with suitable accuracy are possible. Fortunately, the match of ECE temperature diagnostics to tokamaks is a natural one and the techniques are well established in the field [46, 45, 47, 48, 49]. This chapter gives a brief overview of the ECE system on Alcator C-Mod and then focusses on the issues of key importance to evaluating and optimizing the performance of the grating polychromator (GPC) instrument. The GPC is the main diagnostic used in the physics studies in later chapters. The adaptation, installation and operation of the GPC on Alcator C-Mod was primarily the responsibility of the author.

5.2 Quasioptical Beamline

In Alcator C-Mod, 2^{nd} harmonic electron cyclotron emission falls within the range 150 - 600 GHz. The detectors used for this frequency (see §5.4.3) had to be located outside of the experimental cell because of their sensitivity to both radiation and vibration and to provide easier access for maintenance of the cryogenic cooling

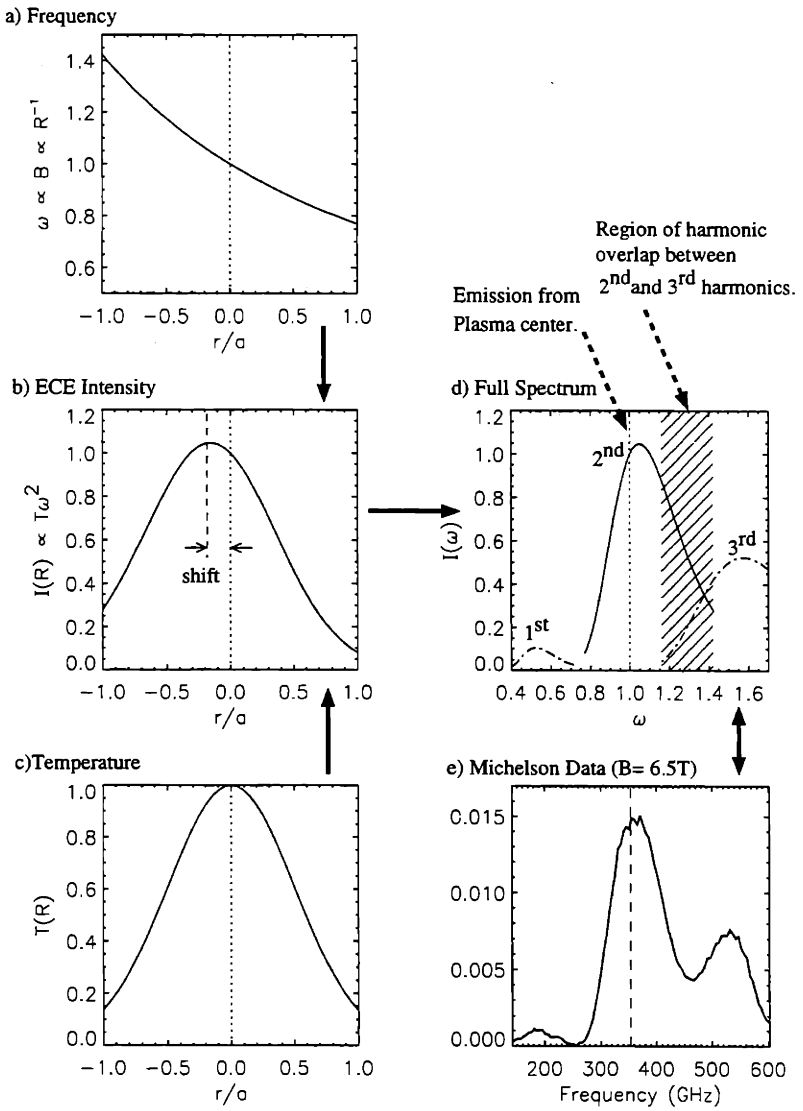

Figure 5-1: These schematic plots illustrate the fundamentals of ECE (X-mode) in tokamaks. Panels a)→ c) show typical poloidal profiles of temperature and magnetic field and the resulting ECE intensity. The curve in panel a) provides a simple mapping between position and frequency. The resulting shape of the second harmonic frequency spectrum is shown in panel d). Also shown are the shapes and approximate amplitudes of the neighboring harmonics. For comparison, panel e) shows a measured frequency spectrum from a C-Mod plasma.

systems. To avoid absorption by water vapour along the path from the tokamak to the detectors, the beam path had to be evacuated. To make useful measurements, the delivery system was also required to have good spatial resolution and low losses.

A quasioptical beamline consisting of a system of polished aluminum mirrors enclosed by oversized stainless steel vacuum pipes was designed and built to provide the front end for a fast scanning Michelson interferometer in 1992 [11]. The term "quasioptical" is used because the wavelengths of the radiation involved ($\lesssim 3$ mm) are not always much smaller than the dimensions of the "optical" elements of the system, as is explicitly assumed in the limit of geometrical optics.

An important feature of the beamline allows *in situ* calibration of the Michelson. The mirror closest to the tokamak can be rotated such that the Michelson instrument views either the tokamak or the calibration source which houses two viewing dumps with known temperatures. The calibration is described in §5.5. Here a brief note is made on the use of this scanning feature of the last mirror. In normal operation, the final optic axis is nearly collinear with the tokamak midplane. After a major maintenance period, this alignment can be performed by scanning this first mirror between shots for a few reproducible plasmas. As the optic axis moves away from the midplane, channels at fixed magnetic fields are scanned to larger values of normalized flux. By noting the nature of the sawteeth, an accurate location of the q=1 flux surface can be mapped out. Thus two-dimensional profile information can be obtained. From an operational standpoint, the flux surface contours, see Fig. 5-2, allow an accurate alignment of the beamline optics.

5.3 Michelson Interferometer

A Michelson interferometer [50] may be used to measure the frequency spectrum of a beam of incident light by monitoring the interference of two overlayed portions of the beam as one portion is forced to travel a varying optical path length compared to the other. The first ECE temperature diagnostic on Alcator C-Mod was a fast scanning Michelson interferometer. Each scan of a reciprocating mirror produces an

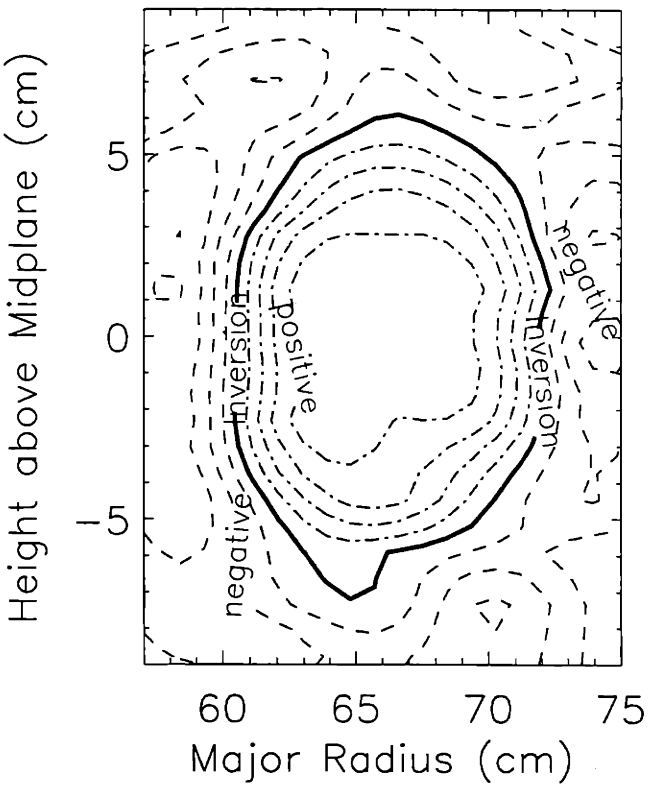

Figure 5-2: Sawtooth phase contours used for mirror alignment

ECE frequency spectrum typically covering the first three harmonics of the emission from the plasma. The electron temperature profile can be determined from the 2^{nd} harmonic emission as discussed in Chapt. 4. Driving the mirror with a motorized linkage at several thousand RPM produces temperature profiles with $\gtrsim$ 15 msec time resolution. The interferometer is calibrated directly using the *in situ* calibration source (see §5.5). The Michelson interferometer has been in routine operation on Alcator C-Mod since its commissioning in June, 1993.

5.3.1 Time resolution

The main limitation of the Michelson interferometer is its time resolution. An implicit assumption in the analysis of the Michelson data is that the changes in the ECE being analysed are slow compared to the scan time. However, the electron temperature in C-Mod plasmas exhibits a variety of large amplitude, high speed transients. Examples

include the fast thermal quench of the plasma following the injection of pellets [51], full plasma disruptions [52], and most importantly, the ubiquitous periodic partial disruptions caused by magnetohydrodynamic (MHD) instabilities commonly called "sawteeth" [48]. Electron temperatures for each of these plasma phenomena can vary by $\lesssim 50\%$ in intervals $\lesssim 0.5$ msec which introduces artifacts into the interference patterns and produces errors in the temperature profiles generated from them. Much better time resolution is required if the physics of these interesting phenomena is to be studied.

5.4 Grating Polychromator

In this section we describe the performance of another ECE diagnostic which uses a diffraction grating and multiple detectors to measure the frequency spectrum with much better time resolution, the grating polychromator (GPC). The GPC was originally designed at the University of Maryland [53] for use on MTX [1], and was commissioned on Alcator C-Mod in May 1994. The polychromator and the Michelson interferometer now share the radiation collected by the quasioptical beamline and together form a powerful pair of complementary ECE diagnostics.

5.4.1 GPC layout

Figure 5-3 shows an isometric view of the grating polychromator instrument. The beamline from the tokamak comes into the ECE diagnostic lab through a hole in the shield wall (see Fig. 1-4). The beamline optics image a point on the magnetic axis of the tokamak to an aperture at the input to the Michelson and grating polychromator diagnostics. A wire-grid polarizer passes X-mode radiation and reflects the O-mode into an Eccosorb beam dump. A second, rotatable polarizer acts as a variable beamsplitter, reflecting $\approx 60\%$ of the ECE signal toward the GPC. Acrylic tubing (I.D.

[1] MTX (Microwave Tokamak eXperiment) operated at Lawrence Livermore Natation Lab from 1989-1992 and used the vacuum vessel and magnet system of the Alcator C tokamak. The grating polychromator is currently on loan from LLNL.

$\equiv 2a = 7$ cm.) serves as a low-loss dielectric waveguide in which the radiation propagates with an intensity profile well approximated by a gaussian with a waist given by $w = 2a/3$ [54]. A polarization rotator prepares the polarization of the light from the beamsplitter (parallel to the wires) so that it is perpendicular to the rulings of the GPC gratings. Near the GPC the dielectric waveguide terminates and a TPX lens and off-axis paraboloid mirror form a confocal Gaussian telescope which images the waist at the mouth of the waveguide onto the rectangular input slit as shown in Fig. 5-5. Before entering the main instrument enclosure a low-pass filter grating (see §5.4.6 and appendix B) diffracts unwanted high frequency ECE radiation out of the beamline into Eccosorb dumps. Two more mirrors focus the image of the input slit onto rectangular input apertures to the detector for nine different frequencies determined by the geometry of the main diffraction grating (see Fig. 5-4). All of the optics are under vacuum to reduce the effects of strong water vapor absorption[2]. A quartz window near the tokamak separates the high vacuum of the tokamak ($\approx 10^{-7}$ torr) from the rough vacuum of the ECE system ($\lesssim 50$ mtorr).

5.4.2 Grating equation

Applications of diffraction gratings for spectral analysis in physics are commonplace and any optics text will give a fairly complete discussion of the principles involved [50]. The basic grating equation which describes the direction of diffraction for the m^{th} order of diffracted light from a planar grating with regular rulings of period d is given below:

$$\begin{aligned} m\lambda_i &= d\,(\sin\theta + \sin\delta_i) \\ \text{or}: m\lambda_i &= 2d\,\sin(\theta + S_i)\,\cos S_i \end{aligned} \tag{5.1}$$

where θ is the angle of incident beam to the grating normal, S_i is the deflection of the i^{th} diffracted ray[3] from the incident beam, and δ_i is the deflection of the diffracted

[2]The two strongest water absorption lines for water molecules occur at 557 and 752 GHz. [55]

[3]The geometry of the grating polychromator optics fix the diffraction angles S_i. For the nine-channel instrument on Alcator C-Mod these angles range from $S_1 = 11.01° \pm \approx 0.02°$ to $S_9 = 20.65°$

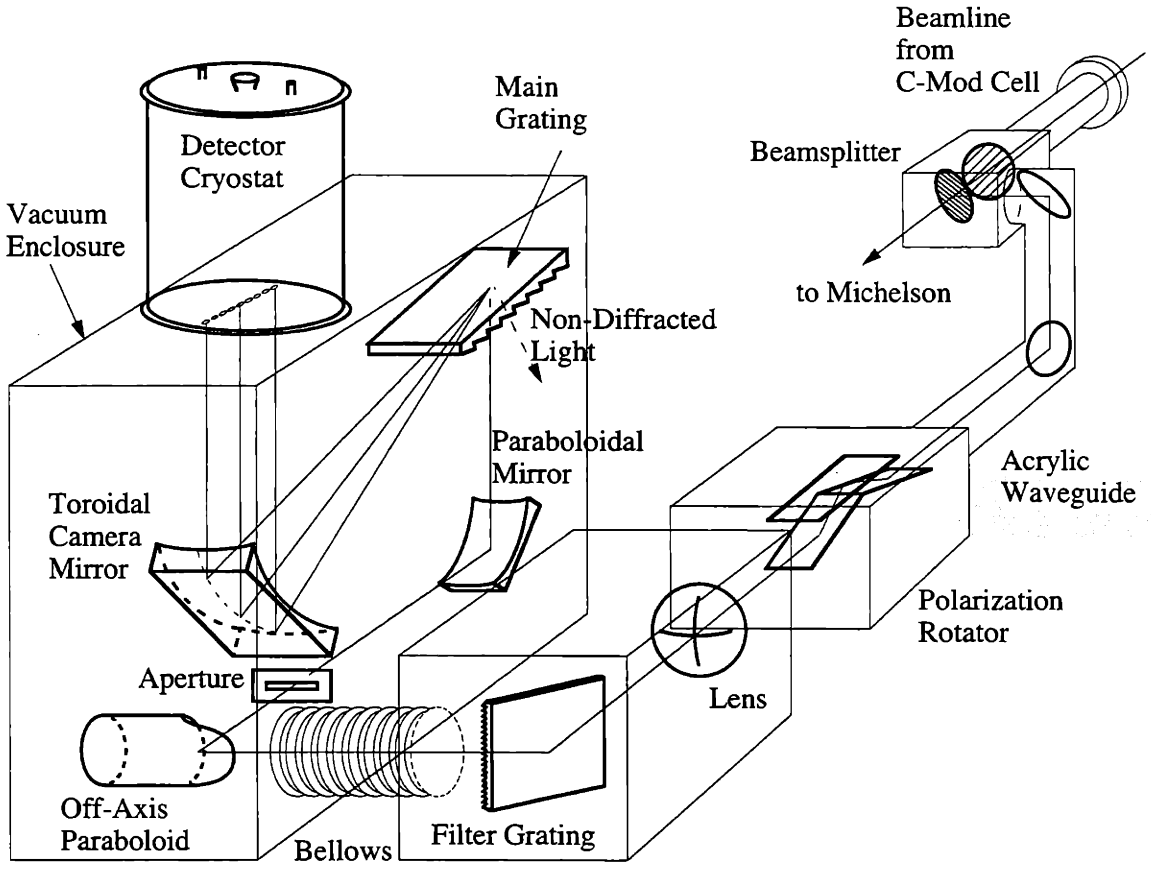

Figure 5-3: Sketch showing the layout of the polychromator system. The entire ECE diagnostic system, including the beamline from the tokamak cell, in-situ calibration source, Michelson interferometer and GPC are within a vacuum enclosure to reduce attenuation of the signal due to water vapour absorption.

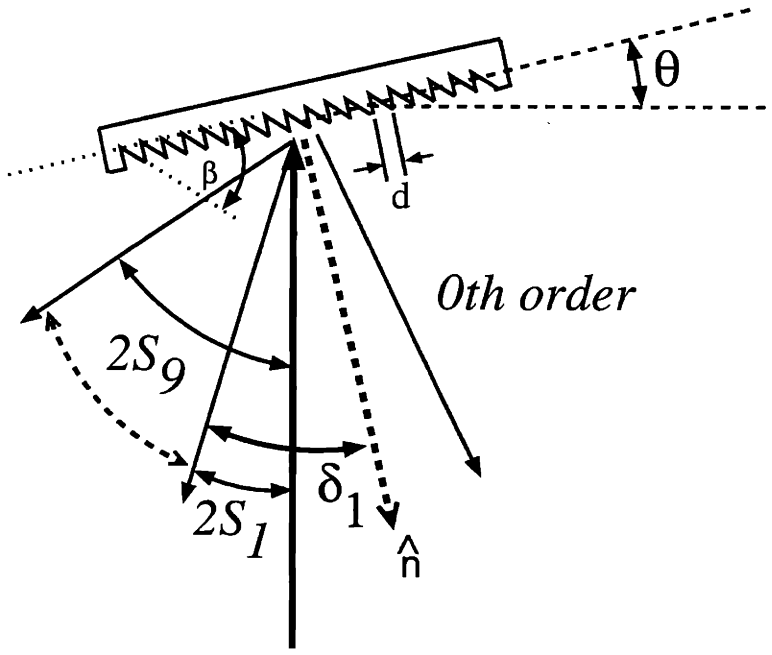

Figure 5-4: Basic grating geometry and angle conventions. The incident beam (thick vertical arrow) is comprised of emission over a range of frequencies and strikes the grating at an angle θ relative to normal. Reflected light corresponds to order $m = 0$ in equation 5.1. Rays 1→9 show the effects of diffraction for light with successively *increasing* wavelengths for a given (*negative*) diffraction order. The corresponding diffraction angles, S_n, are positive as sketched here. The diffraction angle may also be specified relative to the grating normal, δ. The rulings used in these experiments are specified by period, d, and blaze angle, β.

ray from the grating normal (note $\delta_i \equiv 2\ S_i + \theta$). A diagram illustrating the standard grating geometry and sign conventions for the angles is shown in Fig. 5-4. For a given order of diffraction and angle of incidence, the angle of diffraction varies continuously with the wavelength. This familiar dispersive property of gratings [4] is used to sample different parts of the ECE frequency spectrum with different detectors as shown schematically in figure 5-5.

(see Fig. 5-4).

[4]The same principle gives rise to the rainbow patterns of light "reflecting" from the surface of a compact disc.

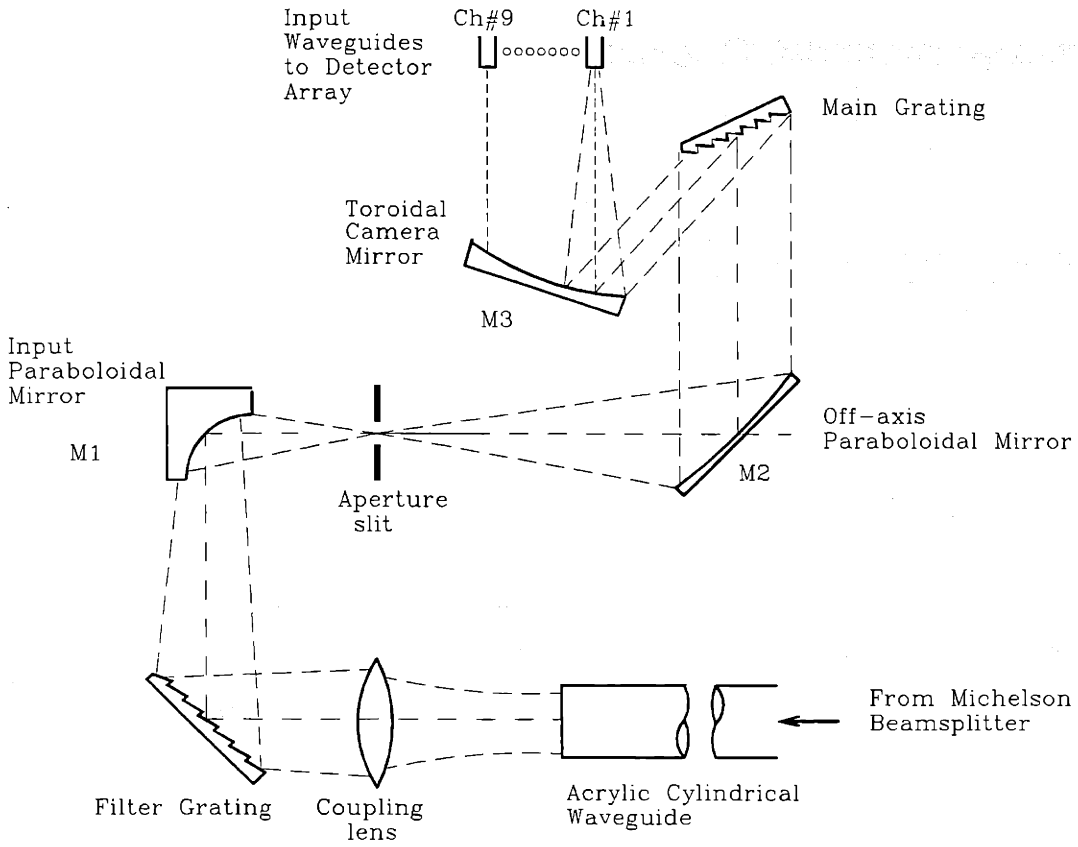

Figure 5-5: Schematic diagram showing the main polychromator optics. The coupling lens and mirror M1 form a confocal Gaussian telescope which focuses the light emerging from the cylindrical waveguide on the rectangular aperture slit. The combined effects of the main grating and mirrors M2 and M3 create images of the aperture slit on the detector waveguides for nine different frequencies.

Parameter	Optimal value	units
Bias current	30-45	μA
Optical responsivity	2.5-3.5	kV/W
Noise (measured)	2.5-4.0	$nV/Hz^{1/2}$
D.C. Resistance	5-10	$k\Omega$

Table 5.1: Table indicating typical characteristics near the optimal operating point for the liquid helium cooled InSb detectors used for each channel of the grating polychromator.

5.4.3 Detectors

Using ECE as a temperature diagnostic for tokamaks is predicated on the availability of sensitive detectors in the millimeter wavelength range. Solid state detectors with suitable sensitivity have been available for many years [56], though despite incremental improvements in the original technology, operation at liquid helium temperatures is still required. The detectors for the Alcator C-Mod experiments are Indium Antimonide (InSb) hot electron bolometers [5]. Infrared power is absorbed efficiently through direct coupling to the "plasma" of carrier electrons within the crystal. The absorbed power increases the electron plasma temperature and causes the resistivity to drop ($\propto T_e^{-3/2}$). A constant bias current is run through the detector element and modulation of the resistance appears as a voltage across the device. The low thermal mass of the carrier electrons and their short lifetimes makes for short rise and decay times respectively, creating excellent time response ($\approx$ 1 μsec). Sensitivity drops off rapidly for emission above $\gtrsim 800GHz$.

5.4.4 Electronics / Time resolution

To take advantage of the good response time of the detectors, similarly fast components must be used in the data aquisition train. University of Maryland preamplifier circuits provide both the bias current and a voltage gain of 300. Based on the OP-37 operational amplifier, they have a half-power high-frequency cutoff frequency of $\approx$ 900

[5] QMC Instruments Ltd. model QFI/3.

kHz and a measured noise figure near the operating point of 2 dB, corresponding to a noise temperature of 180 K [53]. Jorway Corporation's 12 bit Aurora 14 transient recorders are used to digitize the signals, allowing a maximum sampling rate of 1 MHz and up to 128 kilosamples of memory per channel. An MPB decoder module provides a programmable clock to the digitizers from the 1 MHz master clock signal of the C-Mod serial highway, providing synchronization with other plasma diagnostics. For standard operation, a sampling rate of 20 kHz is used throughout the shot with an optional burst of fast digitization which can be set to capture fast transients. To accommodate this option, a set of anti-aliasing filters with a cutoff frequency of 15 kHz was built which is bypassed with the same signal used to gate the high frequency clock.

5.4.5 Spatial Resolution

The optics of the polychromator are designed such that each of the nine detectors is nominally tuned to be sensitive to the frequency component of the input radiation given by equation 5.1. Using the EFIT code [6] the locations along the view of the instrument are determined at which the ECE frequency corresponds to each detector frequency. However it is also very important to know the radial resolution of this mapping from polychromator channel to tokamak position. A finite frequency resolution translates to a finite radial resolution as was illustrated in Fig. 4-2. There are three main factors which contribute to finite radial resolution:

1. The combined effects of finite spot size of the viewing beam in the plasma and magnetic flux surface curvature.

2. Frequency broadening of the cyclotron emission combined with optical depth considerations.

3. The finite frequency resolution of the instrument.

[6] Developed at General Atomics by L. Lao [57], EFIT solves the Grad-Shafranov equation and by fitting to real-time measurements in the plasma edge, infers details of the plasma's internal magnetic fields.

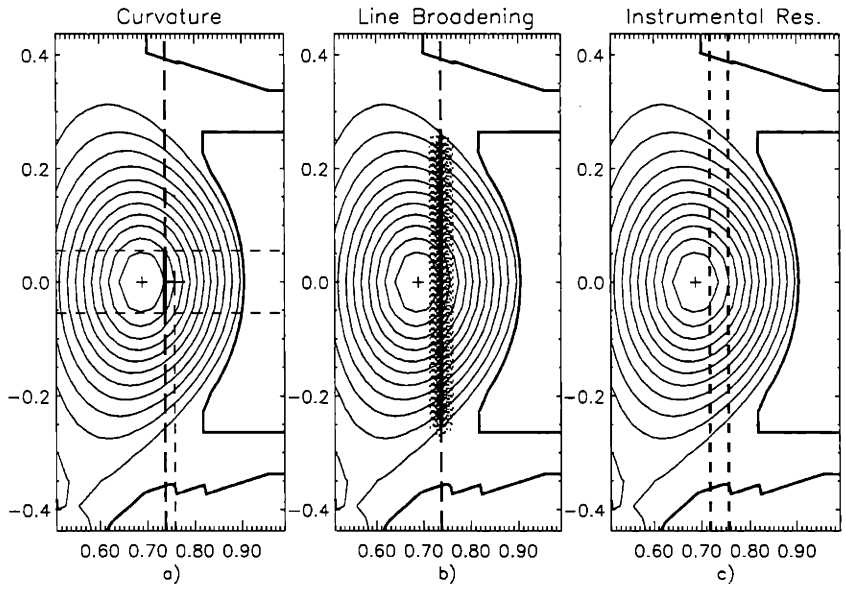

Figure 5-6: Illustration of the three main effects contributing to finite radial resolution. In each case the nominal cyclotron resonance is at $\approx 72cm$.

Qualitative sketches of each of these effects are shown in figure 5-6. An exact calculation of the overall resolution is difficult and must take into account all of these effects and how they interact. In the interest of calculational simplicity, each effect will be assumed to to act independently, which is a good approximation when each effect in itself is small ($\delta R|_{res} \ll a$).

Geometrical effects

The curvature of the poloidal magnetic flux surfaces effectively introduces a spread in radial sensitivity when viewing with an optics system with a spot size of finite vertical extent. Due to the large thermal conductivity along magnetic field lines, the temperature is constant over flux surfaces. The experimenter would like therefore to probe as narrow a range of poloidal flux surfaces as possible. It is the toroidal field which largely determines the location of the cyclotron resonance however. The toroidal field is roughly constant in the vertical direction, so that resonant surfaces are approximated by vertical cylinders. The ECE instrument collects radiation from

the area in the plasma which is the intersection of the relevant resonant surface and the collection beam of the optics. This area has curvature only in the toroidal direction and thus subtends a range of poloidal flux surfaces in its vertical extent. By inspecting the sketch shown in Fig. 5-6, it is seen that this effect systematically shifts the sensitivity of the instrument to flux surfaces outside that surface which is tangent to the resonant layer.

Fundamental line broadening effects

Equation 4.13, $\omega_m = m\Omega(1-\beta^2)^{1/2}/(1-\beta_{\|}\cos\theta)$, expressed the kinetic mechanisms by which the cyclotron resonance is broadened in a thermal plasma. The denominator represents Doppler broadening and for a thermal plasma gives a symmetric Gaussian broadening about the nominal frequency by an amount:

$$\Delta\omega_{dop_{FWHM}} \approx 1.7\sqrt{\frac{T_e}{m_e c^2}}m\Omega cos\theta \tag{5.2}$$

The numerator represents relativistic mass increase and shifts the peak of the emissivity curve down in frequency from the nominal cyclotron resonance by an amount given by equation 5.3. The relativistic line width is of the same order as the shift.

$$\Delta\omega_{rel} \approx -\frac{T_e}{m_e c^2}m(m+1/2)\Omega \tag{5.3}$$

In non-relativistic plasmas, the doppler broadening will dominate *except* for propagation which is *very* close to perpendicular to the magnetic field. Broadening of the *emission* is dominated by relativistic effects for $cos\theta \ll \beta$, which is true in an average sense for the collection optics of the ECE diagnostic on Alcator. Other fundamental broadening mechanisms such as radiation damping and collisional broadening are negligible in fusion grade plasmas. If we consider a specific frequency, a downshift in emission frequency means the diagnostic is sensitive to emission from plasma at magnetic fields higher than at the nominal resonance layer, or for a tokamak, smaller major radius. This radial spread in emission can be several centimeters for modest values of the electron temperature ($\approx$ 1 keV). This loss of spatial resolution is strongly mitigated by reabsorption as the light propagates to the low field side of

the tokamak in optically thick plasmas. The diagnostic "sees" only a few e-foldings into the emissivity profile, which for $\tau_{max} \gg 1$, typical of the core plasmas of Alcator C-Mod, drastically reduces the effects of broadening. This is illustrated in Fig. 5-7.

Instrumental resolution

The instrumental resolution was measured using a 110 GHz Gunn diode[7] to provide a very narrow band source ($\pm \lesssim 25kHz$). The setup for the tests is sketched in Fig. 5-8. Power was directed with a horn through a vacuum enclosure port near the main beam splitter, and modulated with a chopper. To enhance harmonic content, thereby producing power at frequencies more relevant to ECE experiments, the diode output was first run through a mixer. The amplitude modulation of the GPC signals at the chopper frequency was obtained for each point of a detailed scan of the main grating angle. Examples of the results are shown in figure 5-9 where two peaks are seen on one output channel showing the width of the 2^{nd} and 3^{rd} harmonics. The widths of these peaks indicate the finite frequency resolution of the GPC. Figure 5-10 shows in detail one of the peaks resolved during these tests. Angle scans with four different gratings (with ruling widths, 0.94 mm $\leq d \leq$ 1.65 mm) resolved the 2^{nd}, 3^{rd}, and 4^{th} harmonics on various GPC channels and represent a study of nearly the entire operating range of *all four* basic variables in equation 5.1, θ, d, λ, and S. Twenty separate peaks were resolved in detail and their widths were measured to establish the instrumental resolution. The polychromator was designed such that the contribution to the resolution due to the finite aperture size of the output waveguides was roughly equal to the fundamental grating resolution [58]. The expression for aperture limited resolution is obtained by taking the appropriate derivative of Eq. 5.1 and yields:

$$R_{aperture} \equiv \frac{f}{\Delta f} = \frac{\sin(\theta + S)\ \cos S}{\cos(\theta + 2S)\ \Delta S} \tag{5.4}$$

where ΔS is the FWHM angular span of each detector as seen by the main grating, here $\approx$ 4.6 mrad. The resolving power of a diffraction grating in first order is usually

[7]Millitech varactor tuned Gunn oscillator model: GDU-10-3-13I

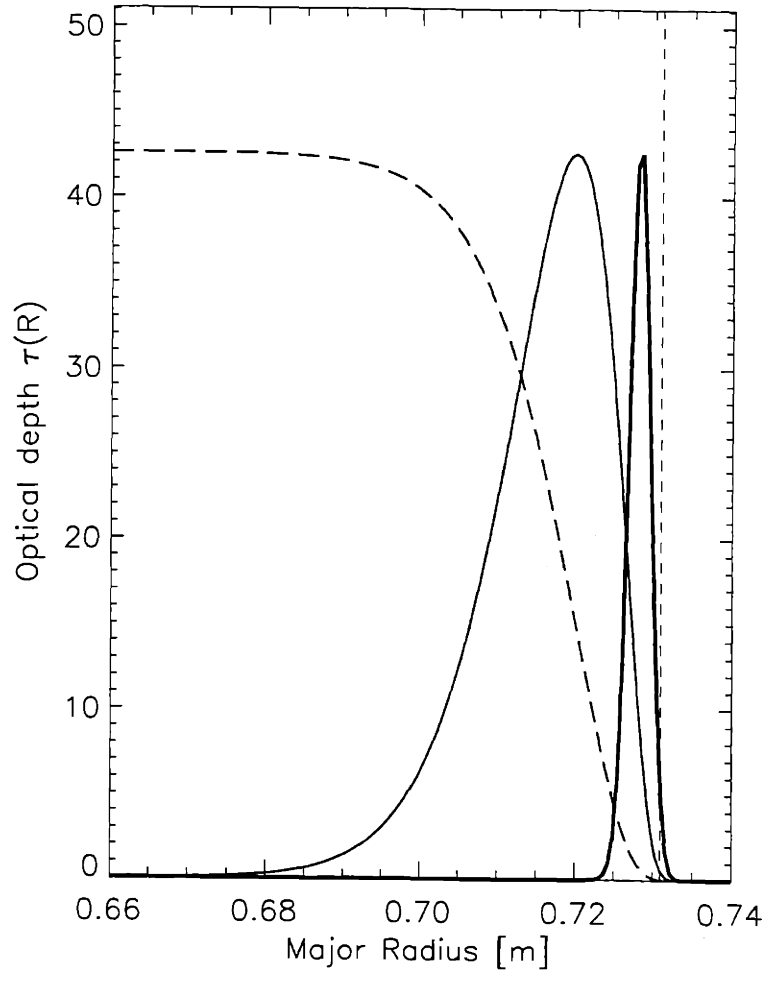

Figure 5-7: Line broadening due to doppler and relativistic effects and the effective width after optical depth is taken into account. The dashed line is the optical depth function for the frequency with a nominal resonance at 73.1 cm. as a function of radius. The thin solid line is the emissivity line shape including relativistic and doppler broadening, while the thick solid line shows the overall line shape after reabsorption has been accounted for. Plasma parameters for this calculation were $n_e \approx 2 \times 10^{20}\ m^{-3}$ and $T_e \approx 3$ keV.

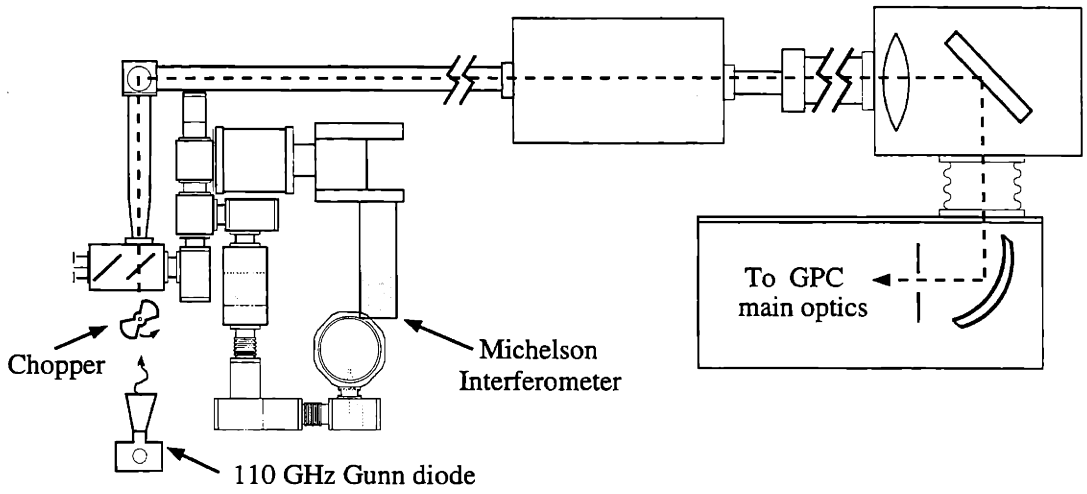

Figure 5-8: Plan view schematic of the setup for GPC resolution measurements. A 110 GHz Gunn diode provided a narrow band emission source. An open port on the vacuum enclosure near the main beam splitter was illuminated as shown. The amplitude modulation of the GPC response at the chopper frequency was measured as the main grating angle was stepped to sweep the $m = 2, 3, \& \ 4$ harmonics across the channels.

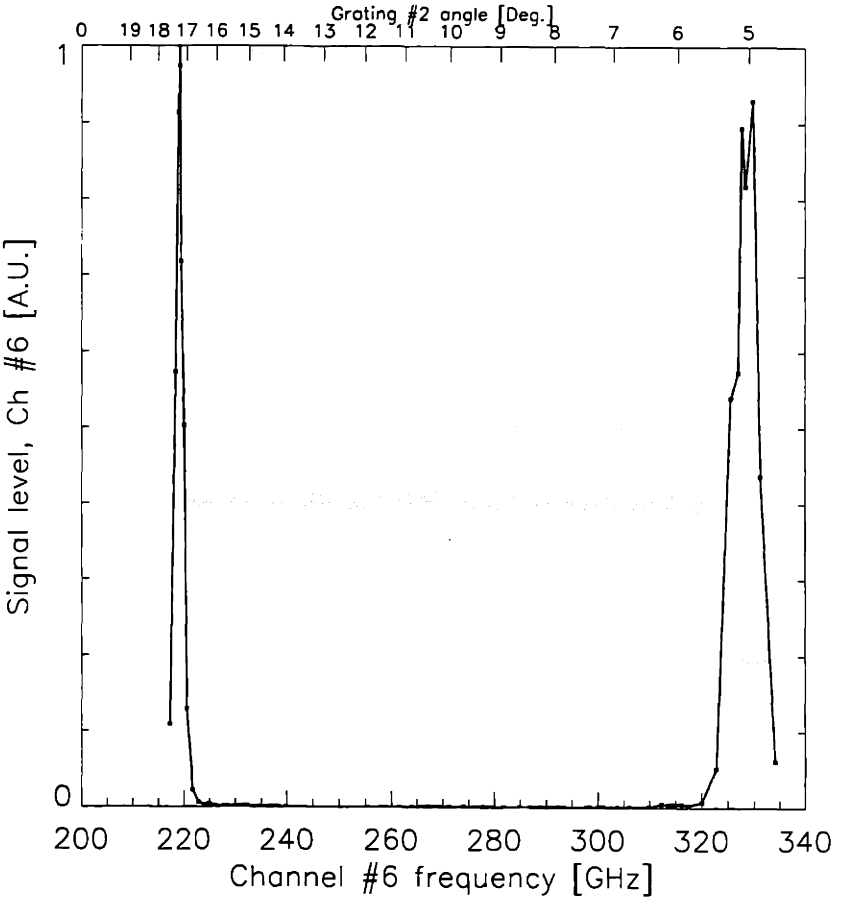

Figure 5-9: Example frequency spectrum from GPC resolution tests. Peaks near the second and third harmonics of the 110 GHz source are resolved as grating #2 is scanned over a large range of angles. The bandwidth of the source is $\pm \lesssim 25kHz$ so the width of these peaks is due to the instrumental resolution.

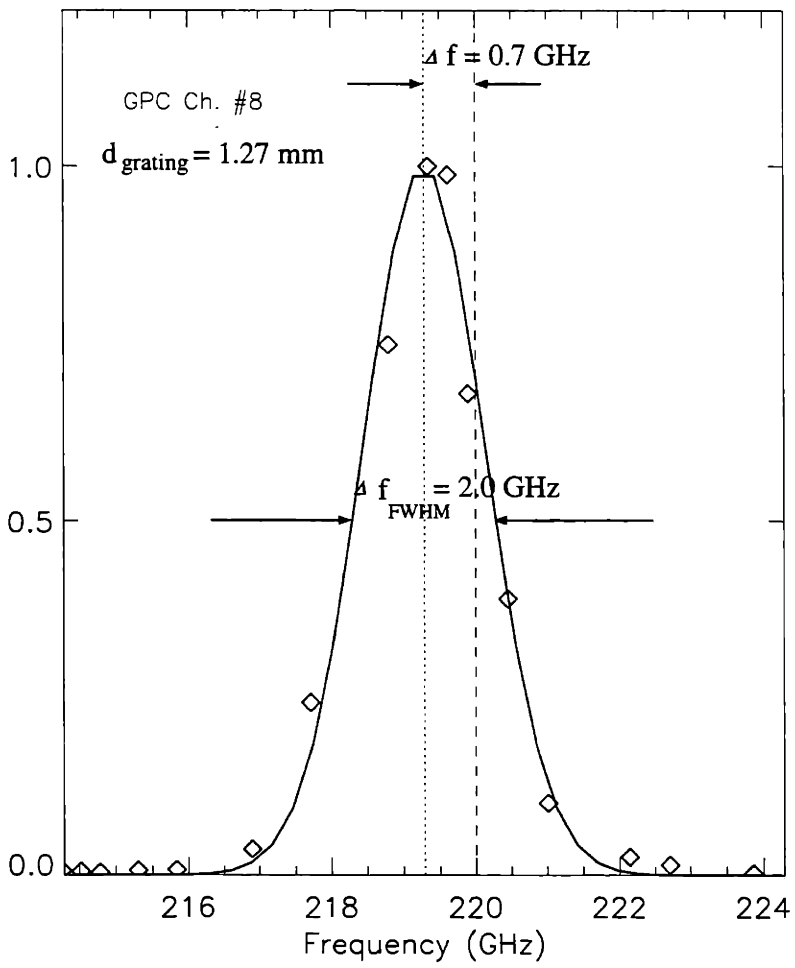

Figure 5-10: Line shape of the 2^{nd} harmonic peak as resolved by the GPC. The best-fit Gaussian fit is also shown. The width of the peak indicates instrumental resolution of $f/\delta f \approx 110$ for $\lambda/d = 1.07$. The difference between the peak frequency and the nominal source frequency is due to instrumental error corresponding to a positional error in the tokamak of ≈ 2 mm.

given by:

$$R_{grating} = N \tag{5.5}$$

Where N is the number of uniformly illuminated rulings on the grating. N can depend on the beam divergence over the distance D from the aperture slit (of width "a") to the collimating mirror (M2 in Fig. 5-5). The maximum number illuminated occurs for long wavelengths which diverge beyond the grating width (W), and is simply the total number of rulings (W/d). This is summarized below:

$$N = \text{Minimum} \begin{cases} \frac{W}{d} \\ \frac{2D}{a}\frac{\lambda}{d} \end{cases}$$

It should be noted that Eq. 5.5 is calculated for Rayleigh's resolution criterion [50]. It is easy to show that the FWHM criterion results in a resolving power which is higher by $\approx$ 12%. This difference is ignored here however, as the assumption of uniform illumination overestimates R in partial compensation. The measured resolution and corresponding theoretical predictions are plotted in Fig. 5-11. The effects of finite aperture and finite grating sizes have been added in quadrature for this plot. The agreement is excellent, which indicates near optimal alignment of the optics. The dotted line in the figure is the best fit to the experimentally measured resolution and will be used in the analysis which follows.

Overall resolution

A computer code was written to simulate the effects of each of the three main contributions to radial resolution. Aperture size, diffraction, and magnetic geometry from a typical EFIT equilibrium were taken into account to produce the *geometrical* resolution. The *instrumental* resolution was parameterized using Gaussian line widths consistent with the best-fit to the measurements shown in Fig. 5-11. Doppler and relativistic line broadening were taken to be the independent basic physics effects dominating the emission broadening. The beneficial effects of finite optical depth

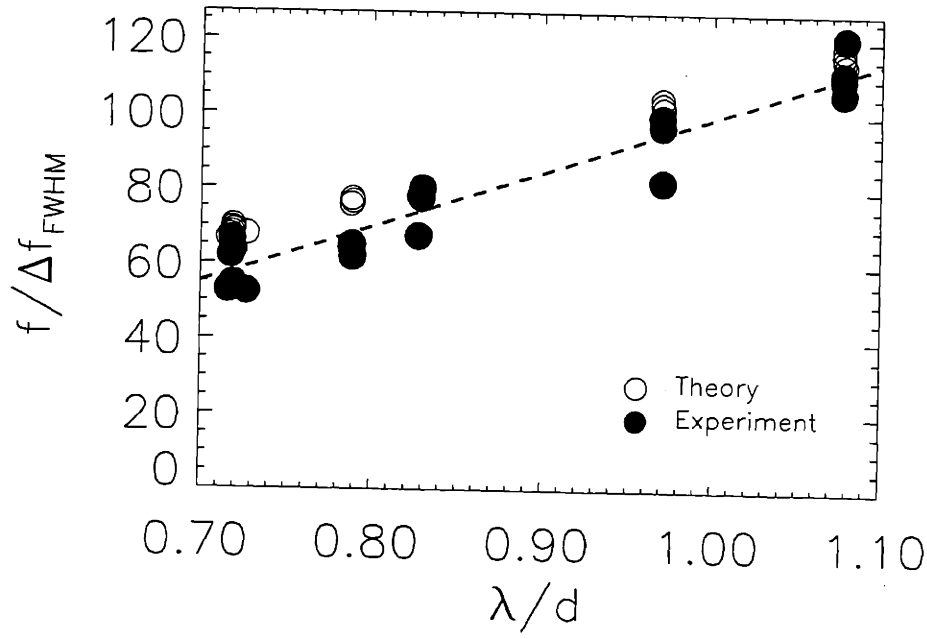

Figure 5-11: Comparison of the measured and theoretical frequency resolutions for the Grating polychromator. The resolution plotted here as "theory" represents the combined effects of finite detector aperture and finite grating size as given by Eqs. 5.4 and 5.5 respectively. The dashed line is the best fit to the experimental data and is used in calculations of radial resolution.

were also included in this calculation of the *fundamental* resolution. All of the above effects were convolved to give the overall radial resolution. In Fig. 5-12, detailed line shapes for each effect are shown for three locations in the plasma. It should be noted that both the geometrical and fundamental line shapes introduce *shifts* from the nominal cyclotron layer as well as broadening. These shifts are in opposite directions for the most typical channel locations on the low field side of the tokamak. Relativistic effects cause the fundamental line shape to be shifted to higher magnetic field. Near the plasma center, the broadening due to geometrical effects can be large, but more importantly, the direction of the shift changes across the magnetic axis. Thus on the high field side of the tokamak, the shift of the overall sensitivity curve can be significant. The net resolution for all nine channels is shown overlayed on a poloidal cross-section of the tokamak in Fig. 5-13.

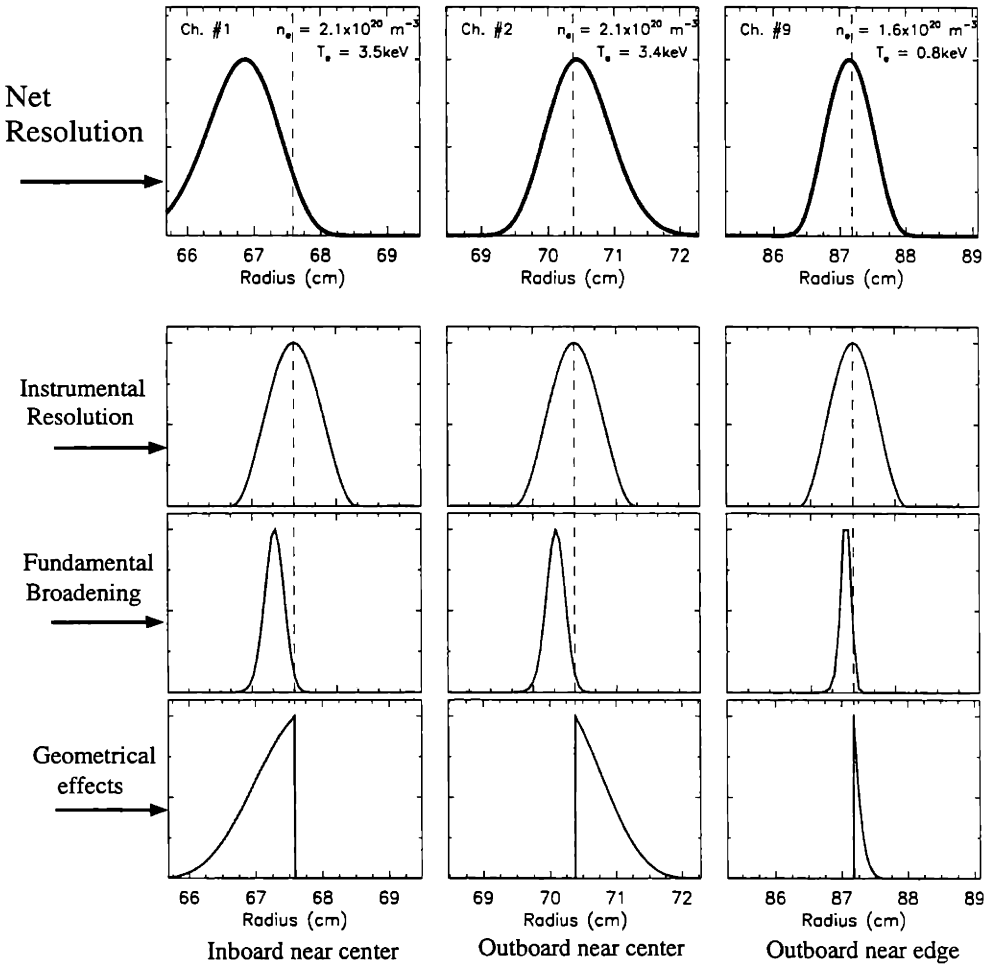

Figure 5-12: Line shapes of the various contributions to the GPC radial resolution. The instrumental resolution typically dominates except near the center where geometrical effects can be large. Note that both the geometrical and fundamental line shapes introduce *shifts* as well as broadening. On the high field side of the tokamak, the shifts are in the same direction and the shift in the overall lineshape can be significant.

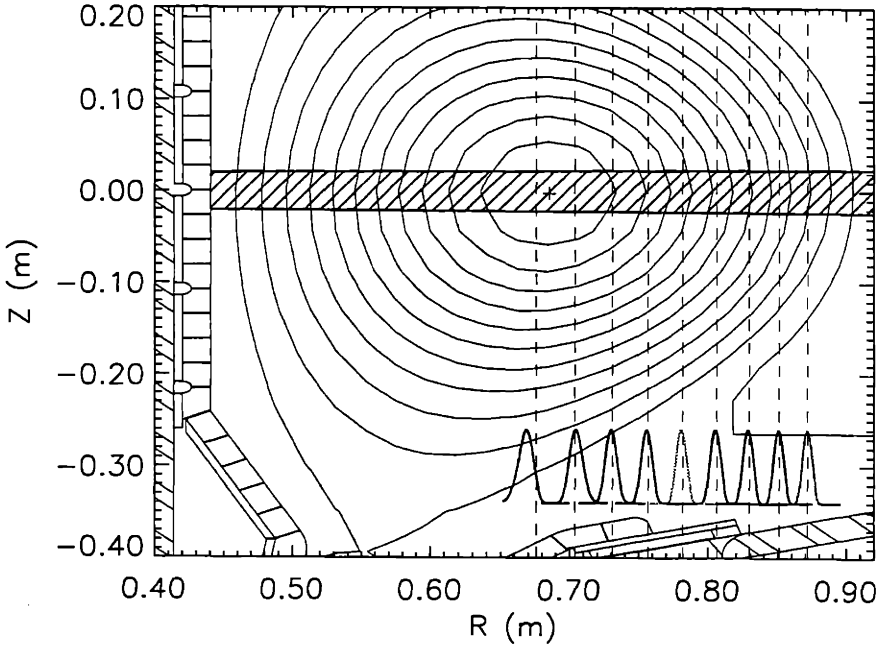

Figure 5-13: Radial sensitivity curves for the nine GPC channels superimposed on a graph of the magnetic flux geometry. The dashed lines show the locations of the nominal resonance surfaces. Calculations are for $n_{e0} = 2 \times 10^{20}\ m^{-3}$, $T_{e0} = 3.5keV$.

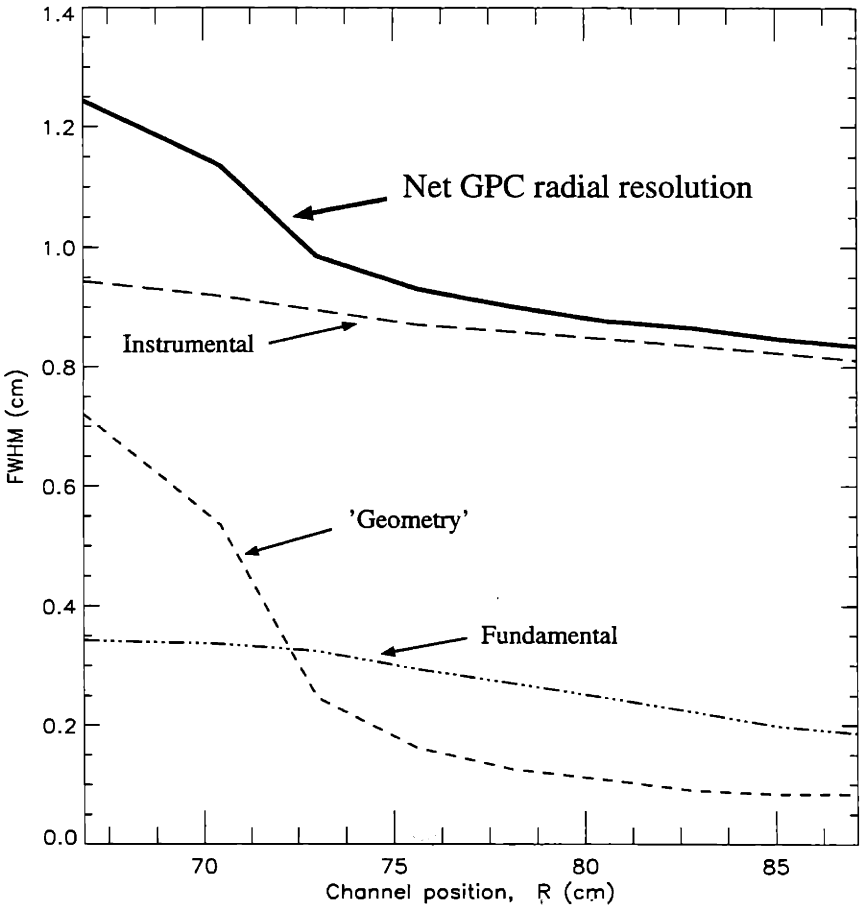

Figure 5-14: Relative importance of different effects on the GPC resolution. The resolution width of each GPC channel is plotted versus plasma position. The solid curve is the net resolution made up of contributions from the three main areas discussed in this section. These calculations assumed $n_{e0} = 2 \times 10^{20}\ m^{-3}$, $T_{e0} = 3.5keV$, and profile shapes typical for C-Mod.

5.4.6 Order overlap: Low-pass filtering

In the previous sections we have considered only first order diffraction in the GPC, ie. we took $m = 1$ in equation 5.1. However, all light incident on the main grating for which the product $m\lambda$ is the same will end up incident on the same detector. Undiffracted (reflected, or $m = 0$) light is deflected out of the system as shown in Fig. 5-5. The design concern here is then the possible contamination of the signals from radiation at twice the frequency to which a detector channel is nominally tuned. For a given cyclotron harmonic in a tokamak, doubling the frequency means halving the radius. The range of major radii in Alcator C-Mod *barely* spans a factor of two and so the source of high frequency contamination comes from 3^{rd} harmonic emission, which when examining the 2^{nd} harmonic at a given radius, R, comes from 3/4 R. This effect is at its worst when studying the outboard edge. In the relatively cool outboard edge of C-Mod where the ECE intensity is low, the potential source of the order overlap contamination is directly at the hot plasma core! In view of the importance of edge temperature measurements to transient transport studies, this problem was given considerable attention. In § 4.6 we considered the question of *harmonic* overlap in which different harmonics of ECE from different regions of the plasma could have the same frequency. This effect sets constraints which are fundamental and cannot be circumvented by the diagnostician. In the case of order overlap however, the undesired emission has a different frequency from the nominal signal. Thus with proper attention to the design of the GPC optics, the problem can be avoided. This can be addressed both by designing main gratings of low second order efficiency, and also by performing low pass filtering to eliminate the higher frequencies before the beam enters the polychromator. Low pass filtering can be achieved with filter gratings used as reflective elements in the beamline before the main optics. Above a certain wavelength they are highly reflective (efficient for diffraction in m=0) but diffract (in order m=1,2,$\cdots$) higher frequency components out of the beamline. Applying this simple strategy for wavelengths of order 1 mm (and thus $\lambda \approx d$) introduces surprising complexity [59, 60, 61]. Appendix B details the salient design formulas tricks to the

art of filter design. Here it will suffice to emphasize that the orientation of the grooves in the filter grating relative to the optics plane *as well as* the electric field vector of the light to be filtered are *independent* issues of great importance to the performance of the filter. The blaze angle (see Fig. 5-4) is also a key parameter [62]. In early operation on C-Mod it was found that mode overlap was a problem near the the plasma edge, but it was not immediately clear how best to improve the situation. The predicted behavior of these filter gratings is both anomalous and sensitive to small changes in geometry and so an effort to characterize their performance in the GPC beamline was made.

The frequency response of several lowpass filters was measured *in situ* using the Michelson interferometer and a mercury arc lamp as shown in figure 5-15. These tests underscore the power, versatility, and complementary nature of the ECE diagnostics system on Alcator C-Mod. Turning the beamsplitter polarizer 90° (by flipping the grid housing 180° about a different axis!) allows the Michelson to view the light transmitted backward through the system to that point. The interferometer was then used to measure the broad-band frequency spectrum for a given filter grating versus a front-surfaced flat mirror. Analysis of the spectra provides a measurement of the filter frequency response. An example of a measured frequency response from these tests is shown in figure 5-16. The half power points measured from the sensitivity curves for three different filters is shown in Fig. 5-17 as a function of the predicted cutoff frequency predicted. These measurements provided strong confirmation of the predicted cutoff frequency, indicated no large filter leakage at the cutoff harmonics and provide an idea of the sharpness of the power roll-off (drops from 90% $\rightarrow$ 10% in $\approx 75GHz$). Based on these measurements a filter design more appropriate for standard operation on Alcator C-Mod (with channels arrayed across the outboard side of the tokamak as in Fig. 5-13) was adopted which places the filter cutoff close to the central 2^{nd} harmonic ECE wavelength. A new set of filter gratings for operation at various fields were built based on the simple formula:

$$d_{grating}(mm) = \frac{7.18}{B_0(T)} \tag{5.6}$$

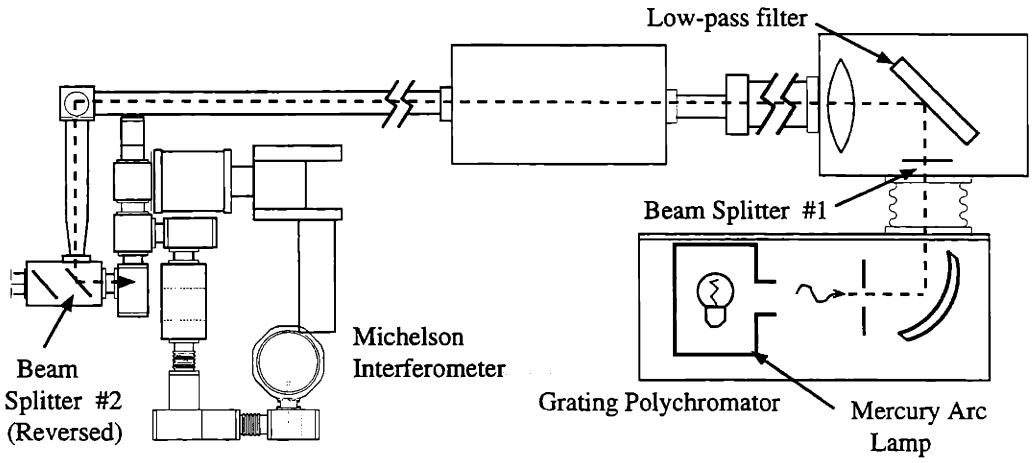

Figure 5-15: Plan-view sketch showing the experimental setup for low-pass filter tests. A mercury lamp was placed inside the GPC enclosure and shone through the aperture and "backwards" through the optics system. With the beamsplitter reversed, the Michelson was used to measure the effect of the low-pass filter on the broad-band transmitted spectrum. Transmission from a flat, front-surfaced mirror was used as a reference to obtain the filter frequency response.

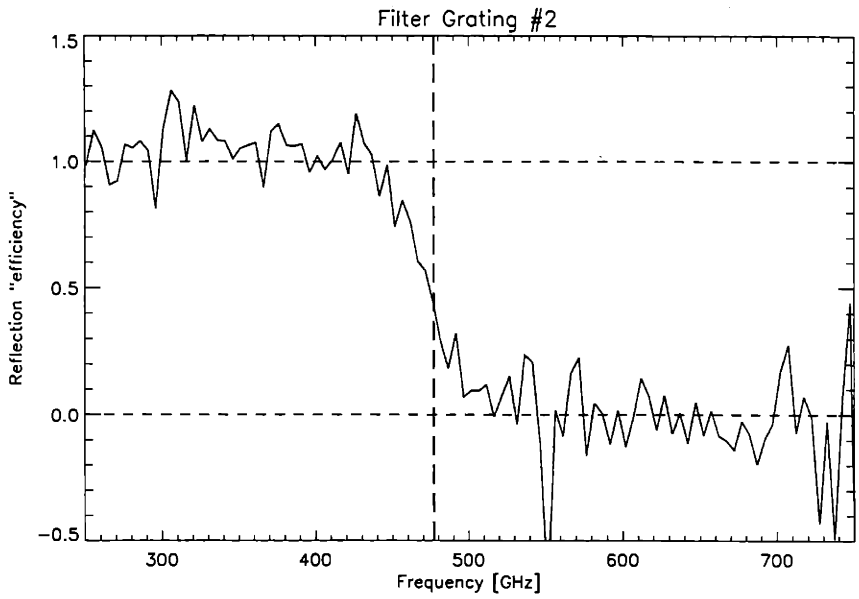

Figure 5-16: Transmission efficiency of a low-pass filter grating of period $d = 0.89mm$, as measured with the test setup sketched in Fig. 5-15. The thick dashed line indicates the location of the cutoff given by $\lambda_c = dcos\theta$ (see appendix B).

Another advantage of orienting the grating groves parallel to optics plane now becomes apparent. For the same chosen cutoff wavelength, comparing Eqs. B.1 and B.2 indicates that the required grating period for our case is more than twice that of the more standard configuration, saving considerably on time (and thus sanity) in the machine shop. It should also be noted here that polychromator systems on other tokamaks [45, 47, 63] very often use multiple filter gratings, often with different grating constants to minimize harmonic leakage [64, 65]. An upgrade to the filter grating hardware was performed which now allows up to three low-pass filters to be easily mounted in series in the existing vacuum enclosure. However, the extra path length introduced defocusses the Gaussian telescope which couples the input beam into the instrument. A new lens is needed to complete the upgrade but present indications show that the optimization of the single-grating filter currently used provides sufficient rejection of the parasitic influence the core plasma on edge temperature measurements. In Fig. 5-18 the edge temperature trace before the filter upgrade shows a strong "positive" sawteeth, a feature only near the plasma core and thus a

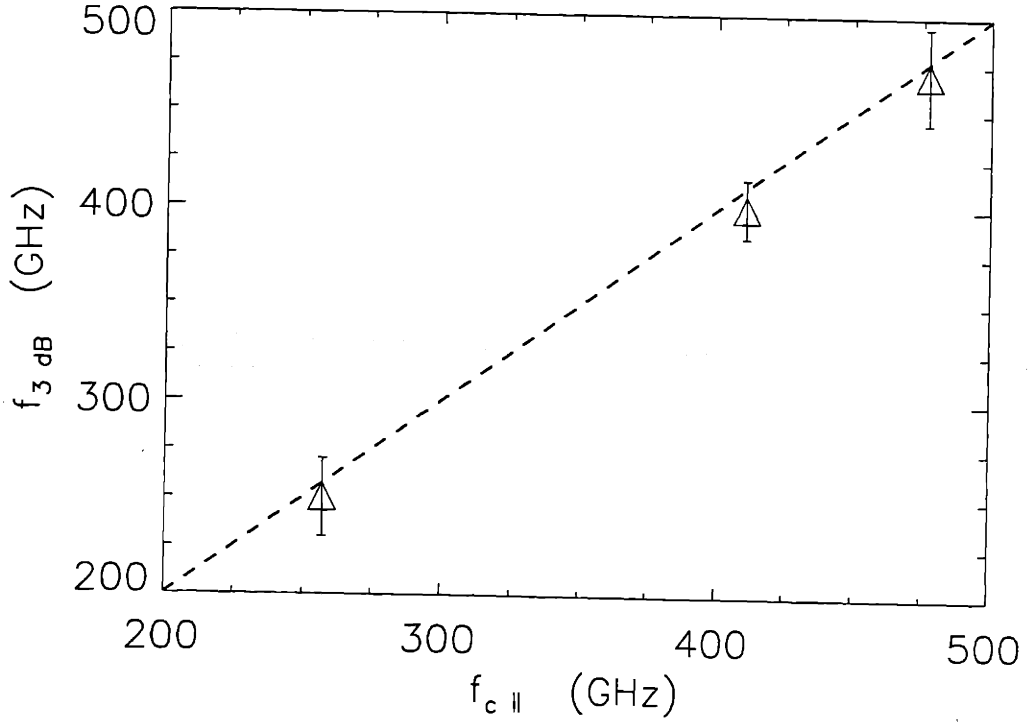

Figure 5-17: Figure showing the measured cutoff frequencies for three GPC low-pass filter gratings versus the predicted cutoff frequency.

strong indication of order overlap. After the filter optimization, and for nearly identical plasma conditions, the edge channel is seen to be largely free from this influence, with perhaps some "inverted" sawtooth behavior visible, the original goal of the upgrade. Though a systematic study of heat pulse dynamics near the plasma edge is not a key part of this thesis (see Chapt. 10), these filtering improvements will make such studies possible. It has also made possible important studies of the behavior and role of the temperature in the formation of transport barriers near the plasma edge [66]. In Fig. 5-19, the structure of an "edge pedestal" near the outboard edge is probed with the grating polychromator by sweeping the outer channels across the region by ramping the toroidal field.

5.5 Calibration of the ECE system

Figure 1-4 shows the layout for the Alcator C-Mod ECE diagnostics system. A very important element is the calibration source located near the tokamak which allows absolute calibration. The steps involved in the calibration process are described below:

1. **Calibration of the Michelson interferometer:** Thermal emission from specially designed sources [11] is detected with the Michelson interferometer. Interchangeable plates of carbon-loaded epoxy tiles, one at room temperature and one at liquid nitrogen temperature (77 K), provide near black-body emission at two known temperatures. The difference in the detected power, P_{det}, at each frequency, ω, is the product of the instrumental sensitivity, $\eta(\omega)_{Mich}$, and the known black body emission, $\Delta I(\omega)\Omega$ (*cf* Eq. 4.16),

$$\Delta P_{det}(\omega)\Omega = \eta(\omega)_{Mich}\frac{\omega^2 \Delta T}{8\pi^3 c^2}, \tag{5.7}$$

where Ω is the acceptance solid angle of the optics, and $\Delta T = T_{"Hot"} - T_{Cold} \approx$ 220 K is the temperature difference between the two sources. The Michelson uses a liquid helium cooled InSb bolometer detector very similar to the GPC

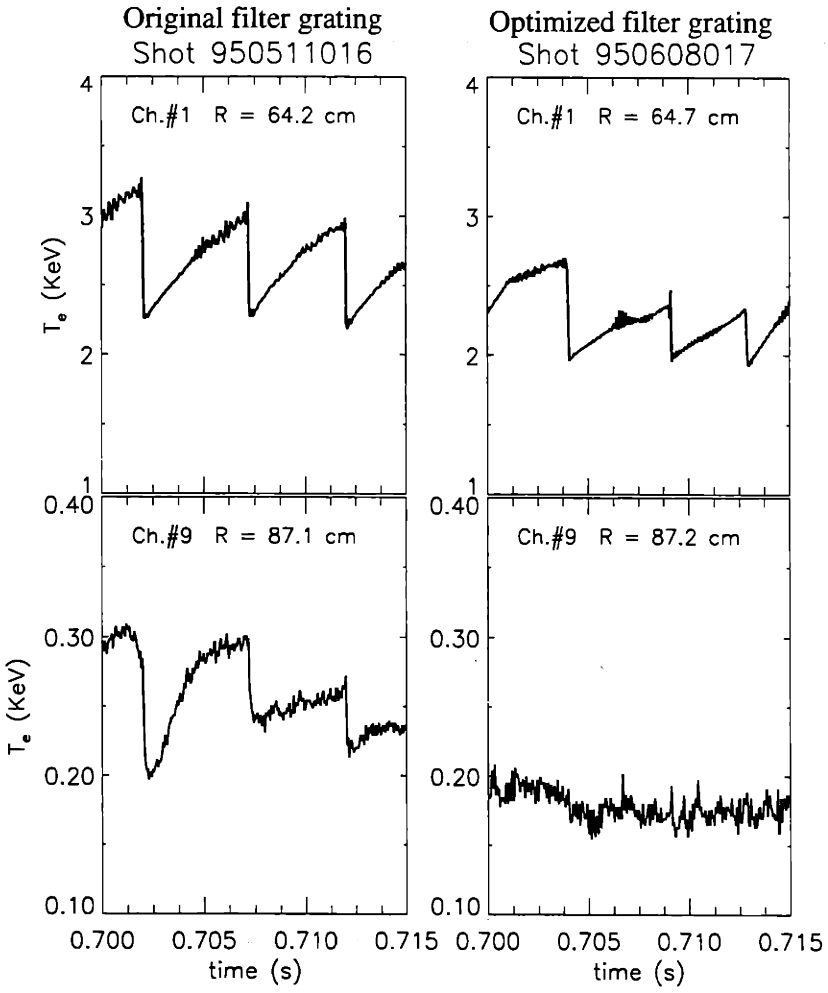

Figure 5-18: Improved filter grating's effect on edge temperature. The left column shows central and edge "temperature" traces before the filter grating upgrade. With poor low-pass prefiltering, the GPC edge channel is sensitive in 2^{nd} *order* of the main grating to 3^{rd} *harmonic* emission from the hot plasma core. The second column shows how the central sawteeth are removed from the outer-most channel after optimizing the filter grating.

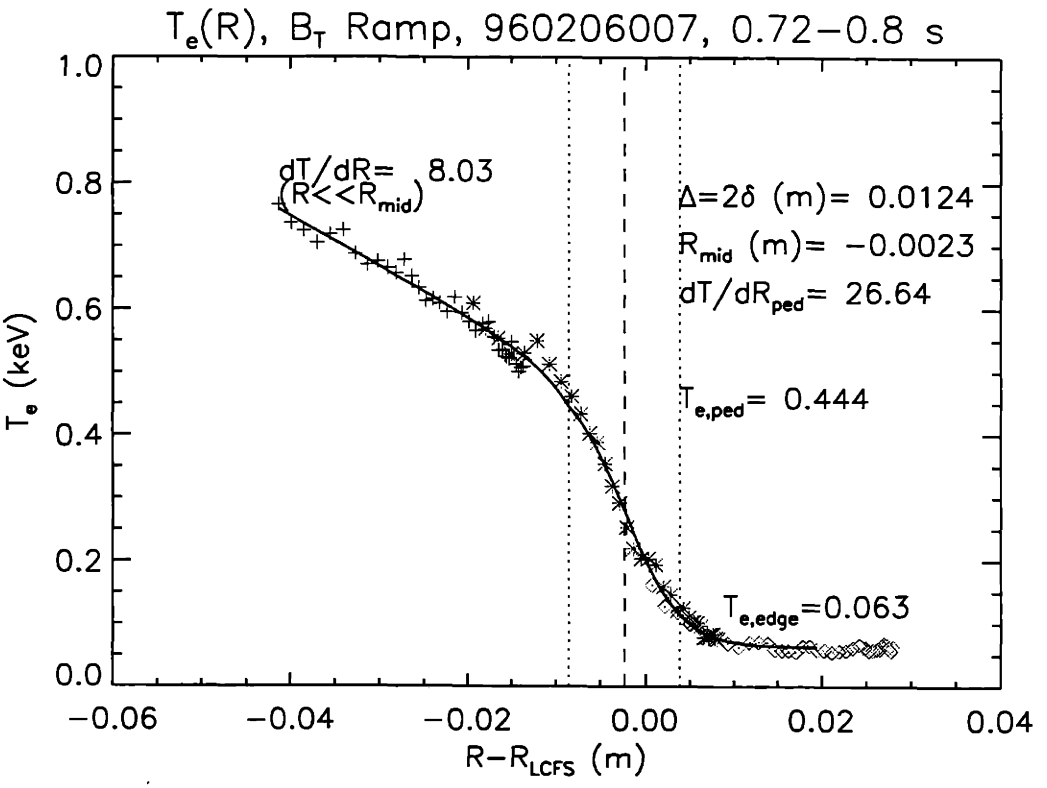

Figure 5-19: Polychromator measurements of an edge temperature pedestal. The magnetic field is ramped to scan the three outermost GPC channels across this distinct feature which forms during "H-modes". Deconvolution of this trace with the radial resolution function for the GPC yields an important measurement of the pedestal width. Note how the profiles from adjacent GPC channels merge together smoothly. The finite amplitude of the signal for large radii indicates the level of signal contamination from order overlap and also the beginnings of harmonic overlap with the first harmonic.

detectors. The detector has been shown to be linear over the $\gtrsim 5$ orders of magnitude in signal power required to extrapolate this calibration to plasma temperatures of order 10^7 K. The calibration signals are very weak and require the averaging of hundreds of thousands of scans to obtain acceptable signal to noise ratios. The calibration process thus requires many delightful hours to accomplish but determines the instrumental sensitivity for the entire operating range of the frequency spectrum and typically needs to be done only once per experimental campaign. This process allows ECE measurements of the electron temperature with a relative error estimated at $\lesssim 15\%$. Agreement of the GPC temperature measurements with Thomson scattering measurements have generally been excellent ($\Delta T/T \lesssim 5\%$) when the latter are available. Although the accuracy of the Thomson scattering temperature measurement is generally higher than ECE measurements, it is technically very difficult to operate and maintain. The polychromator remains the standard source of electron temperature measurements because it is routinely available and has excellent time resolution.

2. **Cross calibration of the grating polychromator:** The spectral range of the grating polychromator is determined by the ratio of the nominal ECE wavelength to the ruling constant of the main grating, λ/d. To maintain spatial coverage of the plasma for large changes in the toroidal magnetic field, the grating must be changed (an overnight proposition). Relatively small changes of the channel positions can be made by changing the grating angle, θ, between shots (*cf* Eq. 5.1). As the efficiency of the grating can be quite sensitive to small changes in the optics configuration [67, 68], it is impractical to calibrate the GPC directly. Instead, the polychromator is cross-calibrated from the Michelson signals after each change in the setup. The Michelson calibration yields a conversion from signal intensity to temperature for the entire frequency range

of operation:

$$T(\omega) = \eta(\omega)_{Mich}\, V_{Mich}(\omega). \tag{5.8}$$

For the i^{th} GPC channel at the frequency $\omega_i = 2\pi\, c/\lambda_i$ where λ_i is the wavelength for the determined from the grating geometry (*cf* Eq. 5.1) the cross calibration coefficient is obtained from matching the inferred temperature at the same Michelson frequency, $T(\omega) = \eta(\omega)_{Mich}\, V_{Mich}(\omega) = \eta(\omega)_{GPC}\, V_{GPC}(\omega_i)$, or

$$\eta(\omega)_{GPC} = \eta(\omega)_{Mich} \frac{V_{Mich}(\omega)}{V_{GPC}(\omega_i)}. \tag{5.9}$$

The outer channel of the GPC is typically located near the plasma edge for the main portion of the plasma discharge. The relatively low temperature near the edge results in a large uncertainty in the ratio $V_{Mich}(\omega)/V_{GPC}(\omega_i)$, as both signals are small. This problem is overcome with a single "cross-calibration" shot in which the magnetic field is ramped down slowly from its nominal value to scan the edge channels of the GPC into the hotter regions of the plasma where the resulting signal to noise for cross calibration is much better.

Chapter 6

Analysis techniques for ICRF experiments

6.1 Influence of ICRF on electron temperature dynamics

In this chapter the issues involved in using highly time resolved measurements of the electron temperature to help diagnose ICRF heating experiments are discussed. The differential equation governing the local temperature evolution can be written in the form:

$$\frac{3}{2}n_e\frac{dT_e}{dt} = p_e|_{tot} = p_e|_{ICRF} + p_e|_{ohmic} + p_e|_{\nabla T_e} + p_e|_{rad} + p_{e/i} + \ldots \qquad (6.1)$$

where the terms on the right hand side of the equation represent (in roughly descending order of importance) the contributions to the total electron heating power density from the ICRF heating, ohmic heating, energy loss due to thermal transport (driven by thermal gradients), radiation losses, and energy exchange with the bulk plasma ions, respectively. For the studies of ICRF power deposition which are the main focus of this thesis, the first term, $p_e|_{ICRF}$ is of greatest interest. In this section the relative magnitudes and the parametric dependences of the terms in Eq. 6.1 are

determined. From this evaluation, the conditions under which $p_e|_{ICRF}$ can be determined are discussed. This discussion will focus on the region near the plasma center ($r/a \lesssim 0.6$) where most of the heating is done.

6.1.1 $p_e|_{ICRF}$ characteristics

- The Alcator C-Mod ICRF system couples up to 3.5 MW into plasmas of volume $\approx 0.8m^3$ corresponding to a *volume averaged* power density $> 4MW/m^3$. Two additional factors determine the peak value of $p_e|_{ICRF}$:

  - **Fraction of the total absorbed power delivered to electrons:** In the case of minority heating, electrons receive ICRF power *indirectly* through collisions with the heated minority ions. As is evident from §3.4.1, the *fraction* of power lost by minority ions going *to electrons* increases as the minority energy increases. Above a critical energy, E_{crit} given in Eq. 3.10, most of the minority ion energy flows to electrons. It is important to emphasize that while it is true that for minority energies below the magnitude of E_{crit}, $p_e|_{ICRF}$ begins to decrease, it is *still* true that it is proportional to the tail energy (*cf* Eq. 3.19). The time response of $p_e|_{ICRF}$ in this case is determined by the overall slowing down time of the minority tail. The *distribution* of minority ion energies must be taken into account for these calculations and the results of some modelling of this problem are shown in Fig. 9-11.

    Mode converted ion Bernstein waves damp *directly* on electrons via Landau damping. This not only means that 100% of the mode converted power contributes to p_e, but more importantly that there is *no appreciable time delay* between the transmitter power and the electron response.

    For the purpose at hand of estimating $p_e|_{ICRF}$, it will later prove to be reasonable to assume that *half* of the launched ICRF power heats electrons when either mode conversion or minority heating dominates.

- **Deposition width:** The volume in which the ICRF power is deposited is only a fraction of the total volume due to horizontal and vertical localization of the heating. The power deposition is in general peaked near a resonance which is localized along the major radius. For mode conversion heating (see Chapts. 7 and 8) electron power profiles can be localized to within a region $0.2a \lesssim \Delta R_{MC}|_{FWHM} \lesssim 0.45a$. ICRF power profiles for minority heating are more difficult to measure. Measurements during $D(H)$ experiments described later in this chapter (see Fig. 6-6) show that at high density the full width of the heating profile is approximately 8 cm. This establishes an approximate lower limit for the minority heating profile width of $\Delta R_{minority}|_{FWHM} > 0.35a$. Measurements during minority heating at low densities suggest a considerably broader heating profile as is expected with a more highly energetic minority population. Toroidal simulations also show that the wave fronts of the magnetosonic wave are focussed as it propagates toward the plasma center. This effect reduces the *vertical* extent of the RF wave fields substantially from a size equal to the height of the current straps at the plasma edge though the finite vertical extent of the wavefields at the resonance can affect the flux surface averaged profile widths.

For a Gaussian profile centered on the magnetic axis with a FWHM width of $\Delta R|_{FWHM} = W$, the central power density is given in terms of the total power absorbed on electrons by the expression

$$p_e|_{ICRF}(0) = \frac{\text{Power to electrons}}{2\pi^2 \sqrt{\kappa}\, R_0\, (3W/5)^2}, \tag{6.2}$$

where R_0 is the major radius and κ is the vertical elongation of the plasma ($\kappa \approx 1.6$ for the discharges considered here). When half the power damps on electrons, we can use the above equation to estimate the central electron heating

power density for two fairly extreme profile widths:

$$p_e|_{ICRF}/P_{transmitter} \approx \begin{cases} 27 \text{ MW}/m^3/(\text{Incident MW}) & \text{for } W = 0.25 \\ 3 \text{ MW}/m^3/(\text{Incident MW}) & \text{for } W = 0.75. \end{cases} \quad (6.3)$$

6.1.2 $p_e|_{ohmic}$ characteristics

- The ohmic heating power density can be estimated fairly easily. For steady conditions, the loop voltage driving the plasma current is fixed and the current density profile, $j(r)$, is determined by the resistivity, (η), of the plasma through Ohm's law, $j = E/\eta$. The resistivity is $\propto T_e^{-3/2}$, so by modelling the temperature profile with $T_e(r) = T_e(0)\ exp(-r^2/b^2)$ and $b \approx 14$ cm, the current density profile can be estimated to be

$$j(r) = \frac{I_p\ exp(-r^2/d^2)}{\sqrt{\kappa}\,\pi d^2(1 - exp(-a^2/d^2))}, \quad (6.4)$$

where I_p is the total plasma current, and $d^2 = 2\,b^2/3$. The electrons carry nearly all of the plasma current so the ohmic *electron* power density is $p_e \approx j^2\,\eta$. Using the Spitzer form for the resistivity, the expression for the power density is

$$p_e(r)|_{ohmic}\ (W/m^3 \approx \frac{I_p^2\,exp(-2r^2/d^2)}{\kappa\,\pi^2 d^4(1 - exp(-a^2/d^2))^2}\ \left(\frac{2.6 \times 10^{-8}}{T_e(keV)^{3/2}}\right), \quad (6.5)$$

where all quantities are in MKS units unless specified. Evaluating this at the plasma center for $I_p = 1$ MA, $d = 11.5cm$ and $T_e = 3keV$ gives $p_e(0)|_{ohmic} \approx 1.8MW/m^3$. Although this power density is not completely negligible compared to the ICRF power density, the following two points indicate how it can be separated from measurements of $p_e|_{tot}$:

  - Long time scales involved: Changes in I_p occur slowly due to its inductive nature. The time scale for current diffusion in Alcator C-Mod is ≈ 1 second. The time dependence of the ohmic heating is dominated by changes in the temperature. The long time scale means that *fast changes* ($\Delta t \lesssim 5$

msec) in the local electron heating are *not* due to changes in the ohmic heating.

- Simple scaling from ohmic conditions: The ohmic heating component during ICRF heating can be obtained to first order simply by scaling the value estimated during the ohmic phase according to $p_e|_{ohmic} \propto I_p^2 T_e^{-3/2}$.

6.1.3 $p_e|_{\nabla T_e}$ characteristics

- This term represents energy diffusion and flow within the plasma, $p_e|_{\nabla T_e} = -\nabla \cdot (n\chi \nabla T_e - nV)$. The dynamics of energy transport are interesting in their own right (see Chapt. 10), but for the purposes of determining the ICRF power deposition, we wish to find circumstances which minimize this term. Again consider two strategies:

  - Minimize temperature gradients: A way of minimizing the influence of transport on power deposition measurements is by taking advantage of situations which minimize the temperature gradients. Such a situation occurs near the plasma center shortly after sawtooth crashes. During a sawtooth crash, magnetic reconnection thermally short-circuits a significant portion of the plasma core. This leads to a prompt flattening of the temperature profile within the so-called *mixing radius* as shown in Fig. 6-1. Following the fast crash, the central plasma begins to "reheat" more slowly until the instability is triggered again and the temperature collapses once more giving the central temperature evolution its characteristic "sawtooth" shape (see Fig. 6-2). The lack of central temperature gradients following a sawtooth crash greatly reduce or eliminate the effects of transport on the temperature evolution. In §6.3 this is described in more detail. Although it is thought that the temperature profile following a sawtooth crash is *completely* flat, we use measured profiles to put an upper bound on the post-crash influence of diffusion. The central temperature follow-

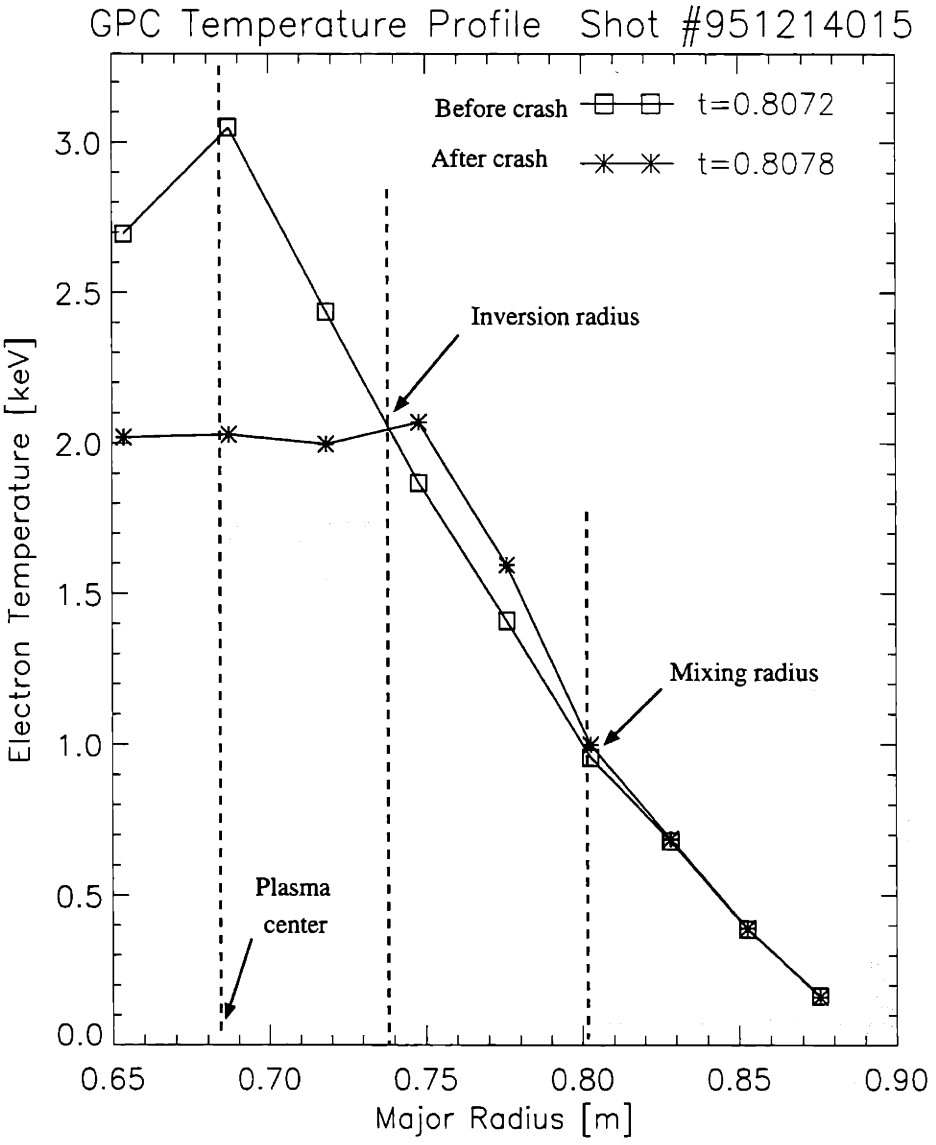

Figure 6-1: Electron temperature profiles before and after a sawtooth crash. Magnetic reconnection within the plasma core flattens the electron temperature profile abruptly as the thermal energy quickly redistributes itself within the "mixing radius". The temperature near the center drops quickly giving rise to the characteristic "sawtooth" time trace seen in Fig. 6-2. The heat lost from the center causes the temperature at larger minor radii to quick rise, creating "inverted" sawteeth. The "inversion radius" separates these two regions.

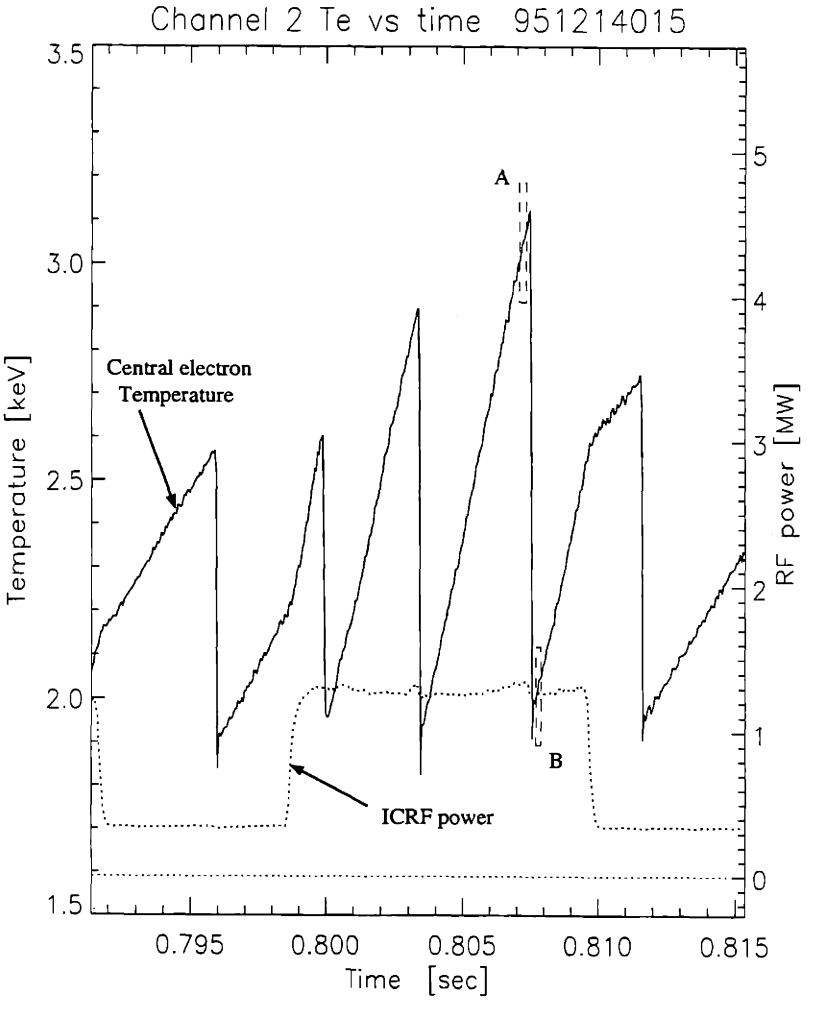

Figure 6-2: Typical time history of the central electron temperature in a tokamak exhibiting "sawtooth" oscillations. The change in the spatial profile of the temperature as a result of a sawtooth "crash" (comparing time 'A' with time 'B') is shown in Fig. 6-1. Note also the prompt response of the rate of the temperature rise to sudden changes in the ICRF power. This indicates that the RF is heating electrons directly.

ing the sawtooth crash in Fig. 6-1 varies by $(\Delta T_e)_{rms} \lesssim 0.05$ keV out to the inversion radius at $r_{inv} \approx 6.5$ cm. Near the plasma center we can conservatively estimate $\chi \approx 0.5\ m^2/s$ (see Chapt. 10). To estimate the corresponding diffusive "power density", model the central temperature profile immediately after the crash with a *broad* Gaussian profile such that $T_e(r_{mix}) = T_e(0)\, exp(-(r_{mix}/l)^2) = T_e(0) - (\Delta T_e)_{rms}$. The central power loss due to diffusive transport under these circumstances is

$$p_e(0)|_{\nabla T_e} \lesssim \frac{4\, n\, \chi\, (\Delta T_e)_{rms}}{r_{mix}^2} \approx 0.6\ \mathrm{MW}/m^3 \tag{6.6}$$

- Using fast time scales: The time scale for the diffusion of energy between flux surfaces in the plasma separated by a distance Δr can be shown (*cf* Eq. 10.5) to be

$$\Delta t_{diff} \approx \frac{3\,\Delta r^2}{2\chi}, \tag{6.7}$$

where χ is the thermal diffusivity. On time scales shorter than this, the diffusion of heat from regions beyond Δr will not affect the local temperature evolution. The radial separation of the GPC channels is ≈ 3 cm and determines Δr for measurements of $p_e|_{ICRF}$. With $\chi \approx 1\ m^2/s$, we obtain $\Delta t_{diff} \approx 1.4\ msec$. This will prove to be the upper limit on the time scale for inferring ICRF power deposition from the temperature response to power transitions.

6.1.4 $p_e|_{rad}$ characteristics

- Quasi-continuum line radiation from ionized impurity atoms is the dominant source of radiation in Alcator C-Mod. The fraction of the input power lost to radiation can range from 10% $\rightarrow$ 80%, though at the low plasma densities considered in this thesis, the total radiated power ranged from $\approx$ 10% $\rightarrow$ 35%. Electrons provide the energy source for these processes through collisional ex-

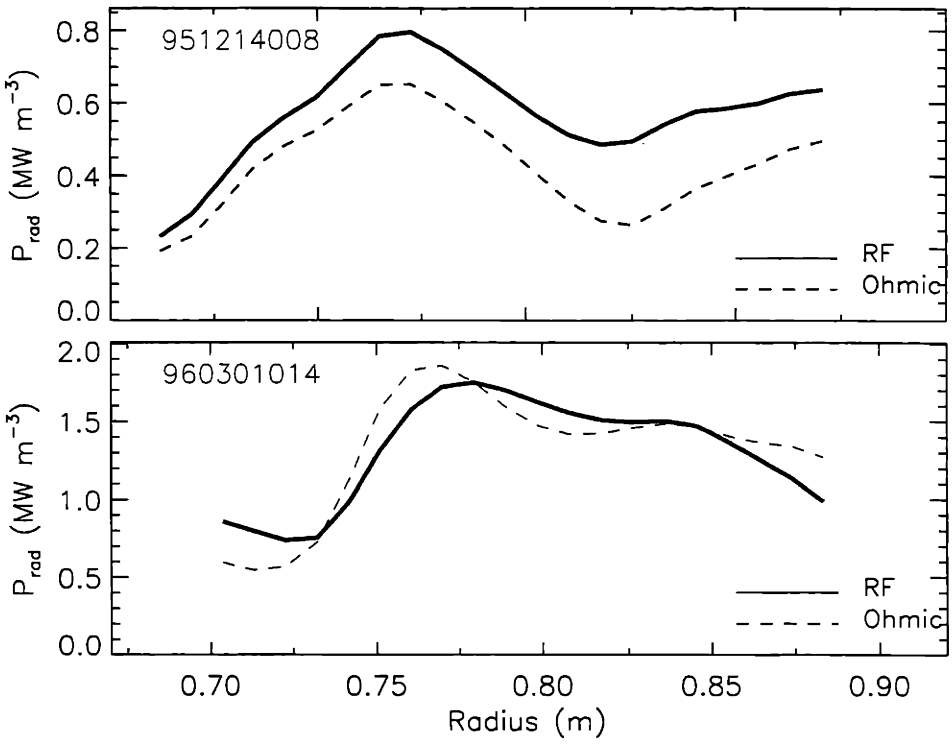

Figure 6-3: Figure showing bolometer measurements of radiated power densities versus major radius for two shots representative of plasmas analysed in this thesis. Both plasmas have a central density of $n_e(0) \approx 1.6 \times 10^{20}\, m^{-3}$. The top panel is for 0.8 MW of $H - He^3$ mode conversion heating with $T_e(0) \approx 2.1$ keV. The bottom panel is for 3 MW of $D(H)$ minority heating, and $T_e(0) \approx 3.5$ keV. The solid lines show the radiation levels during ICRF heating and the dashed lines are the levels ≈ 30 msec *after* the RF is turned off.

citation and ionization so radiation appears as a sink in the electron power balance equation. Most of the radiation occurs at relatively low temperatures near the plasma edge. The high temperatures of the plasma core limit atomic radiation to high-Z impurities. Molybdenum, the material from which most plasma facing components in the tokamak are made (see Fig. 3-1), dominates the core radiation in Alcator C-Mod [69]. Figure 6-3 shows profiles of radiation emissivity as measured by the bolometer array for two different Alcator C-Mod discharges. For 0.8 MW of $H - He^3$ mode conversion heating, the power density of the central radiation is $p_e|_{rad} \lesssim 0.3\ MW\, m^{-3}$. For 3 MW of $D(H)$ minor-

ity heating, $p_e|_{rad} \lesssim 0.9\ MW\,m^{-3}$. In both cases, the total radiated power is $\approx 25\%$ of the total radiated power and half of the radiated power is emitted from beyond $r/a \approx 2/3$. Also shown in Fig. 6-3 are the radiation profiles ≈ 30 msec after the ICRF power is turned off. The absolute change in the central radiated power density is $\lesssim 0.3\ MW\,m^{-3}$ in both cases, which is very small compared to the nominal ICRF power densities estimated above.

6.1.5 $p_{e/i}$ characteristics

- When the ion and electron plasma temperatures are different, power flows to equalize them. For $T_i \approx T_e$, the temperature equilibration power density seen by the electrons is:

$$p_{e/i} = \frac{3\,n_e(T_i - T_e)}{2\,\tau_{e/i}}, \tag{6.8}$$

where $\tau_{e/i}$ is the thermal equilibration time given by:

$$\tau_{e/i} = 6.7 \text{ msec } \frac{M_i\,T_e(keV)^{3/2}}{n_e(10^{20})\,Z_i^2}. \tag{6.9}$$

For a deuterium plasma ($M_i = 2$) with density $2 \times 10^{20}\ m^{-3}$ and $T_e = 3.5$ keV, $\tau_{e/i} \approx 44$ msec. The ion temperature is obtained from measurements of X-rays and of neutrons on Alcator C-Mod (see §1.3.3), and is generally found to be quite similar to T_e. Even at low density, the $\left|\bar{T}_e - \bar{T}_i\right| / \bar{T}_e < 10\%$, whether heating through mode conversion or minority heating. Here $\bar{T}_e$ is the electron temperature averaged over a sawtooth. This difference is equal to zero within the measurement errors. Taking the temperature difference to be 500 eV for the plasma conditions considered above gives an upper estimate on the electron-ion exchange power to be $p_{e/i} < 550$ kW/m^3 which is *at least* a factor of 5 less than $p_e|_{ICRF}$ as calculated from Eq. 6.3 for heating with 1 MW of injected power.

Measurement techniques which are particularly sensitive to the ICRF power component will be discussed in the following sections.

6.2 Sawtooth compensation

Sawtooth oscillations occur universally in Alcator C-Mod discharges except during a few transient phenomena such as pellet injection or severe ICRF power transitions. These sawtooth oscillations can be of large amplitude ($\lesssim 60\%$ of T_e) and of frequencies ranging from 60Hz $\rightarrow$ 600Hz. Sawteeth are of interest to study in themselves and in Chapt. 10 they will be used to provide information on electron thermal transport. However, for many other applications, sawteeth provide nothing but complication. The complicating effects of sawteeth on other tokamaks may often be avoided during operation through sawtooth suppression techniques or by performing experiments during the flat-top of a "monster" sawtooth [70]. This has not been possible on Alcator C-Mod however. Sawteeth must be dealt with in the analysis. In this chapter, the measurement of dynamic temperature phenomena will be described which can be woefully affected by the presence of sawteeth. Thus where possible it is often useful to compensate for sawtooth behavior, removing the sawtooth influence to help bring out the details of another transient effect. Though the variety of sawtooth behavior observed on Alcator C-Mod is large, the behavior is often very repetitive for a given steady state plasma condition, making sawtooth compensation feasible. Figure 6-4 shows an example of the results.

The basic idea of sawtooth compensation is simple. For each steady state segment of a plasma discharge, a prototype "sawtooth" is built up by averaging the sawteeth on each channel of the GPC. For each sawtooth, the baseline temperature is first subtracted so that each sawtooth prototype begins at zero and is generally positive everywhere. No truncation or stretching is performed to combine all of the sawteeth which have slightly varying lengths. Instead, as a running average of the sawteeth is performed, the tails of extra long sawtooth traces are added to the prototype trace with a scale factor applied to avoid discontinuity at the boundary.

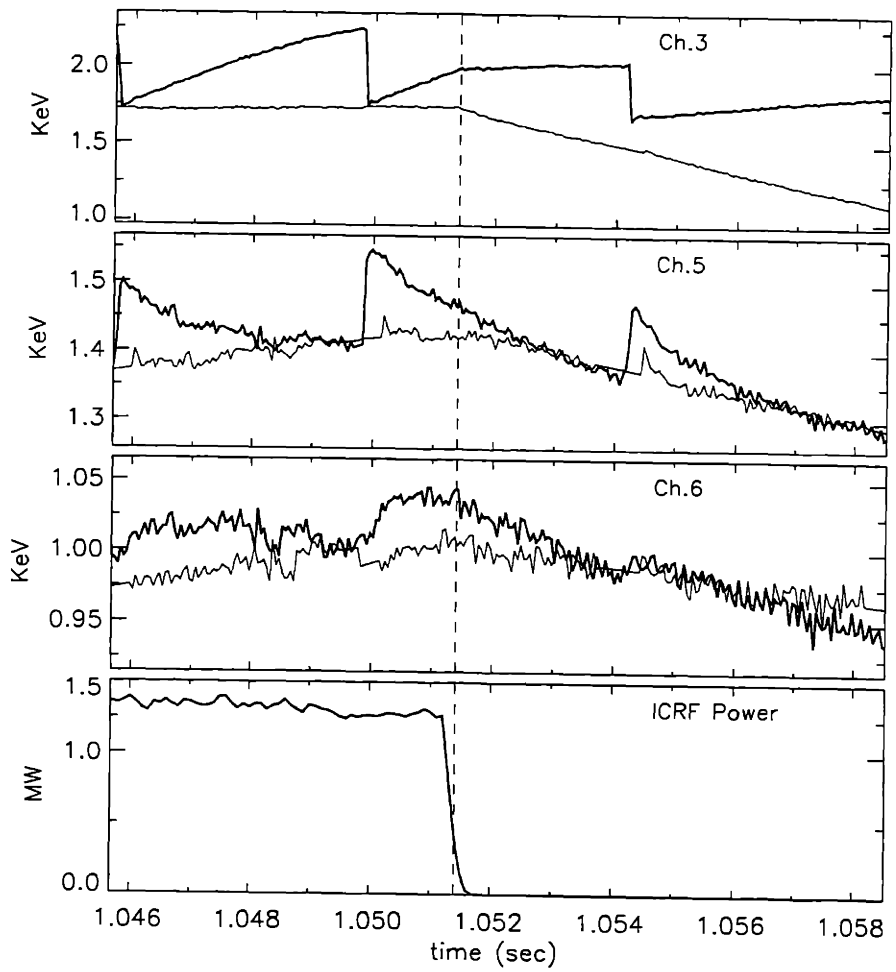

Figure 6-4: Figure showing electron temperature responses (upper three panels) to suddenly turning off the ICRF power (lowest panel). The thick traces indicate the raw temperature data. The thin traces show the same data after the subtraction of the average sawtooth behavior. In this application the compensation is designed to reduce systematic errors in the break-in-slope measurement of the direct electron heating profile (see §6.4).

A further refinement which can be of benefit is to perform a parametric fit to each prototype waveform in order to reproduce the basic form with a waveform that is locally smooth. This reduces the amount of high frequency noise added when attempting to subtract out the sawtooth behavior. For radii outside the inversion radius, the average sawtooth signal is fit with the five parameter fitting function:

$$T_{ST}(t) = a\,t^b\,exp(-(t/\tau)^c) + e\,t^2. \tag{6.10}$$

Figure 6-5 shows examples of sawteeth as seen on various channels of the GPC and how this general function is able to fit them. This is an extension of rather simplistic sawtooth compensation done in other analysis [71] using a linear model for the sawteeth. Either the average prototype or the parameterized fit may then be subtracted from a given sawtooth with the same steady state plasma conditions in order to compensate for the presence of sawtooth behaviour to first order.

6.3 Sawtooth reheat rate

Although problematic at times, the ubiquitous presence of sawteeth does provide some benefit to the experimentalist. As seen in §6.1.3, the temperature gradients vanish within the mixing radius immediately after the crash eliminating thermal diffusion from the power balance equation. For a short time therefore, the temperature evolution near the plasma center is determined solely by the local electron power density. Measuring the instantaneous *sawtooth reheat rate* with the grating polychromator (near the point labelled "B" in Fig. 6-2) thus provides a useful measurement of the power density near the plasma center.

Examination of the various terms described in the previous section shows that even moderate levels of ICRF heating can dominate the power sources at center and indicates how the effects of the other terms can be estimated. Ohmic heating is not small but can be estimated fairly accurately and subtracted. Radiation losses are small near the plasma center and do not change greatly during low density ICRF

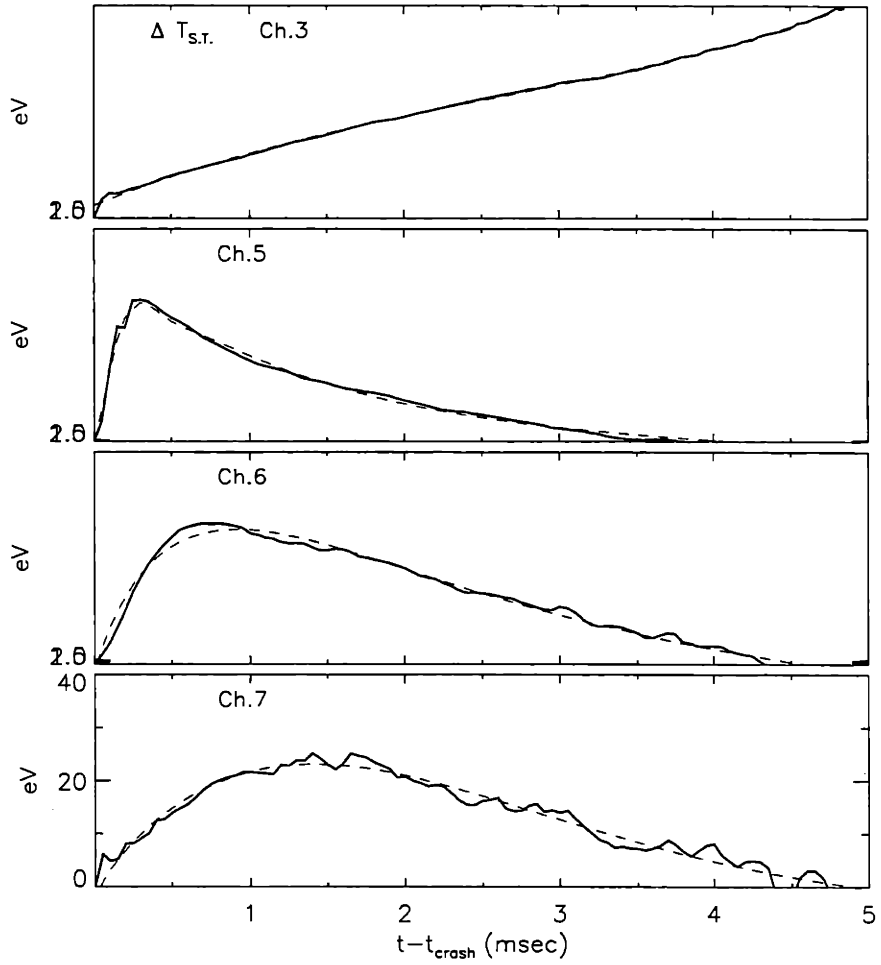

Figure 6-5: Figure showing examples of sawtooth signals as measured on different channels of the GPC for the same shot. The thick lines indicate the results of averaging several sawteeth together as described in the text. The thinner curve in each case is the parametric fit obtained using the function given in Eq. 6.10.

operation so that subtraction of the ohmic reheat power densities from the ICRF levels corrects for radiation to first order for the plasmas considered in this thesis. Power exchange with ions can also be corrected for to first order using equation 6.8 and the experimentally measured central ion temperature. In Chapt. 9 example data will be examined which show that this term can also be quite small.

Spatial information from the sawtooth reheat measurements

The temperature profile flattening which allows power deposition profiles to be inferred from sawtooth reheat rates extends out to a radius which scales like $r \propto I_p/B_T$. In Fig. 6-1, for which the plasma current was $I_p = 800$ kA and the toroidal field was $B_T = 6.5$ Tesla, this radius is approximately $r/a \approx 1/3$. Thus the ability of the reheat rate to provide information about the spatial profiles of ICRF power deposition is limited. Only two or three channels of the GPC may be used for this measurement, providing minimal informal about profile widths for standard heating experiments. Figure 6-6 shows central reheat power measurements from a series of D(H) minority heating shots in which the location of the hydrogen cyclotron resonance was scanned off axis by increasing the magnetic field from the standard value of 5.3 Tesla. When the resonance is on-axis, the enhancement of the central power density over ohmic levels is considerable, and ICRF heating dominates. In this case, the decay of this enhancement as the resonance is moved off axis provides information about the width of the deposition profile.

Time-scale information from the sawtooth reheat measurements

Even in situations where the ICRF power density is large enough to measure accurately with the sawtooth reheat rate, there can remain an ambiguity as to the identity of the heating mechanism as minority heating or direct damping on electrons from the IBW. In steady state, these processes can not be easily distinguished and time dependant methods are generally required (see §6.4 and §9.1.5). The time resolution of the reheat measurements is ultimately determined by the sawtooth frequency, which is generally much too slow for distinguishing between minority and mode conversion

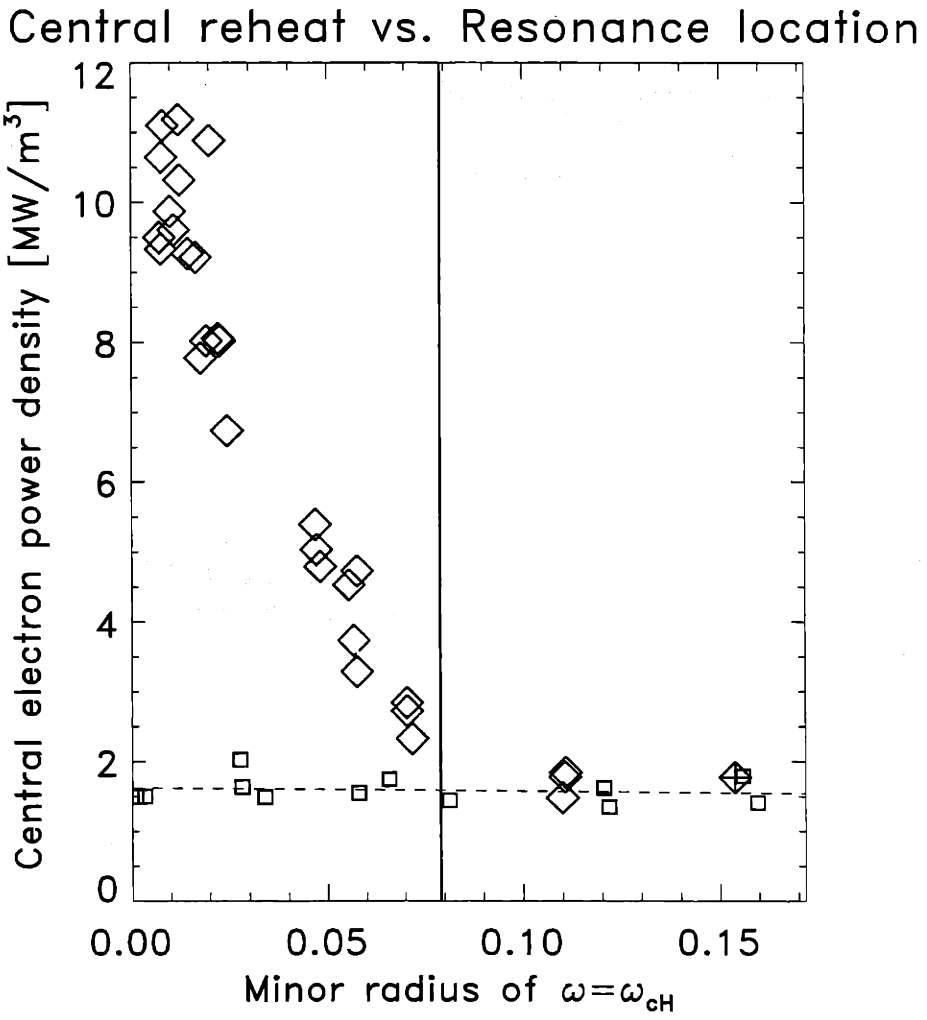

Figure 6-6: Variation in the *central* electron power density (as measured with the sawtooth reheat technique) with the position of the hydrogen minority resonance for a toroidal field scan in D(H) plasma. The diamonds indicate data for ICRF power of $\approx 2.4MW$. The squares indicate the ohmic reheat power levels for the same shots, $I_p \approx 1$ MA. All shots achieved H-Mode during RF, with central electron densities $2.1 < n_{e0}$ $(10^{20}\ m^{-3}) < 3.8$. The vertical line shows the average location of the sawtooth inversion radius for these discharges.

heating. The slow decay of the sawtooth reheat rate can be useful in studying high energy minority tails, as will be seen in Chapt. 9.

6.4 Detection of direct electron heating

Figure 6-7 shows the electron temperature evolution as measured by the GPC for an ICRF heated $H(He^3)$ plasma. The lower panel shows the time trace of the transmitter power. The rates of temperature rise during the sawtooth cycle at the plasma center shows obvious discontinuities at the times of the power transitions. The change in the slope can occur with no measurable time delay and on the same time scale as the drop in RF power (observed to occur in $\leq 10^{-4}$ seconds). This is much faster than a tail slowing down time and indicates that there is a strong direct electron heating channel. This is the strong damping of the IBW on electrons near the mode conversion layer.

6.4.1 Basic break-in-slope technique

To diagnose a source of strong direct electron heating with a time resolved electron temperature diagnostic is straightforward in principle. When there is no mediating minority ion species between the ICRF transmitters and the electrons, there is no time delay in the electron temperature response to a sudden change in the transmitter power. The local electron heating power density is then given by:

$$p_e(r)|_{direct} = \frac{3}{2} n_e(r)\, \Delta \frac{dT_e(r,t)}{dt}\bigg|_{transition} \tag{6.11}$$

When the direct electron heating is very strong and obviously dominates the immediate time dependence of the temperature, obtaining the instantaneous break in slope is a straight forward measurement. In general, however, the influence of the direct electron heating power must compete with the effects of other plasma dynamics and noise. In Chapt. 10 the deposition profile will be used as the "known" time dependent source term in transient thermal transport studies. Significant effort is

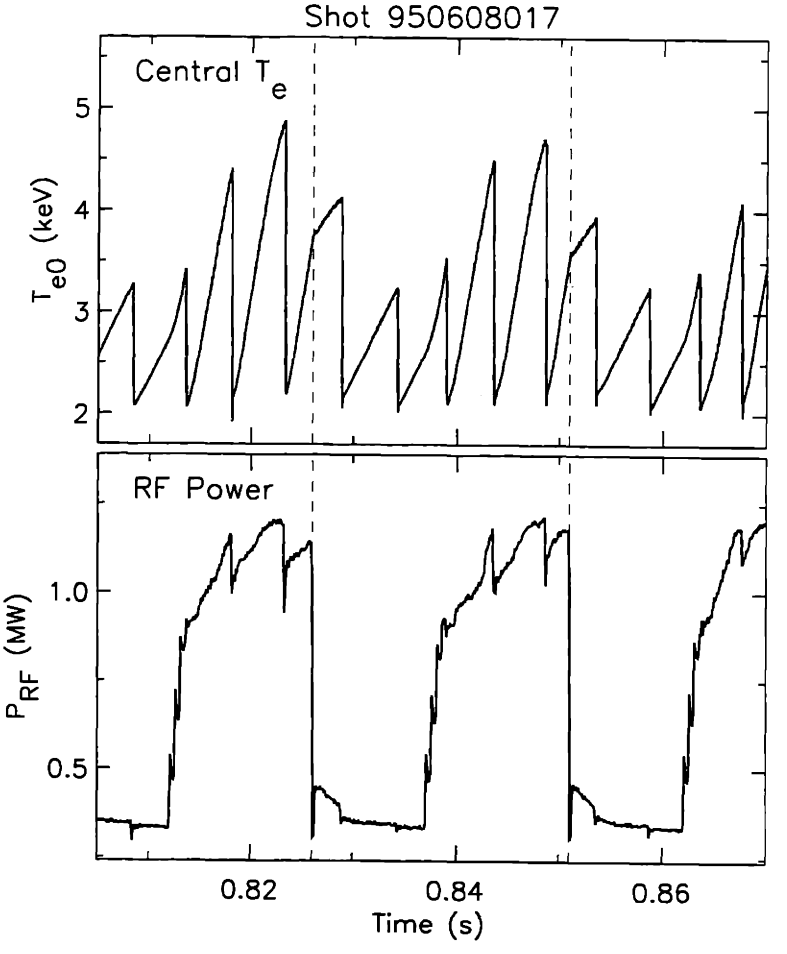

Figure 6-7: Figure showing the evolution of the electron temperature as measured on the central channel of the grating polychromator during modulated mode conversion heating in a $H(He^3)$ plasma at 6.4 Tesla. The sharp break in slope indicates strong localized electron heating. The results from each GPC channel were used to generate the direct electron heating profile shown in Fig. 6-9.

thus made here to measure power deposition profiles accurately at all radii. To best characterize the mode conversion heating, it is desirable to reduce the uncertainties in the estimated power profiles and also to ensure that the technique is insensitive to *indirect* power sources. Some degree of automation for the data analysis is also desired to allow the examination of very many power transitions and to ensure that the analysis technique is consistent. For these reasons, care and energy were devoted to developing optimized power profile analysis techniques. A discussion of the main issues considered is given below.

6.4.2 Fitting procedure

Here we consider how best to measure the *instantaneous* change in the slope of a time trace of electron temperature. To ensure that the measurement selects against *indirect* electron heating, the time interval used for the fitting procedure should be as short as possible. In order to minimize the sensitivity to noise, the fitting interval should be as long as possible. An algorithm was developed which attempts to optimally satisfy these conflicting considerations. It is briefly described here.

The temperature signals before and after a power transition are least-squares fit with both linear and quadratic polynomials over a range of time intervals. The optimal fitting intervals are taken to be the intervals of maximum length for which the normalized chi-squared errors of the linear fits are within 1.5 % of that for the corresponding quadratic fits. Using these intervals, a best fit is obtained to a function consisting of two straight line segments, kinked at the transition time (three parameter fit for two lines). For each line segment, the fitting error in the slope, $error(m)$, is

$$error(m) = \frac{\sigma_T|_{fit}}{\sqrt{\sum_{i=1}^{N}(t_i - \bar{t}_i)^2}} \qquad \sigma_T^2|_{fit} = \frac{\sqrt{\sum_{i=1}^{N}(T_i - T_{ifit})^2}}{N - 1.5} \tag{6.12}$$

and the total error in the break-in-slope measurement is the quadrature sum of the

two fitting errors:

$$error(\Delta m) = \sqrt{error(m_{before})^2 + error(m_{after})^2}. \tag{6.13}$$

Equation 6.11 shows that the calculated break-in-slope power is also proportional to the electron density. For this analysis, the results of the two-color interferometer density inversion [72] were used for $n_e(r)$. This introduces an additional, mainly systematic error of $\approx 15\%$ into the power profiles. Results given in this thesis (see Figs. 6-9 and 6-10) show the errors estimated from temperature measurements alone.

6.4.3 Sawtooth effects & the break-in-slope method

It is obvious from Fig. 6-7 that sawteeth can be large on Alcator C-Mod. Closer examination of the figure also shows how sawtooth dynamics can complicate the process of extracting electron heating profile with the *break-in-slope* technique.

Even with a prompt electron response to a sharp power transition, finite time intervals on both sides of the transition time are required in practice to derive experimentally the break in slope. These intervals must be unbroken by a sawtooth crash and through this consideration the break-in-slope technique selects for analysis those power transitions which occur near the middle portion of the sawtooth phase. Because the heat pulse from a sawtooth crash takes a finite time to propagate to the outer edge of the plasma, the peak of the sawtooth rise at radii outside the mixing radius (see §10.6.2) lags the sawtooth crash. Thus there is a radius, call it R^*, where the peak in the periodic sawtooth time behavior occurs near the middle of the central sawtooth phase where a given power transition occurs. Evaluating the break in slope at this location where the sawtooth behavior produces a time trace $Te(R^*, t)$ which is concave down, will tend systematically to reduce the break in slope. The plasma volume within a given ΔR around flux surfaces also increases with minor radius, thus "diluting" the ICRF power and making the break in slope harder to detect.

In order to reduce the sensitivity to this sawtooth effect, sawtooth compensation can be used. In the most direct approach, the "expected" sawtooth waveform (as

obtained from averaging sawteeth from the same shot, see §6.2) for the pre-transition power level is subtracted from the sawtooth trace in which the power transition occurred. Then the standard break in slope measurement can be made on the compensated time histories as shown in Fig. 6-4. This method, though sound in concept, is in practice susceptible to noise and sporadic sawtooth behaviors.

A simpler technique has been adopted which in practice proves to be much more robust. In this method, the standard break-in-slope method is applied to the uncompensated temperature data at the power transition time. It is then *also* applied to the temperature traces of the *previous* sawtooth period at the same sawtooth *phase* as the power transition. The results from this "dummy" transition are taken to represent the unperturbed sawtooth behavior and they are subtracted from those of the real transition time. This technique proves to be particularly useful because it can be easily adapted to analyse power transitions occurring very near sawtooth transitions for which the standard analysis would be too problematic. Consider a power transition occurring very *early* in the sawtooth phase. In this case, the pre-transition slope will be difficult to obtain reliably because of the sawtooth crash, so the standard pre versus post transition slope comparison will fail. With the assumption that the pre-transition sawtooth crash brought the plasma conditions to approximately the same state as the crash before it, we can still infer the *direct* electron heating by comparing the post-transition slope to that at the dummy transition time of the previous sawtooth. In the case of a power transition very *late* in the sawtooth phase, useful measurements may still be made with a further approximation. One can skip ahead in time to just *after* the sawtooth crash and evaluate the slope there and again use the corresponding slope for the previous sawtooth crash for sawtooth compensation. If the time interval skipped is short compared to the expected slowing down time for a minority tail, then the derived power density still represents a measurement of the *direct* electron heating. Thus with only small loss in time resolution, this method can be extended to provide heating results for transitions which occur quite close to sawtooth crashes. A good example of this adapted break-in-slope method is shown in Fig. 6-11. The power transition occurs very near to a sawtooth crash and

although close examination of the time traces clearly show prompt temperature response ($< 100\mu$sec), precise measurement of the change in slope is impossible. Fitting line segments to the traces starting $\approx 500\mu$sec after the power transition and comparing the slope to that of the previous crash clearly indicates strong off axis electron heating (see Fig. 10-3). Figure 6-8 shows an example of the grating polychromator data for a case of off-axis electron heating in a $D-He^3$ plasma. Examples of electron heating power profiles measured with the break in slope technique are shown in the following figures. Figure 6-9 indicates central electron heating in $H(He^3)$ plasmas at 6.4T with approximately 25% helium. Figure 6-10 shows off axis heating in $D(He^3)$ plasmas with $n_{He^3}/n_e \approx 22\%$ and $B_T = 7.9T$. The locations and widths of these power profiles are in good qualitative agreement with predictions from theory. For a systematic quantitative analysis of these results, refer to Chapts. 8 and 7 respectively.

6.4.4 Power profiles and integrated power

The break-in-slope technique produces measurements of the direct electron heating power *density* at nine locations along the major radius on the midplane of the tokamak. These power densities are assumed to reflect flux surface averaged values and the total absorbed power is obtained from the integral over the plasma volume:

$$P_{absorbed} = \int_0^\rho p_e(\rho) dV(\rho), \tag{6.14}$$

where ρ is the normalized midplane minor radius of the flux surfaces. The EFIT code calculates the position of the magnetic axis and volume elements of the flux surfaces reconstructed from magnetics measurements. The above integral can be calculated numerically after careful consideration of the following points:

1. **Accurate mapping of flux surfaces:**

   Both EFIT and the Grating Polychromator have errors in their calculated major radii. It is important that discrepancies be kept to a minimum, especially for narrow profiles peaked on axis. The GPC was run such that the high field

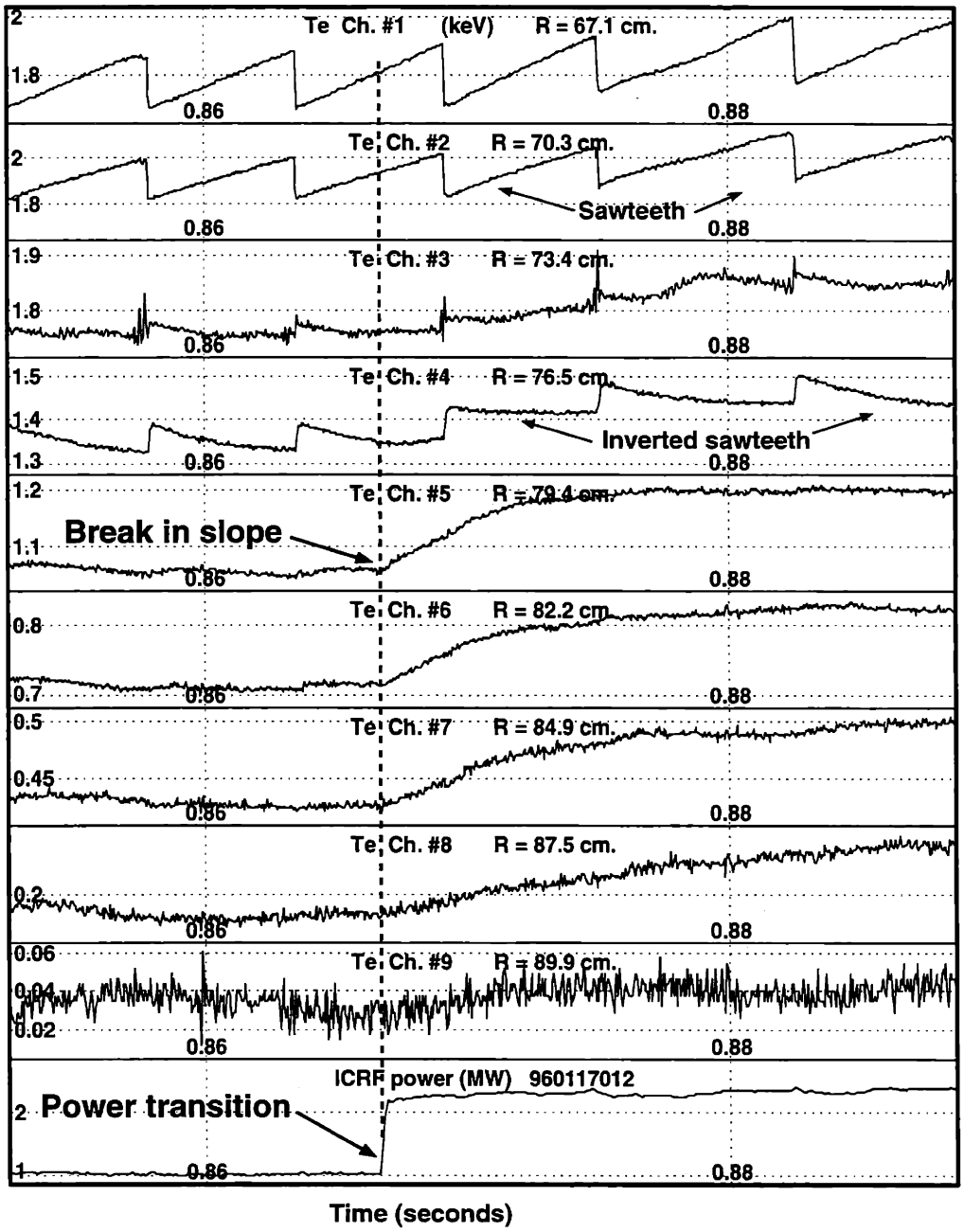

Figure 6-8: Raw Grating polychromator data clearly showing the prompt break in slope in response to an ICRF power transition. Break-in-slope measurements for this shot were used to generate the estimate direct electron power profile shown in Fig. 6-10.Here there is essentially no response on axis with clear breaks at the outer radii indicating off axis power electron heating. This was a $D - He^3$ plasma, at 7.9T, with a Helium fraction $n_{He^3}/n_e \approx 20\%$.

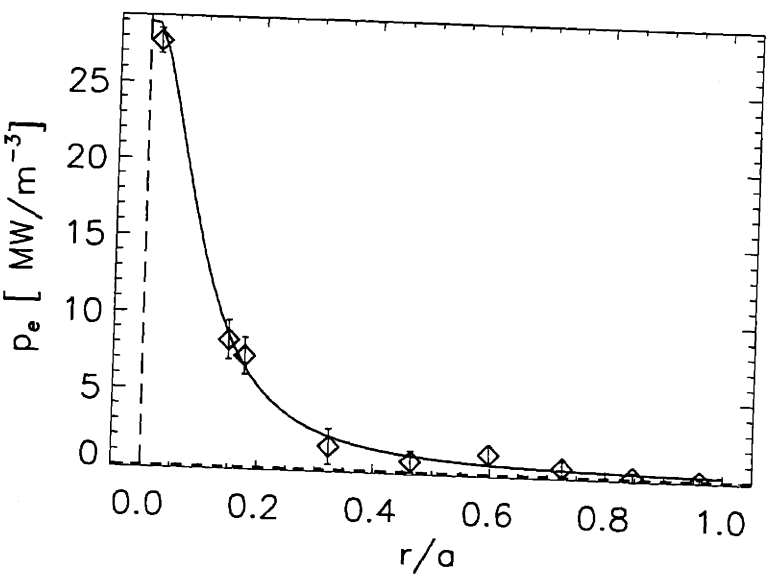

Figure 6-9: Break in slope derived power for $H(He^3)$ plasma, 6.4T, normalized to 1 MW of incident ICRF power. The on-axis point of this profile was derived from the raw data shown in Fig. 6-7. The volume integrated power in this case is estimated to be $75 \pm 15\%$ of the total ICRF power.

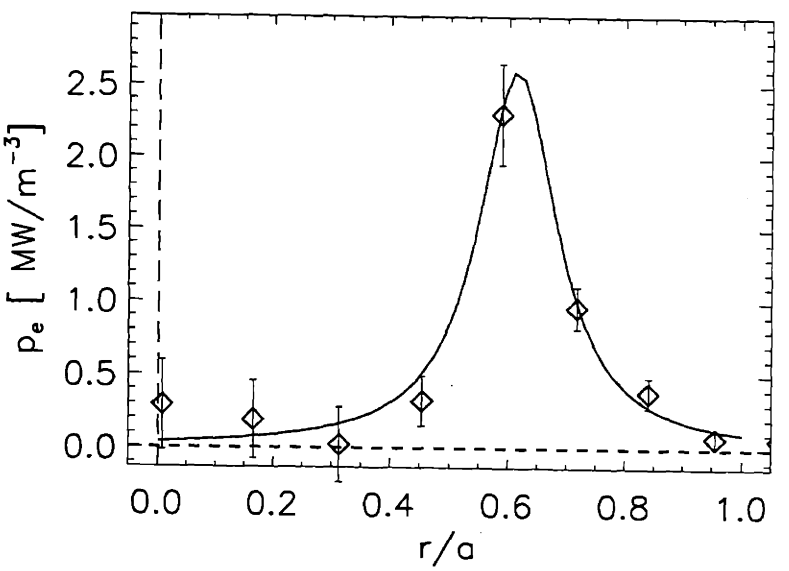

Figure 6-10: Break in slope derived power for $D(He^3)$ plasma, 7.9T, normalized to 1 MW of incident ICRF power. This profile was derived from the raw data shown in Fig. 6-8. The volume integral of the profile fit to these measurements (see §6.4.4) indicates that $\approx 45\%$ of the RF power is absorbed directly by electrons in this case.

channel lay to the high field side of the magnetic axis in order to use the symmetry of the power profiles across the magnetic axis as a tool for aligning the two coordinate systems. It is important to note that an *even more* sensitive indicator of the magnetic axis as measured from ECE comes from sawtooth precursors. Looking at the radial variation of large m=1 oscillations is a very sensitive indicator because the phase jumps by 180° in crossing the axis. For integration purposes, the GPC power profiles are shifted so that the plasma center found by estimating the location of the null in the sawtooth precursors coincides with the EFIT magnetic axis. The magnitude of this shift is typically $\lesssim 5$ mm, similar to the estimated error in the code calculation [73].

2. **Fit to experimental data:**

For integration purposes, a generalized Lorentzian function is used to fit continuous curves to the nine discrete power density measurements:

$$p_e(r)|_{fit_L} = A\left(\frac{1}{1+(r-r_0)^2/w^2}\right)^b, \tag{6.15}$$

where A is the peak power density occurring at the minor radius, r_0, and w and b together determine the width and shape of the profile. This adhoc function was found to fit the measured profiles quite well except for cases when the heating was only slightly off axis. In this case, flux surface averaging leads to asymmetric profiles which can be matched well with the addition of a central Gaussian component with one free parameter:

$$p_e(r)|_{fit_2} = p_e(r)|_{fit_L} + B\,exp(-1.5\times r^2/r_0^2). \tag{6.16}$$

The fitting procedure has additional constraints which force the fit strongly towards zero for radii near the last closed flux surface.

6.4.5 Error estimates for the absorbed power

The errors in the power density measurements were discussed in §6.4.2. In order to estimate the error in the integrated power, each of the nine power density measurements were independently varied according to a normal distribution determined from the break-in-slope fitting error for that channel. For each of an ensemble of fifty profiles, the fitting and integration were carried out with an automated process. The standard variation in the resulting integrals was taken as the error due to the temperature measurements.

6.4.6 Other measurements of absorbed power

The total absorbed ICRF power can be estimated with a break-in-slope method applied to measurements of the total stored energy (W) of the plasma at a sharp step transition in the ICRF power:

$$P_{ICRF}|_{Absorbed} = \Delta \frac{dW}{dt}\bigg|_{transition} . \tag{6.17}$$

There are different methods for measuring W. For the break-in-slope method, which requires relatively good time resolution, the diamagnetic stored energy measured with flux loops mounted inside the vacuum vessel can provide a useful comparison. This method is sensitive to all absorption mechanisms in the plasma. Figure 6-11 shows a comparison of the responses of the electron temperature and the diamagnetic stored energy to turning on the ICRF heating. The fraction of the total forward power seen in direct electron heating inferred from the break in slope of the GPC signals is estimated to be 41%. The error due to the analysis of the temperature is $(\Delta P/P)_{\text{break-in-slope}} \lesssim 10\%$. Uncertainty in the electron density introduces an additional error, $(\Delta P/P)_{dens} \approx 15\%$. The break in the stored energy indicates $\approx 45\%$ total absorbed power, indicating that absorption due to minority ion heating and other processes is small for these conditions (6.5 Tesla, $n_{He^3}/n_e \approx 8\%$).

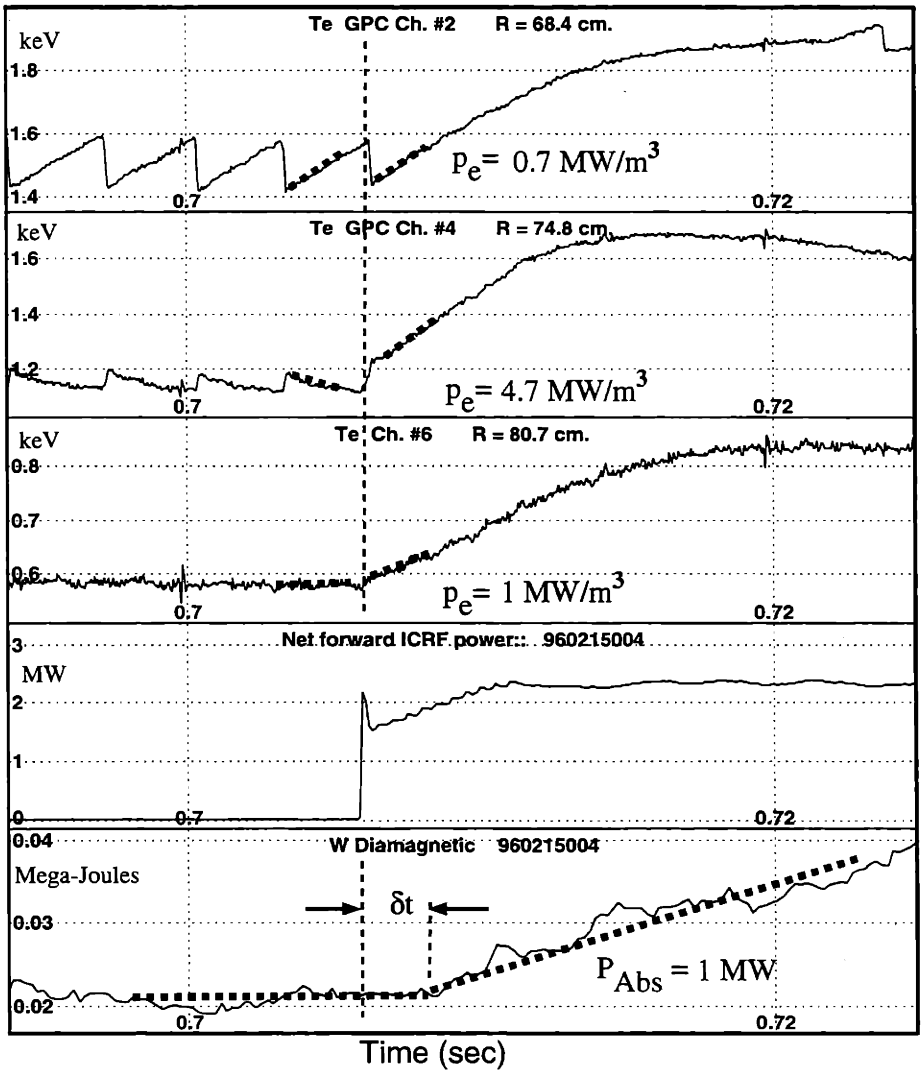

Figure 6-11: Figure comparing the evolutions of the electron temperature and the total plasma stored energy as measured with diamagnetic flux loops after turning on the ICRF power. The sharp break in slope on channel #4 of the GPC indicates strong off-axis electron heating. Break-in-slope analysis of the GPC traces yields an electron heating power density profile shown normalized to a 1 MW power transition in Fig. 10-3. The volume integral of this profile indicates that 41±3% of the ICRF power is absorbed by electrons (the central electron density used was $n_e(0) = 1.8 \times 10^{20}\, m^{-3}$ and introduces an additional uncertainty of $\approx 15\%$). The break in slope of the stored energy (delayed δt by filtering circuits) indicates that $\approx 45\%$ of the ICRF power is absorbed by the plasma.

6.5 Distinguishing between direct and indirect heating

A vanishing time delay of the electron heating to sharp power transitions is a sure sign of direct electron heating. When the time resolution of the break-in-slope technique is limited (by low signal-to-noise or by the finite time for the ICRF power to change substantially), the distinction can become blurred between direct electron heating and fast decay times for low energy ion "tails". In the case of mode conversion, however, the peak in the power deposition for these two cases is spatially separated. Mode conversion occurrs well away from the cyclotron resonance, removing the ambiguity. As will be seen in Chapt. 9, the distinction between the spatial location of minority heating and direct electron damping of the fast wave need not be so clear.

Chapter 7

Results from D(He^3) experiments

7.1 Introduction

In Chap. 3 the basic physics involved in ICRF heating of tokamaks was described. In particular, it was shown that two very different wave damping mechanisms can occur, depending on the plasma conditions. The launched fast magnetosonic wave can either damp on minority ions near their fundamental cyclotron resonance, or else mode conversion to the ion Bernstein wave can occur which generally leads to electron heating. Section 3.7 discussed the conditions for and the nature of the competition between these two processes. Analyses of $D(He^3)$ heating experiments on Alcator C-Mod are presented in this chapter which reveal the unanticipated result that minority ion heating is *not* the dominant heating process. Mode conversion heating can absorb up to 50% of the launched ICRF power and evidence for relatively weak minority ion heating is obtained only at very low He^3 concentrations ($n_{He^3}/n_e \approx 1\%$). These results are shown below to run counter to *a priori* predictions based on previous code simulations. These discrepancies as well as the qualitatively different results obtained on other tokamaks are discussed in terms of the unique plasma conditions of Alcator C-Mod under which these experiments were run.

7.1.1 Conditions for $D(He^3)$ heating experiments

The geometry of the wave resonances for the standard experimental conditions is shown in Fig. 7-1. To the end of the campaign ending March 1^{st}, 1996 this heating scenario has only been attempted at a nominal magnetic field of 7.9 Tesla. For this magnetic field, the launched waves (at the transmitter frequency of 80 MHz) experience the fundamental cyclotron resonance of He^3 at the plasma center. Data analysis will be limited to Helium concentration scans which were conducted on two different run days, 960117 and 960131, for plasmas with peak electron densities $\approx 2.1 \times 10^{20}\ [m^{-3}]$.

7.1.2 Measurement of the He^3 concentration

Quantifying the He^3 concentration in the plasma will be critical to the analysis and discussions of the heating experiments of this chapter and Chap. 8. Appendix A describes in some detail the methods used to obtain an estimate of the ratio n_{He^3}/n_e. Briefly, a calibrated piezoelectric valve is pulsed for a controlled interval near the plasma flat-top allowing a known amount of neutral He^3 into the vacuum vessel. Measurements of the resulting density and $Z_{effective}$ for many gas puffs indicates that $\approx 40\%$ of the puffed He^3 gas enters the plasma. It is assumed that the n_{He^3}/n_e fraction is roughly constant throughout the plasma and during the remainder of the shot. The relative uncertainty in n_{He^3}/n_e is $\approx 10\%$.

7.2 Mode conversion in $D - He^3$ plasmas.

The ion-hybrid resonance for this mix of plasma species follows from Eq. 3.24 and is given by

$$\omega_{MC}|_{D-He^3} = \Omega_{c_{He^3}} \sqrt{\frac{3X_{He^3}+6}{10X_{He^3}+6}} = \Omega_{c_{He^3}} \sqrt{\frac{6-3f_{He^3}}{4f_{He^3}+6}}, \tag{7.1}$$

$$\text{where } X_{He^3} \equiv n_{He^3}/(n_H + n_{He^3}),$$

$$\text{and } f_{He^3} \equiv n_{He^3}/n_e.$$

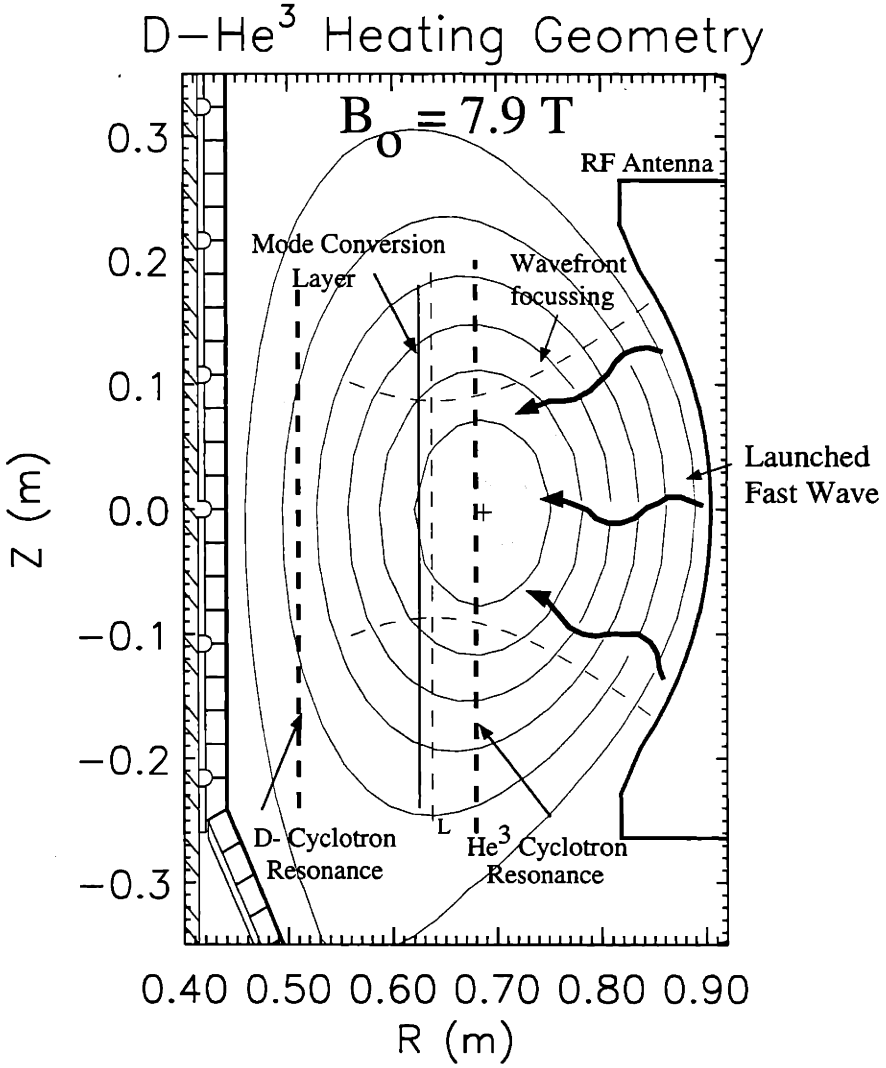

Figure 7-1: Tokamak cross-section showing the approximate locations of the resonances for typical $D-He^3$ ICRF heating experiments. The antenna launches the fast magnetosonic wave which propagates toward the plasma core. It encounters the cyclotron resonance of the minority He^3 ions near the plasma center. Power not absorbed by ions at this resonance is incident on the ion-ion hybrid resonance layer where mode conversion to the ion Bernstein wave (IBW) can occur. Partial reflection of the fast wave also occurs due to the associated $N_{||}^2 = L$ cutoff.

The resonance lies inboard of the He^3 resonance on the high-field side of the tokamak and moves further inboard as the helium concentration is increased. All of the mode conversion data to date for this heating scheme thus correspond to off axis heating. Contours of the cold plasma cutoffs and resonances as well as computed power deposition profiles for fairly high He^3 concentration ($n_{He^3}/n_e \approx 25\%$) are shown in Fig. 7-2, indicating that mode conversion heating was predicted for large minority fractions.

7.2.1 *Standard* operation to date: $3\% \lesssim n_{He^3}/n_e \lesssim 25\%$

During scans to high He^3 concentration in deuterium plasmas at 7.9 Tesla, strong direct electron heating was indeed observed. For strong helium puffing, producing $n_{He^3}/n_e \gtrsim 20\%$, the heating was well off axis, in good agreement with the predictions shown in Fig. 7-2. In Figs. 6-8 and 6-10 the basic analysis analysis techniques used to measure *direct* electron heating were demonstrated. Using these same techniques, further analysis indicated significant direct electron heating down to $n_{He^3}/n_e \approx 3\%$ which represented the minimum concentration used in $D(He^3)$ heating experiments to August, 1996. This result was *not* anticipated and as will be shown below, indicates that minority ion heating is much weaker than originally predicted.

Heating location

Figure 7-3 shows how the position of the peak in the break-in-slope measured direct electron heating profiles was seen to vary as the He^3 concentration was scanned. It should be noted that the GPC can be used only on the outboard side of the the plasma (see §4.5) As the true location of the the expected mode conversion heating moves to *smaller* major radii, the GPC will see the temperature response on the corresponding flux surfaces move to *larger* major radii. That direct electron heating is observed and that the location of the heating follows the ion hybrid resonance and moves off axis as the He^3 concentration is increased, is clear evidence of IBW mode conversion. Also shown in this figure are the positions of the peaks in the mode conversion heating profiles computed using FELICE, a full wave 1-D ICRF modelling code. Although

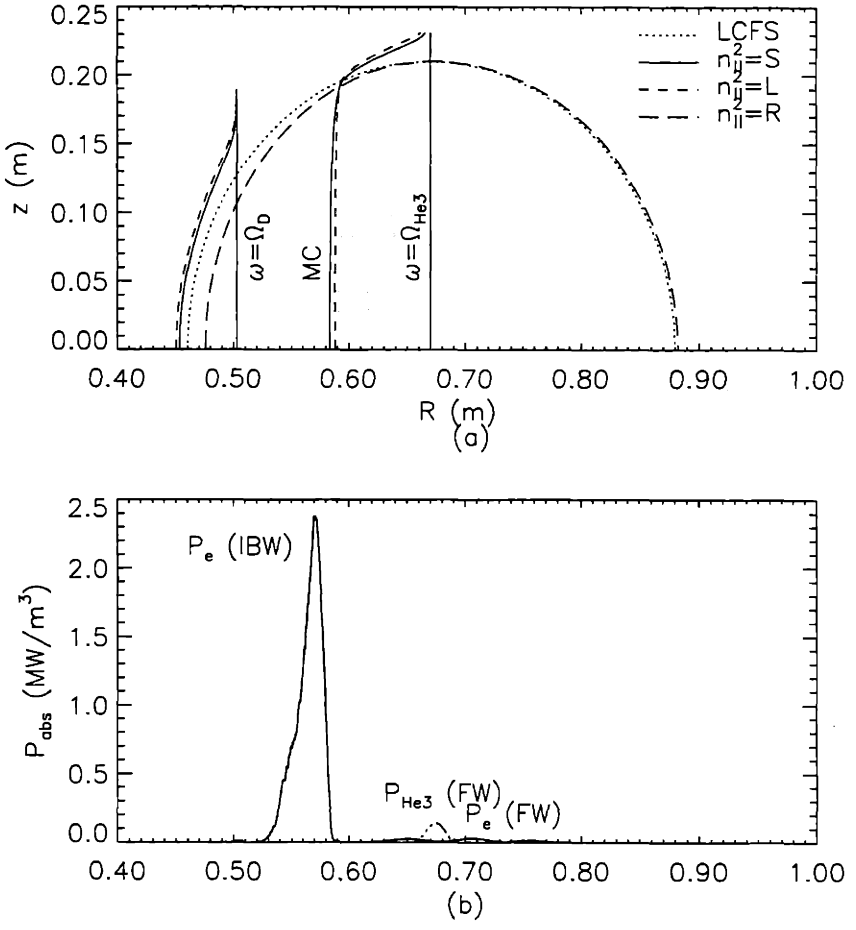

Figure 7-2: Half poloidal cross section of the tokamak showing **a)** the locations of the cutoff and resonance layers as calculated from the cold plasma dispersion relationship and **b)** the corresponding power deposition profile from FELICE for conditions similar to those of shot #960117012 ($B_T = 7.9$ Tesla, $n_e(0) \approx 2.3 \times 10^{20}$ m^{-3}, $T_e(0) = 2$ keV, $n_{He^3}/n_e \approx 25\%$).

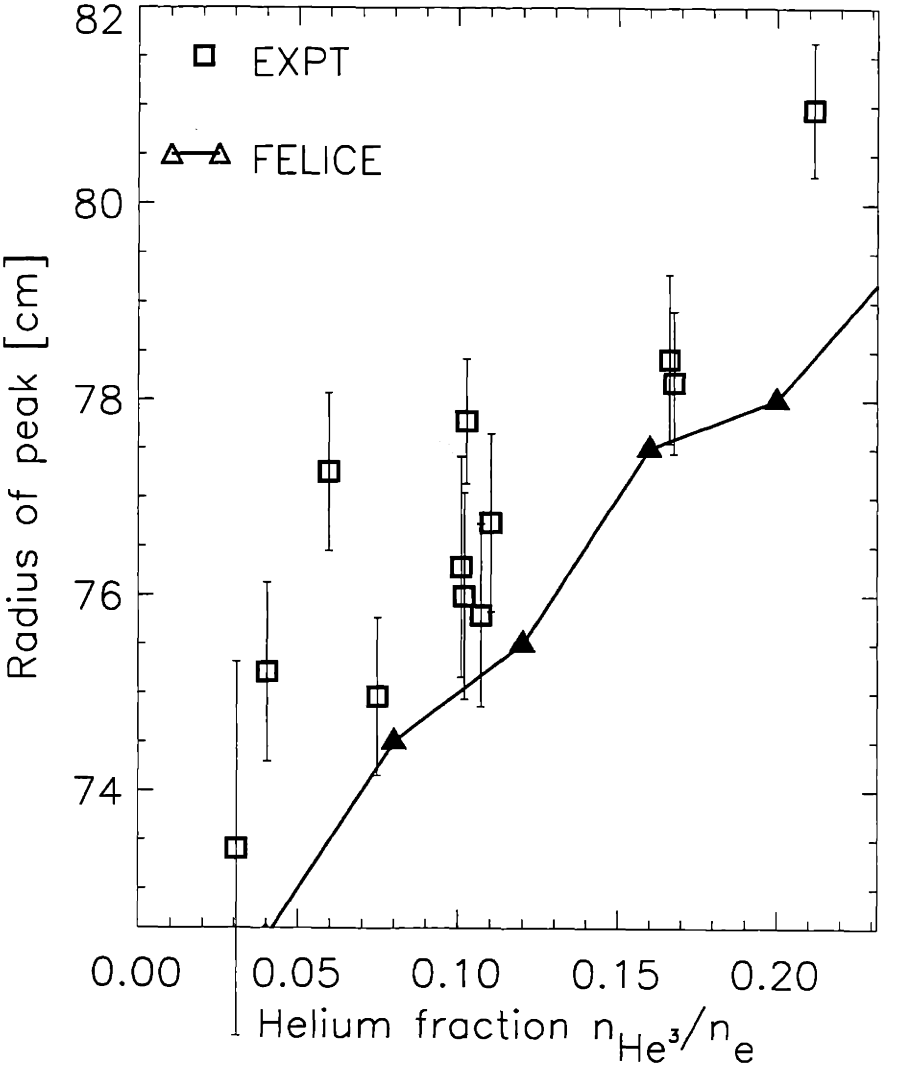

Figure 7-3: Location of the peak of the electron heating profile as a function of He^3 concentration in $D - He^3$ plasmas. Squares correspond to the peaks of measured profiles. Triangles are values calculated from FELICE simulations for similar conditions. Note that the effect of curved flux surfaces is not included in the slab geometry of the simulation and tends to move the peak of the heating to larger minor radii which brings the two calculations into better agreement.

the dependence of the heating location on the He^3 concentration agrees well with the expected behavior, there is a nearly constant discrepancy between the experimental data and the FELICE prediction. Although a $\approx 10\%$ *systematic* underestimate of the He^3 concentration for these shots could explain this difference, a more likely explanation is the effect of the curved flux surface geometry on power deposition (*cf* §5.4.5). This effect is not included in the slab geometry of the simulation of FELICE and moves the positions of the peak in the expected power profiles to larger minor radii, in better agreement with the experimental data. The presence of background levels of hydrogen ion "impurities" in this $D(He^3)$ plasma (see Chapt. 8) is not expected to have significant effect on the heating profile because of the relatively large distance between the hydrogen cyclotron resonance and mode conversion layer ($\Delta R \approx 1.5a$) and because the levels of hydrogen as estimated from charge exchange neutral particles are small ($n_H/n_D < 5\%$).

Heating efficiency

We can also compare the experimental measurements of absorbed power to theoretical predictions. Figure 7-4 compares measurements of the volume integrated break-in-slope power profiles to the corresponding predictions made with standard modelling codes. FELICE can calculate the mode conversion efficiency of the incident fast wave to IBW *for a given set of plasma parameters.* A critical parameter in this calculation is the energy of the minority ion species, here He^3. FPPRF is a Focker-Planck code which solves for the steady state velocity distribution for minority ions under specified heating conditions, and predicts minority tail energies of up to several hundred keV for $D(He^3)$ experiments on Alcator C-Mod. For the theoretical curves of Fig. 7-4, two widely different estimates of the minority energy were used as input to FELICE. The curve with dashed lines and triangles shows the predicted direct electron heating when the FPPRF tail energies are used. Agreement is poor. The solid line and filled triangles show the the FELICE results for the assumption of *no* minority tail, i.e. with the He^3 ions at the bulk plasma temperature. The agreement with experimental measurements is much better in this case. The increased electron heating in this case

results from the narrower doppler width of the cyclotron resonance and reduces the competition of minority ion heating with mode conversion to the ion Bernstein wave. These results indicate that the FPPRF code *over-estimates* the minority ion energy.

7.3 Minority heating results

7.3.1 Low He^3 concentration: $n_{He^3}/n_e \lesssim 1\%$

Because of code predictions (see §7.2.1) and efficient minority heating on other tokamaks, the results of Fig. 7-4 showing relatively strong direct electron heating were somewhat surprising. The typical ion concentration in *standard* $D-He^3$ operation to date has been $n_{He^3}/n_e \approx 5-15\%$. In an attempt to observe stronger minority heating of ions, the minority fraction was reduced. Following a calibration of the He^3 solenoid valve (see Chapt. A), very low concentration ($n_{He^3}/n_e \lesssim 1\%$) heating was attempted briefly on the last day of the 1996 campaign. Heating was observed but the efficiency was low ($\eta_{RF} \approx 15-20\%$) No *prompt* electron temperature response was observed (break-in-slope analysis yielded the data point at the lowest value of n_{He^3}/n_e in Fig. 7-4) indicating that the heating was not due to mode conversion but to minority heating instead. Although minority heating will not produce prompt electron heating, in steady state the electrons near the resonance *will* be heated by collisions with the minority ions. The total electron power density near the plasma core can be obtained by measuring the reheat rate immediately following a sawtooth crash (see §6.3). The difference in the local steady state reheat rates with and without the application of ICRF (appropriately corrected for changes in ohmic power) yields the total power to the electrons due to the external heating. This technique alone cannot distinguish between direct heating from the IBW and power to the electrons from minority ions slowing down. Here (for $n_{He^3}/n_e \lesssim 1\%$) the null result from the break-in-slope technique allows the power to be attributed to minority heating.

For the same shots considered in the previous section, the sawtooth reheat rate

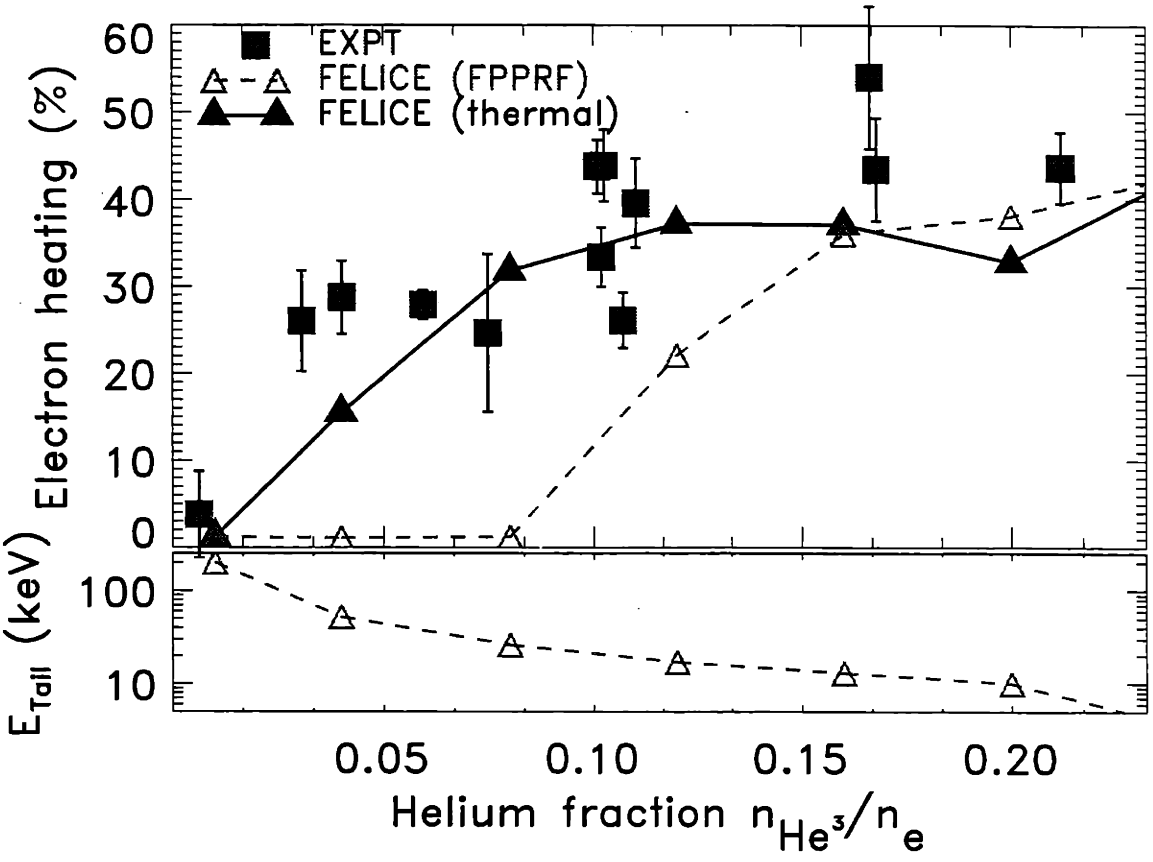

Figure 7-4: Top panel shows direct electron heating efficiency as a function of He^3 concentration in $D - He^3$ plasmas. Squares correspond to the volume integrated break-in-slope power profiles. Dashed triangles are FELICE predictions assuming a radiative boundary condition on the high field side of the tokamak, with $E_{He^3} \approx E_{He^3}^{FPPRF}$ (shown in the bottom panel). Agreement is poor. *Solid* triangles are the FELICE predictions assuming $E_{He^3} \approx T_D$. Agreement is much better.

technique was used to obtain the central electron power density. The results are shown in the top panel of Fig. 7-5. This figure shows that a significant ICRF component to the *central* power density (attributed to minority ion heating at the central cyclotron resonance) is found only at the lowest minority fraction considered. Shown in the bottom panel of this figure are the corresponding FELICE predictions for the minority ion heating efficiencies for the two minority tail models considered previously. The sawtooth reheat technique does not provide a complete power profile from which the total absorbed power can be calculated. Although this means that a direct *quantitative* comparison with theory is not possible in this case, the central power density due to minority heating *is* monotonically related to the total minority heating power. The observed continuous decline of the central power with minority fraction is thus inconsistent with the peak at finite minority fraction of the heating efficiency curve predicted using the minority tail energies as calculated by FPPRF. Together with the results shown in Fig. 7-4 these data indicate that minority heating in the $D - He^3$ scenario is quite weak.

The absorbed power fraction for the two very low He^3 concentration shots was estimated to be $\approx$ 33% from the change in slope of the total stored energy of the plasma in response to turning on the ICRF power. This measurement provides a single experimental point for comparison with theory and is shown by a solid diamond on the lower panel of Fig. 7-5. This absorbed power is significantly higher than the FELICE prediction for thermal minority ions ($\approx$ 10%). This FELICE calculation used a dissipative boundary condition for the ICRF power not absorbed in the first pass through the plasma. In practice, the power not absorbed by minority ions at the plasma core is *not* strongly absorbed by mode conversion heating at this low concentration and so reflections from the cutoff on the high-field side of the tokamak can be significant and lead to further absorption during multiple passes. This effect does not alter the basic shape of the absorption curves however and the conclusions made previously remain unchanged. The amount of data from this minority heating regime in $D(He^3)$ plasmas is currently very limited. The calibration of the helium puffing system which is described in appendix A will allow a more systematic study of

this regime and the details of the cross-over to the mode conversion regime in which nearly all of the heating experiments have been conducted to date.

7.4 Discussion of results

Though the results shown in this chapter were not predicted *a priori* with simulations, proper adjustment of the assumptions used this analysis has been shown to give reasonable agreement with observations. This reflects the complexity of the interactions of ICRF waves with the plasma rather than a failure of the basic theory. Here an attempt to describe the basic principles behind these results is made. To do this it is helpful to compare the results of "minority heating" experiments on Alcator C-Mod to those found on other tokamaks.

7.4.1 Comparison with results on other tokamaks

To establish some context for the results presented in this chapter, a brief description of the results obtained on the PLT [74] tokamak are given here. A more complete picture is obtained if the results from $D(H)$ experiments on both Alcator C-Mod and PLT are included as well. In Chap. 9 it will be seen that in the $D(H)$ scenario, ion cyclotron damping is the dominant heating mechanism and attempts to characterize the resulting hydrogen minority tails are made. Power absorption efficiency can be very high, $\eta_{RF} \approx 60\% \rightarrow 90\%$ [75] as estimated from time resolved measurements of the stored energy (Eq. 6.17). The results for $D(He^3)$ and $D(H)$ minority heating experiments as well as some tokamak and plasma parameters for the two machines are given in table 7.1 [76]. The minority heating results for these two machines seem at first to be at odds with each other. The more efficient heating on PLT was for the $D(He^3)$ scenario, and the opposite is true for C-Mod. Perhaps more striking is the large qualitative difference in the results represented by the relatively strong ($\eta_{ICRF} \lesssim 50\%$) mode conversion heating. These differences can be reconciled by considering the implications of the largely different plasma densities in the two devices. This is discussed below.

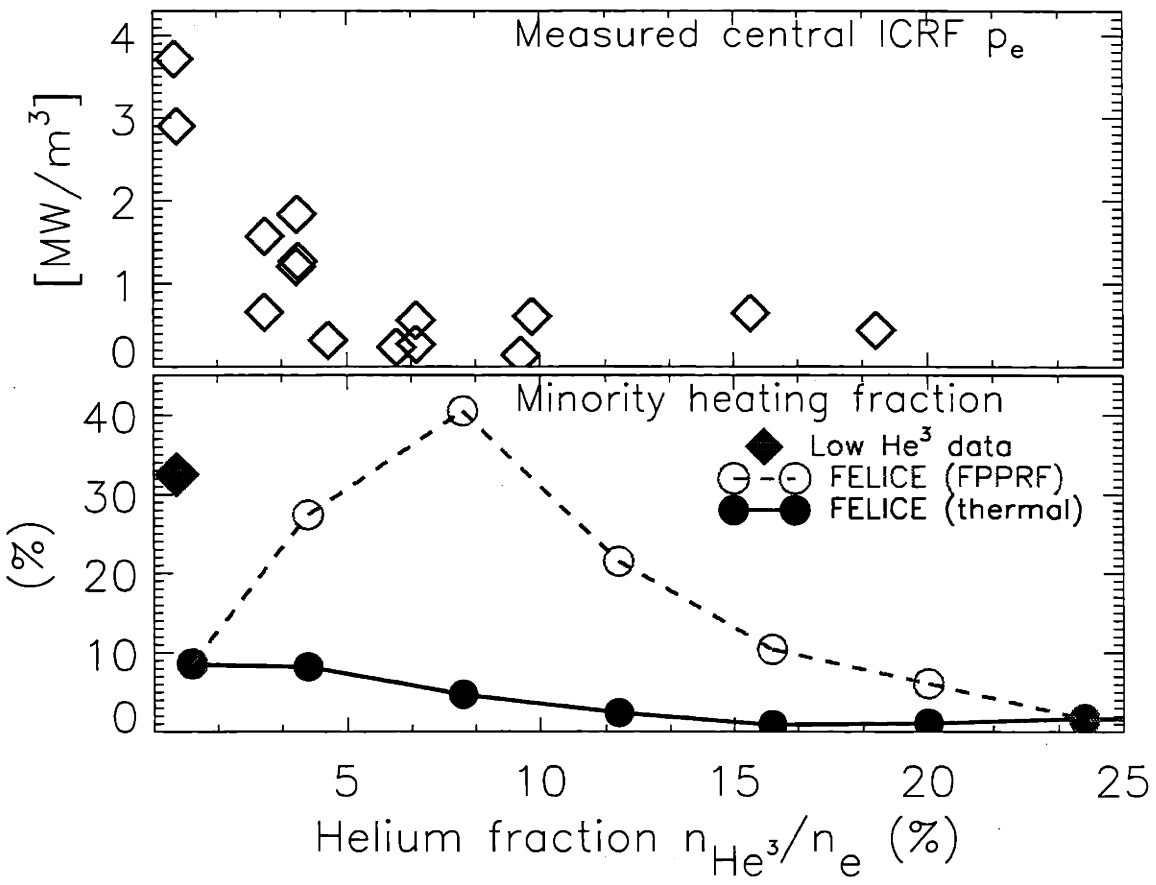

Figure 7-5: Measurements and code predictions pertaining to He^3 minority ion heating for the same data set examined in Fig. 7-4. The upper panel shows the RF component of the central density of power to the electrons versus the He^3 concentration in $D-He^3$ plasmas with the He^3 cyclotron resonance on axis. The increase at very low concentration is attributed to minority heating. The circles in the lower panel show the predictions from the FELICE code for He^3 ions at the the bulk plasma temperature (solid line) and for the tail energies as calculated by FPPRF (dashed line). The monotonic decrease in the central RF power density is not consistent with the assumption of a high energy minority tail.

Parameter	*C-Mod*	*PLT*
Major Radius, $R_0(m)$	0.67	1.35
Minor Radius, a (m)	0.23	0.4
Frequency, f_{ICRF} (MHz)	80	25, 42
RF Power, P_{ICRF} (MW)	2.5	1.5
RF Power Density, $< P >$ (MW/m^3)	3.5	.35
Electron Density, n_e ($10^{20}m^{-3}$)	2.0	0.2
Electron Temperature, T_e (keV)	3	2
Ion Temperature, T_i (keV)	3	$\leqslant 4$
$D(He^3)$ ion heating η loss mechanism	$< 35\%$ mode conversion (!)	$\lesssim 100\%$ –
$D(H)$ ion heating η loss mechanism	$\lesssim 100\%$ –	$\lesssim 60\%$ orbit losses
$F_{Tail} = \frac{<P>T_e^{3/2}}{n_e^2}$ (a.u.)	$\equiv 1$	≈ 5

Table 7.1: Alcator C-Mod vs. PLT "minority heating" results.

7.4.2 Expected minority "tail" energies

As seen in Chap. 3, the *assumption* of a highly energetic minority tail, $E_{Tail} >> E_{crit}$, allows one to give a scaling for the tail energy based on plasma and heating parameters (Eq. 3.11). Based on this scaling, and assuming that the minority fractions are the same on both machines, one can generate a "tail factor", F_{Tail}, which can be used to compare the expected tail energies on the two machines for the same heating scenario:

$$F_{Tail} \propto \frac{< p > T_e^{3/2}}{n_e^2}. \tag{7.2}$$

This factor is given in table 7.1, normalized to the value on Alcator C-Mod, implying that the tail energies on PLT are expected to be ≈ 5 times as high. From measurements of charge exchange neutrals and charged fusion products, minority ion energies between $90 - 200$ keV were detected in both minority heating scenarios on PLT. High overall heating efficiencies were measured in the PLT $D(He^3)$ scenario, while the $D(H)$ heating was significantly less efficient. An explanation of this difference is suggested by the observation of orbit losses of energetic ions from the plasma midplane during $D(H)$ heating, while none were seen during $D(He^3)$ experiments. Examining Eqs. 3.11 and 3.7 shows that the greatest source of difference between the minority

energies for the two heating scenarios enters through polarization effects in $< P >$. Although the integrated power ion cyclotron absorption on PLT was obviously high for both heating schemes, the local power density in the $D(H)$ case can be up to nine times higher. This leads to higher minority energies, higher prompt orbit losses and may explain the decreased efficiency observed on PLT for $D(H)$ plasmas.

Scaling down the tail energies observed on PLT ($\lesssim 200keV$) by the PLT "tail factor" (≈ 5, see table 7.1) gives a rough estimate for the tail energies expected on C-Mod, E_{Tail}(C-Mod) $\approx$ 40 keV. This should be considered an underestimate in the $D(H)$ case on C-Mod because the at these lower average tail energies, prompt ion losses should be small. Dividing by the PLT $D(H)$ heating efficiency corrects for this consideration to first order and predicts $E_{TailD(H)}(C-Mod) \approx 70$ keV. It will be seen in Chap. 9 (Eq. 9-14) that this estimate is similar to estimates of the hydrogen tail energies based on decay times of the ICRF electron heating.

At this point the current working assumption that $E_{Tail} >> E_{crit}$ must be re-examined. Equation 3.10 gives $E_{critD(H)} \approx 50$ keV, and $E_{critD(He^3)} \approx 150$ keV for the Alcator C-Mod. The assumption that He^3 ions are dominated by electron drag is no longer appropriate, and ion drag may in fact dominate. The implications are considered in the following section and are of great importance to the results of this chapter.

7.4.3 Ion drag: the minority tail "burn-through" problem

Assuming $E_{Tail} << E_{crit}$ is equivalent to saying that the drag on minority ions are dominated by interactions with bulk plasma ions,

$$\langle p_{min} \rangle = (E_{min} - T_i)/\tau_{Ei}, \tag{7.3}$$

where $\langle p_{min} \rangle$ is the ICRF *ion* heating power density (*cf* Eq. 3.5), and τ_{Ei} is the energy slowing down time for ions on ions (see Eqs. 3.15 and 3.18). This allows a simple expression to be written which gives the basic scaling of the minority energy with

plasma parameters, or the *low*-energy analog to equation 3.11:

$$(E_{min} - T_i) \propto \langle p_{min} \rangle \frac{E_{min}^{3/2}}{Z_{min}^2 \sqrt{M_{min}} n_{min}} \frac{M_f}{n_f Z_f^2} \tag{7.4}$$

This equation has two interesting properties which are of importance to the considerations of this chapter:

1) The $E_{min}^{3/2}$ dependence gives rise to an interesting dynamic for low minority ion energies. The energy of the minority ions above the bulk ion temperature is proportional to the ion heating power as can be expected, but the energy "gain" from the power is itself a sensitive function of the energy. This indicates that at low energies it is most difficult to impart energy to minority ions and it becomes easier and easier as the energy increases towards E_{crit}. This suggests that there is a critical ion power density required to "burn-through" this initial low energy barrier.

2) The minority species specific dependence of the minority energy scaling for *high* energies, $E_{tail}(E >> E_{crit}) \propto \frac{M_{minor}}{Z_{minor}^2}$, was relatively insensitive to the difference between He^3 and H minorities, with hydrogen giving 33% higher energies. At low energies the result is $E_{tail}(E << E_{crit}) \propto 1/(Z_{min}^2/\sqrt{M_{min}})$. This means that for a given ion heating power density, it is *seven* times more difficult for a He^3 tail to burn-through the bulk ion background than for H.

The energy dependence of the minority ion drag for low energies is shown for $D(He^3$ and $D(H)$ plasmas in Fig. 7-6. This figure clearly shows that the dynamics of minority tail formation at *low* energies is distinctly different for the two heating scenarios. In this figure, the effects of electron drag are also included and mask the "barrier" feature due to ions, which is small for $D(H)$. On lower density machines (or more correctly, for machines with higher "tail factors") this qualitative difference between the two heating schemes disappears as the *high* energy behavior of the ion drag is very similar. The considerations of this section indicate that the properties of Coulomb collisions is of key importance for our experiments and can help explain the distinct nature of the heating seen in the $D(He^3)$ scenario on Alcator C-Mod.

These slowing down dynamics are *independent* of the compounding effects due to

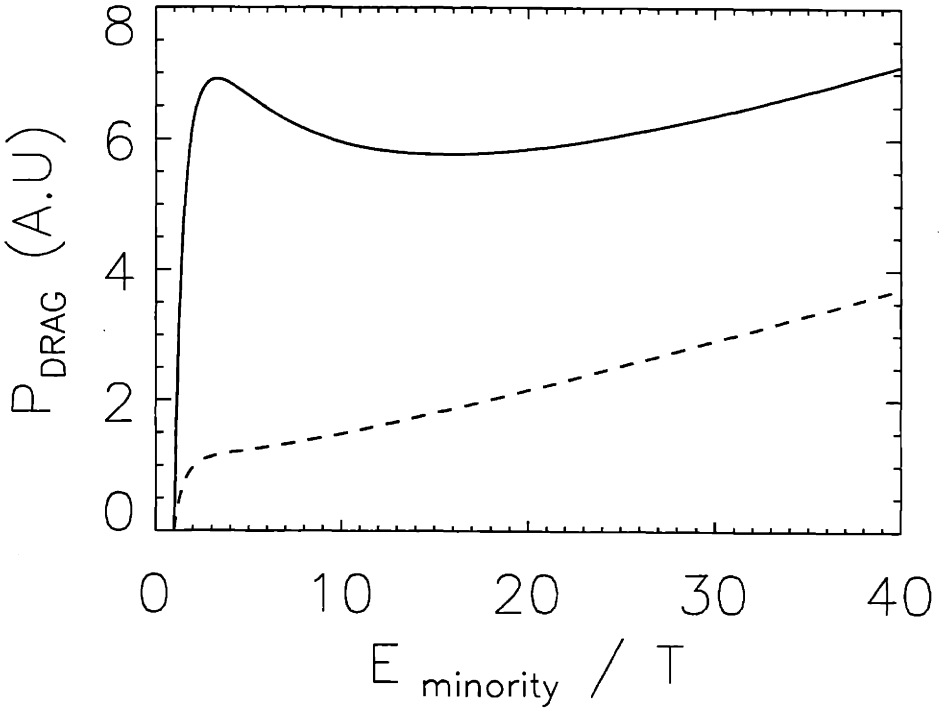

Figure 7-6: Energy dependence of the collisional drag on minority ions at low energies (*cf* Eq. 3.22). The solid curve shows the drag on He^3 minority ions in a background deuterium plasma at temperature T. For the same conditions, the drag on a H minority ion is also shown. This figure clearly shows the low energy power threshold which must be overcome in the case of $D(He^3)$ heating and is of critical importance for the low tail energies seen on Alcator C-Mod.

considerations of the fast wave polarization (see Eq. 3.7). The ion heating polarization is reduced at low minority energies due to a reduction of the doppler width of the minority cyclotron resonance. Although this effect occurs with roughly the same strength for H, and He^3 minorities, the basic strength of the polarization which is modulated is *nine* times weaker in the case of $D(He^3)$ heating (see table 3.1).

7.4.4 Estimated He^3 energies

From the various discussions and observations of this thesis it is possible to make several rough estimates of the He^3 minority energy.

The simple scaling from PLT tail measurements just considered provides an upper bound of $E_{Tail} < 40$ keV because it assumes electron drag levels which is an underestimate below E_{crit} ($E_{crit} \approx 150KeV$, here).

Examining Fig. 7-4 shows that the discrepancy between FELICE predictions and measurements of the absorbed power begin to vanish when the tail energy used in the calculation falls to ≈ 13 keV. This too should be viewed as an upper bound.

Equation 3.27 gives a necessary requirement for mode conversion heating which is sensitive to the minority concentration and $k_{\|}$ of the fast wave. Taking $k_{\|} \lesssim 15\,m^{-1}$ and observing that mode conversion heating efficiency drops towards zero for $n_{He^3}/n_e \lesssim 3\%$, this yields another estimate for the tail energy, $E_{Tail} \approx 12$ keV.

Chapter 8

Results from H(He^3) experiments

8.1 Overview of $H - He^3$ heating experiments.

Most of the dedicated, deliberate mode conversion heating experiments performed on Alcator C-Mod to date have been conducted in $H - He^3$ plasmas. The ion-ion hybrid resonance occurs between the ion cyclotron resonances of hydrogen and helium 3 which, for 80 MHz, are at magnetic fields of 5.3 Tesla and 7.9 Tesla respectively. A schematic diagram of this heating scenario is shown in Fig. 8-1. Equation 3.24 in this case specifies the approximate location for the ion-ion hybrid resonance as:

$$\begin{aligned} \omega_{MC}|_{H-He^3} &= \Omega_{c_{He^3}}\sqrt{\tfrac{6X_{He^3}+3}{X_{He^3}+3}} = \Omega_{c_{He^3}}\sqrt{\frac{3f_{He^3}+3}{3-2f_{He^3}}} \qquad (8.1) \\ \text{Where: } X_{He^3} &\equiv n_{He^3}/(n_H + n_{He^3}) \\ f_{He^3} &\equiv n_{He^3}/n_e \end{aligned}$$

The goal during most of these experiments was to obtain electron heating from mode converted ion Bernstein waves near the plasma center. The typical plasma parameters used to achieve this were an on-axis magnetic field of ≈ 6.4 Tesla, $n_{He^3}/n_e \approx 0.2$, and electron densities $\approx 1.8 \times 10^{20}$ $[m^{-3}]$. Figure 8-3 shows detailed contours of the resonance and cutoff layers as calculated from the cold dispersion relation (which were sketched in Fig. 8-1). Shown below this figure are the power deposition profiles

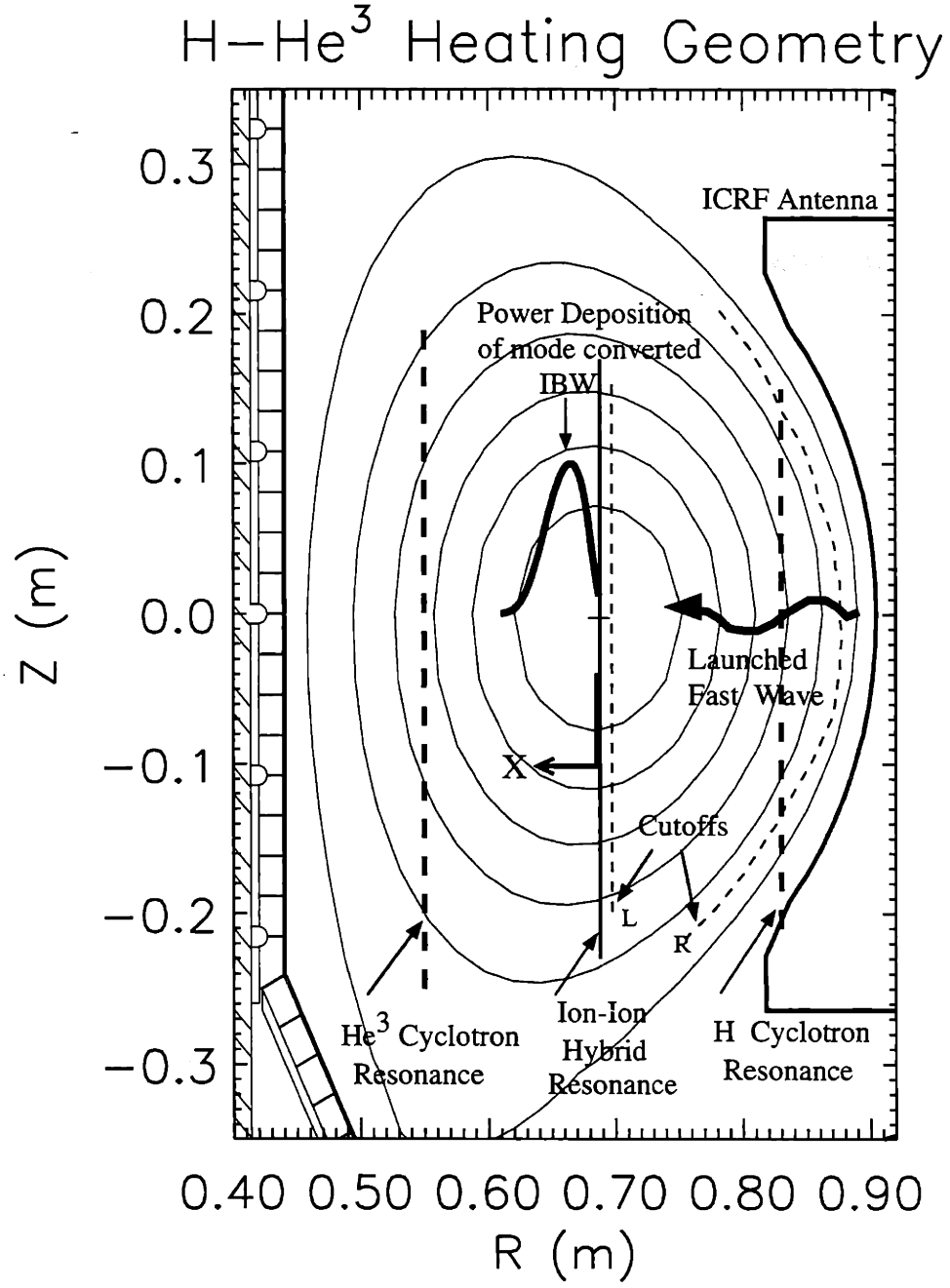

Figure 8-1: Tokamak cross-section showing the approximate locations of the resonances and cutoffs for typical $H - He^3$ mode conversion experiments (for $B_T = 6.5T$ and $n_{He^3}/n_e \approx 0.25$). As indicated, the fast wave must penetrate two cutoff layers to reach the ion-ion hybrid resonance. Also shown is a damping profile for the IBW as calculated in §8.3.

as predicted by the FELICE code [1]. This figure indicates that electron heating can dominate over minority ion heating, and be localized near the IBW mode conversion layer. Well localized power deposition profiles were sought in experiments in order to conduct heat transport studies (see Chapt. 10) in which the ICRF provides an external heat source. $H - He^3$ experiments were conducted during several runs. Early experiments were very promising in this regard. The first experiments were run during the 1995 summer campaign. Figure 8-2 shows that break-in-slope derived power profiles from early results could be localized ($FWHM \approx 0.2\,a$), and yielded record high power densities for Alcator C-Mod ($p_e \gtrsim 25 MW/m^3$). Following a major venting of the machine for routine maintenence, these experiments were repeated during parts of three different run days during the winter 1995-1996 campaign in order to attempt parameter scans for transport studies. Like the earlier experiments, strong mode conversion was routinely achieved with absorbed power efficiencies in the range $25\% \lesssim P_{abs}/P_{launched} \lesssim 80\%$. The location of the heating was observed to depend on the magnetic field and relative ion concentration in good agreement with mode conversion theory. However, these latter runs failed to reproduce the highly localized heating characteristic of the earlier results. The following sections describe and explain the observed differences in these results.

For simplicity in this chapter, I will refer to the run period ending in June, 1995 as the "summer" campaign, and the run period from October, 1995 until March, 1996 as the "winter" campaign. Two days were dedicated to mode conversion experiments in $H - He^3$ plasmas during the summer campaign, as were parts of three run days during the winter campaign. The inner walls of Alcator C-Mod were coated with a boron compound (or "boronized" as is said in the fusion community) midway through the winter campaign. This occured for the first time just *before* the second of the three $H - He^3$ run days of the winter campaign. The significance of this fact is discussed in the following sections.

[1] Slab geometry, full-wave code for integration of the FLR wave equations. Developed by Dr. M. Brambilla (IPP, Garching).

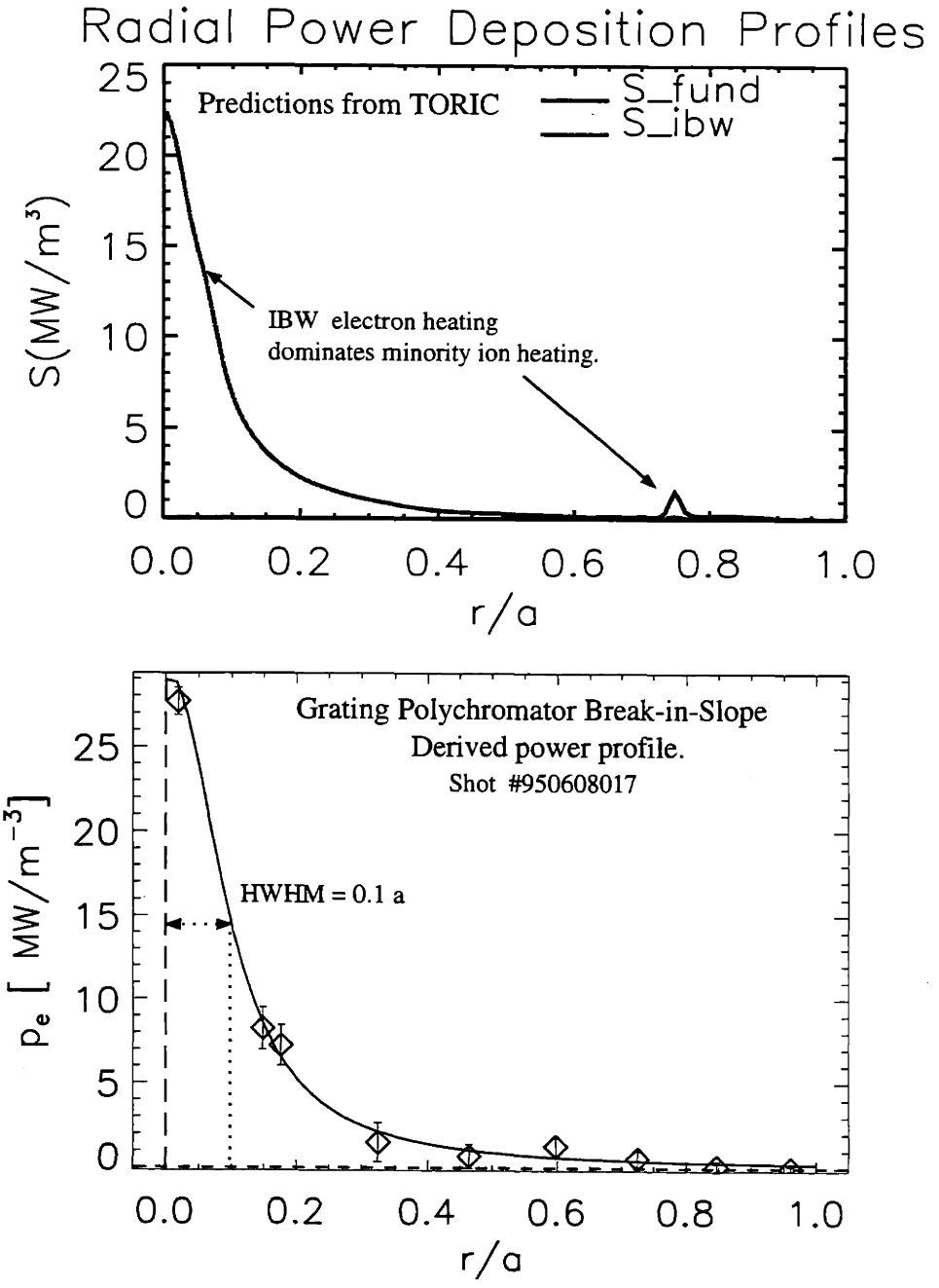

Figure 8-2: Comparison of calculated and measured electron power profiles for $H - He^3$ mode conversion, showing excellent agreement. This result represents a record high power density for Alcator C-Mod.

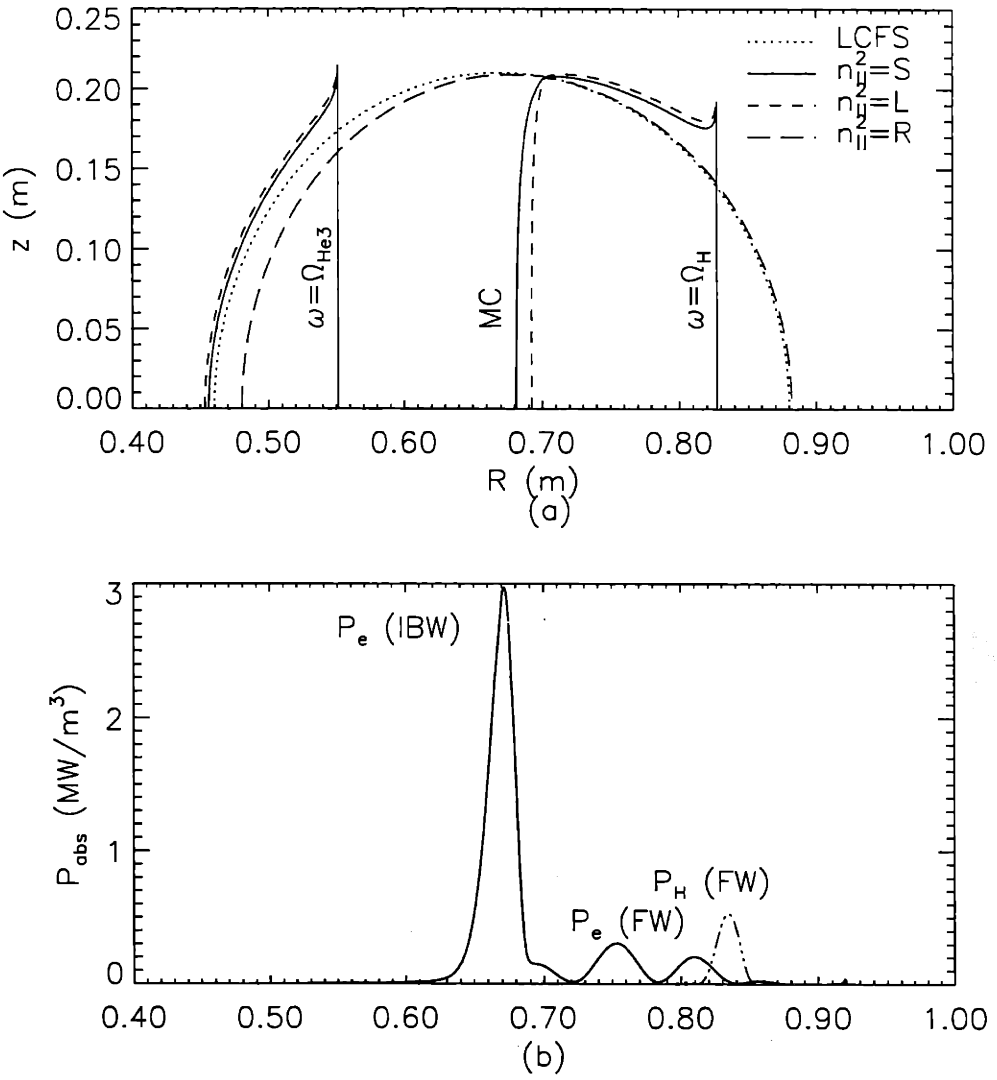

Figure 8-3: Half poloidal cross section of the tokamak showing **a)** the locations of the cutoff and resonance layers as calculated from the cold plasma dispersion relationship and **b)** the corresponding power deposition profile from FELICE for conditions similar to those of shot #950608017

8.2 Observed effects of Deuterium on "$H - He^3$" heating.

8.2.1 Ion-ion resonance shift due to presence of third ion

When attempting to return to the heating results of the summer campaign, it was noticed that less He^3 was needed to obtain centrally peaked electron heating than had been the case earlier. This was later attributed to the presence of greater concentrations of deuterium. In a *three* ion species plasma, cold plasma theory in general predicts two ion-ion hybrid resonances, given by the condition $N_{\|}^2 = S$. For the plasma conditions examined to date the additional resonance created by the presence of small amounts of a third plasma ion is virtual, meaning that it exists at a magnetic field and density not present within plasma. However, the introduced ion species still influences the nature of the *original* ion-ion hybrid resonance. Using Eq. 2.15 one can perturb the two ion solution to the ion-ion hybrid resonance condtion and calculate the change in the ion hybrid frequency caused by displacing plasma species "1" with small concentrations of a third ion species:

$$\Delta\omega_{ii} \approx \frac{X_3}{2\omega_{ii_o}} \left[\frac{Z_3^2/M_3}{\omega_{ii_o}^2 - \Omega_3^2} - \frac{Z_1^2/M_1}{\omega_{ii_o}^2 - \Omega_1^2} \right] / \left[\frac{X_{1_o} Z_1^2/M_1}{(\omega_{ii_o}^2 - \Omega_1^2)^2} + \frac{X_2 Z_2^2/M_2}{(\omega_{ii_o}^2 - \Omega_2^2)^2} \right] \tag{8.2}$$

In general, increasing the fraction of a given ion species moves the ion hybrid resonances *away* from the corresponding ion cyclotron resonance layer. Thus in the case of adding D to a $H - He^3$ plasma, there is a shift towards *lower* magnetic field, as was observed on Alcator C-Mod. Once this effect was recognized, attempts to compensate for the increased presence of deuterium were made by either reducing the helium concentration or reducing the toroidal magnetic field (or both). Figure 8-4 gives measurements of the deuterium fraction as obtained from the charge-exchange neutral particle analyser for runs before and after the summer 1995 maintenance period. On average, the levels of deuterium during the winter campaign were approximately double the concentrations seen during the summer campaign, before the vent, result-

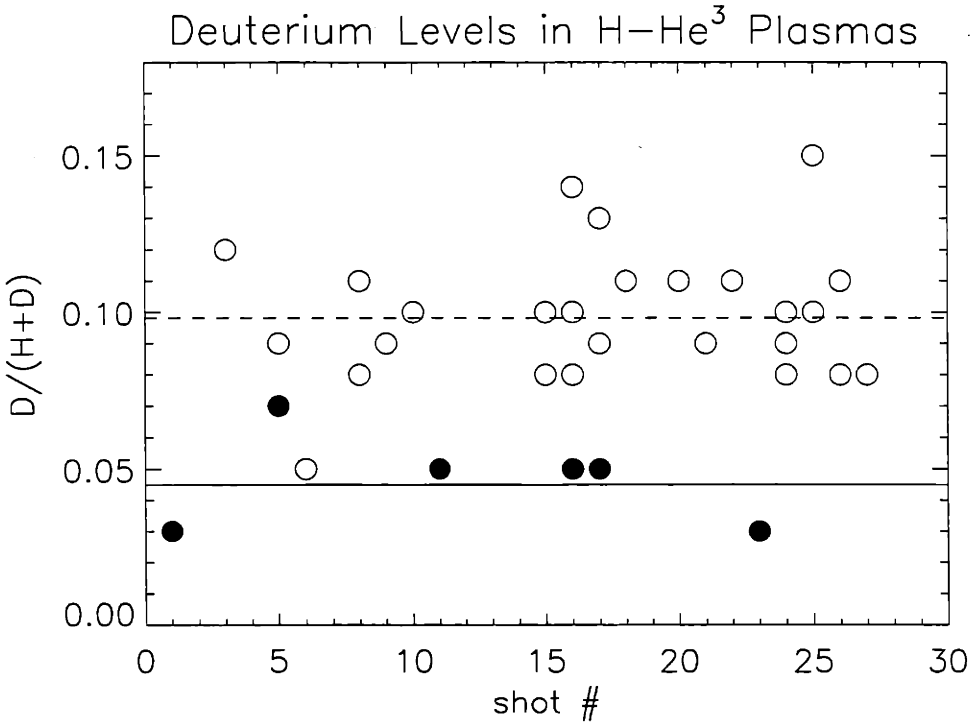

Figure 8-4: Measurements of the deuterium fraction as a function of the shot number for different $H - He^3$ runs. The solid symbols are for shots toward the end of the summer 1995 campaign. The open symbols are from early in the 1995-1996 campaign and show systematically higher levels. Discharge cleaning in hydrogen was performed overnight prior to all runs.

ing in an average outward shift of the mode conversion layer of $\approx 1cm$. Although on average the deuterium level rose, the variation of the concentration during any given run day was high enough to confound attempts to locate the resonance at the plasma center. The following sections will show that the effects of deuterium on the *location* of the mode conversion heating were perhaps of less importance than an unforeseen effect on the damping *width*.

8.2.2 Resonance broadening due to third ion species

The peak power densities during the $H - He^3$ runs of the winter campaign were reduced from previous levels. It was originally thought that this was due to a failure to

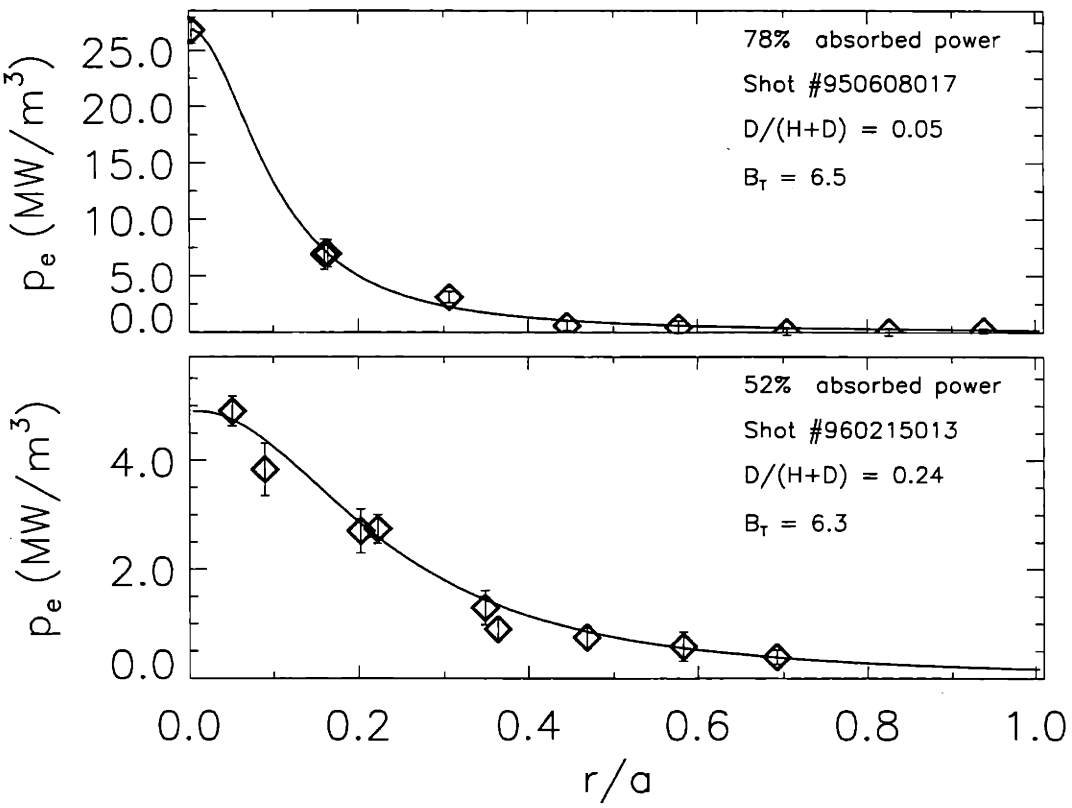

Figure 8-5: Direct electron power deposition profiles for $H - He^3$ discharges with different deuterium 'impurity' levels. For central heating, the effect of deuterium is seen most strongly in the reduction of the maximum power density (notice the different y-axis scales!).

position the resonance precisely on the magnetic axis because of the varying deuterium "impurity" levels. The deposited power is averaged over flux surfaces and the flux surface volume $\propto r$, thus one expects reduced central power density when failing to locate the heating source precisely at the plasma core. However, this effect alone cannot explain the observed peak power density reduction. Figure 8-5 shows examples of measured power profiles for shots with different deuterium concentrations. A small correction to the magnetic field was made for the shot of the lower panel to obtain central electron heating but the plasmas were very similar otherwise. The figure shows that in the higher deuterium fraction case, the central power density is smaller by a factor of $\gtrsim 5$. Figure 8-6 shows the simulated effect of a simple shift of a narrow heating source on the flux-averaged power density. The upper bound on the reduction

of the central power density for profiles similar to those of Fig. 8-5 is only ≈ 2.

Any doubt that another effect was at work in causing lowered peak power densities was removed on the final $H - He^3$ run of the winter campaign. The run of 960215 was intended to allow a carefully controlled parameter scan with modulated heating with profiles suitable for transport studies. Although a complete run was obtained with steady discharges and well modulated RF power, the plasma deuterium levels rose steadily throughout the run, creating an unplanned parameter scan. Figure 8-7 shows the deuterium concentration levels measured as the run day progressed.

Direct electron heating was still observed even at the highest levels of deuterium. The effect on the heating profile shapes was now unmistakeable. Figure 8-8 shows electron heating profiles measured early and late in the day on 960215. The integrated power is about the same in each case but the profile in the high deuterium case is significantly broadened. In each case $n_{He^3}/n_e \approx 8\%$, placing the peak in the heating to the high field side of the magnetic axis. This removes the uncertainty in the estimate of the damping width associated with estimating the precise location of the magnetic axis.

8.3 Deuterium effects on $H - He^3$ heating.

As discussed in Chapt. 3 and shown in the sketch of Fig. 8-1, the IBW is "born" near the ion-ion hybrid resonance from mode converted fast wave energy. For plasma parameters typical of our experiments and $N_{||} = 10$, the hot plasma dispersion relationship can be solved numerically for the ion Bernstein wave root as a function of the deuterium fraction, along the plasma midplane near the mode conversion layer. Having obtained $k_{\perp Re}$ and $k_{\perp Im}$ near the mode conversion layer, the basic damping characteristics of the IBW can be investigated with the simplifying assumption of propagation along the midplane. The general problem of IBW propagation and damping is much more difficult [77] and has been a subject of some debate in the recent past. For the purposes of isolating the influence of deuterium, the complications of a general treatment of propagation are ignored. The damping profile in this case

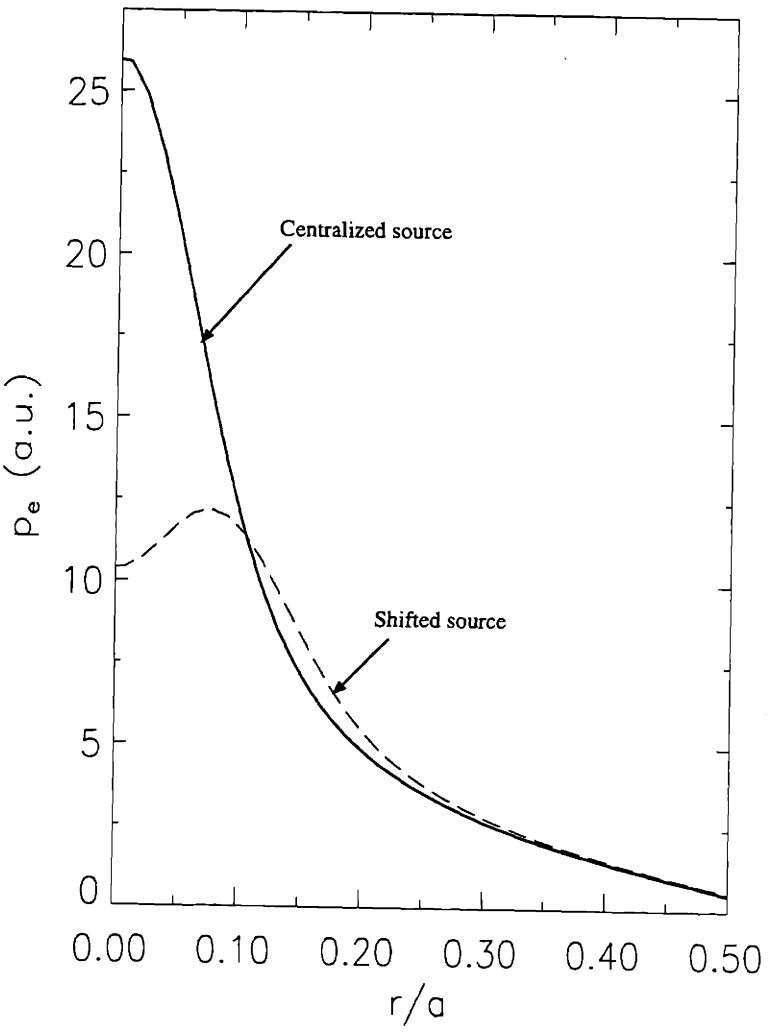

Figure 8-6: Effects of small position shifts on peaked power density profiles. In this simulation, a narrow gaussian heating source is shifted off axis and the flux surface averaged power density profiles are computed before and after the shift. The central power density is seen to drop by a factor of two for a shift of 1.5cm. This shift is large in comparison to the uncertainty in the source *location* due to the influence of deuterium impurities on the mode conversion electron heating $H - He^3$ plasmas. The shift reduces the peak power density by roughly a factor of 2. This result should be compared with the observed deuterium effects shown in Fig. 8-5.

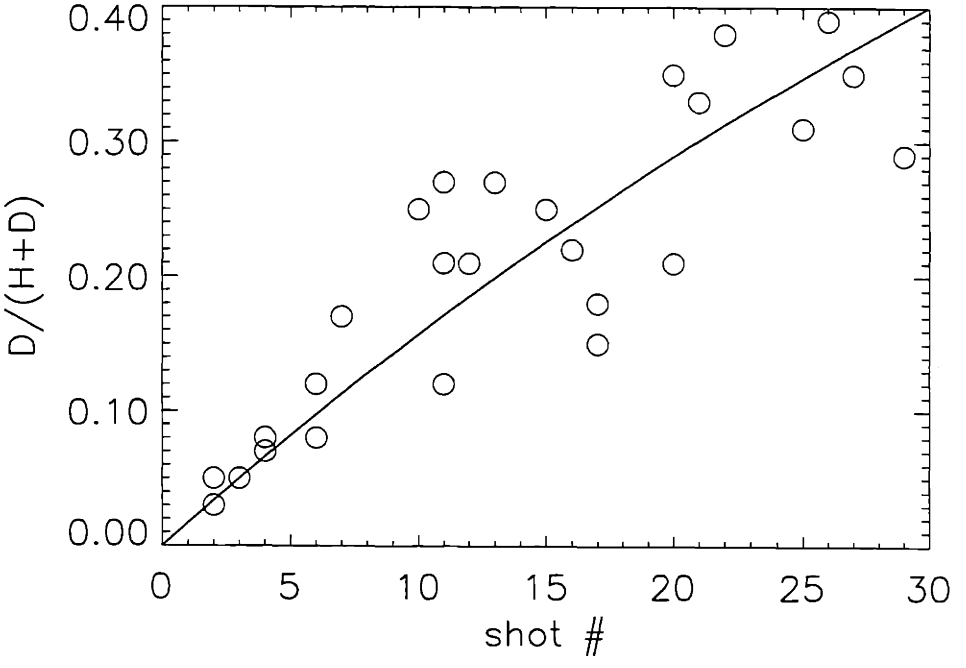

Figure 8-7: Measurements of the deuterium fraction versus shot number for run number 960215. Overnight discharge cleaning in hydrogen produced low levels early in the run. However, the deuterium fraction rose steadily as the day progressed to levels of $\approx 40\%$ late in the day. The vacuum vessel had been boronized 2 days previous to this run.

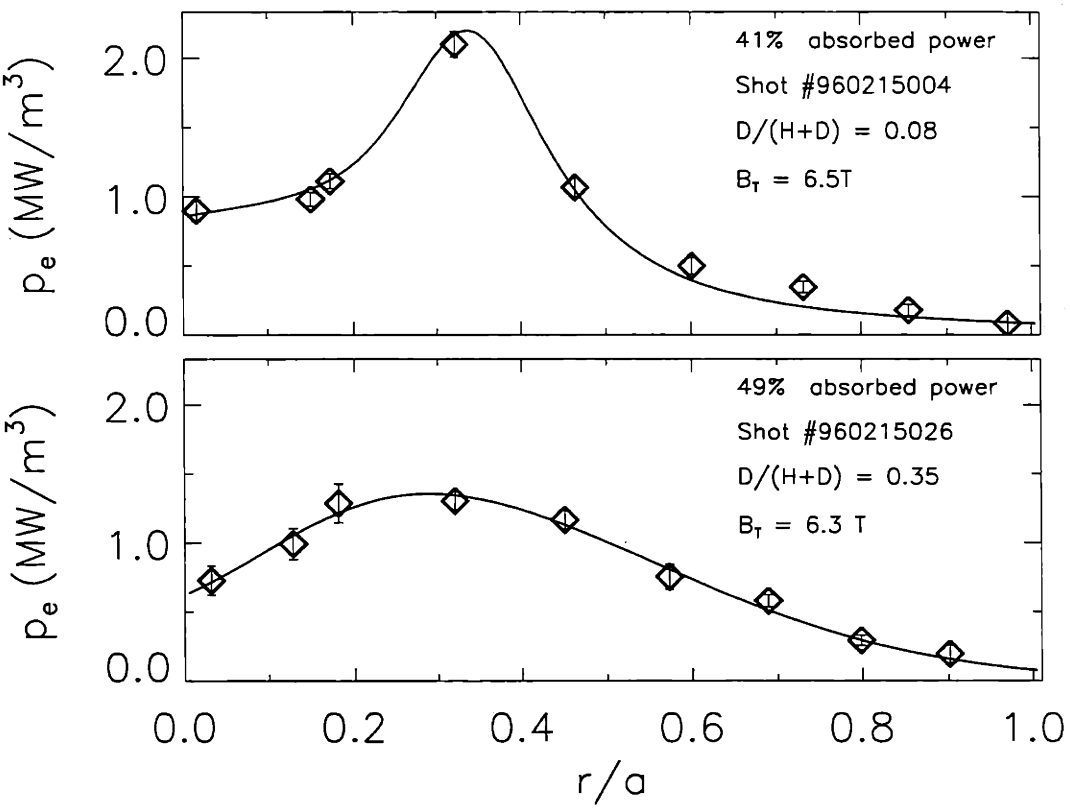

Figure 8-8: Direct electron power deposition profiles for $H - He^3$ discharges with different deuterium 'impurity' levels. The effect of deuterium is seen most strongly in the broadening of the power density profiles. Note that the magnetic field had been lowered in the high deuterium level shot in an attempt to compensate for the shift in the peak of the heating. All other parameters were nominally constant.

is

$$P_{abs}(X) = 2K_{\perp Im}\left(1 - exp(-\int_{R_{MC}}^{R-X} 2K_{\perp Im}(R')\,dR'\ )\right) \tag{8.3}$$

where "X" is the coordinate measuring distance to the high field side of the mode conversion layer as shown in Fig. 8-1.

8.3.1 Resonance shift and profile broadening

Figure 8-9 displays the effects of increasing levels of deuterium impurity on the IBW damping profile as calculated numerically. The solid black curve in each panel indicates the shape of the damping profile as calculated from Eq. 8.3. Also shown in each case are the real and imaginary parts of $k_\perp$. It should be noted that as the deuterium fraction is increased, the resonance moves to larger major radius, as expected. More interesting is the marked increase in the damping length as the level of deuterium increases. This is in agreement with the profile broadening observed in the experiments.

8.3.2 Dependence on the parallel wave number

Although the qualitative behavior of the damping shown in Fig. 8-9 agrees with observations, the calculated profiles are still much narrower than those measured in the experiments (compare with Fig. 8-8). The calculated damping profiles assume propagation along the midplane with a parallel wavevector equal to the nominal value of the launched fast wave, $k_{||} \approx 15m^{-1}(n_{||} = 10)$, as given by Eq. 3.2. As discussed in §3.2, the two-strap antennas on Alcator C-Mod produce power with a continuous spectrum of parallel wave numbers. Simulations for different wavenumbers shown in Fig. 8-11 indicate that the damping width is a sensitive function of $k_{||}$ which *increases* for *decreasing* $N_{||}$, suggesting that $k_{||}$ components *smaller* than the peak in the *vacuum* spectrum can account for the profile widths observed in the experiments. This can be explained in terms of a "filtering" effect of the plasma on the vacuum power spectrum. Figure 8-1 indicates that two regions of cutoff exist between the antenna

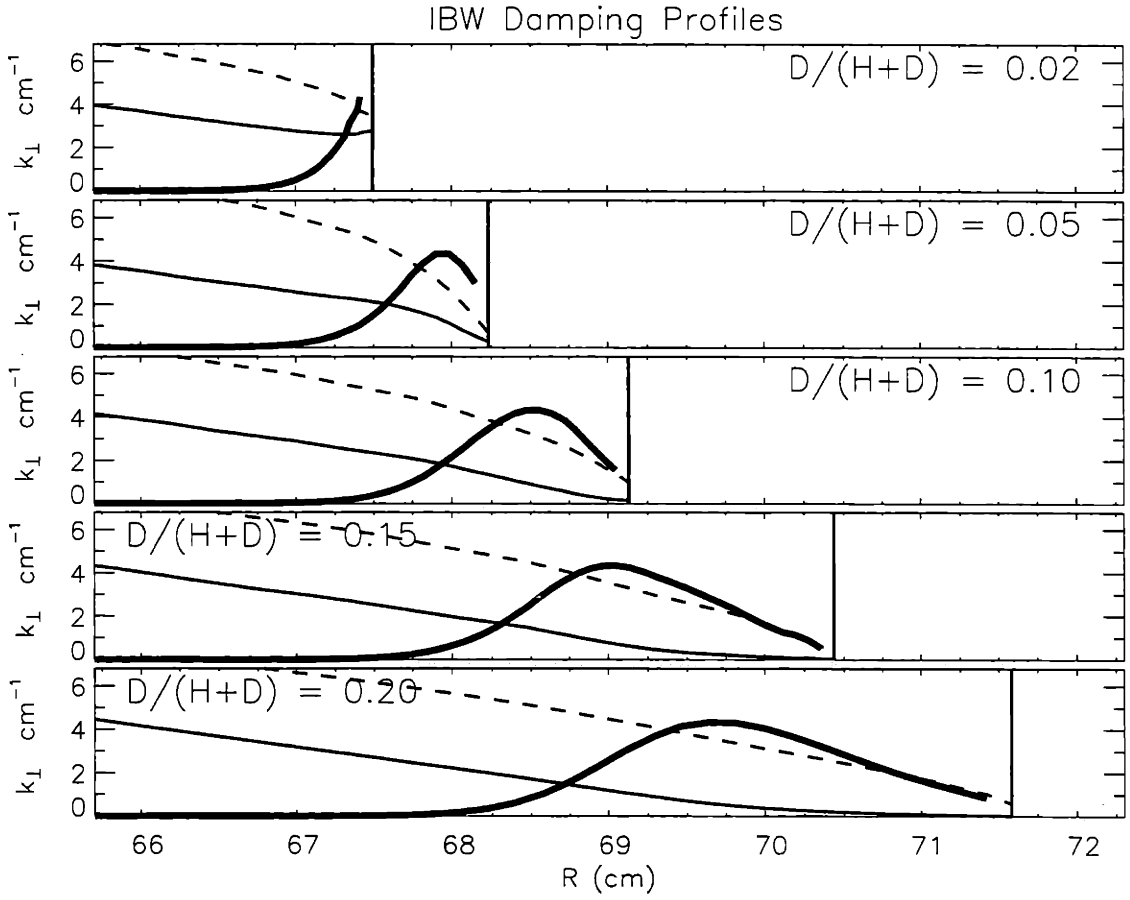

Figure 8-9: Scan of the deuterium concentration showing the broadening of the IBW damping profile. Each panel shows the region near the center of Fig. 8-1. The thick solid curves are the modelled power deposition profile *shapes*. The thin solid line is the $k_{\perp Im}$ and the dashed line is $k_{\perp Re}/3$ as calculated numerically using the hot-plasma dispersion relationship. The vertical line is the location of the cold-plasma hybrid resonance. All calculations are for $n_{\parallel} = 10$, $Te_0 = 2.2$ keV, $ne_0 = 1.8 \times 10^{20} m^{-3}$. The broadening of the profile with increasing amounts of deuterium confirms the effect observed in experiments.

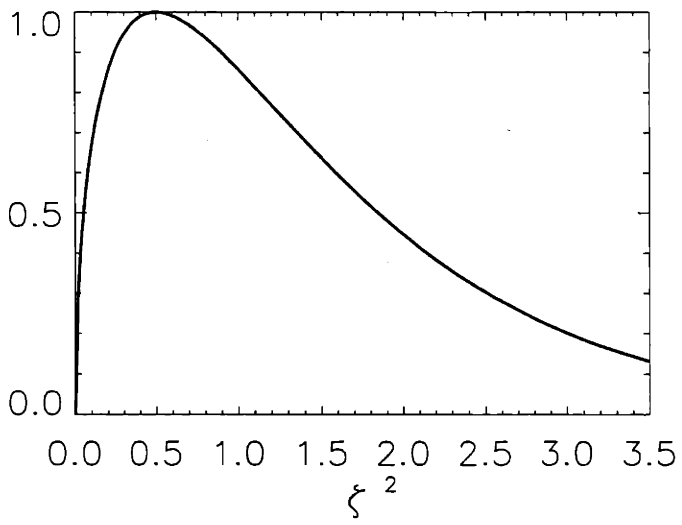

Figure 8-10: Dependence of Landau damping on $k_{||}$. Landau damping is the dominant contribution to IBW power absorption. The damping strength is shown versus $\zeta^2 = (\omega/(k_{||} v_{the}))^2$.

and the mode conversion layer in this heating scenario. The evanescence of fast waves in these regions favors the transmission of *low* $k_{||}$ components of the power spectrum to the mode conversion layer. The inclusion of the finite power spectrum of $N_{||}$ *below* the main peak in the vacuum spectrum shown in Fig. 3-2 results in much broader damping profiles. The additional effect of the finite vertical extent of the wavefields and flux surface averaging adds further broadening in the manner described in detail in §5.4.5. Together these effects predict profile widths in much better aggreement with observations.

Finally, as a rough check on the calculated $k_{||}$ dependence of the IBW damping, compare these results with the basic form expected for Landau damping [15], $k_{\perp Im} \propto \zeta\, e^{-\zeta^2}$, where $\zeta = \omega/(k_{||} v_{the})$. This formula indicates that the strongest damping is expected near $\zeta \approx 0.7$ and begins to drop quickly for large ζ. The sketch in figure 8-10 shows the basic dependence. A convenient formula for determining ζ uses $n_{||} \equiv c\, k_{||}/\omega$:

$$\zeta^2 \approx \frac{250\ keV}{n_{||}^2\ T_e} \tag{8.4}$$

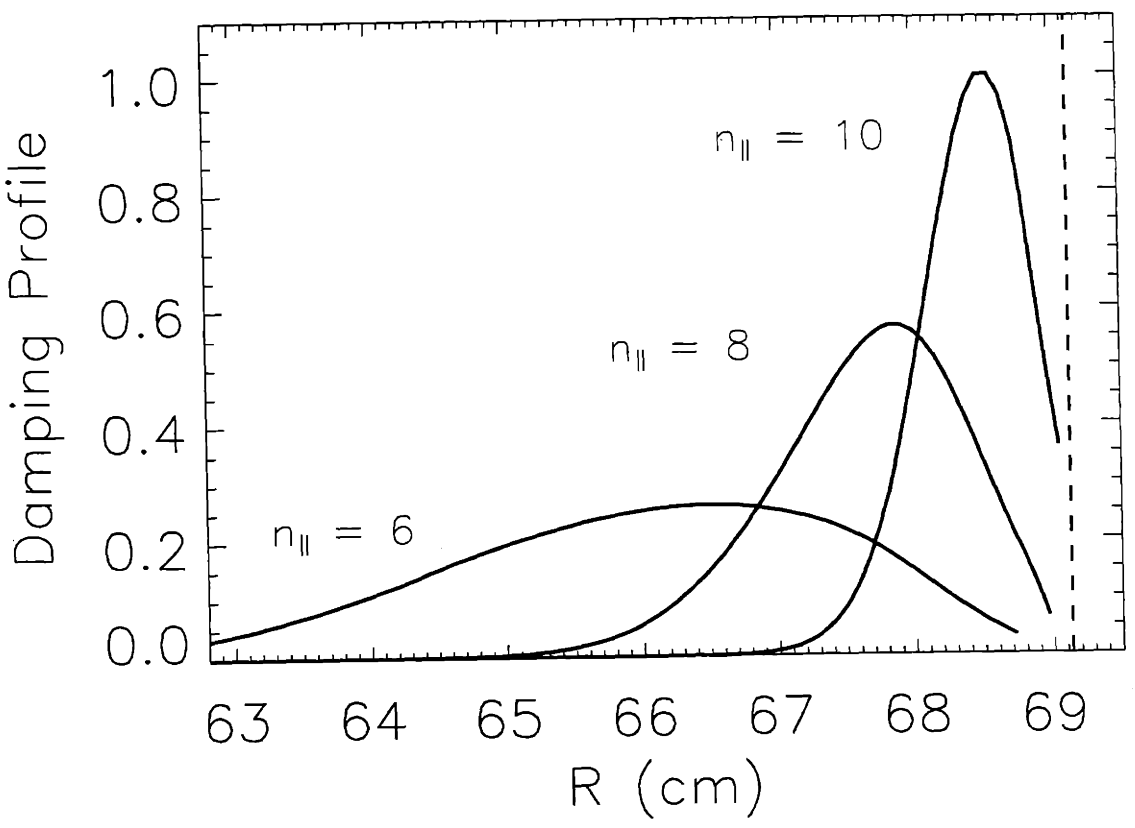

Figure 8-11: Dependence of the damping width on $n_{||}$. For a fixed deuterium concentration of D/(H+D) = 10%, Te_0 = 2.2 keV, $ne_0 = 1.8 \times 10^{20} m^{-3}$, the damping width is indicated for three values of $n_{||} \equiv c\,k_{||}/\omega$.

For the lowest value of $n_{||}$ considered in Fig. 8-11, the above formula yields $\zeta^2 \approx 3$ which indicates Landau damping is at $\approx 20\%$ of its peak strength and is drops quickly with further reductions of $k_{||}$.

8.3.3 Interpretation in terms of the dispersion relation

The ion Bernstein wave damps predominantly on *electrons* through Landau damping and transit time magnetic pumping. These processes depend most strongly on the parallel phase velocity of the waves in relation to the thermal motion of the electrons and should *not* be affected strongly by the presence of deuterium. Introducing deuterium *does* significantly change the propagation of the wave however. To illustrate how wave dispersion can affect the damping profile, we can write a simple

weak-damping expression for the immaginary part of the wave vector:

$$k_{\perp Im} \approx -\epsilon_{Im} / \frac{\partial \epsilon_{Re}}{\partial k_{\perp Re}} = -\epsilon_{Im} / \left(\frac{\partial \epsilon}{\partial \omega} V_{group} \right) \tag{8.5}$$

where ϵ is the complex dielectric constant. In this more formal description, the numerator contains the effects of electron damping while the denominator contains basic dispersion effects such as the group velocity of the wave, $V_{group} \equiv \partial\omega/\partial k_{Re}$. The x-axes in Fig. 8-9 map to frequency and thus the slopes of the $k_{\perp Re}$ curves are inversely proportional to the perpendicular group velocities. The *increase* in the group velocity near the mode conversion layer as the deuterium level is increased strongly contributes to the profile broadening.

8.4 Implications for future experiments

In this chapter we have considered mode conversion heating in three ion plasmas. We have seen that deuterium levels $\gtrsim 5\%$ can significantly affect mode conversion heating in $H - He^3$ plasmas. It is important to note that the presence of "impurity" ions is of significance to ICRF heating only when they introduce a new value of Z/M. Fully ionized states of low-Z impurities have $Z/M \approx 1/2$ and thus produce effects similar to deuterium. Impurities with high atomic numbers *can* remain only partially ionized giving charge to mass ratios *less* than $1/2$. For example, near the core of Alcator C-Mod, Molybdenum has an effective charge to mass ratio of $Z/M \approx 1/3$. The cyclotron resonance layers for such high-Z impurities are even further from the mode conversion layer than that of deuterium, in fact they are out of the plasma even at 7.9 Tesla. Because of this and because the density of these high-Z impurities is so small, their influence on the heating dynamics should be small compared to that of deuterium. The presence of Li^7 as a third ion has been observed to strongly interfere with D-T mode conversion experiments on the TFTR tokamak at Princeton [78]. However, the observed effect of Li^7 was to eliminate mode conversion heating by "parasitically" absorbing power through minority ion heating. The results of this

chapter are distinctly different in that they describe the strong *qualitative* modification of an existing resonance due to the introduction of a non-resonant ion. Although the observed behavior has been seen to be well described by existing theory, this is the first known documentation of such an effect which can have important consequences for future ICRF mode conversion heating and current drive experiments. A brief discussion of these findings in the context of future heating experiments is given here.

Effects of Boronization

Boronization of Alcator C-Mod was undertaken to reduce the levels of high-Z impurity radiation in the plasma by affecting the plasma-wall interaction chemistry. This has been largely successful, though the edge physics and chemistry behind the effect are not fully understood. The experiments in this chapter provide some insight into the effects of boronization on low-Z ions. During the standard operation in $D(H)$ or $D(He^3)$ plasmas, the vacuum vessel walls of C-Mod become "loaded" with deuterium. Despite running electron cyclotron discharge cleaning (ECDC) in Hydrogen overnight before $H - He^3$ runs, the walls retain a significant reservoir of deuterium. Plasma-wall interactions during a discharge can desorb deuterium and effectively replace a portion of the hydrogen. Figures 8-4 and 8-7 suggest that boronization has significantly changed the behaviour of hydrogen isotopes in Alcator C-Mod. The effective wall reservoir of deuterium appears to be have increased with boronization, and the characteristics of Fig. 8-7 may be useful for investigations of the surface chemistry of boronized tokamaks. It should also be noted that there was no observed effect of boronization on the helium levels in these experiments.

Boronization will likely continue on Alcator C-Mod, making it difficult if not impossible to reproduce the results of the summer campaign in the future (Boronization *could* be carried out with B_2H_6 instead of "heavy" diborane, B_2D_6, and extended runs in hydrogen could diminish the wall inventory of deuterium, but neither is currently planned for future Alcator C-Mod operation). Pure, two-ion plasma heating experiments will be restricted to $D - He^3$, where deuterium is no longer considered an impurity ion. Mode conversion experiments for these plasmas have been limited

to off-axis heating in the past. The commissioning of a new 40 MHz ICRF system in the upcoming 1997 run campaign should allow the extension of mode conversion heating experiments to the plasma core.

Current drive experiments

The relatively strong electron damping seen in $D-He^3$ mode conversion experiments is proposed as a mechanism for achieving off-axis current drive in upcoming Alcator C-Mod experiments. A combined minority heating and off axis current drive scenario has been proposed for the $D-He^3-H$ three ion plasmas. The broadening of the IBW damping observed in this chapter may reduce the localization of the mode conversion current drive achieveable in such a scenario.

Chapter 9

Results from D(H) experiments

9.1 Minority tail energy measurements

9.1.1 Introduction and motivation

In Chapt. 3 we saw how measurements of the power to the electron species from the slowing down of the minority tail, $p_e|_{min}$, can in principle provide useful information about the minority tail energy. In this section, issues affecting the experimental realization of this concept will be examined. In particular, the discussion from Chapt. 6 is revisited to determine the circumstances under which the slowing down of minority ions dominates the the electron power balance equation. This method for estimating the minority ion energy is novel and finds motivation on Alcator C-Mod because the standard method of high energy neutral particle analysis [ref hammit] is not routinely possible. The high operating densities on C-Mod prohibit the propagation of high energy charge exchange neutrals created in the plasma center to the edge. In Chapts. 7 and 8, we were able to measure *mode conversion* power profiles effectively from electron temperature measurements. The mode converted IBW damps *strongly* and *directly* on electrons giving rise to large heating power densities that respond *immediately* to changes in the transmitter power. The break-in-slope technique took advantage of both of these properties. In the minority heating scenario, heating profiles are broader and the slowing down time of the minority tail establishes a

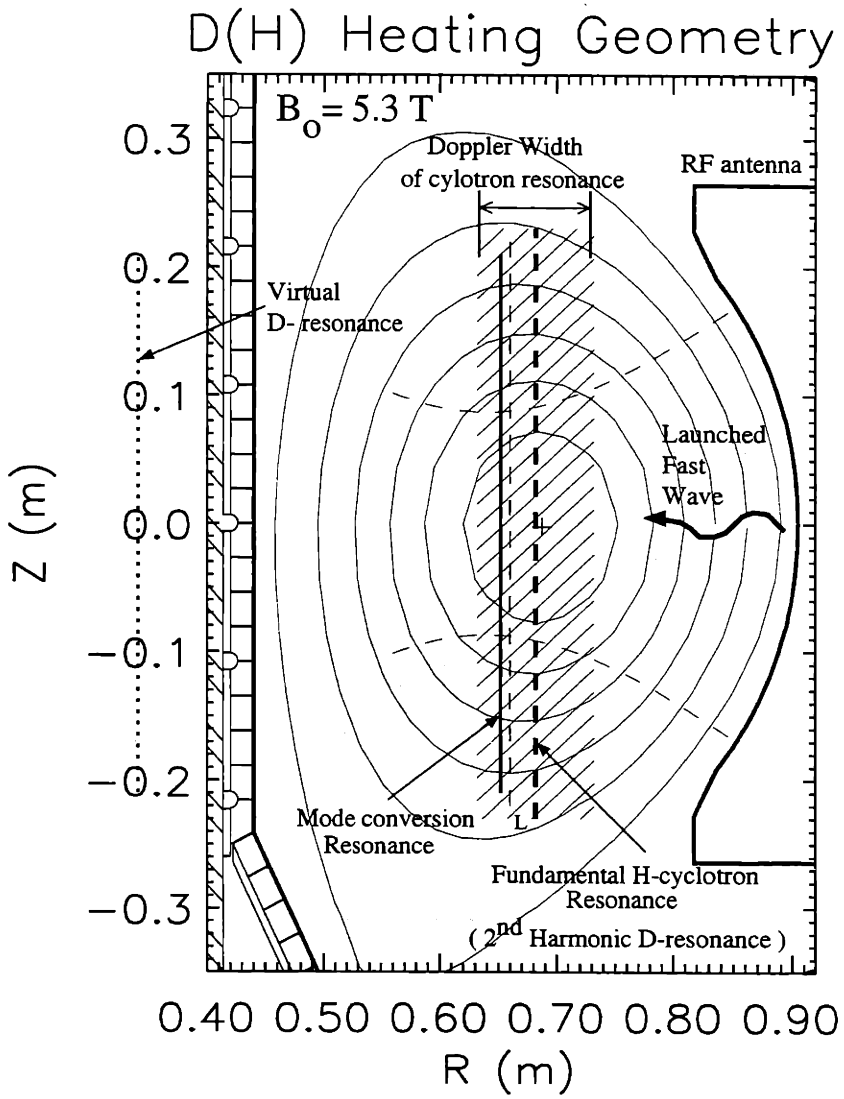

Figure 9-1: Tokamak cross-section showing the relative locations of the resonances for typical $D(H)$ minority heating experiments (for $B_T = 5.3T$ and $n_H/n_e \approx 4\%$). The scale length of the critical region near the tokamak core has been exaggerated to illustrate the relation between the doppler broadening and mode conversion location. The fundamental deuterium cyclotron resonance is outside the plasma.

minimum response time of the heating to changes in the transmitter power. The finite response time reduces the power of techniques based on fast changes in the transmitter power. The broader profiles and the fact that minority ions damp on both ions and electrons reduce the magnitude of the *electron* power. These considerations indicate that minority tail measurements are considerably more difficult than were the studies of mode conversion heating. However, analysis methods described later in this chapter indicate that useful information about minority ion energies can still be extracted.

9.1.2 Inferring $p_e|_{min}$ from $p_e|_{tot}$

The electron power balance equation examined earlier (*cf* Eq. 6.1) is given again here for convenience:

$$\frac{3}{2}n_e\frac{dT_e}{dt} = p_e|_{tot} = p_e|_{ICRF} + p_e|_{ohmic} + p_e|_{\nabla T_e} + p_e|_{rad} + p_{e/i} + \ldots \qquad (9.1)$$

In Chapt. 6 we introduced the use of the "sawtooth-reheat" technique as a method for reducing the effects of energy transport on the total power to electrons, $p_e|_{tot}$. This is of course still valid in the case of minority heating, and central measurements of sawtooth reheat during and after ICRF power in a 5.3 Tesla, D(H) plasma are shown in Fig. 9-6. This figure shows that the ICRF very significantly enhances the electron heating power at the cyclotron resonance. As *increasing* the RF power will if anything *reduce* $p_e|_{ohmic} + p_e|_{rad}$ (radiation *losses* can increase with ICRF power and heating the plasma reduces ohmic power for constant current), and the reheat method allows us to neglect $p_e|_{\nabla T_e}$, we conclude that the ICRF power has increased $p_e|_{ICRF} + p_{e/i}$.

Evidence for mode conversion heating in D(H) plasmas has been obtained in only very special circumstances (see §9.2), so here $p_e|_{ICRF}$ is indirect ICRF heating due to the damping of minority ions on electrons. The minority ions also heat the majority ions and thus we can in general expect a change in $p_{e/i}$, the power exchange between bulk ions and electrons. Without closer analysis, one might conceive of a situation

where the minority ions were heated efficiently but had such a low energy that they slowed down almost entirely on bulk ions. The ion temperature could then increase to large enough values that the ions would begin to lose large amounts of power on the electrons, thus accounting for most of the observed enhancement in the electron power. The form of the electron-ion power exchange term was specified in Eqs. 6.8 and 6.9. These equations can be used to express the temperature difference required to produce a given power flow between electrons and bulk ions (atomic number Z_i and mass unit M_i):

$$(T_i - T_e)_{p_{e/i}} = \frac{2\,\tau_{e/i}\;p_{e/i}}{3\,n_e} \approx 0.28 \;\; (\mathrm{keV})\; \frac{p_{e/i}(\mathrm{MW\ m^{-3}})\; T_e^{3/2}(\mathrm{keV})\; M_i}{n_e^2(10^{20}) \quad Z_i^2} \qquad (9.2)$$

Figure 9-6 shows that the central electron power density is enhanced by *at least* 5 MW/ m^3 during ICRF heating. In order for the bulk ions to be providing *one quarter* or more of this power, Eq. 9.2 indicates that $(T_i - T_e) \gtrsim 2.1$ keV. This hypothesis that bulk ions are providing significant power to the electrons can be checked by examining the central ion temperature, also shown in Fig. 9-6. The ion temperature is in fact shown to be *lower* than the mean electron temperature by $0.6 \rightarrow 0.9$ keV. Conservative estimates of the errors in both the electron and ion temperature measurements can be taken to be $\Delta T/T \approx 15\%$. The maximum ion-electron temperature difference within these error intervals can account for at most 10% of the enhancement of the electron power during ICRF heating, and so we conclude instead that minority ion slowing down dominates the ICRF electron heating in this case. For demonstration purposes, the methods of this section were applied to a series of $D(H)$ shots for which the minority heating was similarly strong. A distinguishing feature of this run day (March 1^{st}, 1996) was that the machine was run with "reversed field". By this it is meant that the directions of both the toroidal magnetic field and the plasma current were reversed from those of the standard operational configuration. This transformation preserves the magnetic field line helicity but changes the direction of the ion "grad-B" drift ($\propto \mathbf{B} \times \nabla B$) so that it is directed *away* from the divertor region. In this configuration, it is much more difficult to achieve H-modes. This is desirable

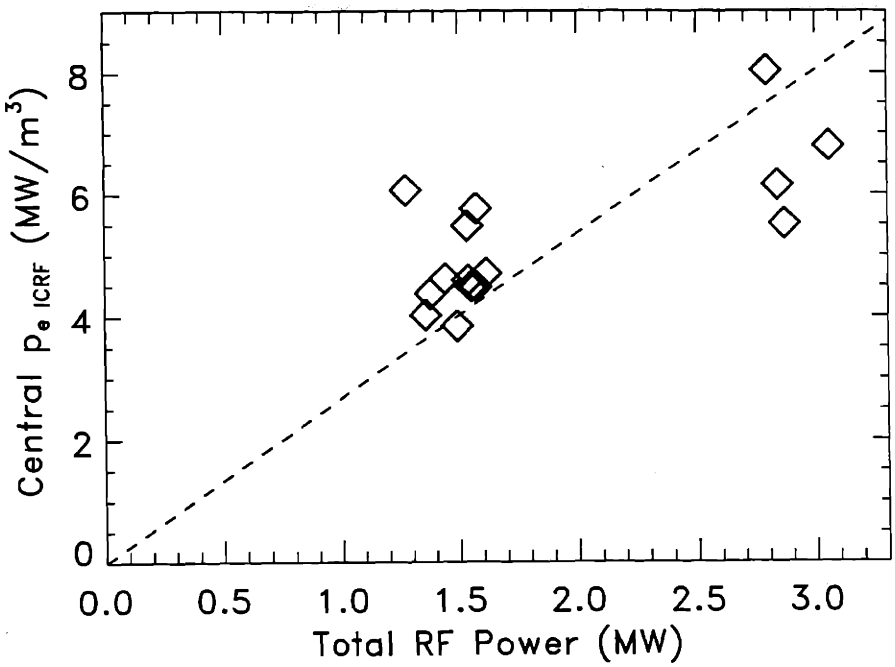

Figure 9-2: Plot showing the central electron power density from hydrogen minority slowing down versus ICRF power for a series of reversed field D(H) heating shots.

for these studies because transitions out of H-mode which often accompany power transitions would create an undesirable additional transient which would be difficult to separate from the decay of the ion tail. Consequently, despite ICRF power levels of up to 3 MW in these experiments, only two discharges achieved H-mode. The hydrogen fraction ($n_H/(n_H + n_D)$), as measured with the neutral particle analyzer near the beginning of the shots ranged from 2% $\rightarrow$ 8%. Figure 9-2 shows the electron heating power density near the plasma center after the estimated contributions from other sources has been removed.

9.1.3 Steady state measurements of $p_e|_{min}$

In Eq. 3.19 we saw that the electron heating power density of the minority tail depends on the product of the minority ion density and the tail energy. Thus, to the degree that the minority ion concentration is known, even a steady state measurement of

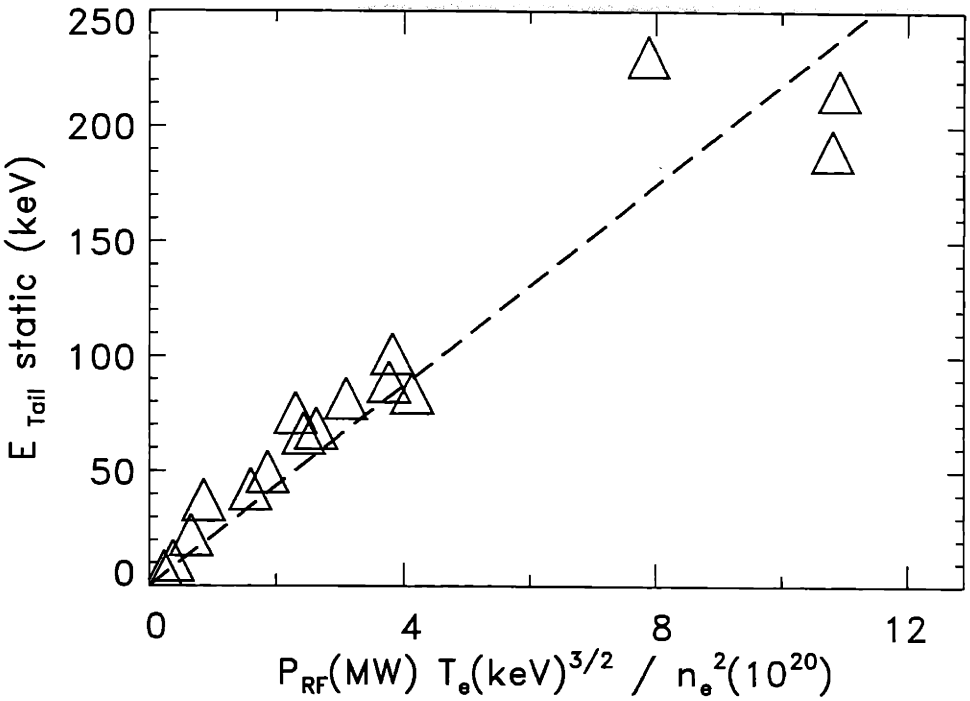

Figure 9-3: Minority tail energies estimated from central reheat powers in D(H) plasmas, assuming $n_H/n_D \approx 4\%$. The data plotted here are the same as in Fig. 9-2 but the x and y coordinates are multiplied by a factor $\propto T_e^{3/2}/n_e^2$.

the minority ion electron heating can provide a measurement of the tail energy,

$$E_{tail} = p_e|_{min}\, \tau_{\epsilon e}/n_{min}, \tag{9.3}$$

where $\tau_{\epsilon e} \propto T_e^{3/2}/n_e$ is the energy slowing down time for minority ion slowing down *on electrons*. The n_H/n_D ratio can be measured from the ration of the hydrogen to deuterium flux seen on the neutral particle analyzer. Signal to noise considerations usually limit this measurement to a brief period early in the shot when the density is still relatively low and temperature is high. An estimate of the energy of minority tails responsible for the heating plotted in Fig. 9-2 is obtained using $n_H/n_D \approx n_H/n_e = 4\%$, the average minority fraction measured by this method. These estimated energies are plotted in Fig. 9-3. Deuterium gas is puffed into the tokamak during the density ramp. Once the discharge is well established, recycling of gasses at the plasma-wall interface can provide a significant gas source and external

puffing must be reduced to maintain the target plasma density. For particularly low target density plasmas, the deuterium puffing was stopped completely. All of the hydrogen in these discharges comes from wall recycling and is not directly controllable. This implies that the hydrogen fractions measured *early* in the discharges most likely provide *underestimates* of n_H/n_e and the tail energies shown in Fig. 9-3 are *overestimates.*

9.1.4 Comparison of E_{tail} values from steady state reheat measurements and FPPRF predictions

The FPPRF (see Chap. 7) code was used to calculate the minority tail energies for the plasma conditions corresponding to each data point shown in Fig. 9-3. Figure 9-4 shows the head-to-head comparison. Though the reheat measurements likely overestimate the tail energy, they consistently fall *below* the FPPRF values. FPPRF does not simulate the effects of sawteeth. Mixing of the fast minority ions during sawtooth crashes would reduce the code predicted energies and produce better agreement with the measured values. It is revealing to examine the scaling of the FPPRF tail energies with plasma parameters. Equation 3.10 indicates that in these plasmas, for $E_{Tail} \gtrsim$ 50 keV the drag on the minority tail is dominated by electrons. In this case, the parametric dependence of the tail energy (*cf* Eq. 3.11) is approximated by [19]

$$E_{tail} \propto \frac{< p > T_e^{3/2}}{n_e\, n_{min}}. \tag{9.4}$$

Figure 9-5 shows that the FPPRF tail energies do not exhibit this expected behavior, especially at higher energies where it is expected. This indicates that there may be a problem with the FPPRF tail energy calculation. The peaks of the radial profiles of the minority energy in these calculations were seen to move back and forth from the plasma center to distances of a few centimeters off axis as the density was varied. This is the cause of very strong variations in the *peak* minority energy which are reduced but not eliminated by averaging over a small region near the center. The variation is most likely due to the formation of standing wave patterns in the wave

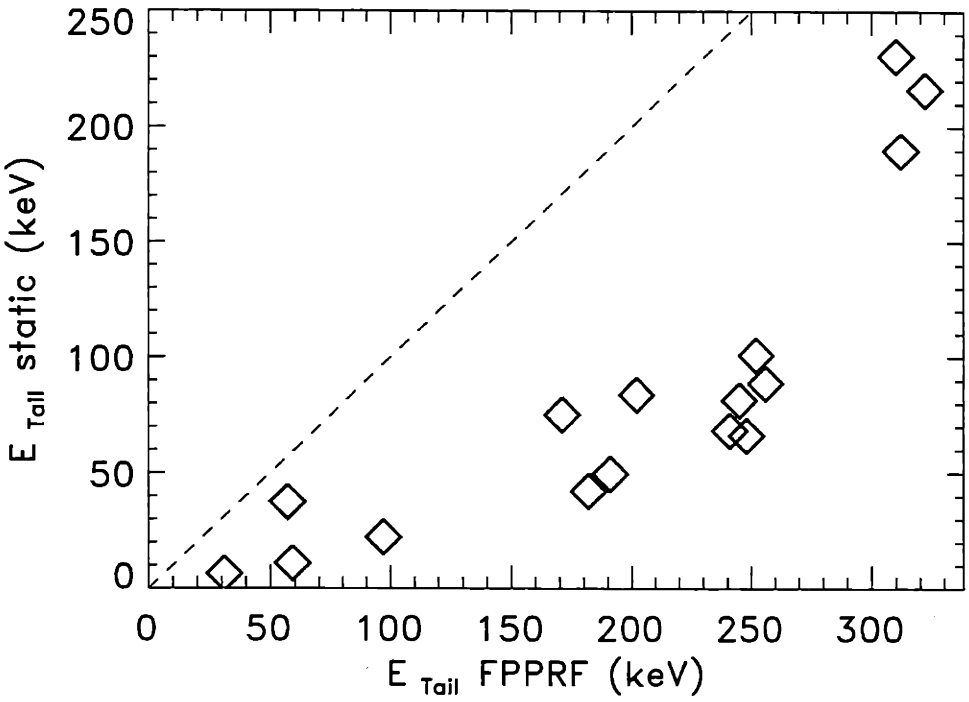

Figure 9-4: Comparison of the minority tail energies, as estimated from central reheat powers and as calculated by FPPRF for identical plasma conditions. Both methods assume $n_H/n_D \approx 4\%$. The reheat measurements are thought to be *overestimates* of the tail energy yet consistently fall *below* the FPPRF values. The dashed curve indicates $E_{FPPRF} = E_{reheat}(4\%)$.

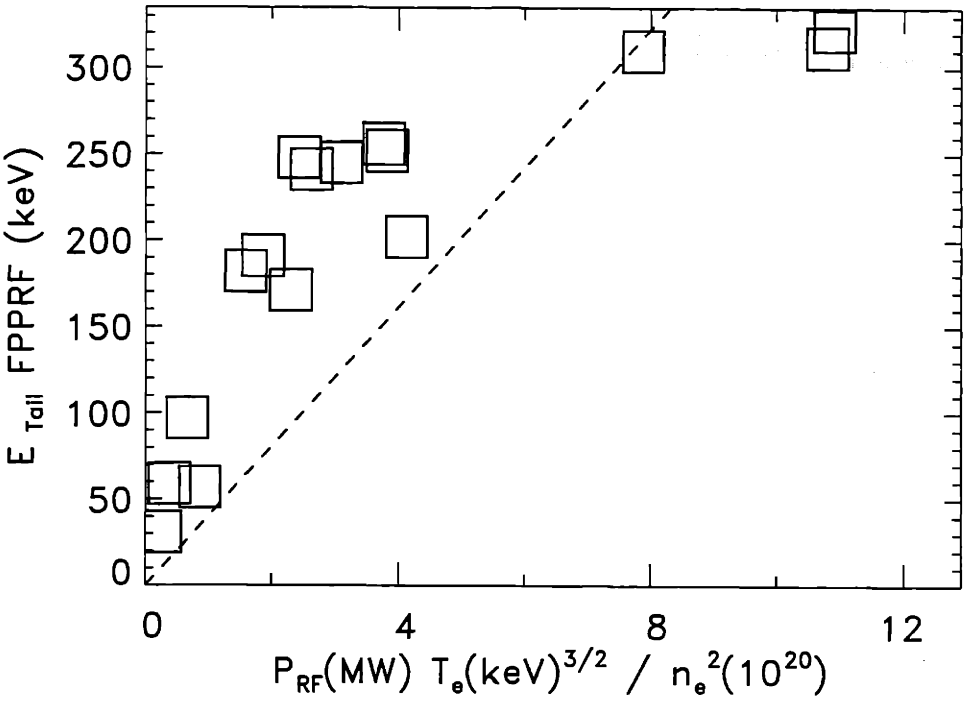

Figure 9-5: Minority tail energies as calculated by FPPRF for the same plasmas conditions of the data in Fig. 9-3,and assuming $n_H/n_D \approx 4\%$. The tail energy is expected to scale as $\propto < P > T_e^{3/2}/n_e^2$ for energies $\gtrsim 50$ keV in which case the points would lie on a straight line from the origin in this plot. The discrepancy is most likely due to changes in the standing wave field patterns as the density is varied. A single value of $k_{||} = 11m^{-1}$ is used in the calculation.

fields from caused by reflected power at the high field side of the antenna. For a single value of $k_{||}$, the peak field intensity (and thus power deposition) will move back and forth as seen as the density is varied. This effect could be reduced or eliminated by convolving the power profiles for a finite $k_{||}$ spectrum. The general result that the FPPRF tail energies are higher than observed in experiments would remain but the scatter in Fig. 9-2 would be greatly reduced.

9.1.5 Transient measurements of $p_e|_{min}$

There are two main reasons why it is also important to study the temporal decay of the electron heating following an ICRF power turn-off:

1. In practice, there is significant uncertainty in the absolute minority ion concentration; the steady state measurements alone cannot uniquely determine both $n_{minority}$ and E_{tail}. Time resolved measurements of the electron heating power can remove this uncertainty. Because the minority ion concentration is roughly constant throughout a shot, the time dependance of the response to RF power transients is determined by the time dependance of the tail energy. Further, the slowing down time of the minority tail does not depend on the minority concentration. Thus the combination of the steady state power deposition and the turn-off transient measurement allow the tail energy to be determined experimentally.

2. We have seen in §6.4 that the instantaneous break in slope of electron temperature traces in response to ICRF power transitions is used to infer direct electron heating in mode conversion experiments. The transient response of the electron heating to a power transition is a strong basis for distinguishing between mode conversion and minority heating. So perhaps an even more important reason to perform analysis of the transient response of the plasma to ICRF power transitions during minority heating is to establish a consistent analysis approach. This dual approach was useful when examining the "cross-over" between minority ion heating and mode conversion electron heating regimes in $D(He^3)$

plasmas as the amount of He^3 was varied.

Figure 3-6 shows that the decay of the mean minority energy, though a result of the weighted sum of the non-exponential decays of ions of various energies, can be reasonably modelled by a simple exponential decay. As the power to the electron species is directly proportional to the instantaneous tail energy (*cf* Eq. 3.19) then, following the abrupt turn off of the ICRF power (at t_0) the power into the electrons can be modelled as:

$$p_e(t)|_{minority} = n_m \frac{E_{tail}}{\tau_{ee}} e^{-(t-t_0)/\tau_{tail}} \tag{9.5}$$

Sawtooth reheat decay method

The sawtooth reheat rate technique, described in §6.3, allows $p_e|_{total}$ to be measured directly. Thus if the portion of the total electron heating that is due to minority ion slowing down can be determined, then we obtain a direct measure of τ_{tail} by fitting its decay to an exponential. An example of the implementation of this technique is shown in Fig. 9-6, which demonstrates the ion tail diagnostic for an example with a particularly long decay time. As the time resolution of this method is on the order of the sawtooth period, its utility diminishes as the tail energy decreases. This is demonstrated in Fig. 9-7. In this higher density case, the decay is faster than the sawtooth period and the method can only make estimates for the *upper bound* of the slowing down time. Figure 9-8 shows a comparison of the experimentally determined energy decay time to that expected for a tail energies estimated using the steady state reheat measurements and and assuming the minority fraction is 4%. It should be noted that the effects of sawteeth on the spatial distribution on the minority ions can be important [79, 80]. In general sawteeth tend to reduce the average minority energy near the center from what would be expected in an non-sawtoothing discharge. This is important to consider when comparing results with those calculated with the FPPRF code, for which no sawtooth model was used. The sawtooth reheat method is sensitive to the *minimum* of the central minority energy and localized heating that occurs during each sawtooth will in general result in a time averaged energy which is

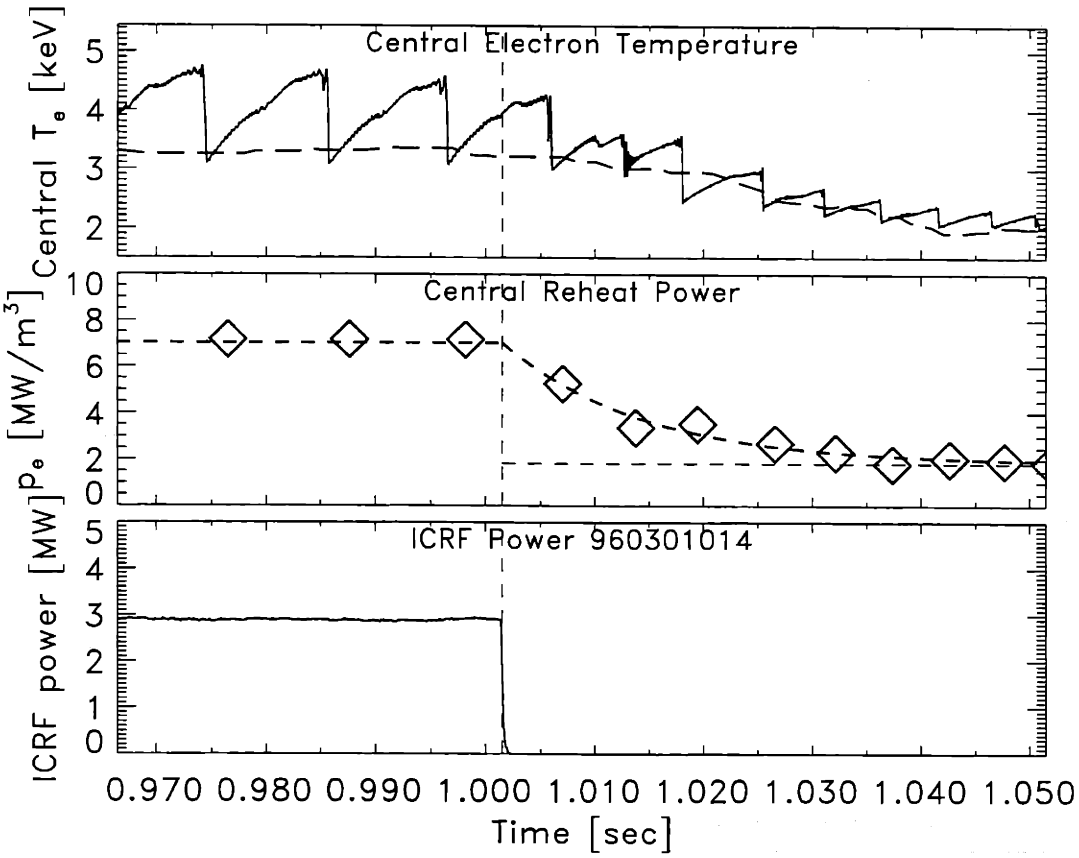

Figure 9-6: Time history of the central sawtooth reheat rate following ICRF turnoff. The top panel shows several sawtooth crashes on the central electron temperature (the dashed line is the central ion temperature from neutron measurements). The bottom panel shows an ICRF power transition. Plotted in the middle panel are electron heating power densities derived from the reheat slopes following each sawtooth crash. The thick dashed line represents the best fit of the decay of this power from the steady state value during the rf, to the steady ohmic value (shown with the faint dashed line). The best fit decay constant yields $\tau_{tail} \approx 13$ msec. The central electron density at this time was $n_e = 1.4 \times 10^{20} m^{-3}$, and $n_H/n_e \approx 4\%$.

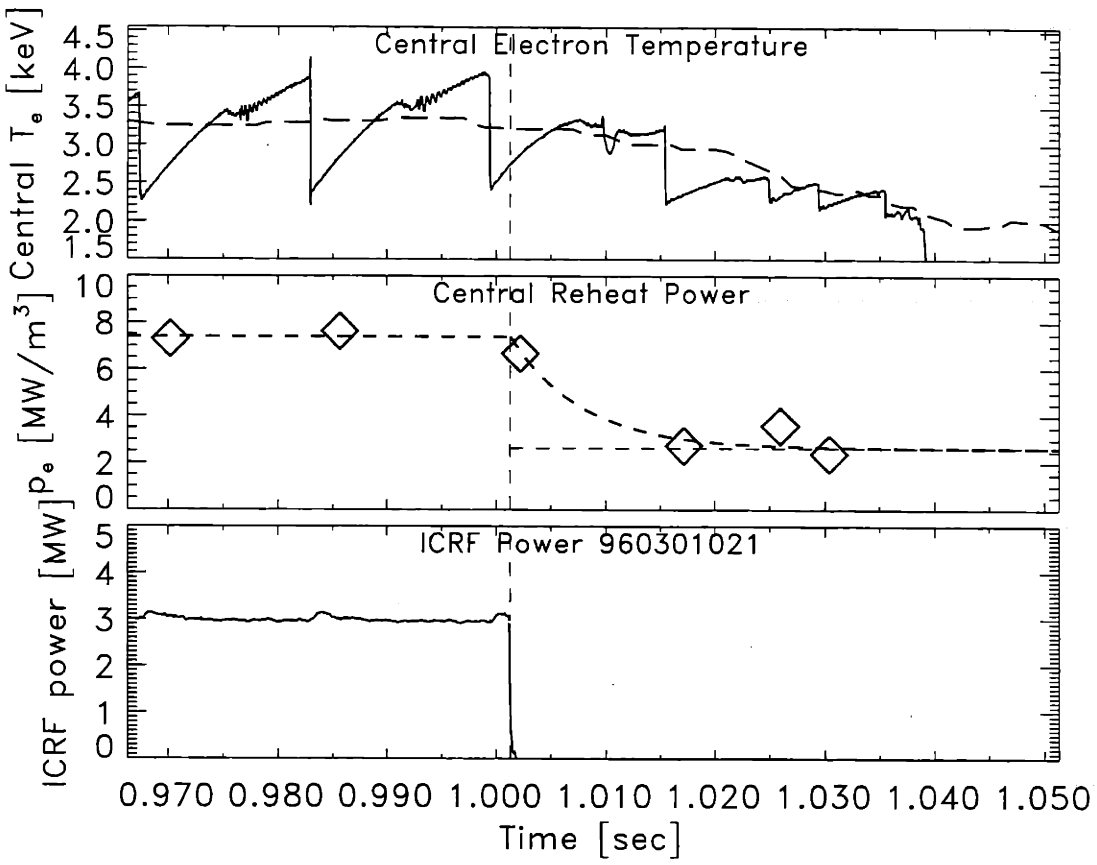

Figure 9-7: Time history of the central sawtooth reheat rate following an ICRF turnoff. The top panel shows several sawtooth crashes on the central electron temperature (solid line) and the ion temperature measured from the neutron flux (dashed line). The bottom panel shows the ICRF power transition. Plotted in the middle panel are the electron heating power densities derived from the sawtooth reheat. The thick dashed line represents the best fit of the decay of this power due to minority ion slowing down. The limited time resolution of the measurement allows one to make the statement that $\tau_{tail} < 6.5$ msec. The central electron density and minority ion fraction were $n_e = 2.0 \times 10^{20} m^{-3}$, and $n_H/n_e \approx 4\%$, respectively.

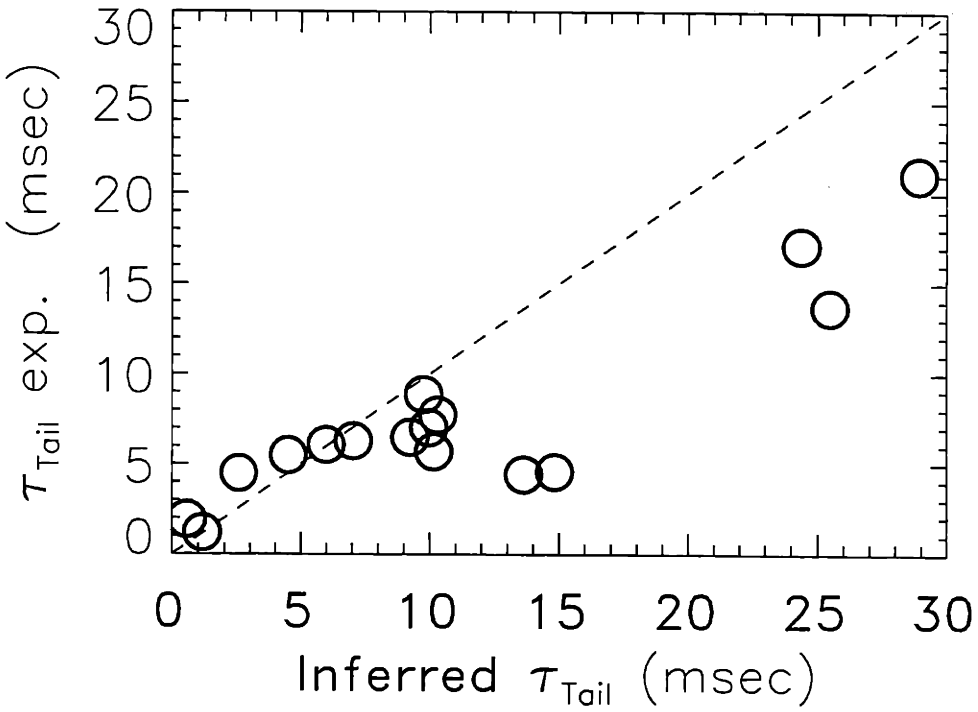

Figure 9-8: Comparison of the experimentally determined minority tail decay time with that calculated from theory assuming the energies of the minority ions at the time of the power transition obeyed the Stix distribution calculated for similar plasma conditions using Eq. 3.8 and a minority fraction of $n_H/n_e = 4\%$. The decay of the sawtooth reheat power was used to obtain the experimental results here. Underestimates of the minority fraction can explain the general overestimates of the predictions at the longer decay times.

higher than that measured with this technique.

Sawtooth droop method

Motivated by the desire for better time resolution on the minority ion decay, to investigate the possible effects of the sawteeth on the minority ions, and to make contact with the analysis which will be used to analyze mode conversion heating, another technique has also been developed. The sawtooth reheat rate allowed the electron power density to be measured directly at discrete times by measuring the *time derivative* of the central temperature following a sawtooth crash. A more general approach is to recognize that the entire time history of each sawtooth rise is in some sense an integral of the local electron heating. Of course thermal transport and sporadic MHD activity are convolved also into the power balance. However in cases where the steady state behavior of the sawteeth is well behaved and reproducible, we can attribute the *deviation* of the temperature trace from the steady state sawtooth wave-form as representing the integrated difference in the local electron heating. Let the time trace of the temperature evolution of a single sawtooth period be denoted by $T_e^{ST}(t)$. The governing differential equation can be written in the form of equation 6.1. The working assumption behind this technique is that the *difference* between the sawtooth in which the power transition occurs and that of the sawteeth during steady state ICRF is determined principally by the change in the minority ion heating. The corresponding mathematical statement describing the technique is that to leading order:

$$\begin{aligned} \frac{3}{2} n_e \frac{d}{dt} \Delta T_e^{ST} &\equiv \frac{3}{2} n_e \frac{d}{dt} \left(T_e^{ST}\big|_{Transition} - T_e^{ST}\big|_{S.S.} \right) \equiv \Delta\, p_e|_{tot}\,(t) \\ &\approx \Delta\, p_e|_{minority}\,(t) \end{aligned} \qquad (9.6)$$

Upon turning off the ICRF power, the power density due to minority ions slowing down on electrons is assumed to decay away exponentially so that

$$\Delta\, p_e|_{minority}\,(t) = p_e|_{minority}\,(t_0) \left[\, e^{-(t-t_0)/\tau_{tail}} - 1 \right] U(t-t_0) \qquad (9.7)$$

Here $U(t-t_0)$ is the Heavyside step function. The temperature deviation from steady state sawtooth behavior is obtained by integrating the above equation and we obtain:

$$\Delta T_e^{ST}(t) = -\frac{2\ p_e|_{minority}(t_0)}{3\ n_e}\left[(t-t_0)+\tau_{tail}\left(e^{-(t-t_0)/\tau_{tail}}-1\right)\right]U(t-t_0) \quad (9.8)$$

This procedure is illustrated in Fig. 9-9 for the same power transition shown in Fig. 9-7 for which the resolution of the previous method was stretched to the limit.

Comparison of transient measurement techniques

The two methods (reheat decay and sawtooth droop) for estimating the minority tail energy by measuring power turn-off transients are complementary. The sawtooth reheat method relies on multiple sawteeth to estimate a decay time and is thus limited by the sawtooth period in the minimum value it can reliably measure. The sawtooth droop method works within a single sawtooth and thus has limited power for very long decay times. In addition, by its nature, the latter technique is unaffected by the potentially dramatic effects of the sawtooth crash on the distribution of minority ions. For a subset of the shots analysed on the above run day, both techniques provided usable results. These shots provide a valuable comparison of the two techniques. Figure 9-10 makes this comparison. It should be noted that the shots included in this figure are by definition near the margin of the applicability for either or both of the methods. In this sense this is a worst case comparison. That the data lie around the line of unity slope is some indication that sawtooth effects on the minority redistribution are small.

9.1.6 Combining steady state and transient methods

The previous discussions have established the elements of a new technique for minority ion energy. It is based solely on measurements of electron temperature. This may sound improbable at first, so here the methodology is presented step by step with references to previous discussions where necessary:

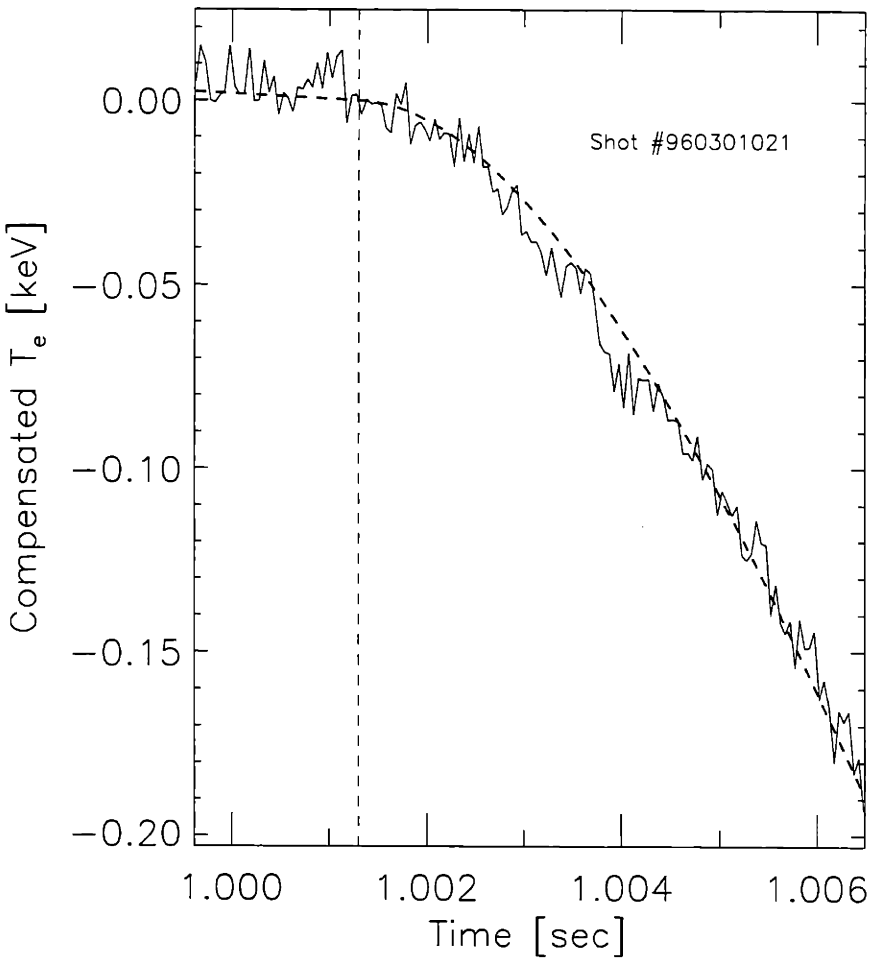

Figure 9-9: Time history of differential sawtooth response following an ICRF turnoff. The time of the ICRF power turn-off is shown with the vertical dashed line. Following the turn-off, the temperature evolution begins to gradually lag that of the previous sawtooth because the minority ion population's energy is decaying with time. The decay time estimated from fitting the function of Eq. 9.8 is $\tau_{tail} \approx 5.3$ msec. The data here are from the same power transition shown in Fig. 9-7. The central electron density at this time was $n_e = 2.0 \times 10^{20} m^{-3}$.

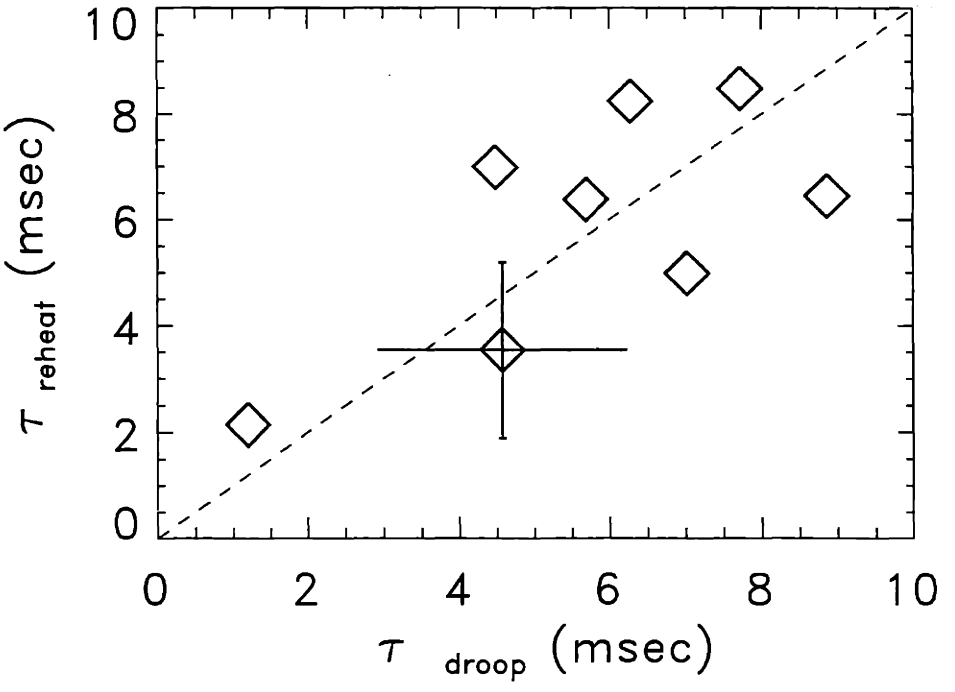

Figure 9-10: Figure showing a comparison of the results of the two different measurement techniques for the minority ion decay time. This plot represents the data from all of the shots on 960301 where both methods were able to produce reasonable fits to the data.

1. **Steady State measurement:** Using the steady state ICRF electron heating power, obtain the experimental estimate for the product of $n_{min} \times E_{tail} = p_e|_{min}\ \tau_{ee}$ from a measurement of the steady state electron power due to the minority heating from Eq. 3.19. The *hydrogen* minority concentration is known experimentally only to within a factor of approximately two at best. [1] Thus a second measurement is needed to uniquely obtain the tail energy.

2. **Tail Decay measurement:** Obtain an experimental measurement of the ion tail total energy decay time, τ_{Etot}, by either the "reheat decay" or the "sawtooth droop" methods (properly corrected for plasma temperature changes) described previously.

3. **Model predictions for tail dynamics:** Using the methods of Chapt. 3, calculate the theoretical values for tail energy and corresponding total energy decay times (see Eq. 3.23) for a range of parameters and tabulate the results. Example results for a particular power density and electron density are shown in Fig. 9-11. The input parameters to the model are the input power density, electron density, minority ion concentration, and electron temperature. So for the measured values of n_e, and T_e, we can obtain the model predictions: $E_{tail} = E_{tail}(p_{\perp i}, n_{min j})$ and $\tau_{Etot} = \tau_{Etot}(p_{\perp i}, n_{min j})$. These together with the measurement of the steady state electron heating due to minority ions provide three equations with which to solve for E_{tail}, n_{min}, and $p_\perp$.

4. **Obtain the best-fit $\mathbf{E_{tail}, n_{min}}$:** For each test value of $n_{min j}$, we find the $p_\perp$ value which corresponds to the conjugate E_{tail} value. From each of these $p_\perp$ values, we can directly obtain the model prediction for the decay time. Matching the model prediction to the experimental measurement allows a unique solution. To demonstrate this process, the data shown in Fig. 9-8 are re-examined with no assumptions about the minority con-

[1] The He^3 concentration can be determined more accurately (see appendix A). Evidence indicates that the He^3 "tail" energy in $D(He^3)$ experiments on C-Mod is $\lesssim 12keV$ (see §7.4.4).

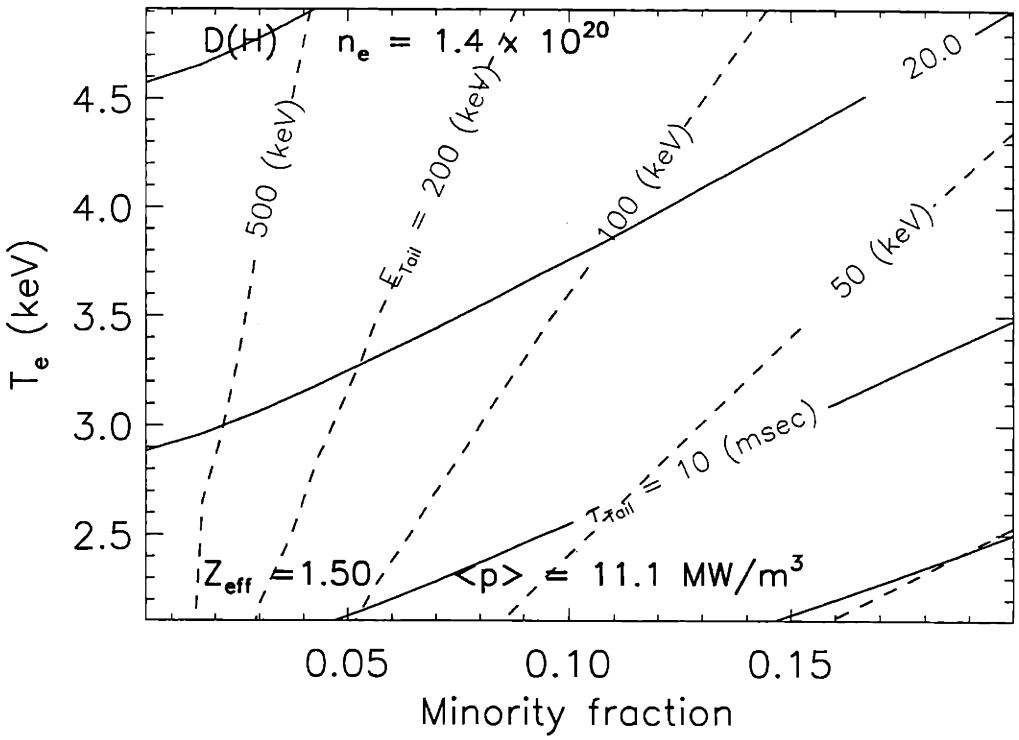

Figure 9-11: Calculated tail energy decay times for minority ion populations satisfying the Stix distribution (Eq. 3.8). Solid lines are contours of the best fit exponential to the decay of the distribution averaged energy (initial energies shown with dashed contours) after the source power, $\langle p \rangle$, is turned off. The energies of individual ions within the initial energy distribution decay according to the electron temperature and their instantaneous energies as shown in Fig. 9-12

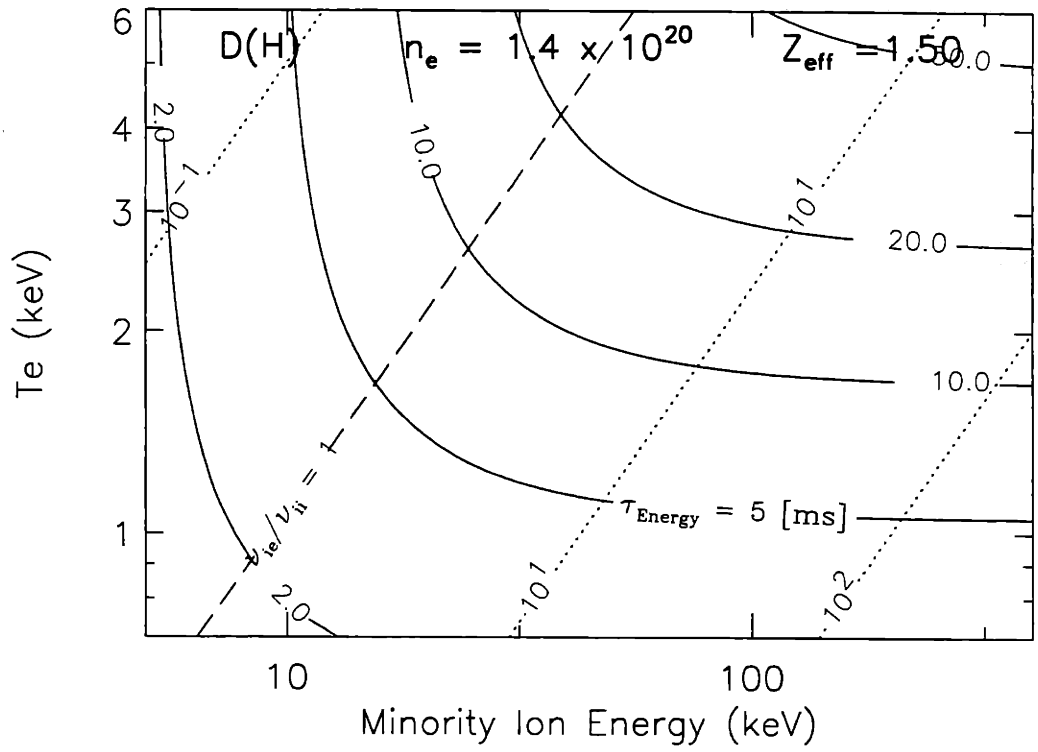

Figure 9-12: This figure characterizes the minority ion energy slowing down times needed to model the decay of the energy of the minority ion population following turn-off transients of the ICRF power. The solid lines give the energy decay time as determined by collisions with both bulk ions and electrons. The dashed contour indicates the partition between the electron drag and the ion drag regimes.

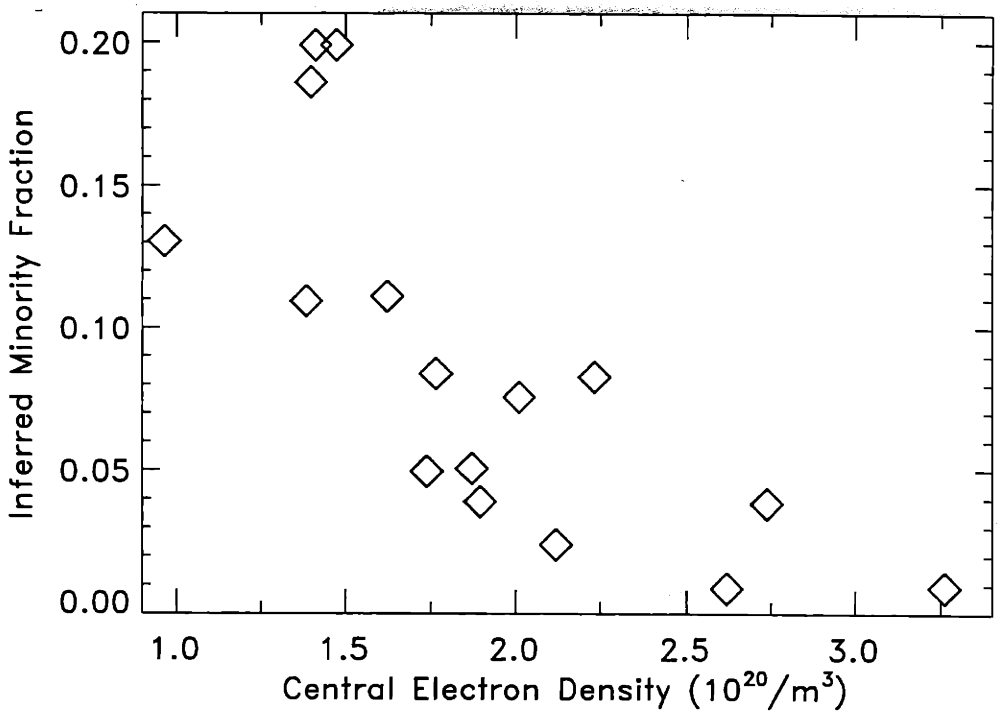

Figure 9-13: Minority fractions inferred from static and dynamic D(H) minority heating measurements. Increased hydrogen concentration at low plasma density is consistent with the gas puffing in these experiments. Recycling from the plasma walls is responsible for the hydrogen in the plasma and recycling plays a more dominant role at lower densities where less deuterium puffing is required to sustain the discharge.

centration. The "inferred" decay time on the x-axis is a function of the minority fraction assumed. *Doubling* the minority fraction *halves* the estimate of the tail energy obtained from Eq. 9.3 and the inferred decay time also decreases. For the minority fractions shown in Fig. 9-13, the predicted tail energies (shown in Fig. 9-14) and decay times from steady state and dynamic measurement techniques are brought into agreement as shown in Fig. 9-15.

The tail energy, E_{tail}, and the total ICRF heating power density, p_e, are important fundamental diagnostics of the minority heating experiments. For typical operation, no other measurements are made of these quantities. For *extremely* low density operation, the neutral particle analyzer can see hot minority ions from the plasma

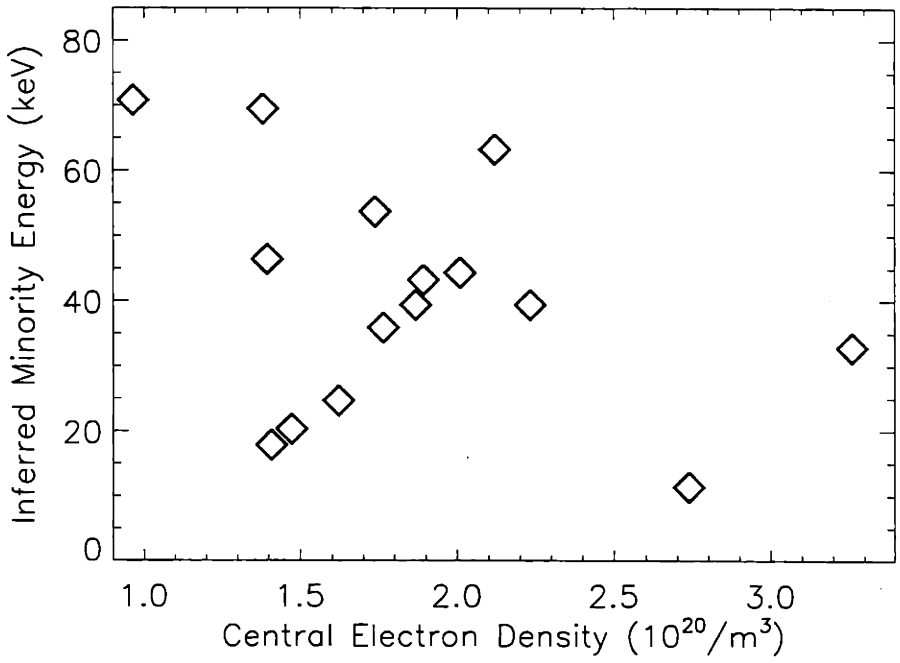

Figure 9-14: Minority energies inferred from static and dynamic D(H) minority heating measurements. These data are complementary to the minority fractions shown in 9-13 which together produce tail energies estimates consistent with both the static and dynamic measurements of minority heating power density.

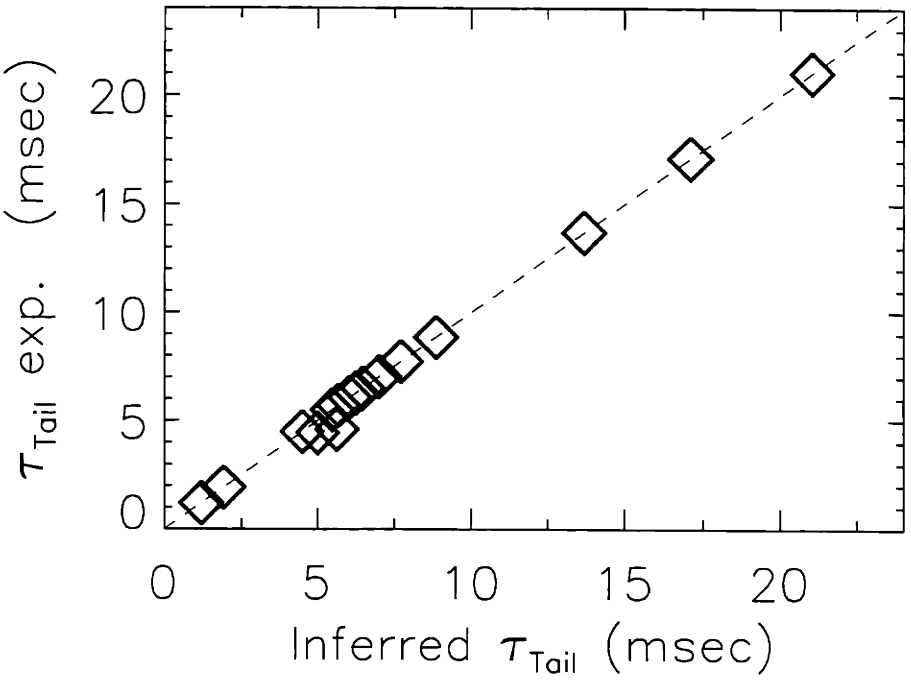

Figure 9-15: Two consistent "measures" of the minority energy decay time. The agreement shown here is a result of adjusting the minority ion concentration such that the decay time inferred from a measurement of the steady state minority heating power density agrees with the measured decay characteristics after turning off the ICRF power. This figure should be compared with Figs. 9-8 and 9-13.

core. *Effective* hydrogen ion temperaures ($T_{eff} \neq E_{tail}$ [12, 18]) of $\gtrapprox 10keV$ have been estimated from the energy spectrum of the hydrogen flux, in qualitative agreement with these observations. Another check of the validity of the method is to compare the minority fraction used in the solution with measurements provided by spectroscopic measurements. This measurement was not available for the shots analysed in this chapter.

9.1.7 Further considerations

The above treatment serves as a demonstration of methods for estimating the minority ion energy with electron temperature measurements. To the author's knowledge, these methods are described elsewhere in the literature. Future experiments and analysis can further refine the process. Experimentally, it should be noted that the GPC was *not* ideally configured for the reversed field runs. The innermost channel was located at a minor radius of between $1.5cm < r < 3.5cm$. It is best to sample the plasma as close to the center as possible, both for the use of the sawtooth reheat method and because the minority ion energy distribution is expected to be peaked on axis. As mentioned previously, it would be very useful to use the University of Maryland spectrograph to make independent measurement of the H/D ratio during the flat-top portion of the plasma when charge exchange fluxes are small. Another issue which can be addressed is that the analysis shown here assumes a constant background temperature. In practice, when the ICRF power is turned off, the *temperature* decays along with the central power (see Fig. 9-6). This changes the electron slowing down time and produces two effects which counteract each other to a degree:

1. **Total energy decay speeds up.** The electron drag increases as the temperature decays and this in turn speeds the decay of the ions. This Interpreting the results with a constant temperature assumption with tend to underestimate the ion tail.

2. **The proportionality in Eq. 9.5 changes in time.** For a given tail energy, the power that is seen by the electrons increases as the temperature decreases.

Thus the reheat signal decays at a rate slower than the decay of the ion tail energy and this will result in an overestimate of the real decay time and thus tend to overestimate the tail energy.

These two effects do not exactly cancel, however, the temperature as a function of time and can be taken into account in the analysis. With a simple scaling, the reheat rate decay can be corrected to reflect the real decay of the tail energy. Then a slightly more sophisticated modelling of the total decay which allows the *electron* portion of the total drag to vary in time is required before comparing to the measurements.

9.1.8 Limits of applicability

It is useful to express the ratio of the electron heating from the minority and majority ions respectively (*cf* Chapt. 6):

$$\frac{p_e|_{min}}{p_e|_{maj}} = \frac{2\,n_{min}}{3\,n_{maj}}\left(\frac{Z_{min}}{Z_{maj}}\right)^2 \frac{E_{tail}}{T_i - T_e} \tag{9.9}$$

The average energy of the minority ion distribution, E_{tail}, is the unknown quantity of interest in these studies. This equation is thus of greatest use as a *post priori* validity check on the assumptions used in estimating the tail energy. For the data shown in Fig. 9-6 and most of the shots analysed in this chapter, this equation estimates that at the initial turnoff, $p_e|_{min}/p_e|_{maj} \gtrsim 10$ and it is reasonable to neglect the the majority energy exchange term.

9.2 D-H mode conversion (?)

The standard source of auxiliary heating on Alcator C-Mod is hydrogen minority heating in deuterium plasmas at 5.3 Tesla. This source of heating has proven to be both efficient (with nearly 100 % of the ICRF power as confirmed by measurements of $\Delta(dW/dt)$) and (as seen in Chapt. 3) mediated by the minority ions. The fraction of hydrogen in these discharges is typically $\lesssim 5\%$. The amount of hydrogen required is

so small that the background level of hydrogen that naturally occurs due to plasma-wall interactions is typically sufficient for good minority heating performance. As discussed in section §3.7, increasing the minority fraction tips the scales towards mode conversion and away from minority heating. This transition between these two very different heating regimes was seen in §7.2 for $D-^3He$ plasmas. However, three factors make mode conversion more difficult in $D-H$ plasmas than in the $D-^3He$ case:

1. Polarization: The left hand circularly polarized component of the fast wave at the minority resonance in $D-H$ is three times that in $D-^3He$, helping minority absorption.

2. Slowing down: H loses energy to the bulk plasma slower than ^3He at a given energy, resulting in higher energy H tails for a given ICRF power.

3. Tunneling: The difference between the resonance frequencies in $D-H$ is greater than that in $D-He^3$, resulting in larger tunneling lengths for the fast wave between the $n_\parallel{}^2 = L$ cut-off and the $n_\parallel{}^2 = S$ ion-hybrid resonance in the D-H case.

Although $D(H)$ plasmas have been studied extensively on many tokamaks worldwide, mode conversion heating for low B-field side launch has not yet been demonstrated in these discharges. There is interest in observing this particular scenario of heating in order to extend the parameter space over which mode conversion has been studied. In addition to the considerations above which make D-H mode conversion more *difficult* to observe, the degeneracy of the 2^{nd} harmonic cyclotron resonance of the deuterium majority with the 1^{st} harmonic (fundamental) cyclotron resonance of the hydrogen minority creates a distinctly *different* nature for the mode converted IBW. Near a cyclotron resonance of the majority ion, the Bernstein wave has a small perpendicular wave vector, $k_\perp$, which can be expected to impact on the wave damping dynamics. Alcator C-Mod provides a unique facility in which to search for this heating as it has high ICRF power density and ECE temperature diagnostics on a high-field tokamak

are particularly sensitive. An unintentional vent of the tokamak to air during the previous campaign caused water vapour contamination of the inner walls. This gave rise to a brief period of operation with plasmas with relatively large hydrogen concentration. During a few of these "cleanup" shots, ICRF power was injected into the plasma in order to look for heating. Heating was in fact observed and the analysis described below indicates that the most likely explanation is D-H mode conversion. A systematic study under controlled conditions should be performed, but a careful examination of the limited results obtained to date (only one shot where both heating was observed and the RF transmitters operated for a significant portion of the discharge) is provided here because successful heating in this scenario has not been observed previously.

Because the hydrogen concentration was changing from shot to shot, it was not possible to know precisely where the mode conversion heating could be expected. A direct electron heating source will give prompt breaks in electron temperature evolution in response to abrupt changes in the source power. If the heating source is weak, it is best observed near the plasma center where the flux surface volumes are small and the resultant power *density* would be maximized. Thus in order to search for possible mode conversion heating, the ICRF transmitters were modulated as the toroidal magnetic field was scanned to move the cyclotron layers across the plasma. Figure 9-16 shows temperature data from this shot which clearly indicates heating but it is not immediately clear what the heating mechanism is. The power transitions are not clean enough nor is the heating response strong enough to infer a direct electron heating profile from a single transition. However, through analysis of the entire power modulation train, it may be possible to determine whether or not the heating is due to mode conversion.

Another happy match of the GPC to ICRF heating diagnosis now becomes apparent. It is a result of the fact that both systems rely on cyclotron phenomena. The ICRF transmitter frequency is fixed at 80 MHz. Each channel of the grating polychromator is fixed by the geometry of the grating optics to detect a fixed frequency of emission. Cyclotron frequencies (electron *and* ion) are directly proportional to

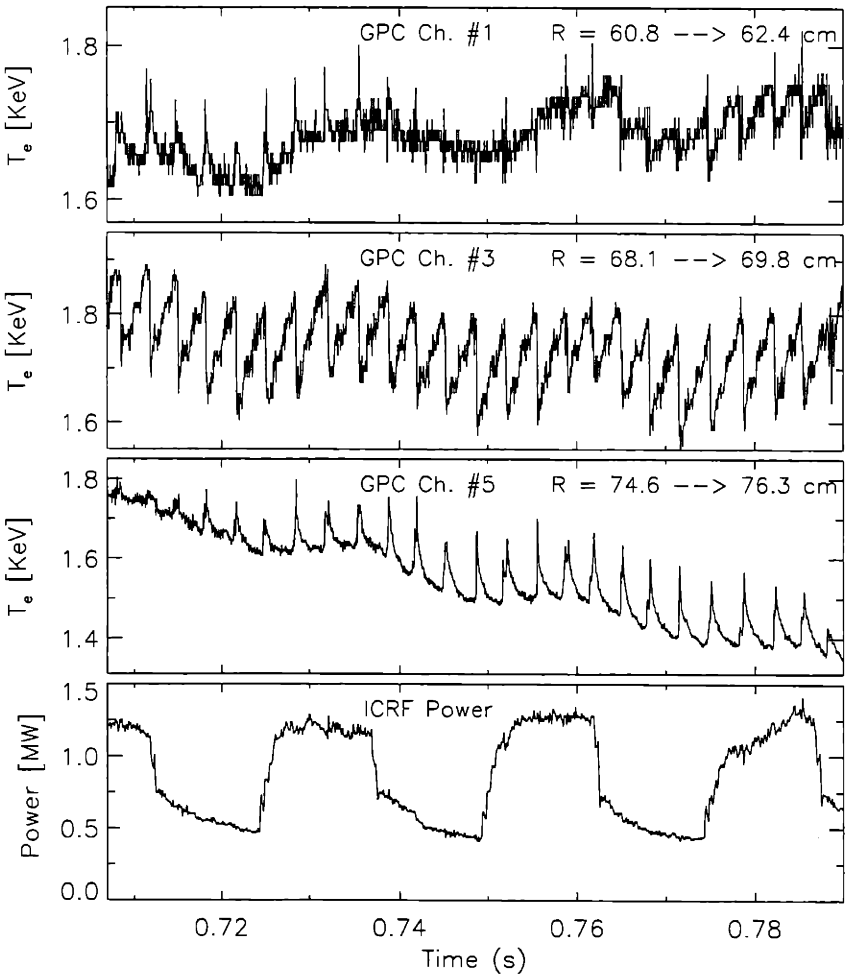

Figure 9-16: Figure showing raw data from shot 960822047. Shown is the electron temperature response on three of the GPC channels to the modulation of the ICRF power. The toroidal field is ramping up and the range in the radial positions of the GPC radii is indicated. The overall temperature modulation indicates heating near the plasma core though the hydrogen cyclotron resonance layer is located well off axis. The power transitions are not clean enough nor is the heating response strong enough to accurately infer a direct electron heating profile from a single transition. The entire power modulation train is analysed in order to best identify heating mechanism.

the magnetic field. The fact that both the ion cyclotron heating and the electron cyclotron emission diagnostic are linked to specific *cyclotron* frequencies means that both are linked to certain magnetic fields. Ramping the magnetic field changes the location within the plasma of a specific magnetic field. Both the ICRH resonance and where a given channel of the GPC is looking are tied to a specific magnetic field. Thus even though a source of mode conversion heating may not be obvious as it passes through the plasma center, it will stay fixed on a specific GPC channel. So even with a field ramp, the cumulative response of the electron temperature on a given channel will yield information about where the heating is occurring relative to the cyclotron resonance. The relationship between the source frequency, normalized to the hydrogen cyclotron frequency at a given location in the plasma, and the frequency of the (second harmonic) ECE emission viewed by the corresponding GPC channel is given by:

$$\begin{aligned} \omega_0/\omega_{cH} &= \frac{\omega_0}{\omega_{GPC}} \frac{2m_H}{m_e} \\ \text{Where : } \omega_0 &= 2\pi\, 80\text{MHz} \end{aligned} \tag{9.10}$$

For each power transition, a power profile was estimated by applying the "break-in-slope" technique with a fixed time interval before and after each power transition. Because the RF power was not modulated with sharp transitions, the slope fitting interval was chosen to be 4 milliseconds (roughly equal to the sawtooth period) and the power transition was taken to be the difference between the average powers within these fitting intervals. Summing these power densities for each channel gives an indication of the frequency at which the plasma was being heated. Plotted in Fig. 9-17 is the average of these power densities for each channel versus the source frequency normalized to the hydrogen cyclotron frequency calculated from Eq. 9.10. As the heating response is shown to be greatest for channels well away from those corresponding to the location of the hydrogen cyclotron resonance, minority heating does not appear to be the heating mechanism at work here. Equation 3.24 for the D-H plasma case

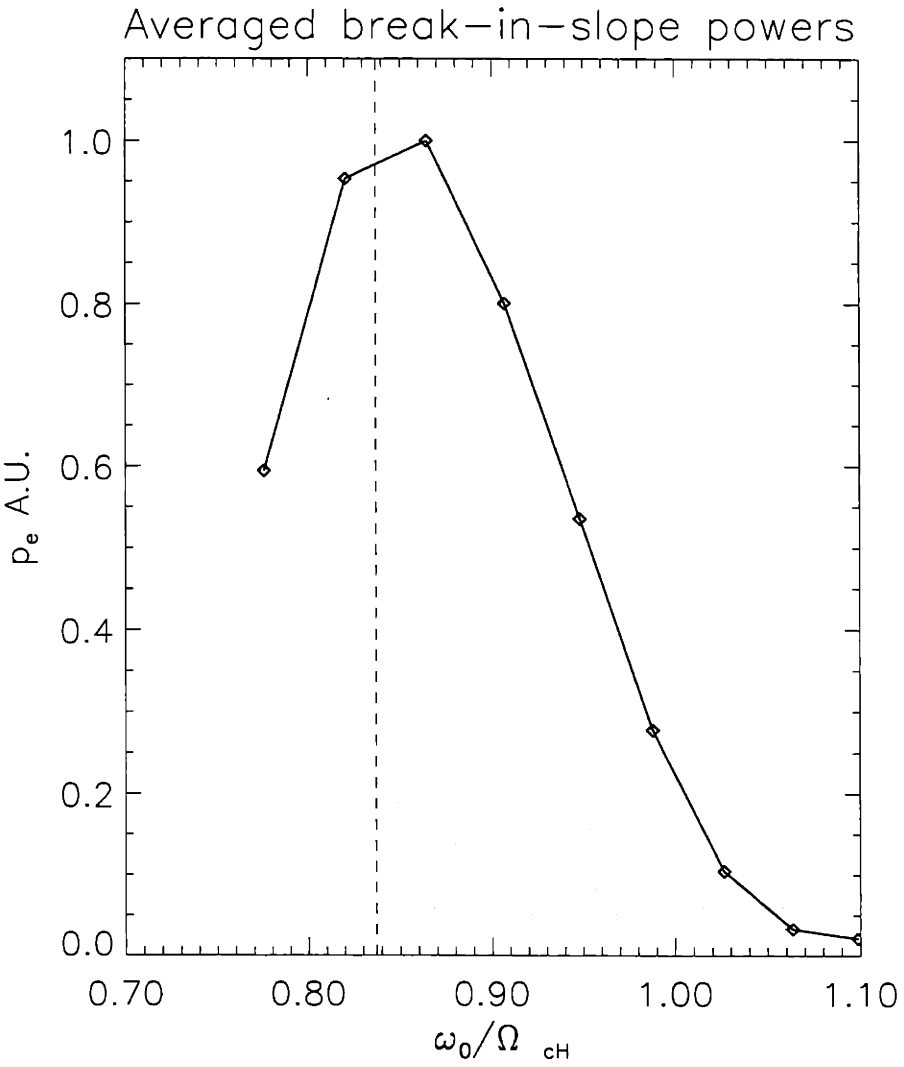

Figure 9-17: Curve showing the shape of the summed power densities for each GPC channel versus the corresponding cyclotron frequency calculated from Eq. 9.10 Although time-varying geometrical effects are folded into the plotted quantity, the qualitative point is made that the heating occurs well away from the cyclotron resonance.

yields the following expression for the mode conversion resonance frequency here:

$$\begin{aligned} \omega_{MC}|_{D-H} &= \Omega_{c_H}\sqrt{\tfrac{2-X_H}{2+2X_H}} \\ \text{Where here : } X_H &= f_H \approx n_H/n_e \end{aligned} \tag{9.11}$$

Measurements with the neutral particle analyzer and spectroscopic measurements indicated that $0.2 \lesssim X_H \lesssim 0.3$ for this shot. From 9.11 then, $\omega_{MC}|_{D-H}/\Omega_H \approx 0.84$. This predicted mode conversion frequency is indicated by the dotted vertical line in Fig. 9-17 and coincides very well with the peak heating response. This strong qualitative result indicates that the heating may be due to D-H mode conversion and motivates a quantitative analysis.

9.2.1 Best fit within the Mode Conversion model

From the break in slope analysis of the power modulation, we have 24 different measurements of power profiles, each at slightly different magnetic fields. If it is assumed that the heating is due to mode conversion, then we can model the expected behavior of the heating profiles throughout the field scan and compare with the measurements. A detailed fitting analysis was performed to obtain the best fit to the experimental data within the assumptions of the mode conversion heating model. Two free parameters within the model were the frequency (or magnetic field) location of the mode conversion heating and the deposition width along the major radius. It was assumed that throughout the field scan the heating efficiency, damping width, and poloidal structure of the absorption region were constant. By correctly performing the flux surface averaging of power absorption within the model, a quantitative estimate of the heating efficiency can be obtained from this model. The poloidal structure of the

actual power deposition was modelled with the following functions:

$$P_{abs}(R,Z,t) = \eta\ P_{RF}(t)\ S(R)\ S(Z) \qquad [MW/m^2] \tag{9.12}$$

Here S(R), S(Z) are normalized shape functions for the deposition:

$$S(R) = \frac{exp(-(R - R_{MC}(t))^2/W^2)}{\sqrt{\pi}\ W}$$
$$S(Z) = \frac{\Gamma(\alpha + 3/2)}{H\sqrt{\pi}\ \Gamma(\alpha + 1)}(1 - Z^2/H^2)^{\alpha}$$

In the above equation, $W \equiv W_{FWHM}/2\sqrt{\ln 2} \approx 3W_{FWHM}/5$ is the width of the damping, H is the effective vertical extent of the wave fields, and η is the fraction of the total ICRF power absorbed. The shape functions were selected to provide a good match to theoretical deposition profiles from TORIC, and are normalized such that $\int_{R_0-a}^{R_0+a} dR \int_{-a}^{a} dZ\ S(R)S(Z) \equiv 1$. Consistent with the assumption of mode conversion heating, the major radius of the deposition centroid was assumed to be locked to the magnetic field such that:

$$R_{MC} = constant\ \times R_{\Omega_{cH}}(t) \approx R_{\Omega_{cH}}(t) - \Delta R \tag{9.13}$$

The radius of the cyclotron resonance was taken to match that in the field ramp experiment. The above relationship describes the parameterization of the region of power deposition as a function of time. However, the deposited power must also be properly averaged over flux surfaces to generate the experimentally measurable quantity $p_e(R,t)$ which has units of MW/m^3. To account for the elongation of the plasma to first order, assume the flux surfaces are well described by ellipses of constant elongation, κ. Transforming the Z-coordinates of the tokamak according to:

$$Z' = Z/\kappa \tag{9.14}$$

creates flux surfaces of circular cross section. For calculation of the power density at the midplane, the flux averaging may now be done easily:

$$p_e(r,t) = \kappa \frac{\int_0^{2\pi} d\theta \; P_{abs}(R,Z',t)}{4\pi^2 R_0} \qquad [MW/m^3] \tag{9.15}$$

where

$$\begin{aligned} r &= \sqrt{(R-R_0)^2 + Z'^2} \\ \theta &= tan^{-1}\frac{Z'}{(R-R_0)} \end{aligned} \tag{9.16}$$

Note that the vertical extent of the wavefields should also be adjusted to account for this "compression" of the vertical coordinate.

The flux averaging creates a power density profile which is symmetric about the magnetic axis of the plasma. Depositing power at a point off axis will result in power density at that location but also at the "mirror" image of the point across the magnetic axis. For a given power transition, the polychromator measurement of the power deposition from the resulting break in slope cannot *a priori* distinguish between local power deposition and the "image" of power deposited on the other side of the magnetic axis. However, in scanning the magnetic field this ambiguity is removed. Power deposition due to mode conversion will move to larger *major* radii as the magnetic field is increased, but the "image" of this power will move in the opposite direction. So although a given GPC channel can detect this mirror-image power at a given magnetic field, the image will move to a different channel as the field is ramped. Only those channels sensitive to the fields where the actual power deposition is occurring will continue to see power signals throughout the field scan.

For a given assumption for the *position*, ΔR, and *width*, W, of the mode conversion power deposition, the above model makes a prediction for the *shape* of flux averaged power profile at each power transition that occurred in the experiment. The best fit to the ensemble of data for these assumed parameters is obtained by adjusting the absorption efficiency scale factor η, in Eq. 9.12. Figure 9-18 shows comparisons of

measured and modelled power profiles for several power transitions which occurred during the field ramp. Note that the heating occurs well away from Ω_{cH} and is seen to peak slightly as the field ramp progresses. Note also how the positions of the GPC channels *and* the cyclotron resonance move toward larger major radii as the field is ramped up. These plots represent the mode conversion model's best fit to the data, predicting $\approx$ 15% absorbed power and $\approx$ 25% hydrogen concentration. The quality of the overall fit is measured by calculating the RMS error between the model-predicted and the experimentally measured power profiles at each power transition and for each channel of the GPC:

$$\chi^2{}_{fit}(\Delta R, W) = \sum_{transitions_i} \sum_{channels_j} \frac{(p_{emodel} - p_{eexp})^2_{i,j}}{\sigma^2|_{pe}} \tag{9.17}$$

Thus every pair of profile parameters, ΔR and W, has associated with it a best-fit absorption efficiency, and a fitting error. A two dimensional search of the fitting parameters was conducted to find the best fit within the mode conversion heating assumption. Contours of the fitting error are shown in Fig. 9-19.

9.2.2 Fast Wave electron damping model

The above considerations show that the heating observed on shot 960822047 is consistent with 15% mode conversion to the IBW at the ion hybrid resonance layer. As the heating occurs well away from cyclotron resonances and the raw data seem to indicate direct electron heating, the only other plausible mechanism is direct damping of the fast wave due to electron Landau damping. The damping rate for propagation perpendicular to the magnetic field can be expressed as the ratio of the incremental power absorbed by electrons to the Poynting flux as [15]:

$$2K_{\perp Im} = \frac{P_{abs}}{S_\perp} = \frac{\sqrt{\pi}}{2}\frac{\omega}{\omega_{ci}}\frac{\omega_{pi}}{c}\beta_e\,\zeta_e\,e^{-\zeta_e^2} \;\propto\; n^{\frac{3}{2}}\,T_e\,B^{-3}\,e^{-250\,keV/n_\parallel^2 T_e} \tag{9.18}$$

where: $\zeta_e = \dfrac{\omega}{k_\parallel v_{the}}$ and $v_{the} = \sqrt{2T_e/m_e}$

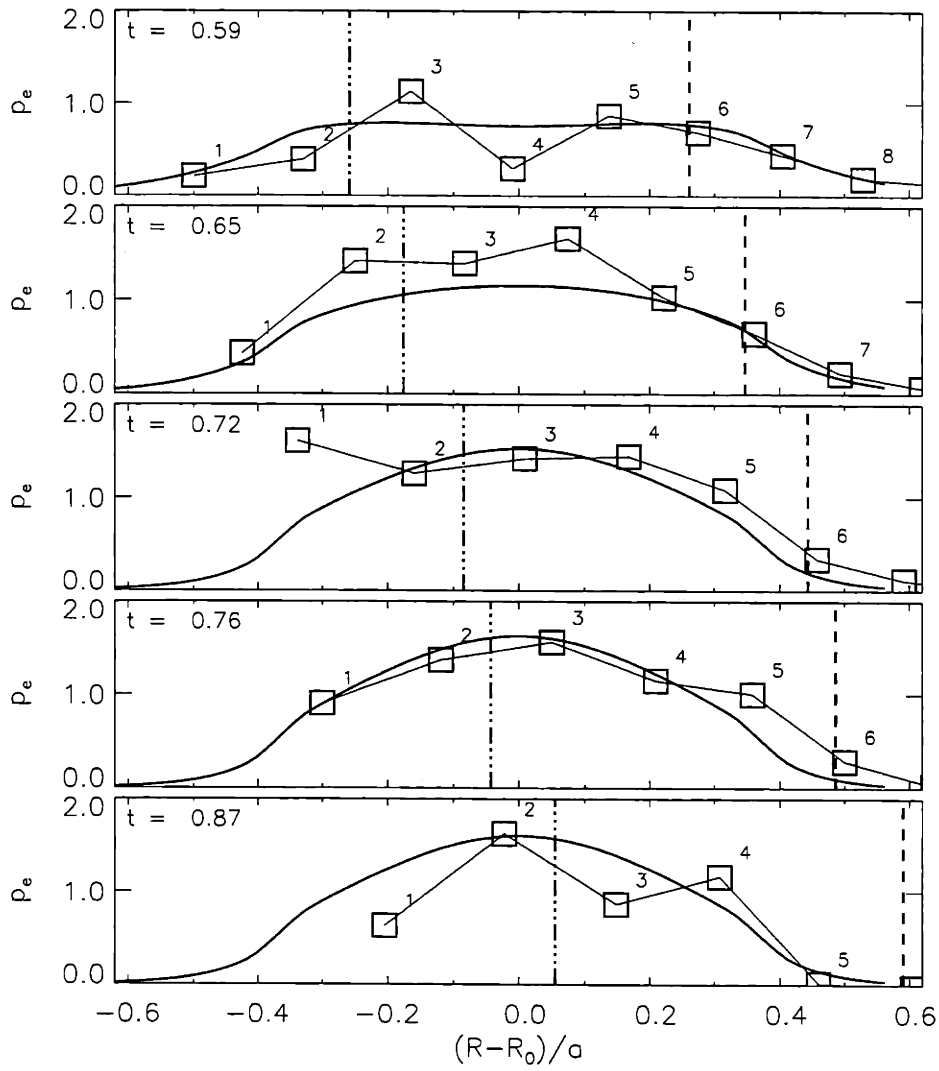

Figure 9-18: Figure showing the comparison of the mode conversion model power profiles (solid lines) to experimentally measured power profiles (numbered squares corresponding the nine GPC channels) for several power transitions throughout the magnetic field scan on shot 960822047. The locations of the hydrogen cyclotron layer (dashed lines) and the modeled center for the absorption of mode converted power (dot-dashed lines) are indicated. Power densities are normalized to each correspond to 1 MW power transitions.

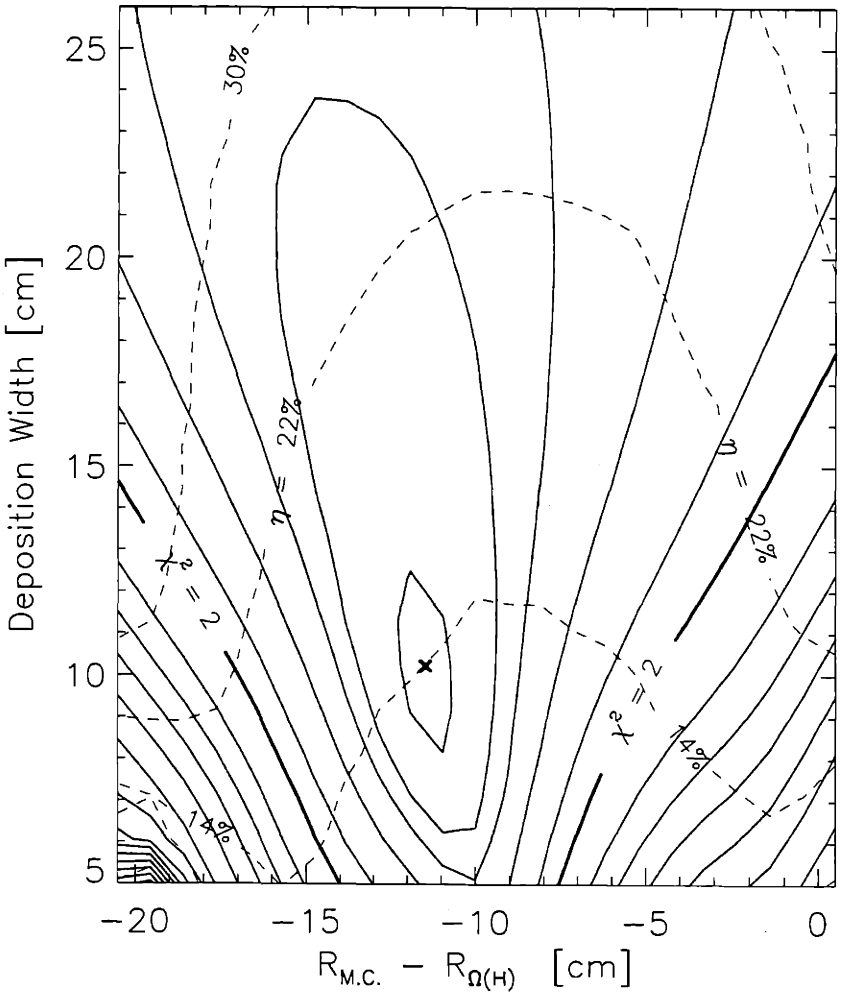

Figure 9-19: Figure showing the contours of normalized fitting error of the D-H mode conversion model to the heating observed on shot 960822047, a plasma with $\approx$ (75% D − 25% H) plasma. "X" marks the minimum in the normalized χ^2 for the model. The model indicates electron heating $\approx 11.5cm.$ to the high field side of the hydrogen minority resonance and with a FWHM deposition width of 10.5 cm. The location of the heating agrees well with the location of the IBW mode conversion layer for the measured minority fraction.

Because of the temperature dependence of the exponential factor, fast wave damping is maximum at the hot plasma core and will remain centrally peaked as the magnetic field is scanned. As the expected location for the mode conversion heating was intentionally scanned through the plasma center, the power profiles for mode conversion heating will be somewhat similar to those for fast wave heating. However, there are still sufficient differences in the physics of these two scenarios that a more careful examination can hope to distinguish between them. Although the fast wave heating remains at the plasma center, Eq. 9.18 shows that the *strength* of the damping is $\propto B^{-3}$ and thus decreases by a factor of ≈ 1.5 as the field is scanned through its full range. It should also be noted that whereas the resonant nature of the *mode conversion* heating extends the deposition region vertically along surfaces of constant magnetic field to the extent of the wave fields, in the *fast wave* case the vertical extent of the power deposition is determined mostly by temperature and is thus more localized to the center. Figure 9-20 shows a plot of $K_{\perp Im}$ along the tokamak midplane for the conditions of shot 960822047 and for $K_{\|} = 13\,m^{-1}$. An important result is obtained by estimating the single pass absorption due to direct damping of the fast wave by integrating Eq. 9.18 as below:

$$\left.\frac{P_{abs}}{P_{inc}}\right|_{\text{single pass}} = 1 - exp(-\int_{R_0-a}^{R_0+a} 2K_{\perp Im}(R)\,dR\,) \tag{9.19}$$

$$\text{For weak damping:} \approx \int_{R_0-a}^{R_0+a} 2K_{\perp Im}(R)\,dR$$

$$\approx 2.5\%\text{ , here.} \tag{9.20}$$

While this absorption factor is already very low, it represents the *upper limit* of the single pass absorption. As $K_{\perp Im}$ drops exponentially as one moves off axis, the same integration performed for rays passing above or below the midplane result in considerably reduced absorption. This implies that if electron damping of the fast wave is responsible for the heating, we require very many passes of the fast wave across the tokamak cross-section. For this reason the width of the centralized power deposition profile was allowed to vary for a fast wave modelling of the power

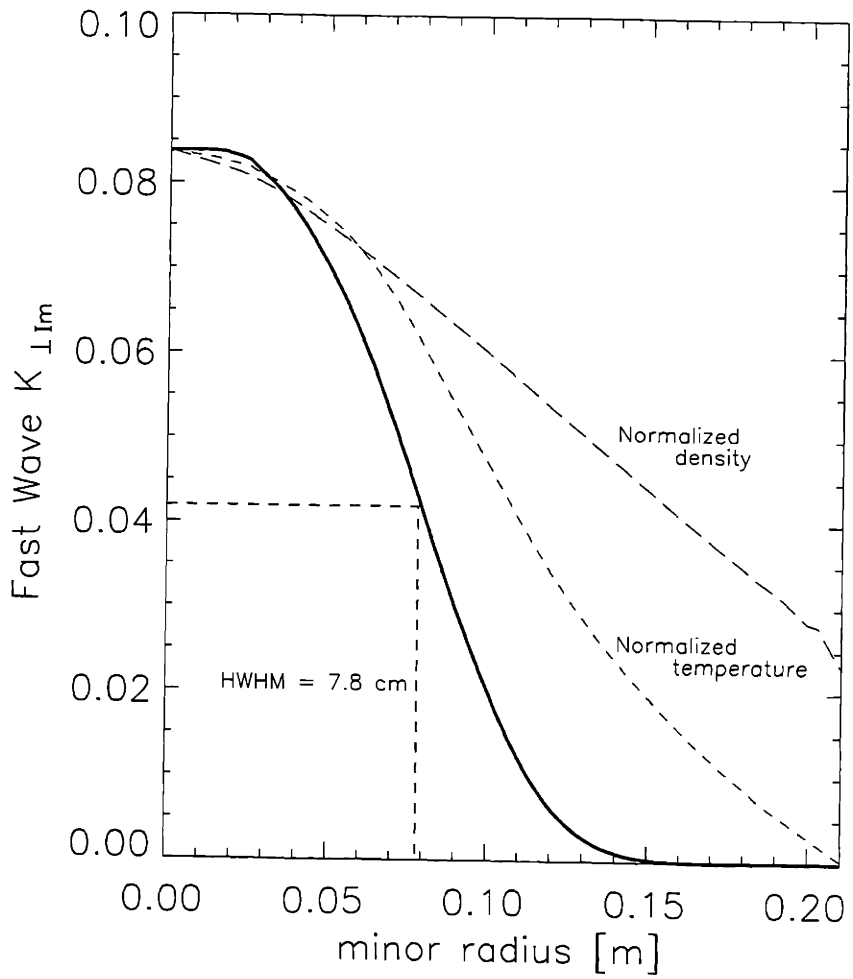

Figure 9-20: Figure showing the midplane profile of $K_{\perp Im}$ (as given in Eq. 9.18) for electron Landau damping of the fast wave for shot 960822047. Because the damping is very weak, this is also roughly the expected shape of the power deposition profile. The profile width of $\approx 14cm$ is similar to the best fit to the experimental data (see Fig. 9-21) but the single pass power absorption of $\approx 2.5\%$ is much lower than the observed heating implies. The central electron temperature and density were $1.8KeV$ and $\approx 3 \times 10^{20}\ m_{-3}$, respectively.

absorption. For each FWHM width assumed, an ensemble fitting error and inferred heating efficiency were generated as was done in the case of the mode conversion model for this heating. The results are shown in Fig. 9-21. For comparison with the mode conversion model, the error as a function of deposition width for the optimal ΔR is also shown.

While the width of the deposition for the best-fit within the fast wave damping model is consistent with that expected for $K_{\|} = 13m^{-1}$ and measured plasma parameters, this leaves one with the question of the very low single pass absorption of the fast wave and the also the fact that the fit to the data is better for the mode conversion model. Furthermore the best fit within the mode conversion model implies a hydrogen fraction which is in very good agreement with that measured by both the neutral particle analyzer and the U of M spectrograph. For these reasons, it is believed that this heating represents the first evidence for mode conversion heating of $D(H)$ plasmas in a tokamak.

To obtain an absolutely certain signature of mode conversion heating in future experiments, attempts to observe heating which is off axis *and* far from cyclotron resonances should be made. As the tunneling distance between the $n_{\|}^2 = L$ layer and the mode conversion layer is roughly proportional to the density, these experiments should be attempted at lower density.

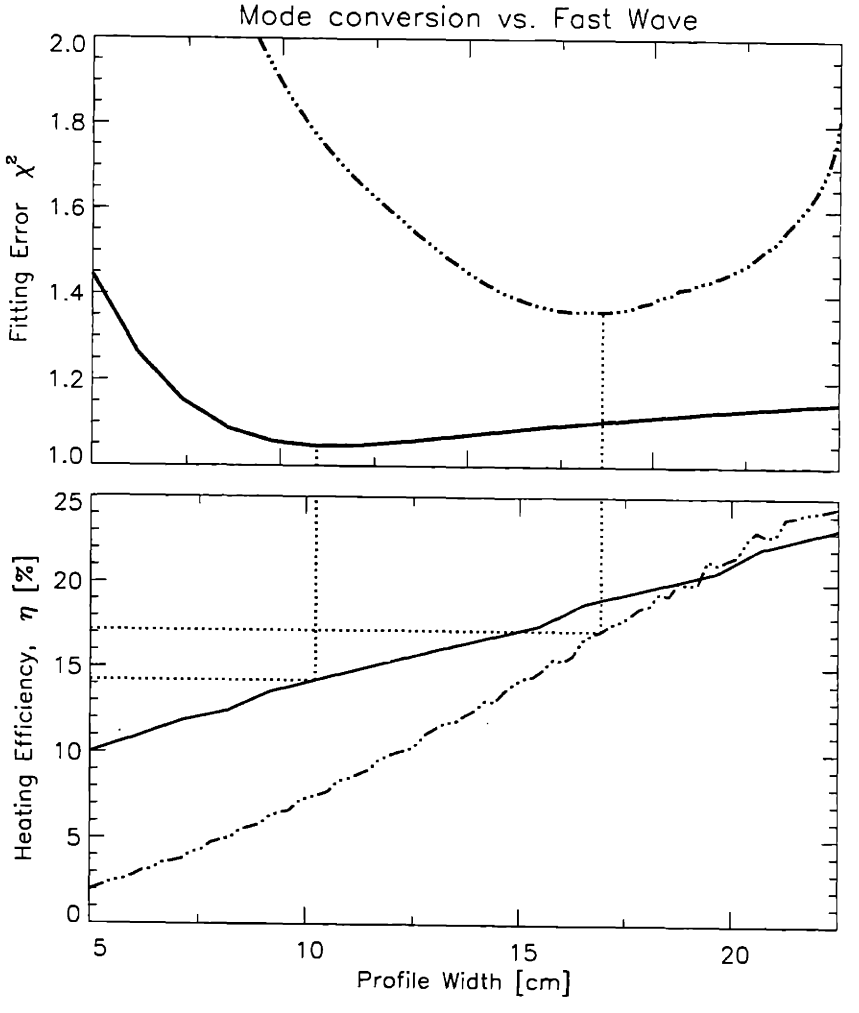

Figure 9-21: The upper panel shows a comparison of the fitting errors to the ensemble of experimental power profiles for the assumption of fast wave heating (dot-dashed line) and mode conversion heating (solid line) as a function of the deposition width in both cases. The curve for the mode conversion case corresponds to a vertical cut through the error contours of Fig. 9-19 at the best-fit separation ΔR. The mode conversion model provides a significantly better best-fit. The lower figure shows the corresponding predictions for the heating efficiency for the two models.

Chapter 10

Transient Transport

10.1 Introduction

In previous chapters, we have examined some of the physics involved in the heating of tokamak plasmas in the ion cyclotron range of frequencies. We have seen how plasma conditions may be adjusted to directly heat either minority ions or electrons with the same antennas. Achieving efficient heating in both of these heating regimes in the high plasma densities of Alcator C-Mod is an important result which indicates the efficacy and versatility of ICRF as a heating source for future reactors. However, to achieve the temperatures necessary for ignition, the plasma must also efficiently retain the externally delivered power. Whereas the theory of plasma waves has been very successful in describing many crucial plasma phenomena (in this thesis we have used it to treat the propagation, coupling and damping of two very different ICRF waves and also the ECE used to diagnose them), a fundamental theory which accounts for the observed confinement performance of experimental magnetic fusion devices is still an elusive goal for the fusion community. Calculations of cross field diffusion as driven by Coulomb collisions provide expressions representing the irreducible ideal limit. These "classical" expressions [81] for straight magnetic field lines must be strongly modified to yield the so-called "neoclassical" values which account for the toroidal curvature and helical nature of the field lines in tokamaks [82]. Transport levels above the neoclassical values are termed "anomalous" and as yet are not well described by

theory. Although ions in tokamaks have been observed to exhibit transport near neoclassical levels, electron transport remains highly anomalous [83]. As a result, the study of transport mechanisms (for particles and momentum as well as energy) is an area of active research .

Sophisticated theories have treated many and varied phenomena which generally lead to the microturbulence which is thought to be responsible for anomalous transport [84]. Many diagnostic techniques have also been developed to study directly some of the physical mechanisms thought to contribute significantly to transport [85, 86, 87, 88, 89, 90]. Direct study is almost always difficult and any specific diagnostic tool can investigate only a small portion of the parameter space of interest. To help narrow the field of mechanisms thought to be responsible for tokamak transport, a far more general approach must be taken. The gross transport of the plasma is characterized as precisely as possible and the parametric scaling is compared to that of theories to determine the dominant mechanisms at work. Though a large step removed from basic physics, this work provides valuable feedback to theorists and a wide variety of techniques have been used [91].

In this chapter, a brief description is given of experiments carried out to characterize the electron thermal transport on Alcator C-Mod. With the grating polychromator (GPC) providing fast electron temperature measurements, we focus on the dynamic response of the electron species to time varying thermal perturbations. Particular attention is given to a set of experiments performed by modulating the ICRF power during efficient mode conversion heating of electrons in $H(He^3)$ plasmas. Though a systematic study was not possible because of the complicating effects of deuterium (see Chapt. 8), example results are given and compared to those of more standard techniques. This presentation is intended simply to bring out some of the general characteristics of thermal transport on Alcator C-Mod. This will hopefully help to better understand the performance of the tokamak and to stimulate and aid further studies. Features of the transient transport equations and observations from earlier chapters are considered which indicate clear ways to optimize future modulation experiments.

10.2 Basic transport equations

Treating the plasma as a collection of fluid species, gross plasma observables may be expressed as moments of the single-particle velocity distribution functions. The Boltzmann equation which governs the behavior of the distribution functions provides conservation laws for these observables. Local conservation of energy for the electron species is obtained from the second velocity moment of the Boltzmann equation and is expressed as

$$Q = \frac{\partial}{\partial t}\left(\frac{3}{2} n\, T\right) + \nabla \cdot \left(\frac{5}{2}\Gamma\, T + \mathbf{q}\right) \tag{10.1}$$

where n and T are the electron density and temperature respectively. Q represents an external heat source which is balanced on the right hand side of Eq. 10.1 by changes in the thermal energy (1^{st} term) and energy transport (2^{nd} term). Energy is carried by both particle flux, Γ, and heat flux $\mathbf{q}$. The heat flux in turn can expressed by

$$\mathbf{q} = -n\, \chi\, \nabla T + n\, \mathbf{U} \tag{10.2}$$

where χ is the diffusivity, and $\mathbf{U}$ is a convective velocity of the electron fluid. This equation can be used when considering slow evolution of equilibrium plasmas [92] but may also be linearized to allow the description of the dynamics of small thermal perturbations to the steady state solution:

$$\frac{\partial \tilde{T}}{\partial t} = D\, \nabla^2 \tilde{T} - \mathbf{V} \cdot \nabla \tilde{T} - \frac{\tilde{T}}{\tau} + \tilde{S} \tag{10.3}$$

where the set of *effective* transport coefficients in this perturbed energy equation have been defined here whose general forms are as detailed by Luce [93]:

$$D = \tfrac{2}{3}\left(\chi + \tfrac{\partial \chi}{\partial \nabla T} \cdot \nabla T_0\right), \tag{10.4}$$

$$\begin{aligned} \mathbf{V} \equiv\ & \tfrac{2}{3}\left(\mathbf{U} - \tfrac{\partial \chi}{\partial T}\, \nabla T_0 + \tfrac{\partial \mathbf{U}}{\partial T}\, T_0\right) - \tfrac{2}{3}\left(\chi + \tfrac{\partial \chi}{\partial \nabla T} \cdot \nabla T_0\right)\, \tfrac{\nabla n}{n}\ - \\ & \tfrac{2}{3}\nabla\left(\chi + \tfrac{\partial \chi}{\partial \nabla T} \cdot \nabla T_0\right) + \Gamma/n, \end{aligned}$$

$$\frac{1}{\tau} \equiv \frac{Q_{OH}}{nT_0} + \frac{Q_{ei}}{3nT_0}\left(\frac{T_0-3T_i}{T_0-T_i}\right) + \frac{5}{3}\frac{\nabla\cdot\Gamma}{n} - \frac{2}{3}\frac{\Gamma\cdot\nabla n}{n^2} + \frac{2}{3}\frac{\nabla n}{n}\cdot\left(U - \frac{\partial\chi}{\partial T}\nabla T_0 + \frac{\partial U}{\partial T}T_0\right) + \frac{2}{3}\nabla\cdot\left(U - \frac{\partial\chi}{\partial T}\nabla T_0 + \frac{\partial U}{\partial T}T_0\right),$$

$$\tilde{S} \equiv \frac{2}{3}\frac{\tilde{Q}_{ext}}{n}$$

The above equations illustrate why D, $\mathbf{V}$, and τ are termed the *effective* diffusivity, convective velocity and damping rate respectively. Only the radial gradients of temperature are important in the above equations but flux surface geometry remains important and is implicit in the use of the ∇ notation [1]. The names of these variables come from their roles in Eq. 10.3 and their analogies in the true transport Eq. 10.1, more than from the physical mechanisms which give rise to them. For instance, accounting for the temperature perturbation's effect on the local ohmic power density gives rise to a term in the perturbed power balance $\propto T$. Such a term behaves mathematically as damping and thus it appears as the leading term in the expression for τ. Equation 10.3 also shows how each effective coefficient can depend on many different details of the basic transport coefficients. In turn, each coefficient depends on the details of the particle velocity distribution, indicating that Eq. 10.3 represents a greatly simplified representation of the fundamental transport dynamics.

10.3 ICRF Power modulation experiments

Equation 10.3 indicates that in source-free regions of the plasma ($S = 0$) the transport coefficients alone determine the time evolution of temperature perturbations. Thus the heating source used in perturbative heat transport experiments must both deliver enough energy to produce measurable effects and be sufficiently localized to allow observation of diffusion dynamics away from the source. The grating polychromator provides the only highly time resolved temperature profile measurements on Alcator C-Mod and to take full advantage of its capabilities, a source of *direct* electron heating is required. Power modulation during electron cyclotron heating (ECH) is ideal in this

[1] $\nabla\cdot[\sim] \rightarrow 1/V'(\rho)\partial/\partial\rho[V'(\rho)\sim]$, where V' is the enclosed volume of a magnetic flux surface with midplane radius ρ.

respect and has been used extensively [94, 95, 96, 97, 98, 99] for such experiments. We however are forced to examine the possibilities for perturbative transport experiments using the ICRF system on Alcator C-Mod.

Modulation during ICRF minority heating is not ideally suited for transport measurements. The spatial extent of the heat source tends to be broad due to both doppler broadening and the relatively large poloidal size of the antennas involved. In addition, the finite slowing down time of the minority ions puts a lower limit on the time scale over which the effective heat source may be varied. These limitations blur the distinction between the effects of the heat source and diffusion, and the resulting conclusions are weak [71]. Better results are achieved when the fast waves launched by ICRF antennas damp significantly on electrons [22], however as seen in Chapt. 9, the electron β is too low on Alcator C-Mod to heat efficiently in this regime. Results from efficient direct electron heating via mode conversion to the IBW in $D - He^3$, and $H - He^3$ plasmas have been presented in Chapts. 7 and 8 respectively. Damping of the mode converted IBW on electrons provides a direct electron heating channel the location and time dependance of which can be controlled by the experimenter. Mode conversion heating thus provides the best opportunity on Alcator C-mod for controlled perturbative transport studies. The modulation experiments carried out to date have been almost exclusively in $H - He^3$ plasmas. Observations and analysis in Chapt. 8 have clarified what conditions are necessary for obtaining maximally localized heating profiles which are best suited to these experiments. Although systematic parameter scans under optimal heating conditions were not obtained, some of the better data are examined here to guide more complete future studies.

10.4 Time scales for modulation experiments

Determining perturbed transport coefficients from Eq. 10.3 involves analysis of the temperature response, $\tilde{T}(r,t)$, to the perturbation source, $\tilde{S}(r,t)$. For our experiments, $\tilde{S}(r)$ is due to electron heating from the damping of mode converted ion Bernstein waves (IBW). The time dependance is directly controlled in the exper-

iment by modulating the transmitter power. Although the mode conversion layer may be moved throughout the plasma by adjusting either the magnetic field or the relative concentrations of ion species, sufficient uncertainty exists both in the latter quantity and in the damping physics of the IBW that an independent measurement of $\tilde{S}(r)$ is required. In Chapt. 6 it was shown how the break-in-slope technique was used to determine the electron power profile from the electron temperature response to very fast changes in the ICRF power. Using temperature dynamics to independently determine *both* $\tilde{S}(r)$, *and* the transport coefficients, D, V, and τ may at first seem impossible. The key issue is that of the *time scale* over which the two different responses are measured. Dimensional analysis of Eq. 10.3 establishes a useful relationship between short time intervals, Δt, and the corresponding characteristic diffusion scale length, Δr_{diff}:

$$\Delta r_{diff} \approx \sqrt{\frac{2\chi\ \Delta t}{3}} \tag{10.5}$$

10.4.1 Considerations when determining $\tilde{S}(r)$

In order to measure the heating profile, $\tilde{S}(r)$, the effects of diffusion must be minimized. The *instantaneous* response of the derivative of the electron temperature to sharp changes in ICRF power is proportional to the direct electron heating power density. In practice however, finite signal to noise ratios require finite time intervals in order to *estimate* the instantaneous response. Equation 10.5 establishes the relationship between the time interval for use in the break-in-slope method, and the desired spatial resolution. To eliminate the effects of diffusion in the determination of the power profile, the spatial separation of the samples must be larger than the characteristic diffusion length. For standard operation of the grating polychromator with the nine-channels spanning the minor radius, a, of the plasma, this limits the time of the fitting intervals for the break-in-slope technique to:

$$\Delta t_{Break-in-slope} \lesssim \left(\frac{3}{2\chi}\right)\left(\frac{a}{8}\right)^2. \tag{10.6}$$

As will be seen in the following sections, $\chi \approx 1m^2/s$ is a typical magnitude for the perturbed thermal diffusivity in Alcator C-Mod. This limits the break-in-slope fitting intervals to $\Delta t \lesssim 1.2$ msec. With well localized electron heating, discontinuities in the slope are easily measured within this time interval.

10.4.2 Lower limits to the modulation frequency

The previous section illustrated how diffusion effects on the temperature dynamics are eliminated at sufficiently high frequency. At the other end of the spectrum, one effectively reaches the static limit when the characteristic diffusion length approaches the size of the plasma. Thus in order to observe transport *dynamics* the modulation frequency must satisfy the relation:

$$f_{mod} = \frac{1}{\Delta t_{max}} \gtrsim \left(\frac{3a^2}{2\chi}\right) \approx 12Hz \text{ for C-Mod} \tag{10.7}$$

The "damping" term, $\tilde{T}/\tau$ that appears in Eq. 10.3 is the result of some effects which are not intrinsically related to transport. In particular, the first two terms of equation 10.4 are solely determined by equilibrium quantities. The first term is dominant for Alcator C-Mod and in order to minimize its effects, the modulation frequency should be chosen so that

$$f_{mod} \gg \frac{Q_{ohmic}}{2\pi\ nT_0} \approx 10Hz. \tag{10.8}$$

10.4.3 Upper limits to the modulation frequency

When considering how to effectively eliminate the effects of diffusion on the power deposition measurements, we obtained an upper limit on the time over which the temperature measured by a given GPC channel is unaffected by diffusion of heat from an adjacent channel. When *looking* for diffusive effects, we can reverse this condition

and define a maximum modulation frequency for the study of heat transport:

$$f_{mod} \ll \left(\frac{2\chi}{3}\right)\left(\frac{8}{a}\right)^2 \approx 800Hz \text{ for C-Mod.} \tag{10.9}$$

10.4.4 Practical limits to modulation frequency

Hardware constraints

The time constant of a feedback circuit in the ICRF transmitters established a hardware limit to the turn-on time for the RF power. This limited the modulation frequency to $\lesssim 250Hz$. Experience has shown that the rise and fall times can be considerably faster than this. A series of sharp turn-ons and turn-offs throughout the shot helps greatly in the determination of the heating profiles, and should be pursued in future experiments.

Compatibility with analysis techniques

Square-wave modulation was desired so that periods of steady power levels existed for sawtooth reheat calculations. Square waves also introduce signal power at the third harmonic of the modulation frequency which can be analysed separately with Fourier analysis. The requirement of a flat-top to the power signal further limits the modulation frequency to $\lesssim 100Hz$.

Interference from sawteeth

Very large amplitude sawteeth were observed during nearly all of the mode conversion experiments, ranging in frequency from $120Hz \lesssim f_{S.T.} \lesssim 300Hz$. Their presence can at times greatly complicate both power deposition measurements and diffusion properties. Furthermore, the modulation of the ICRF power was seen to modulate both the amplitude and frequency of the sawteeth, indicating that the two effects are not independent. The independent behaviours can be partially deconvolved in the analysis [99] if the lower sideband of the AM modulation is well separated from the modulation frequency itself. The modulation frequencies chosen for our experiments

ranged from 40 - 80 Hz. Future experiments would likely do best at and above the high end of this range.

10.5 Modulation experiments on Alcator C-Mod

Early mode conversion experiments in $H - He^3$ plasmas achieved efficient direct electron heating with very localized power deposition. With the requirement met for spatial localization, experiments in which the transmitter power was modulated were performed to establish the plasma's dynamic response to a time varying source. Figure 10-1 shows the electron temperature as measured on several channels of the grating polychromator in response to square wave modulation of the ICRF for the off-axis heating case. The broadening of the electron power profiles in $H(He^3)$ mode conversion experiments made a controlled parameter scan for the modulated transport studies impossible. In this section, two shots will be analysed showing the influences of on-axis versus off-axis heating. Break-in-slope analysis provides a measurement of the electron heating power profiles. The heating profiles for these shots are shown in Figs. 10-2 and 10-3, respectively. Also shown in these figures are profiles of the electron temperature response at the modulation frequency, obtained from the *magnitudes* of the FFT of the GPC signals. The temperature response profiles are broader than the power deposition profiles, the "source term", in both cases due to the influence of diffusion. In addition to the amplitude of the temperature response, the phase lag is also measured and both quantities are used to help characterize the thermal transport. Varying the ICRF power provides a time dependent heat source, "S" in Eq. 10.3. Regular square-wave modulation allows the use of Fourier techniques which help to minimize the influence of sawteeth on the measurements.

10.5.1 Numerical solutions to the perturbed heat equation

One can solve the heat equation in cylindrical coordinates analytically for the special case of constant χ_e and no convection. The solutions obtained using this method fail to reproduce the amplitudes and phases of the temperature response to the modulated

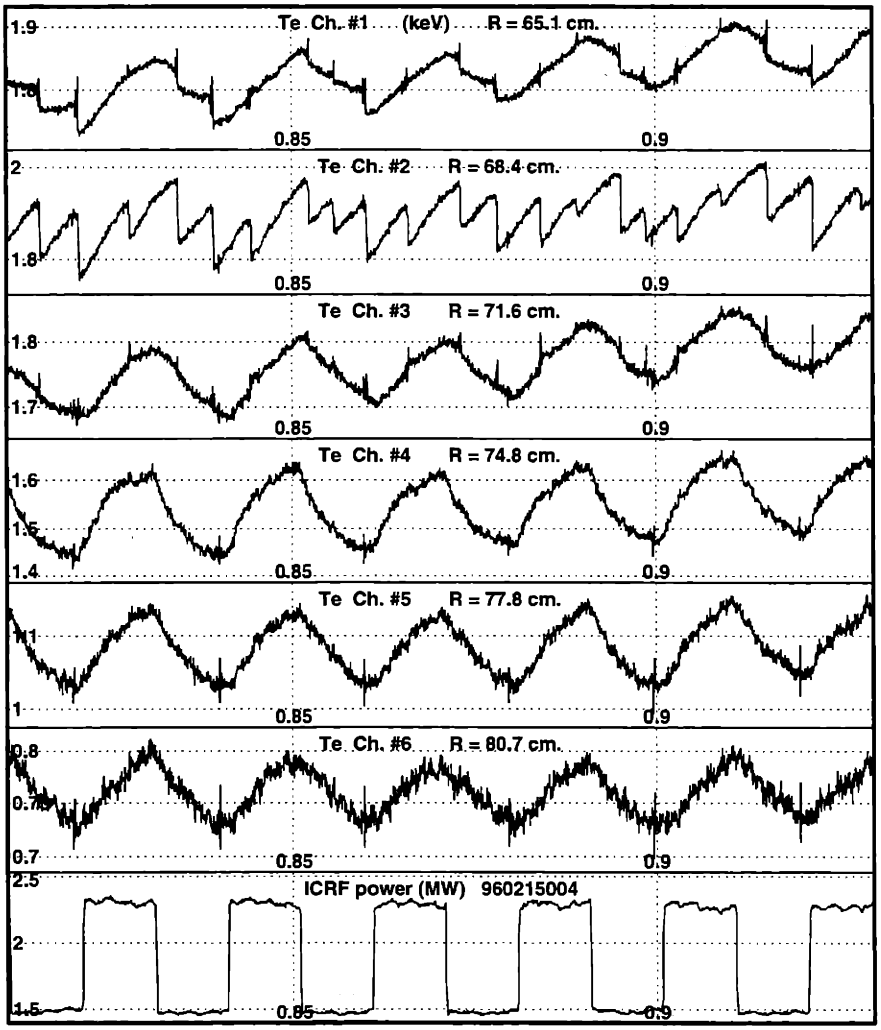

Figure 10-1: Example data from power modulation experiments for off-axis mode conversion heating. The break-in-slope measured power profile and the Fourier amplitudes of the temperature response at the modulation frequency, 50 Hz, are shown in Fig.10-3. The electron heating is strongest on channel four, and examination of this figure shows that the phase lag of the response is smallest at that location. Another interesting feature of this shot is that sawteeth are seen only on the central channel indicating a *very* small inversion radius. The absence of sawteeth helps considerably in the transport analysis. The plasma current was ≈ 650 kA and the central electron density was $\approx 2.2 \times 10^{20}\, m^{-3}$.

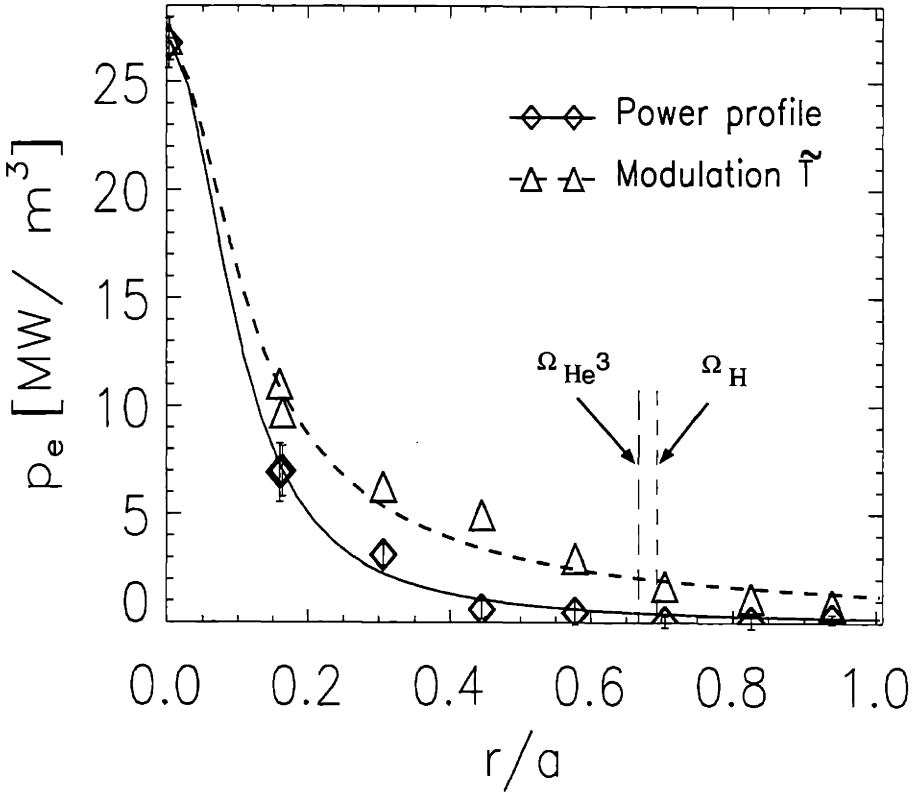

Figure 10-2: Shape comparison of the break-in-slope power profile and the 40 Hz modulation $\tilde{T}$ amplitude profile, for shot #950608017. The latter is broadened due to energy transport.

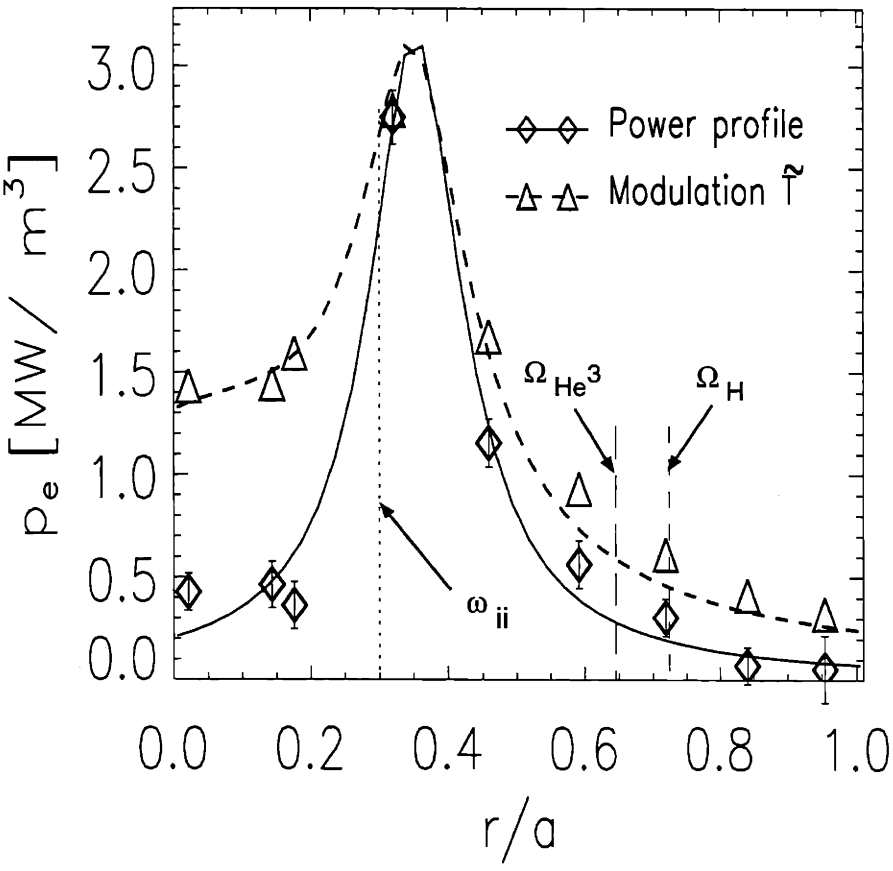

Figure 10-3: Shape comparison of the break-in-slope power profile and the 50 Hz modulation $\tilde{T}$ amplitude profile, for shot #960215004 ($H-He^3$ plasmas). The latter is broadened mainly due to the effects of energy transport.

power for either on axis or off axis heating. These results suggest that a much better fit to the data could be obtained using a spatially varying diffusivity profile, $\chi_e(r)$ which is smaller at the center of the tokamak than at the edge. Solving the perturbed heat equation with spatially varying diffusivity requires numerical methods. The solution method is summarized below:

- Solve the *perturbed heat equation:* With $\partial/\partial t \rightarrow -i\,\omega$ in Eq. 10.3 we obtain the equation to be solved:

$$-i\,\omega\,\tilde{T} = \nabla \cdot (2/3\,\chi(r)\nabla\tilde{T} - V(r)\tilde{T}) - \frac{\tilde{T}}{\tau} + \tilde{S(r)}. \tag{10.10}$$

  The $\tilde{T}$, and $\tilde{S}$ terms represent the fourier components at the modulation frequency. Following convention [100], the quantity solved for will actually be the *relative* temperature perturbation, $\frac{\tilde{T}}{T}$.

- Use a "Two-sweep" algorithm [101]: This numerical method is a convenient numerical approach which allows the boundary conditions on the perturbed temperature of zero-derivative at $r = 0$ and a specified value (amplitude and phase) to be specified at $r = a$.

- Vary the transport parameters: Can specify the diffusivity $\chi(r)$ and convective velocity, $V(r)$, and calculate the temperature response to the measured source, $\tilde{S}(r)$.

- Optimize the fits: Minimize the rms difference between the amplitude and phase of the measured and calculated temperature responses.

In the following four figures, the results of this process are shown for $V(r) = 0$ and a simple four parameter model for $\chi(r)$. The modelled diffusivity was allowed to have two "plateau" values with a smooth quadratic spline between them. The begin and end points for the transition region between the two plateaus provide the third and fourth degrees of freedom. Figure 10-4 shows an example profile which provided the best fit to the measurements for a wide range of values for each of the fitting

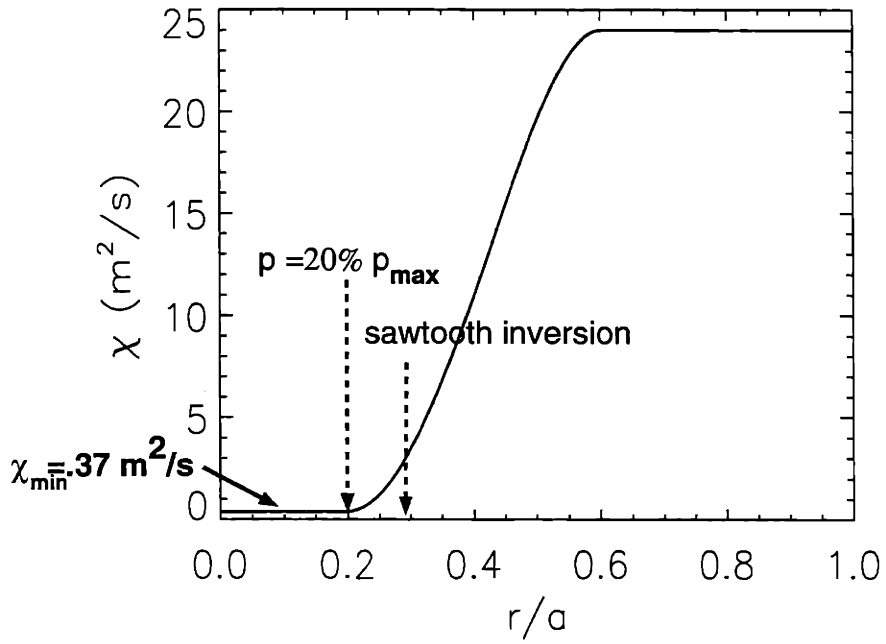

Figure 10-4: Best fit $\chi_e(r)$ profile to modulated on-axis mode conversion data. The perturbed heat diffusion equation is solved for a steady state modulation of the power profile shown in Fig. 10-2. The chi shown here predicts a response which minimizes the error with the experimentally measured amplitude and phase of the electron temperature response, shown in Fig. 10-5

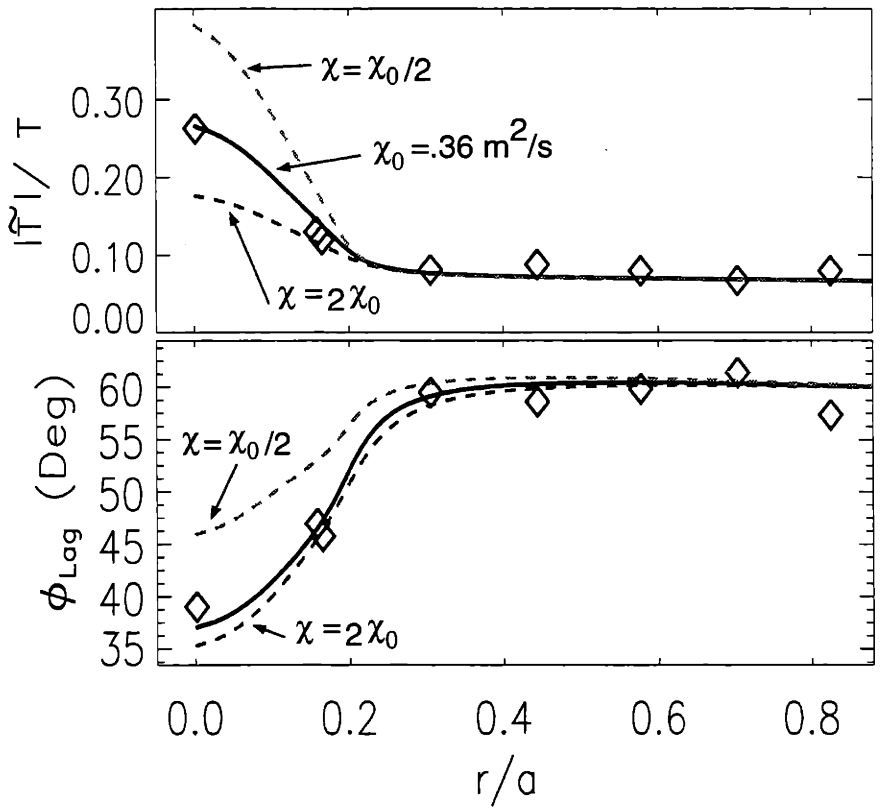

Figure 10-5: Best fits to the on-axis mode conversion power modulation data which result from a measured input power profile and the $\chi_e(r)$ profile shown in Fig. 10-4.

parameters. The most notable feature of this diffusivity profile is that the value inside the inversion radius is very much smaller than the value outside. This is in qualitative agreement with that seen in other tokamaks [99, 102]. Figure 10-5 shows the resulting amplitude and phase of the temperature response compared with measured values. As an indication of the sensitivity of the result, the fits resulting from doubling and halving the central diffusivity are also shown. The results of the same procedure for the off-axis heating case are shown in the following figures. The diffusivity profile needed to obtain the 'best' fit (Fig. 10-7) to the data required an extremely small values of χ_e near the peak in the heating, with a fifth fitting parameter added to allow better agreement with the measurements at the plasma core. The fit is somewhat forced and suggests the inclusion of an inward heat convection term. The following two plots show the results of *another* five parameter fitting scan, with the same four

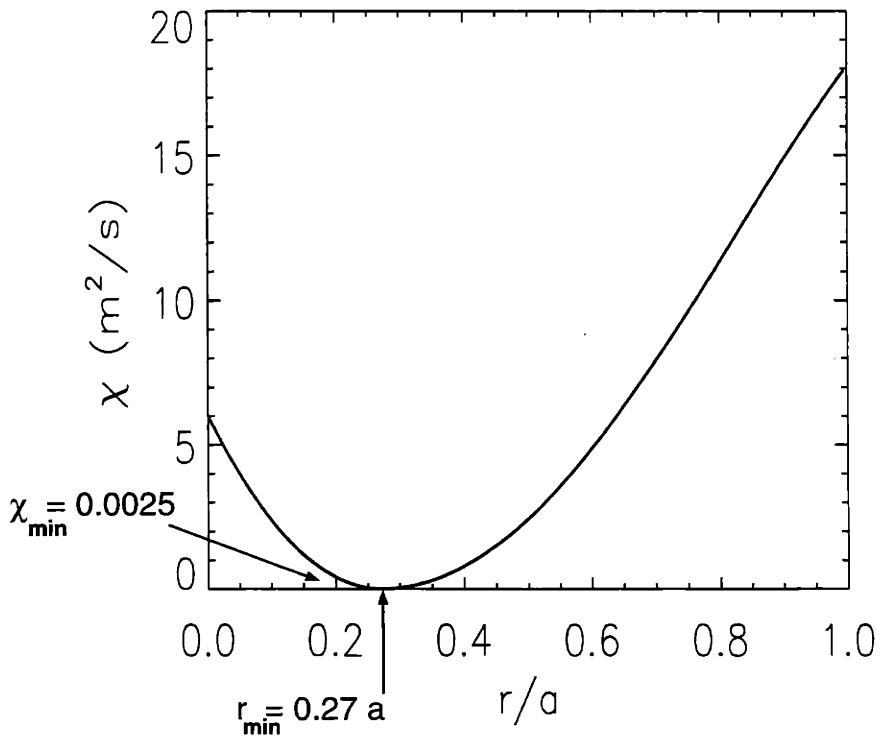

Figure 10-6: Best fit $\chi_e(r)$ profile to modulated off-axis mode conversion data. The perturbed heat diffusion equation is solved for a steady state modulation of the power profile shown in Fig. 10-3. The χ shown here predicts a response which minimizes the error with the experimentally measured amplitude and phase of the electron temperature response, shown in Fig. 10-7

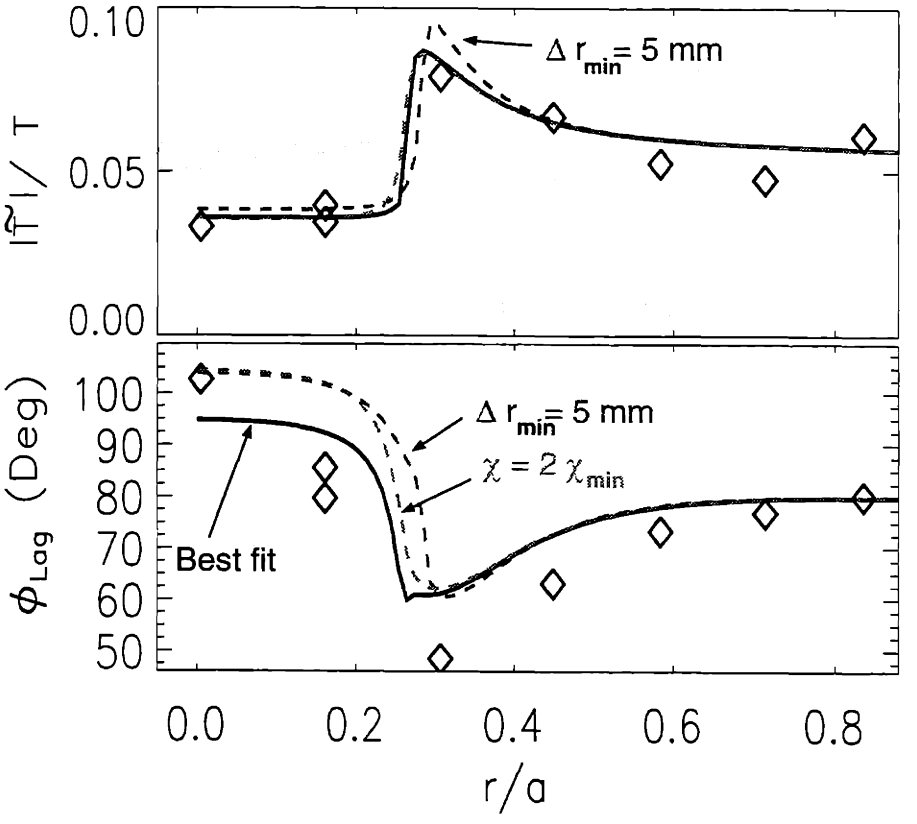

Figure 10-7: Best fits to the off-axis mode conversion power modulation data which result from a measured input power profile and the $\chi_e(r)$ profile shown in Fig. 10-6.

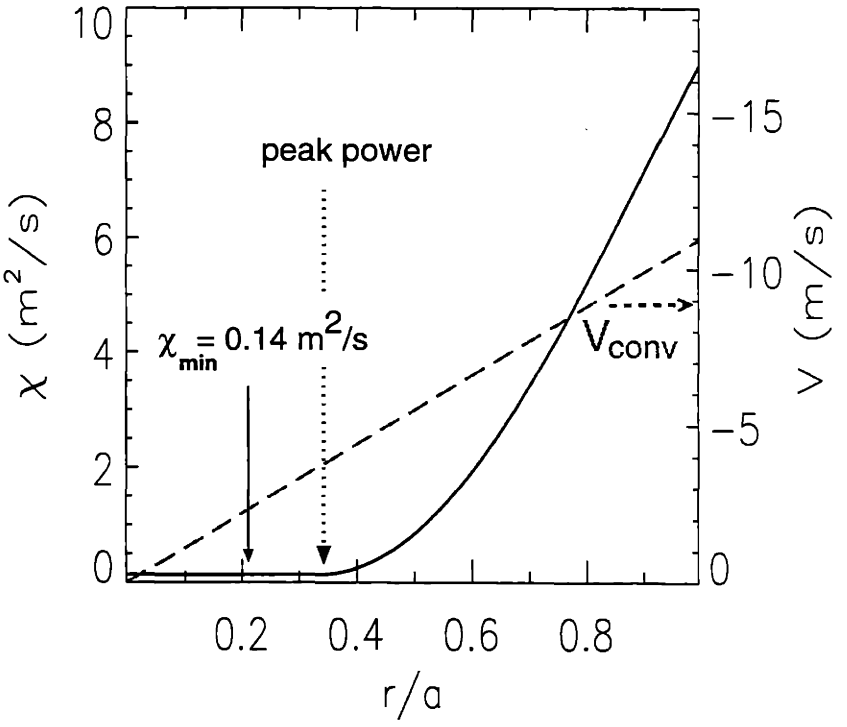

Figure 10-8: Best fit $\chi_e(r)$ and V(r) profiles to modulated off-axis mode conversion data. The perturbed heat diffusion equation is solved for a steady state modulation of the power profile shown in Fig. 10-3. The χ shown here predicts a response which minimizes the error with the experimentally measured amplitude and phase of the electron temperature response, shown in Fig. 10-9

parameters as before for χ and a linear velocity profile (to avoid divergence at r = 0) with a variable amplitude. A much better fit to the data is obtained with the introduction of inward heat pinch. A similar result was obtained from results with modulated off-axis ECH heating on the DIII-D tokamak [97]. To put these results in perspective, the following sections show the results of more standard measurements of the thermal diffusivity, χ.

10.6 Comparison with results from sawteeth

Sawtooth events in the core of the tokamak provide a "natural" source of temperature perturbations. The sudden drop of the central temperature gives rise to a heat pulse

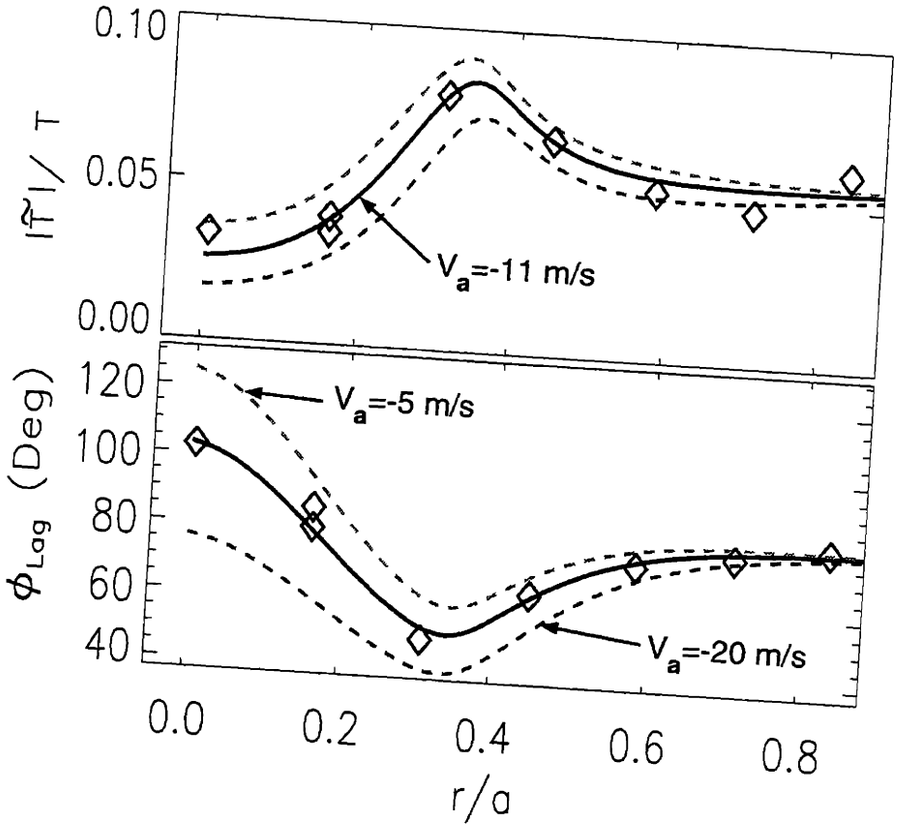

Figure 10-9: Best fits to the off-axis mode conversion power modulation data which result from a measured input power profile and the $\chi_e(r)$ and $V(r)$ profiles shown in Fig. 10-8. The inward convective velocity allows a much better fit than in Fig. 10-7

which propagates outward from the mixing radius. Nearly all C-Mod discharges exhibit sawtooth behavior, and this allows a basis for comparison with the results of power modulation experiments. Two standard analysis techniques and resulting measurements of χ_e are given below.

10.6.1 Phase Gradient method

Transport studies using the dynamics of sawteeth were first performed with measurements of soft x-ray emission [103]. Fourier analysis of a periodic source in Eq. 10.3 established the expected behavior of the phase lag in the sawtooth signal versus distance from the source. These studies established the diffusive nature of sawtooth heat pulses and began the study of transient transport in tokamaks which continues to be an area of active research [91]. Refinements of this first analysis yield a convenient expression for the evaluation of the thermal diffusivity: [104]:

$$\chi_e^{hp}|_{\text{phase}} = \frac{3n\omega_{st}}{4}\left(\frac{d\Psi}{dr}\right)^{-2} \tag{10.11}$$

where : $n\omega_{st}$ is the n^{th} harmonic of the sawtooth frequency.

and : Ψ is the sawtooth phase.

As shown in figure 10-10, the phase gradient for sawteeth can be roughly linear and for the case shown (same shot as the on-axis modulation case in the previous section) and Eq. 10.11 yields an estimate of $\chi_e \approx 0.7m^2/s$.

10.6.2 Time to peak

Near the mixing radius, the sawtooth heat pulse passes quickly and the measurement of the phase lag is adversely affected by noise during the relatively long "tails" which follow the heat pulse peak. Another analysis method [104] uses the delay from the

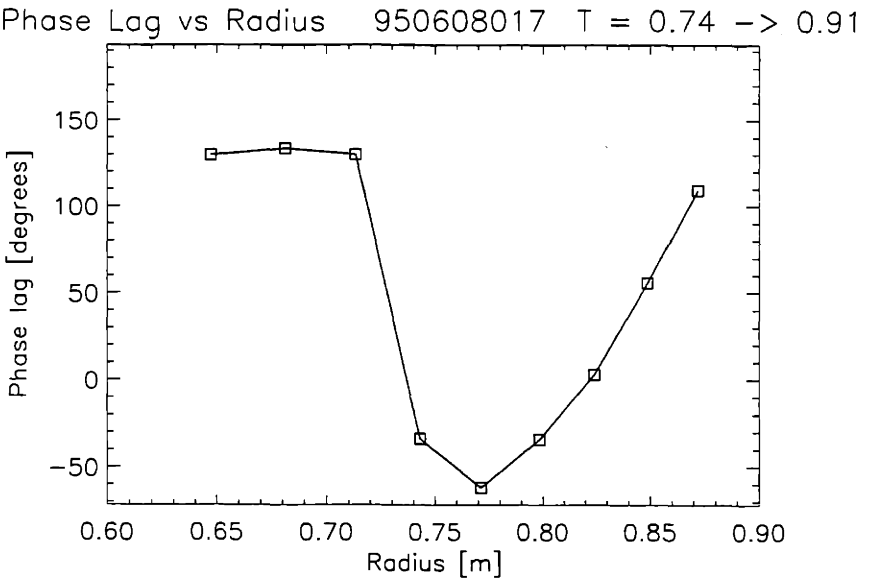

Figure 10-10: Sawtooth phase versus radius for shot 950608017. The roughly linear phase gradient outside the inversion radius is $\chi_e \approx 0.7 m^2/s$.

time of the central temperature crash to estimate χ_e :

$$\chi_e{}^{hp}|_{\text{ttp}} = \frac{1}{8}\frac{r^2 - r_{mix}^2}{t_{peak}(r)} \tag{10.12}$$

where : t_{peak} is the time lag in the temperature peak at minor radius r.

and : r_{mix} is the "mixing radius".

Measurements from the same shot used above (see Fig. 10-11) can be used to estimate the diffusivity and yield $\chi_e \approx 1 m^2/s$. This value is similar to the estimate made using the phase gradient technique and is intermediate to the extremes in $\chi(r)$ shown for the same shot in Fig. 10-4. The assumption of constant χ made in the sawtooth measurements of the diffusivity is an obvious barrier to further comparisons.

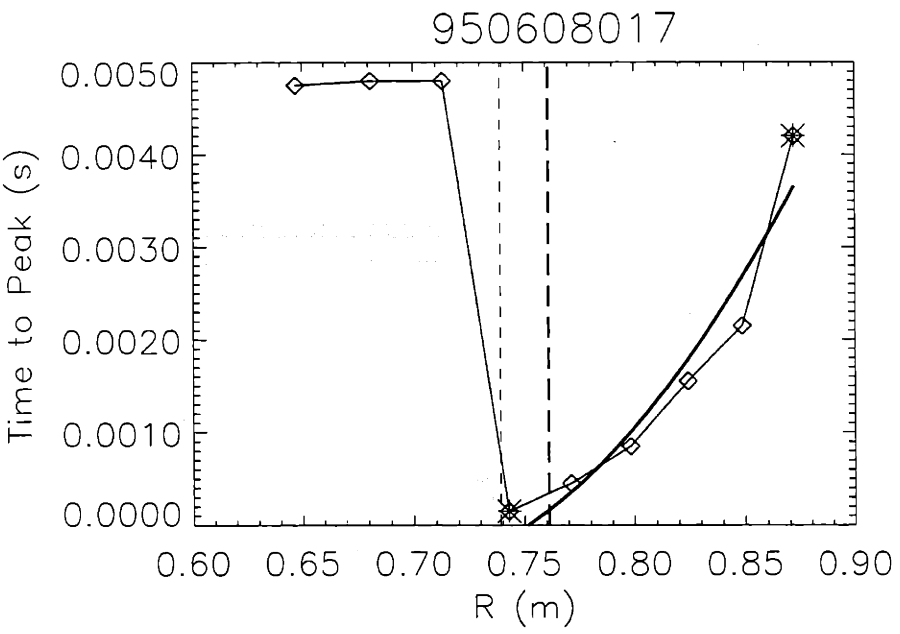

Figure 10-11: Time to peak versus radius for sawteeth on shot 950608017. The dark solid line indicates a parabolic fit consistent with $\chi_e \approx 1m^2/s$.

10.7 Comparison with equilibrium transport

A general result from transport studies in tokamaks is that the perturbed plasma thermal diffusivity is generally higher than the values obtained from steady state analysis. This trend is not well understood, but the expression for the effective diffusion coefficient in Eq. 10.4 suggests a dependance of χ on the temperature gradients may be responsible. The existence of critical gradients giving rise to sporadic microscopic transport events is currently one of the popular theories [84]. Fundamental transport theory is not the topic of this section but rather the motivation for quickly comparing the modulation results with simple steady state values.

10.7.1 Global energy confinement

One of the most important parameters for a fusion grade plasma is its energy confinement time (recall Eq. 1.2) which is related to its total stored energy, W_{tot}, and

total input power, P_{tot} through:

$$\tau_E \equiv \frac{W_{tot}}{P_{tot}} = \frac{< \frac{3}{2} nT > \ Volume}{P_{tot}}. \tag{10.13}$$

As the energy confinement time, τ_E, is ultimately determined by the thermal diffusivity, it is easily expressible in terms of an effective power balance diffusivities, $\chi_{p.b.}$. To provide a simple expression, solve the power balance equation, Eq. 10.1, in steady state ($\partial/\partial t \rightarrow 0$) for zero flows and constant χ. Specifying a power profile yields an equilibrium temperature profile and these can be used to to evaluate τ_E. For a parabolic power profile, the result is

$$\chi_{p.b.} = \frac{a^2}{6\tau_E} \tag{10.14}$$

In general, the thermal transport for ions and electrons in a plasma is different[2]. With appropriate subscripts, the above expressions can be applied equally well either to the entire plasma or to the ion and electron species separately. When the coupling between electrons and ions is strong, the total input power is efficiently distributed between ions and electrons and the overall confinement time is given by

$$\frac{1}{\tau_E} = \frac{1}{\tau_{Ee}} + \frac{1}{\tau_{Ei}} \tag{10.15}$$

independent of which species is being heated directly. With the assumption that $\tau_{Ei} \gg \tau_{Ee}$, Eq. 10.15 yields a conservative estimate for the characteristic electron thermal diffusivity from the global energy confinement time:

$$\chi_e|_{global} \lesssim [0.5 \rightarrow 1] \times \left(\frac{a^2}{6\tau_E}\right) \tag{10.16}$$

The energy confinement time was approximately 30 msec for the examples of modulated transport. This gives a rough estimate from global power balance considerations

[2]Neoclassical theory predicts that the thermal diffusion for *ions* is larger than that for electrons by a factor $\approx \sqrt{M_i/m_e}$, however electron transport is often so "anomalously" high in tokamaks that it can dominate the overall heat transport.

of $\approx 0.15 m^2/s$.

10.7.2 Steady state temperature profiles

A more direct method for making comparisons with equilibrium plasma results is obtained by comparing the edge gradient of the steady state *electron* temperature profile to the estimated power flow across the corresponding flux surface. Assuming that the net power, $P_{enclosed}$ (ohmic plus ICRF minus radiation), which is deposited within the flux surface at radius r diffuses across the flux surface of area $A(r)$ due to the local temperature gradient, we obtain the expression:

$$n\chi\nabla T_e(r) = q(r) = \frac{P_{enclosed}(r)}{A(r)} \tag{10.17}$$

The electron temperature profiles on Alcator C-Mod have a characteristic shape with a nearly linear decay for minor radii $r \gtrsim a/3$. A simple but robust estimate of the temperature gradient toward the outer edge of the plasma is given by $\nabla T_e(0.5a \lesssim r \lesssim 0.8a) \approx T_e(0)/a$. Furthermore, for a wide variety of power profile shapes, a good estimate (producing conservative errors of $\lesssim 30\%$ in the resulting χ estimate) of the power density across the plasma surface at $r \approx 0.7a$ is the corresponding value at the plasma edge, i.e.:

$$\left.\frac{P_{enclosed}(r)}{A(r)}\right|_{r\approx 0.7a} \lesssim \frac{P_{enclosed}(a)}{A(a)} = \frac{P_{tot}}{4\pi^2 R_0\sqrt{\kappa}a}, \tag{10.18}$$

where κ is the vertical elongation of the flux surfaces at the plasma edge. If we further assume that the electrons carry out between $50\% \rightarrow 100\%$ of the total power, we obtain an expression which can be used to estimate the value of χ_e implied by the equilibrium temperature profile:

$$\begin{aligned} \chi_e|_{\text{edge profile}} &= [0.5 \rightarrow 1] \times \left(\frac{P_{tot}}{4\pi^2 R_0\sqrt{\kappa}\ n_0 T_0}\right) \\ &\approx [0.5 \rightarrow 1] \times 1.6\, m^2/s\, \frac{P_{tot}(MW)}{R_0(m)\sqrt{\kappa}\ n_0(10^{20}m^{-3})T_0(keV)} \end{aligned} \tag{10.19}$$

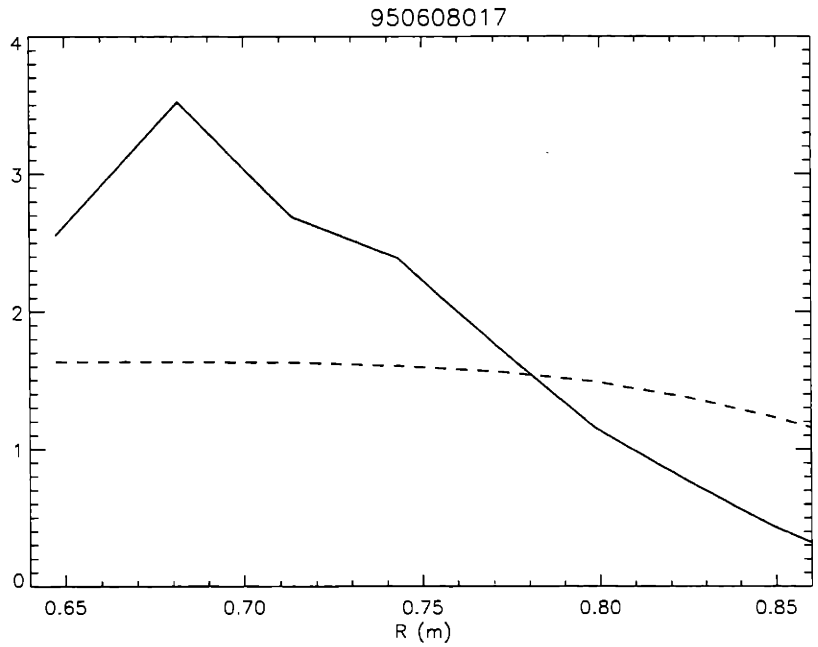

Figure 10-12: Time averaged temperature and density profiles for shot 950608017. The y-axis gives the temperature in keV and the density in units $10^{20}m^{-3}$. Using this profile to estimate χ_e from Eq. 10.19 yields a value of $\chi_e \approx 0.9m^2/s$.

From the profile shown in Fig. 10-12, for which the was approximately 2.5 MW of total power, Eq. 10.19 yields an estimate of $\chi_e \approx 0.9m^2/s$. This value is considerably larger than that obtained from global power balance considerations. Taken together these results suggest that even steady state measurements indicate evidence for a diffusivity profile which is considerably smaller in the core than near the outer edge. The general magnitudes of the steady state diffusivity estimates are smaller than that obtained from the perturbative techniques discussed earlier. This is also consistent with results using a variety of methods on virtually every tokamak [91].

10.8 Future Work

It is hoped that the brief treatment transient thermal transport given earlier in this chapter indicates the usefulness of power modulation experiments on Alcator C-Mod. The method can provide a degree of spatial resolution in χ measurements which is very

difficult to do using other methods. In order for to make important inferences about the underlying causes for the thermal transport in Alcator C-Mod, a systematic scan of plasma parameters is required. To avoid the difficulties associated with heating profile broadening seen in Chapt. 8, it is recommended that mode conversion heating in $D(He^3)$ be used for any future studies. The 80 MHz transmitters used for the experiments in Chapt. 7 limited mode conversion heating to the high field side of the machine. In the coming campaign, ICRF power at 40 MHz will be available for the first time. As discussed in the first part of this chapter, it is also recommended that the power be modulated at higher frequencies than those used here.

Appendix A

He^3 fraction measurement

The behavior of mode conversion heating is sensitive to the relative amount of He^3 in the plasma. Unfortunately, direct measurements of the fraction of He^3 in the plasma core are quite difficult on Alcator C-Mod. Charge exchange spectroscopy of He^3 at the high densities of C-Mod plasmas is very difficult because it requires two charge exchange events which is very unlikely. Spectroscopic measurements of helium radiation are sensitive only to the extreme plasma edge. The helium fraction can in principle be obtained from visible bremsstrahlung measurements which yield the effective atomic number of the plasma, Z_{eff}. A pure deuterium or hydrogen plasma has $Z_{eff} \equiv 1$. The increment to Z_{eff} due to the presence of an impurity ion, i, is given by:

$$\Delta Z_{eff}|_i = Z_i(Z_i - 1)\frac{n_i}{n_e} \tag{A.1}$$

Thus :

$$\left.\frac{n_{He^3}}{n_e}\right|_{\Delta Z_{eff}} = \frac{\Delta Z_{eff}|_{He^3}}{2} \tag{A.2}$$

In practice the noise and uncertainty levels in Z_{eff} make the ΔZ_{eff} measurement useful only for relatively heavy He^3 puffing. As Z_{eff} is also sensitive to radiation from higher Z trace impurities, the method can overestimate the amount of helium

in the tokamak. A more straightforward method of calculating the helium fraction is to observe the response of the total electron density to an injection of He^3 gas. If a short strong puff of He^3 is made, the immediate rise in the electron density can be attributed to the ionization of the helium making it into the discharge. Obviously :

$$\left.\frac{n_{He^3}}{n_e}\right|_{\Delta n_e} = \frac{\Delta n_e|_{He^3}}{2n_e} \tag{A.3}$$

Both of these methods need a strong gas puff to make a reliable estimate of the helium fraction. One cannot in general expect to apply the techniques for every shot. Instead, an absolute calibration is established for a strong puff and then scaled to weaker puffs. This method assumes that the gas feed method can precisely control the *relative* amount of He^3 delivered on a shot and that the *absolute* level can be measured accurately for high puffing levels.

The helium gas was introduced into the discharges through a seperate valve from those controlling the working gas (either deuterium or hydrogen). The piezoelectric valves used have a conductance vs. applied voltage characteristic which is highly nonlinear but do have a well defined "full-on" position. To accurately control the amount of helium introduced into a given discharge, the piezo valve was pulsed fully on with a top-hat voltage signal whose length is assumed to be proportional to the amount of helium introduced. Because helium recycles from the vacuum vessel walls very efficiently, the amount of helium in the discharge is determined solely by the puffing history on that particular shot. A small post puff pedestal voltage was often maintained on the piezo valve to compensate for losses due to pumping. This level was adjusted to maintain roughly constant levels of HeII emission at the plasma edge as seen by the McPherson or University of Maryland spectrograph.

The upshots of these measurements are that the linearity assumption is good, the deadtime is small < 4 ms, the idea of screening is a good one, and the screening measured is $40\% \pm 15\%$

Absolute calibration of the technique was established on shots with a He^3 gas puff of length $\gtrsim 100ms$ by estimating the incremental electron density and Z_{eff}

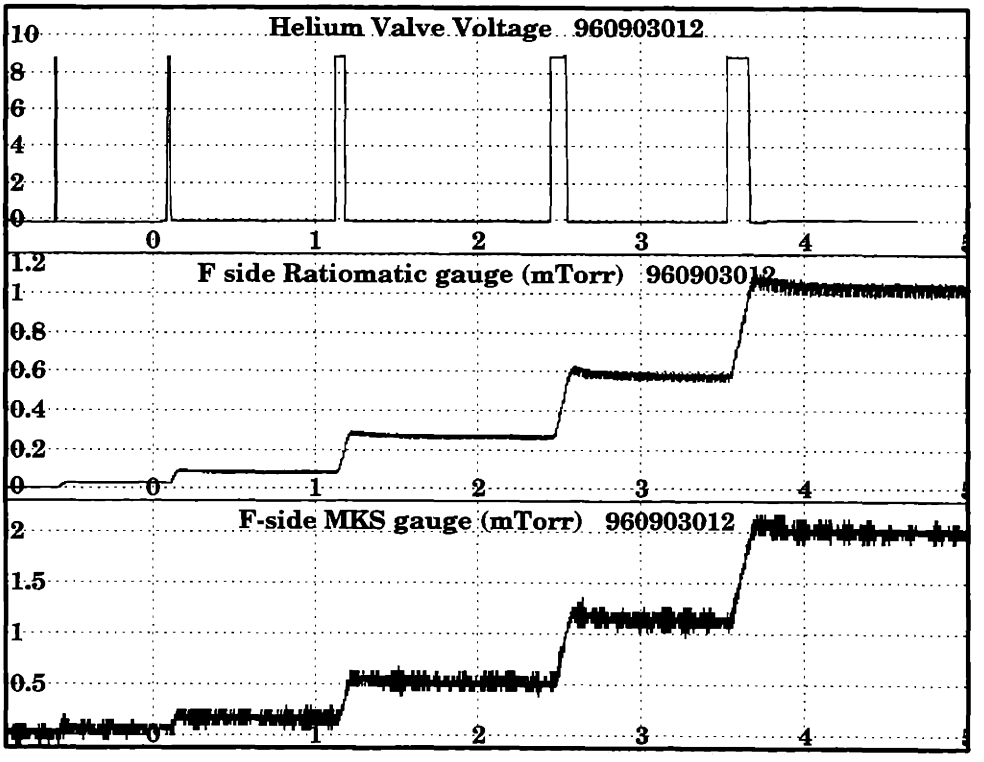

Figure A-1: Helium valve gas puff calibration test shot. He^3 gas was puffed into the evacuated vessel in the absence of plasma with a series of pulses to the piezoelectric valve. The neutral gas pressure response was recorded with both an MKS diaphragm gas gage and the ratiomatic ion gage.

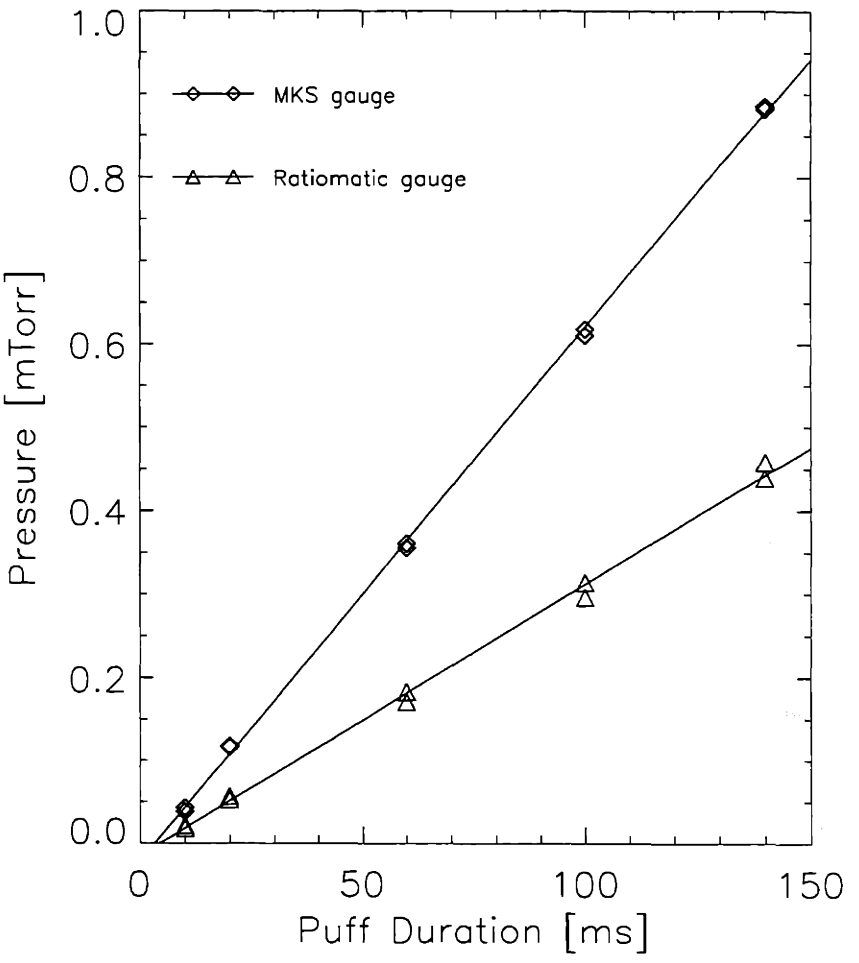

Figure A-2: Analysis of the test data of Fig. A-1. Plotted are the increments in the vessel pressure as measured by the two pressure gages versus the gas puff duration for two identicle test shots. The MKS diaphragm gage is sensitive to direct pressure and is absolutely calibrated. The ratiomatic gage (Granville Phillips series 303) is calibrated for deuterium gas. The sensitivity of the ion gage for deuterium relative to helium is published as 1.96 and with this correction, the two gages agree very well. The valve characteristics are very linear and extrapolation to zero-pressure gives an estimated "dead-time" for the valve of $\approx 3.5 msec.$

as described above. Figure A-3 illustrates the procedure. The helium piezoelectric valve is opened fully at t = 0.55 seconds for 130 milliseconds. The fraction of the density due to helium is inferred from the density rise following the helium puff. As the density begins to rise in response to the strong helium puff, the hydrogen gas puffing stops completely. Previous gas puffing tests under similar conditions (shot #951214004) indicated that the hydrogen density has a 1/e decay time of $\approx 600ms$. After accounting for the decay of the background hydrogen density it is found that at t = 0.7 seconds the fraction of the electron density due to the He^3 puff is $\approx 0.52 \pm 0.1$. The corresponding increase in Z-effective is $\Delta Z_{eff} \approx 0.55 \pm 0.2$, Thus the methods agree and together give an estimate for $n_{He^3}/n_e \approx 0.27 \pm 0.05$. With the assumption that the amount of helium introduced is proportional to the duration of the gas puff, we obtain the following calibration formula for the helium fraction in a given plasma:

$$f_{He^3} \equiv n_{He^3}/n_e = \frac{\text{(puff duration - dead-time)}}{100ms} \quad \frac{0.5 \times 10^{20}[m^{-3}]}{n_e(0)} \tag{A.4}$$

The quantity f is closely tied to experimentally measured values and will be used preferentially to describe ion concentrations in this thesis. However, in the literature and thus in some equations in this document (e.g. 3.24 and 8.2) the density of an ion species is specified by X, the ion density relative to the total *ion* density instead of the total *electron* density.

$$X_i = \frac{f_i}{\sum f_i} \qquad f_i = \frac{X_i}{\sum X_i Z_i} \tag{A.5}$$

For a two species plasma, the two quantities are related through the expression:

$$X_1 = \frac{f_1 \, Z_2}{1 + f_1 \, (Z_2 - Z_1)} \tag{A.6}$$

Thus for mode conversion experiments in either hydrogen or deuterium, we can express the He^3 ion fraction simply by:

$$X_{He^3} = \frac{f_{He^3}}{1 - f_{He^3}} \tag{A.7}$$

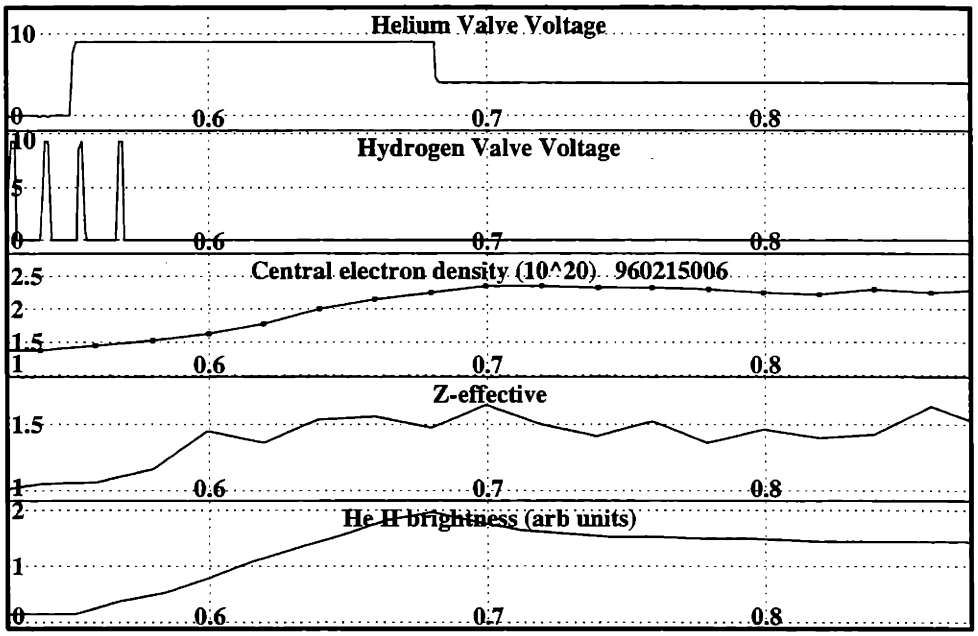

Figure A-3: Helium gas puff calibration shot. At 0.55 seconds, the He^3 piezoelectric valve is pulsed at full voltage for 130ms. The hydrogen gas valve stops puffing shortly after the helium valve opens. The amount of helium introduced is inferred from the rise in both density and Z_{eff}. Equations A.2 and A.3 yield similar estimates for the helium fraction, in this case $n_{He^3}/n_e \approx 0.27 \pm 0.05$.

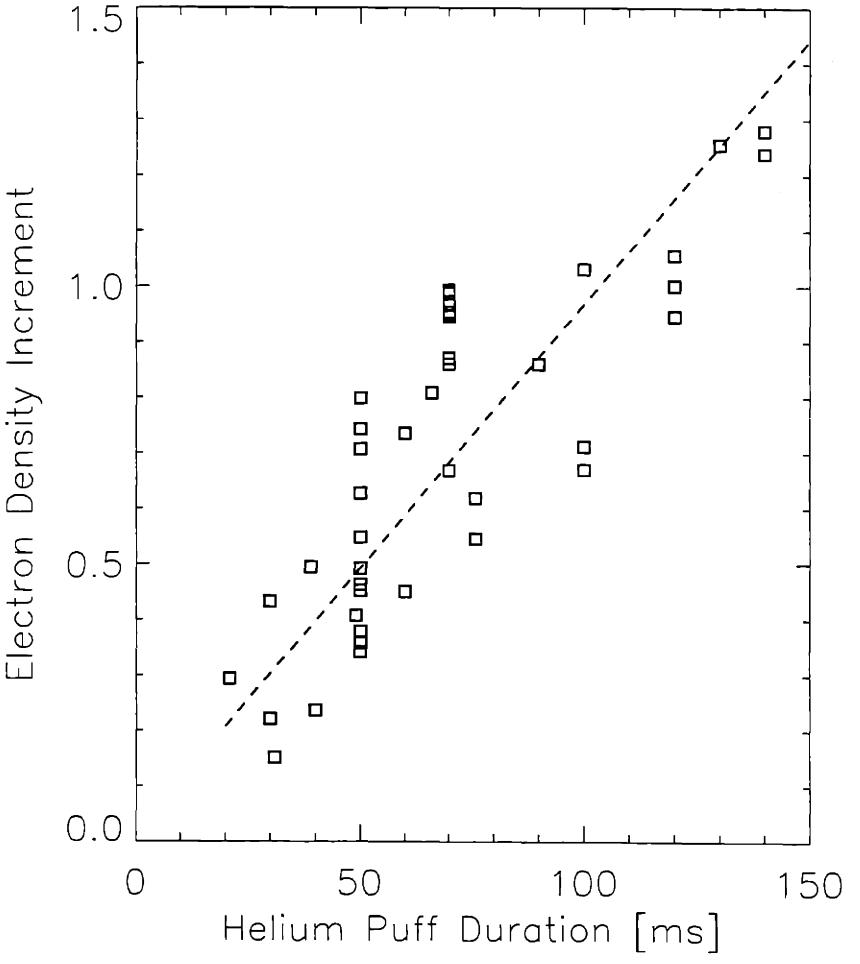

Figure A-4: Figure showing the central electron density rise as a function of the length of time that the helium gas valve was open. The straight line fit is used to determine the He^3 screening ($\approx 40\%$). The units of the y-axis are $10^{20}m^{-3}$.

Appendix B

Low pass filter grating design

In this section, the salient features of the art of filter design are given which motivated the improvements to the existing filter set and which can be a guide if further improvements prove necessary.

It is important to emphasize the importance of the orientation of the filter grating grooves to both the optics plane and the electric field polarization.

B.1 Importance of polarization

In the regime of $\lambda \approx d$, the behavior of diffraction gratings is highly sensitive to the the polarization. Effective low-pass filtering requires the use of linearly polarized light with the electric field oriented *perpendicular* to the grooves of the grating. This so-called "S" polarization exhibits highly anomolous behavior when compared to the more regular behavior of the "P" polarization where the wave electric field runs along the grating grooves. Although these anomolies require the use of sophisticated simulation codes for detailed analysis, they also produce sharp features in the frequency characteristics which are utilized in filter design. The selection of X-mode from the tokamak emission, using a wire grid polarizer, automatically results in linearly polarized light. Care must be taken to maintain the proper polarization throughout the GPC optics. wire grids which split the To produce the proper polarization at the filter grating while maintaining high efficiency power throughput, a polarization ro-

tater assembly (seen sketched in Fig. 5-3) was added to the MTX system by Lasnier, to correct misalignments introduced by the beamsplitter.

B.2 Importance of the optics plane orientation

Figure 5-4 shows the standard grating geometry with the plane of the incident and diffracted beams perpendicular to the grooves. This is the configuration of the main diffraction grating of the GPC. From this figure it should be apparent that there is a cutoff condition for diffraction corresponding to $\delta|_{m=1} = \pi/2$. The grating behaves as a mirror beyond a critical wavelength, $\lambda|_c$, which follows from Eq. 5.1:

$$\lambda_{c\perp} = d\,(\sin\theta + 1) \tag{B.1}$$

For standard C-Mod operation ($\theta \approx 12°$, $d \approx 1.1\ \lambda_{max}$) this cutoff is of little consequence.

The basic geometry for the GPC *filter* gratings is different from the above. The grating still uses the "S" polarization, but the optics axis is oriented *parallel* to the grooves as shown in Fig. 5-3. In this case the diffraction is out of the optics plane and experiences cutoff at the wavelength:

$$\lambda_{c\|} = d\,\cos\theta \tag{B.2}$$

Light with wavelengths longer (lower frequency) than $\lambda_{c\|}$ are reflected efficiently and pass into the main optics enclosure. High frequencies experience significant m=1 diffraction (enhanced by the careful choice of blaze angle, $\beta \approx 18°$ for our filters), deflect out of the beampath and are dumped onto Eccosorb baffles. It should be noted that filter gratings generally have zones of leakage at high frequency near $\lambda_c/2$, $\lambda_c/3$, $\cdots$. The selection of the parallel groove orientation was made partly due to a broader stop band than in the standard orientation.

Bibliography

[1] J. Wesson, *Tokamaks*, Oxford University Press, 1987.

[2] F. F. Chen, *Introduction to Plasma Physics and Controled Fusion*, volume 1, Plenum Press, 1984.

[3] J. Lawson, *Proceedings of the Physical Society B*, **70** (1957).

[4] S. Kaye and R. Goldston, *Nuclear Fusion*, **25**, 65 (1985).

[5] P. Yushmanov, *Nucl. Fusion*, **30**, 1999 (1990).

[6] I. Hutchinson et al., *Phys. Plasmas*, **1**, 1511 (1994).

[7] C. Fiore et al., *Rev. Sci. Instrum.*, **63**, 4530 (1992).

[8] J. Rice et al., *Phys. Rev. A*, **51**, 1995 (1995).

[9] R. Watterson et al., Presented at the 36^{th} annual meeting of the American Physical Society, DPP, 1995.

[10] A. Hubbard, T. C. Hsu, and P. J. O'Shea, Alcator C-Mod papers presented at the 9^{th} joint workshop on electron cyclotron emission & electron cyclotron resonance heating, Technical Report PFC/JA-95-11, MIT Plasma Fusion Center, 1995.

[11] T. H. Hsu, *The submillimeter wave electron cyclotron emission diagnostic for the Alcator C-Mod Tokamak*, PhD thesis, MIT, 1993.

[12] T. H. Stix, *The theory of plasma waves*, McGraw-Hill Book Company, 1962.

[13] J. D. Moody, *Ion Bernstein wave experiments on the Alcator C tokamak*, PhD thesis, MIT, 1982.

[14] F. Perkins, *IEEE Transactions on Plasma Science*, **PS-12**, 53 (1984).

[15] M. Porkolab, Plasma heating by fast magnetosonic waves in tokamaks, in *Advances in Plasma Physics*, 1993, PSFC report no. PFC/JA-93-19, Invited lecture presented at the Stix Symposium.

[16] H. Takahashi et al., *Phys. Rev. Lett.*, **39**, 31 (1977).

[17] N. Ivanov, I. Kovan, and Y. Sokolov, *J.E.T.P.*, **21**, 316 (1976).

[18] G. W. Hammett, *Fast ion studies of ion cyclotron heating in the PLT tokamak*, PhD thesis, Princeton University, 1986.

[19] T. Stix, *Plasma Physics*, **14**, 367 (1972).

[20] T. Stix, *Nucl. Fusion*, **15**, 737 (1975).

[21] R. Prater and R. James, *Plasma Phys. Control. Fusion*, **35**, A53 (1993).

[22] M. Murakami et al., Fast wave direct electron heating in TFTR, Number 289, pages 48–51, AIP, 1994.

[23] P. Bonoli et al., Electron heating via mode converted ion Bernstein waves in the Alcator C-Mod tokamak, Denver,CO, 1996, American Physical Society, Division of Plasma Physics, Invited talk.

[24] R. Majeski et al., *Phys. Rev. Lett.*, **76**, 764 (1996).

[25] B. Saoutic et al., *Phys. Rev. Lett.*, **76**, 1647 (1996).

[26] S. Wukitch, ICRF experiments on ASDEX, Private communication, 1997.

[27] S. Buchsbaum, *Phys. Fluids*, **3**, 418 (1960).

[28] R. Cairns, *Phys. Fluids*, **26**, 1268 (1983).

[29] M. Brambilla and M. Ottaviani, *Plasma Phys. Control. Fusion*, **27**, 1 (1985).

[30] D. Swanson, *Phys. Fluids*, **28**, 2645 (1985).

[31] J. Jacquinot and B. McVey, *Phys. Rev. Lett.*, **39**, 88 (1977).

[32] D. Fried and S. Conte, *The plasma dispersion function*, Academic Press, New York, 1961.

[33] G. Wurden, M. Ono, and K. Wong, *Phys. Rev. A*, **26**, 2297 (1982).

[34] V. Bhatnagar et al., (1992), JET-P(92)49 report. Preprint of paper submitted to Nuclear Fusion.

[35] J. Hosea et al., *Phys. Rev. Lett.*, **43**, 1802 (1979).

[36] J. Adam, *Plasma Phys. Control. Fusion*, **29**, 443 (1987).

[37] C. Chow, V. Fuchs, and A. Bers, *Phys. Fluids B*, **2**, 1089 (1990).

[38] D. Swanson and Y. Ngan, *Phys. Rev. Lett.*, **35**, 517 (1975).

[39] R. Majeski and C. Phillips, *Phys. Rev. Lett.*, **73**, 2204 (1994).

[40] B. Trubnikov and A. Bazhanova, *Plasma physics and the problem of controlled thermonuclear reactions*, volume 3, Pergamon Press, Oxford, UK, 1959.

[41] F. Engelman and M. Curatolo, *Nucl. Fusion*, **13**, 497 (1973).

[42] I. H. Hutchinson, *Principles of Plasma Diagnostics*, Cambridge University Press, 1987.

[43] B. Trubnikov et al., *Soviet Physics-Doklady*, **3**, 136 (1958).

[44] M. Bornatici et al., *Nucl. Fusion*, **23**, 1153 (1983).

[45] G.D.Tait, F. Stauffer, and D. Boyd, *Phys. Fluids*, **24**, 719 (1981).

[46] M. Kimmitt, *Far-Infrared techniques*, Pion Ltd., london edition, 1972.

[47] J. Fischer, D. Boyd, A. Cavallo, and J. Benson, *Rev. Sci. Instrum.*, **54**, 1085 (1983).

[48] C. C. Gomez, *Study of electron temperature evolution during satoothing and pellet injection using thermal electron cyclotron emission in the Alcator C tokamak*, PhD thesis, MIT, 1986.

[49] S. Ishida and A. Nagashima, *Rev. Sci. Instrum.*, **61**, 2834 (1990).

[50] E. Hecht, *Optics*, Addison-Wesley, Menlo Park, CA, 1987.

[51] D. T. Garnier, *Lithium Pellet Injection Experiments on the Alcator C-Mod Tokamak*, Ph.d. thesis, Massachusetts Institute of Technology, 1996.

[52] R. S. Granetz et al., *Nuclear Fusion*, **36** (1996).

[53] S. Guharay and D. Boyd, *Rev. Sci. Instrum.*, **61**, 3520 (1990).

[54] A. Siegman, *Lasers*, University Science Books, Mill Valley, California, 1986.

[55] P. W. Rosenkranz, Absorption of microwaves by atmospheric gases, in *Atmospheric Remote Sensing by Microwave Radiometry*, edited by M. A. Janssen, Wiley Series in Remote Sensing, chapter 2, Wiley, New York, 1993.

[56] E. H. Putley, *Applied Optics*, (1965).

[57] L. L. Lao, H. St. John, R. D. Stambaugh, A. G. Kellman, and W. Pfeiffer, *Nucl. Fusion*, **25**, 1611 (1985).

[58] S. Guharay, Design notes on the U. Maryland Grating Polychromator, 1989.

[59] I. Wilson and L. Botten, *J. Optics*, **8**, 217 (1977).

[60] G. Tait, Diffraction gratings as far-infrared lowpass filters, Technical report, University of Maryland, College Park, Maryland 20742, 1979.

[61] R. Petit, *Electromagnetic Theory of Gratings*, Springer-Verlag, Berlin, 1980.

[62] R. McPhedran and M. Waterworth, *Optica Acta*, **20**, 177.

[63] A. Cavallo and R. Cutler, *Rev. Sci. Instrum.*, **59**, 889 (1988).

[64] O. Tudisco, Grating low-pass filters, Technical report, Area Nucleare, Diparimento Fusione, report no. RT/Nucl/90/38, Frascati, 1990.

[65] S. Guharay, U. of Maryland, Private communication.

[66] A. Hubbard et al., Local plasma parameters and H-mode threshold in Alcator C-Mod, in *Proceedings from the 16th IAEA fusion energy conference*, number IAEA-CN-64/AP2-11, 1996.

[67] P. Belland and J. Crenn, *International Journal of Infrared and Millimeter Waves*, **10**, 1279 (1989).

[68] A. Balkcum, R. Ellis, D. Boyd, and S. Guharay, *International Journal of Infrared and Millimeter Waves*, **13**, 1321 (1992).

[69] M. May et al., Accepted for publication in Nuclear Fusion.

[70] *Fast wave direct electron heating in TFTR*, Boston, MA, 1993.

[71] D. Gambier et al., *Nucl. Fusion*, **30**, 23 (1990).

[72] T. Luke, *Measurement of Particle Transport Coefficients on Alcator C-Mod*, Ph.d. thesis, Massachusetts Institute of Technology, 1994.

[73] S. Wolfe, Alcator C-Mod principal research scientist, private communication.

[74] J. Hosea et al., *Plasma Phys. Control. Fusion*, **28**, 1241 (1986).

[75] Y. Takase et al., (1996), MIT PSFC report no. PFC/JA-96-9, To be published in Plasma Phys. Control. Fusion.

[76] International school of plasma physics, *Course and workshop on applications of RF waves to tokamak plasmas*, volume 1, Italy, 1985, Monotypia Franchi.

[77] A. Ram and A. Bers, *Phys. Fluids B*, **3**, 1059 (1991).

[78] J. Wilson, J.C.Hosea, B. Leblanc, and C. Phillips, ICRF heating experiments on TFTR: an overview, Denver, CO, 1996, American Physical Society, 38^{th} annual meeting of the Division of Plasma Physics.

[79] D. Anderson et al., (1994), JET report JET-P(94)64, preprint of article submitted to Plasma Phys. Control. Fusion.

[80] W. Core, (1994), JET report JET-P(94)02, preprint of article submitted to Nucl. Fusion Letters.

[81] S. I. Braginskii, Transport processes in a plasma, in *Reviews of Plasma Physics*, edited by M. A. Leontovich, pages 205–311, Consultants Bureau, New York, 1965.

[82] F. L. Hinton and R. D. Hazeltine, *Rev. Mod. Phys.*, **48**, 239 (1976).

[83] J. Hugill, *Nucl. Fusion*, **23**, 331 (1983).

[84] B. Carreras, *Plasma Phys. Control. Fusion*, **34**, 1825 (1992).

[85] C. Barnes et al., *Phys. Fluids*, **26**, 2668 (1983).

[86] N. Bretz et al., *Rev. Sci. Instrum.*, **59**, 1538 (1988).

[87] R. Fonck et al., *Rev. Sci. Instrum.*, **61**, 3487 (1990).

[88] D. M. Thomas, *Rev. Sci. Instrum.*, **66**, 806 (1995).

[89] G. Cima et al., *Rev. Sci. Instrum.*, **66**, 798 (1995).

[90] S. Coda, *An Experimental Study of Turbulence by Phase-Contrast Imaging in the DIII-D Tokamak*, PhD thesis, MIT, Cambridge, MA, 1997.

[91] N. Lopes-Cardozo, *Plasma Phys. Control. Fusion*, **37**, 799 (1995).

[92] J. Callen et al., *Nucl. Fusion*, **27**, 1857 (1987).

[93] *Evidence from Modulated ECH for convective-like Transport*, 1993, Paper presented at the Workshop on Local Transport Studies in Fusion Plasmas, GA-A21413.

[94] G. Jahns, S. Wong, R. Prater, S. Lin, and S. Ejima, *Nucl. Fusion*, **26**, 226 (1986).

[95] H. Hartfuß, H. Maassberg, and M. Tutter, *Nucl. Fusion*, **26**, 678 (1986).

[96] L. Giannone et al., *Nucl. Fusion*, **32**, 1985 (1992).

[97] T. Luce, C. Petty, and J. de Haas, *Phys. Rev. Lett.*, **68**, 52 (1992).

[98] G. Gorini et al., *Phys. Rev. Lett.*, **71**, 2038 (1993).

[99] A. Jacchia et al., *Nucl. Fusion*, **34**, 1629 (1994).

[100] J. O'Rourke, F. G. Rimini, and D. F. H. Start, *Nucl. Fusion*, **32**, 1861 (1992).

[101] R. Nachtrieb, Private communication.

[102] G. Cima, Private communication.

[103] J. Callen and G. Jahns, *Phys. Rev. Lett.*, **39**, 491 (1977).

[104] E. Fredrickson et al., *Nucl. Fusion*, **26**, 849 (1986).